TU Delft

Delft University of Technology

It's a Trap

Studying the quantum dot surface on an atomistic scale

du Fossé, I.

DOI
10.4233/uuid:af2ee2aa-564e-4702-bd36-e3c724ac76b8

Publication date
2023

Document Version
Final published version

Citation (APA)
du Fossé, I. (2023). *It's a Trap: Studying the quantum dot surface on an atomistic scale*. [Dissertation (TU Delft), Delft University of Technology]. https://doi.org/10.4233/uuid:af2ee2aa-564e-4702-bd36-e3c724ac76b8

Important note
To cite this publication, please use the final published version (if applicable).
Please check the document version above.

Copyright
Other than for strictly personal use, it is not permitted to download, forward or distribute the text or part of it, without the consent of the author(s) and/or copyright holder(s), unless the work is under an open content license such as Creative Commons.

Takedown policy
Please contact us and provide details if you believe this document breaches copyrights.
We will remove access to the work immediately and investigate your claim.

This work is downloaded from Delft University of Technology.
For technical reasons the number of authors shown on this cover page is limited to a maximum of 10.

It's a Trap

Studying the quantum dot surface on an atomistic scale

Indy du Fossé

It's a Trap

Studying the quantum dot surface on an atomistic scale

Dissertation

for the purpose of obtaining the degree of doctor
at Delft University of Technology
by the authority of the Rector Magnificus Prof. dr. ir. T. H. J. J. van der Hagen
chair of the Board for Doctorates

to be defended publicly on
Wednesday 11 January 2023 at 12:30 o'clock

by
Indy DU FOSSÉ

Master of Science in Chemical Engineering
Delft University of Technology, the Netherlands
born in Spijkenisse, the Netherlands

This dissertation has been approved by the promotors.

Prof. dr. A. J. Houtepen	Delft University of Technology, promotor
Prof. dr. F. C. Grozema	Delft University of Technology, promotor

Composition of the doctoral committee:

Rector Magnificus,	chairperson
Prof. dr. A. J. Houtepen	Delft University of Technology, promotor
Prof. dr. F. C. Grozema	Delft University of Technology, promotor

Independent members:

Prof. dr. Z. Hens	Universiteit Gent, Belgium
Prof. dr. E. A. Pidko	Delft University of Technology
Prof. dr. L. D. A. Siebbeles	Delft University of Technology
Dr. ir. M. A. van der Veen	Delft Univeristy of Technology

Other members:

Prof. dr. I. Infante	BCMaterials & Ikerbasque, Spain

This work received financial support from the European Research Council Horizon 2020 ERC Grant Agreement No. 678004 (Doping on Demand). The computational work was sponsored by NWO Exact and Natural Sciences for the use of supercomputer facilities and was carried out on the Dutch national e-infrastructure with the support of the SURF Cooperative.

ISBN: 978-94-6421-957-9
Printed by: Proefschriften.nl
An electronic version of this thesis is freely available at: https://repository.tudelft.nl

Table of Contents

1

1 Introduction

1

1.1 Introduction to Quantum Dots

When Leucippus and Democritus introduced their philosophy of atomism in the 5th century BCE, they posited that all mater consists of indivisible atoms, and that continuously dividing any object into increasingly smaller portions would eventually result in separate atoms, the characteristics of which (e.g., their size or shape) determine the properties of the bulk material.[1,2] Although their theory turned out to be remarkably similar to our current understanding of atoms, little did these ancient Greek philosophers divine that, if one reduces the dimensions of a material enough, its properties may suddenly start to depend not only on its constituent atoms, but also on the size of the particle. For example, although a gold crystal of a few cm and a gold nanoparticle of ~50 nm are both made up of the same type of atoms, the difference in size causes the former to display the characteristic yellow luster (as shown in Figure 1.1A1), whereas the latter gives a bright red color (see Figure 1.1A2).[3,4]

In order to understand and practically apply these curious phenomena, the past few decades have witnessed an enormous increase in the synthesis and study of nanometer-size particles.[5,6] Although there are many different types of nanoparticles,[4,5,7,8] this thesis will mainly be dedicated to the study of quantum dots (QDs). A QD can be defined as a nanoparticle of a semiconductor material that is small enough for quantum confinement to take place. This phenomenon, which is typically explained by either the particle-in-a-box model[9–12] or the linear combination of atomic orbitals (LCAO) theory[13–15] (and for which the interested reader is hence referred to the cited literature), causes the electronic properties of the QDs to be strongly dependent on the dimensions of the particle.

As a result of quantum confinement, the bandgap and hence the color of the QDs can be tuned simply by changing the size of the particle. For example, whilst CdSe is normally a dark red solid as displayed in Figure 1.1B1, CdSe QDs can be tailored to cover the entire visible spectrum by varying the particle size (see Figure 1.1B2). Add to this size tuneability, high color purity (due to spectrally narrow emission), high photoluminescence quantum yield (PL QY) and relatively cheap and facile synthesis, and it is little wonder that QDs are of great interest for application in optoelectronic devices.[12,16–21] Following their use in general lighting products,[21] QDs found their way to Sony's QLED television in 2013,[22,23] and the QD market has been on the rise ever since.[24]

1.2 Trap states

1.2.1 What is a Trap State?

Due to their small size, QDs have a remarkably high surface-to-volume-ratio. It is therefore not surprising that the QD surface has a significant influence on many of the QD properties,[20,29] like the energy of the band edges vs vacuum,[30–33] phonon modes,[34,35] biocompatibility,[36,37] and functionalization.[36–39] Additionally, and most relevantly for the work presented in this thesis, the surface plays an absolutely pivotal role in the creation of so-called trap states.[20,29,40–42]

A trap (also called an "in-gap state") can be defined as a localized electronic state that leads to the formation of an energy level inside the bandgap of the QD.[40,43] These in-gap

Figure 1.1. Size effects in Au nanoparticles and CdSe QDs. (A1) A synthetically grown gold crystal of a few cm, displaying the well-known yellowish luster. (A2) Reducing the size of the Au particles to ~50 nm suddenly leads to blue to red solutions, due to surface plasmon resonance.[4] (B1) Powder of CdSe, showing its dark red color. (B2) CdSe QDs of a few nm in diameter can be made to cover the visible spectrum by adjusting the size of the particles. Figures adapted from references.[25–28]

levels can capture either a conduction band (CB) electron or valence band (VB) hole, thus leading to lower PL QY.[20,44] As the presence of trap states can hence significantly hinder the efficient use of QDs in optoelectronic devices,[40,45] much research has been dedicated to passivating these traps. The most common method, epitaxial shell growth of a larger bandgap material,[44,46] has currently been optimized to reach near-unity PL QY for a variety of core materials.[47–50] Similarly high quantum yields have been obtained via optimized passivation of the surface with ligands.[51,52] Lastly, although it does not remove the in-gap states, the detrimental effect of trap states can sometimes be removed by filling the traps via chemical, electrochemical, or photochemical means.[53–57] However, note that filling unoccupied in-gap states merely changes an electron trap into a hole trap (assuming no reconstruction takes place upon charge injection), which can also quench the PL even further.[58]

It must be noted that in-gap states are not inherently detrimental to the application of QDs. For example, traps have been shown to catalyze the evolution of hydrogen,[59] and to lead to optical gain in HgTe QDs.[60] Ideally, one would like to understand and control the occurrence of traps on the surface, so that they can be avoided, or designed for a particular application. For that, a fundamental understanding of the atomistic nature of traps is imperative.

1.2.2 Atomistic Nature of Trap States

Although highly efficient methods for passivating traps have been developed, our understanding of the exact atomistic nature of trap states remains limited.[43,51,61] Moreover,

although a large body of work on traps has been published, the large number of different (model) systems and computational or experimental details makes it extremely challenging to unite all results into a single description of the QD surface and its possible structural imperfections (i.e., defects). This section aims to give an overview of how the description of trap states has been changed and refined over time, by introducing five levels of descriptive detail. With each level, the description of traps is refined by taking more details into account, as summarized in Figure 1.2.

At the first and most basic level of trap description, **level 1** in Figure 1.2, the presence of traps is simply posited. Especially in the 1980s and 1990s, at the onset of QD research, unspecified trap states were used to explain sub-bandgap PL,[62–64] or decay kinetics.[65–70] Although it was conjectured that charge carriers would localize at the surface,[65–70] or sometimes more specifically at anionic vacancies,[64,71,72] no description was given of what specific sort of atomistic configuration would lead to charge localization, or which orbitals would be involved.

The next major step in the description of trap states, **level 2** in Figure 1.2, was based on the electronic structure of QDs. In II-VI materials, the VB mainly consists of the bonding interaction between chalcogenide (e.g., S, Se or Te) p orbitals, while the CB is largely composed of the antibonding interaction between the metal (e.g., Zn, Cd or Hg) s orbitals.[43,73] Hence, nonbonding orbitals are likely to lie at an energy between the VB and CB edges, thus forming a trap in the bandgap. Initially, it was assumed that these nonbonding, or "dangling", orbitals originated from any undercoordinated atom. Thus, undercoordinated metal sites form traps closer to the CB, and undercoordinated chalcogenides traps nearer the VB. Based on this model, binding of a ligand to an undercoordinated atom should split the nonbonding orbital in a bonding and antibonding molecular orbital (MO) that, if the bond is strong enough, lie inside the VB and CB, respectively.[40,45,74] Indeed, it has been found that the addition of various types of ligands can increase the PL QY of QDs.[51,52,75–79] However, in 2013 Anderson et al. observed that the PL QY of CdSe QDs significantly increased upon a surface coverage of ~3 carboxylates/nm^2, which was significantly below a complete coverage of ~5.8 carboxylates/nm^2.[79] This suggested that not all atoms have to be fully coordinated to passivate the surface traps, and hence that not *any* undercoordinated atom creates a trap.

Further refinement of the above description of traps required an understanding of the QD surface at an atomistic level that could not (and still cannot) be attained via experimental means. The development of computational modelling has therefore played a pivotal role in the further description of trap states, as it allows one to monitor the position and electronic properties of each atom. Unfortunately, the exact nature of the QD surface remains unclear, leading to a great variety of model QDs that have been used, differing in e.g., size, shape, passivation (e.g., no ligands,[80–82] pseudoatoms,[83,84] or a combination of L-, X- and Z-type ligands[32,43,85–87]), and charge balance. In this thesis, the focus will mainly lie on studies on (initially) charge balanced QDs with explicit ligand passivation (i.e., no pseudoatoms), as these models most accurately capture experimental observations. See section 1.3.2.2 for a more detailed discussion of the strengths and limitations of the QD models used in this thesis, and the definition of charge balance.

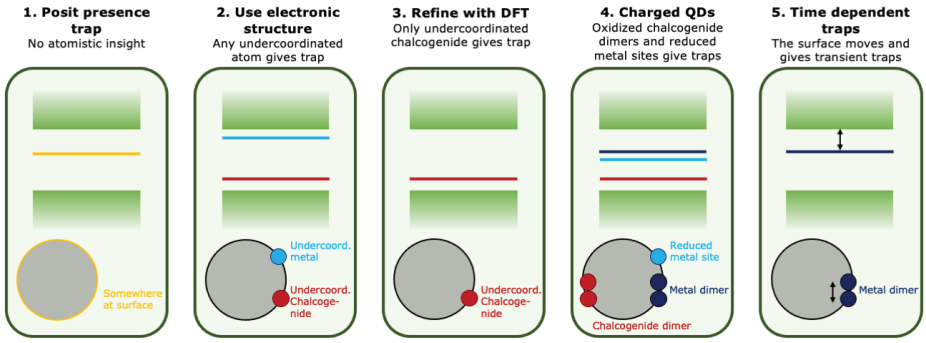

Figure 1.2. Five levels of describing trap states. Level 1: the presence of a trap state is posited; its atomistic origins are not specified. Level 2: based on the QD electronic structure, each undercoordinated atom is assumed to give a trap state. Level 3: DFT calculations show that only undercoordinated chalcogenide atoms give a trap. Level 4: Charge unbalanced QDs can give rise to in-gap states not present in charge balanced QDs, like reduced metal sites and chalcogenide dimers. Level 5: the QD surface is continually in motion, leading to the dynamic formation and disappearance of trap states.

Using density functional theory (DFT, see section 1.3), Houtepen et al. refined the description of level 2 by demonstrating that specifically 2-coordinated chalcogenide atoms are responsible for trap formation in charge balanced II-VI and III-V QDs (see **level 3** in Figure 1.2).[43] Although the effect of 2-coordinated chalcogenides had been reported earlier,[53] Houtepen et al. were the first to explain why the chalcogenide, as opposed to the metal, is responsible for trap formation. As mentioned previously, the VB mainly comprises the chalcogenide p orbitals. If a chalcogenide atom is only coordinated to two neighboring atoms, there will always be one p orbital which sticks out orthogonally to those bonds. This dangling orbital will hence remain in the bandgap as a nonbonding orbital. In contrast, the metal mainly contributes to the CB with an s orbital. Due to the spherical symmetry of this orbital, it will be split into an antibonding and bonding orbital, even for a singly coordinated surface metal atom.[43]

This work then predicts that there is only a single source of surface trapping, namely on 2-coordinated surface anions. However, there are several experimental indications that the nature of in-gap states is more complex. For instance, L-type ligands like amines or phosphines have been observed to increase the PL QY,[51,77,78,88] even though they are expected to bind to the metal ions and not the anions. Additionally, spectroelectrochemical experiments on CdSe and CdTe QDs indicate a distribution of traps states just below the CB,[58] in addition to a distribution of trap states above the VB.[53] The latter are assigned to 2-coordinated surface anions. The former most likely hint to Cd related traps, which are not found in the DFT calculations on neutral, charge balanced QDs.

However, in many applications, QDs that are charge *unbalanced* may be more relevant than charge balanced QDs. An obvious example of this is the electronic doping of QDs to tailor their properties to the specific requirements of an application.[89,90] However, QDs

may also get (temporarily) charged in devices that rely on charge injection into the QDs, like light-emitting diodes (LEDs).[12,91] Likewise, any slight unbalance in the extraction of electrons and holes in QD solar cells may lead to the charging of the QDs.[92,93] The presence of these excess charge carriers can result in the formation of new surface configurations that are not observed in charge balanced QDs. Afterall, it is well established that charging of bulk semiconductors often leads to degradation of the material.[94–97] Hence, the next step in the description of traps is to consider QDs that are not charge balanced (**level 4** in Figure 1.2).

Charge unbalanced QDs can be created by changing the stoichiometry between metal and chalcogenide,[98] varying the amount of X-type ligands on the surface,[41,99,100] or injecting extra electrons or holes.[101–107] In PbS, charge unbalance has been observed to lead to the formation of Pb-Pb dimers,[41,99] or the (partial) reduction of surface Pb.[98,108] As discussed in more detail in Chapter 3, DFT studies on electron injection in CdTe QDs show the same trends. Charging of a perfectly passivated QD eventually leads to the reduction of surface Cd. Upon reduction, the Cd^0 is ejected from the (111) facet and forms a highly localized in-gap state. If an imperfectly passivated QD is charged (i.e., where a Cl^- ligand has been moved to a suboptimal location), Cd-Cd dimers can be formed. In that case, the 5s orbitals of the two Cd atoms start to overlap, pushing a bonding MO into the bandgap, where it forms a trap state.[100] Subsequent studies revealed that the addition of L-type ligands can prevent Cd-reduction, either by sterically blocking the dimerization,[100] or by stabilizing surface Cd.[32]

Although a reasonable amount of work has been published on the formation of trap states in n-doped QDs, research on traps in p-doped QDs remains scarce. For CdSe, it is known that oxidation can lead to the formation of Se-dimers via a process analogous to the formation of metal dimers under electron injection.[29,109,110] A recent study on ZnSe showed that oxidation-induced traps can be removed from the bandgap by increasing the size of the QD beyond a critical diameter.[111] Yet, even for a material as prone to oxidation as InP, studies have mainly been limited to (001) surfaces,[112–114] indicating that still much can be learned about traps in oxidized QDs.

In view of traps that are created through the presence of CB electrons or VB holes, photoexcitation of the QD presents an interesting case. Although the QD remains charge balanced upon excitation, it does contain charge carriers with sufficient electrochemical potential (i.e., an electron in the CB and a hole in the VB) to cause photodegradation in bulk semicondutors.[94] Indeed, as will be described in more detail in Chapter 4, it has been found that in CdSe QDs, a photoexcited CB electron can be trapped in an in-gap state that is formed by the presence of that CB electron. Upon recombination of the trapped electron with a VB hole, or if the electron is de-trapped to the CB, the trap will disappear again.[110]

This type of transient trap states, i.e., traps that are not always present but appear and disappear depending on the conditions, leads to the final level of description of trap states (**level 5** in Figure 1.2). In this description, it is taken into account that QDs are not static. Instead, due to random thermal motion, both the inorganic QD and its ligand shell are

continuously moving, taking on new configurations in the process. To accurately describe these effects, one can no longer consider *one* specific surface configuration to be a trap, but has to consider how the atoms and hence the trap change over time. Voznyy et al. were one of the first to show with molecular dynamics (MD) simulations that random configurational changes due to thermal motion can lead to the temporary formation of surface localized states,[85] a result also found in later studies.[115] MD simulations have also been used to study the transient nature of Cd-Cd dimers,[110] and Se-Se dimers in CdSe QDs.[110,116]

1.2.3 Future Challenges

Although our understanding of trap states has improved significantly during the past few years, some big challenges still lie ahead. One of these, which is addressed in more detail in Chapter 7, concerns the localization of the band edge levels at the surface in DFT calculations of larger QD models, which has been observed both for QDs[85] and nanoplatelets.[117] These effects are most likely related to reconstructions of the surface. Although most QD models present facets that are obtained directly from cleaving the bulk, it is known, especially from studies on bulk GaAs facets, that both the metal-terminated (111) and the chalcogenide-terminated ($\overline{111}$) facets display significant reconstructions.[118] For (111) facets, most literature suggests that reconstruction entails the removal of 25% of the surface metal atoms.[119] Reconstruction of the ($\overline{111}$) facet is more complicated and multiple configurations have been proposed.[120,121] Voznyy et al.[85] showed that the introduction of surface vacancies can prevent localization of the HOMO and LUMO orbitals on the surface. However, it remains unclear if these vacancies are truly present on the QD surface, and, if so, what surface configurations are formed.

Another challenge lies in the creation of model systems that more closely resemble QDs in experiment (see also section 1.3.2.2). To limit computational costs, model systems are often smaller than in experiments, aliphatic X-type ligands are replaced by halides or short-chained carboxylates, and L-type ligands and solvents are often not included. Although all these factors can influence the formation of traps, see for example Chapter 5, calculations on such large and complex systems are often limited by the high computational cost. Recent years have therefore seen the development of computationally less demanding approaches, based on classical force fields.[122,123]

1.3 Density Functional Theory

As already mentioned in the preceding section, computational methods have the distinct advantage over experimental methods that they provide detailed insight on an atomistic scale that is difficult to obtain in experiments. Many of the chapters in this thesis (see section 1.4 for a detailed outline) therefore make use of DFT calculations to study surface traps in QDs. In this section, a brief introduction of the fundamentals of DFT will first be given. Then, we will look into more detail at the limitations of DFT and the specific assumptions that have been made for the work presented in this thesis.

1.3.1 Fundamentals of DFT[124–126]

For many applications, the holy grail of computational chemistry would be to solve the

Schrödinger equation, even if it were only the time-independent and non-relativistic one (equation 1.1), to obtain the ground state wavefunction, and with it, all ground state properties of the system:

$$\hat{H}\Psi(\vec{R},\vec{r}) = E\Psi(\vec{R},\vec{r}) \quad 1.1$$

Here, $\vec{R}$ stands for the spatial coordinates of the nuclei, while $\vec{r}$ refers to the combination of the spatial coordinates and the spin of the electrons. The Hamiltonian operator $\hat{H}$ gives the total energy of the system in terms of, respectively, the kinetic energy of all N_e electrons, the kinetic energy of all N_n nuclei, the electron-nucleus interaction, the electron-electron interaction, and the nucleus-nucleus interaction:

$$\hat{H} = -\frac{1}{2}\sum_{i=1}^{N_e}\nabla_i^2 - \frac{1}{2}\sum_{A=1}^{N_n}\nabla_A^2 - \sum_{i=1}^{N_e}\sum_{A=1}^{N_n}\frac{Z_A}{r_{iA}} + \sum_{i=1}^{N_e}\sum_{j>i}^{N_e}\frac{1}{r_{ij}} + \sum_{A=1}^{N_n}\sum_{B>A}^{N_n}\frac{Z_A Z_B}{R_{AB}} \quad 1.2$$

Here, i and j run over the electrons, whilst A and B run over the nuclei. The wavefunction in equation 1.1 is a function of the spatial coordinates of the electrons and nuclei, and the spin of the electrons, meaning equation 1.1 depends on $4N_e + 3N_n$ variables. For a relatively small QD model, e.g., $Cd_{68}Se_{55}Cl_{26}$, this would already lead to the prodigious number of over 22,000 variables. Clearly, the equation must be significantly simplified to make it practicable.

The first simplification, the well-known Born-Oppenheimer approximation, was proposed in 1927.[127] As nuclei are orders of magnitude heavier than electrons, the former move much slower than the latter. As a result, we can approximate the electrons as moving in an external potential, created by the nuclei at fixed positions. As the nuclei are assumed to be fixed, their kinetic energy is zero, the nuclear-nuclear interaction is a constant, and the positions of the nuclei are now only used as parameters, not variables. This leads to the electronic Schrödinger equation, which uses the electronic Hamiltonian $\hat{H}_e$, and wavefunction Ψ_e:

$$\hat{H}_e\Psi_e(\vec{r}) = E_e\Psi_e(\vec{r}) \quad 1.3$$

$$\hat{H}_e = -\frac{1}{2}\sum_{i=1}^{N_e}\nabla_i^2 - \sum_{i=1}^{N_e}\sum_{A=1}^{N_n}\frac{Z_A}{r_{iA}} + \sum_{i=1}^{N_e}\sum_{j>i}^{N_e}\frac{1}{r_{ij}} = \hat{T} + \hat{V}_{ne} + \hat{V}_{ee} \quad 1.4$$

The attractive interaction between the electrons and nuclei (i.e., the expectation value of $\hat{V}_{ne}$ in equation 1.4) is often referred to as the external potential V_{ext}, although V_{ext} can also contain magnetic, electric or other applied fields. Addition of the nucleus-nucleus interaction (i.e., the last term in equation 1.2) gives the total energy of the system.

In spite of the Born-Oppenheimer approximation, equation 1.3 still depends on over 16,000 spatial electronic coordinates. The next big step, and concomitantly the birth of DFT, came in 1964 with the publication of the seminal paper by Hohenberg and Kohn.[128] In that work, they proved that, instead of the $3N_e$-dimensional wavefunction, the

3-dimensional electron density can also be used to determine the ground state properties of the system. Note how for our simple QD model, this approach suddenly decreases the spatial dimensionality from over 16,000 to 3.

Hohenberg and Kohn's proof is based on two, deceptively simple, theorems. The first theorem states that the external potential (V_{ext}) is a unique functional of the electron density ($\rho(\vec{r})$) (apart from a trivial constant). As a result, knowing the electron density, uniquely defines V_{ext}, which in turn determines $\hat{H}$ and allows one (in principle) to determine the ground state wavefunction Ψ. The second theorem, which is in fact the variational principle expressed in terms of the electron density, states that the electron density that minimizes the total energy of the system is the ground state electron density.

Although fundamentally of great importance, the work by Hohenberg and Kohn could not be immediately used in practice. As shown in equation 1.5, they showed that the total energy of the system could be expressed in a system-dependent part due to electron-nucleus interactions, and a system-independent part (the Hohenberg-Kohn functional $F_{HK}[\rho]$), that accounted for the kinetic energy, the Coulomb interaction between electrons, and the non-classical self-interaction correction, exchange and correlation effects.

$$E[\rho(\vec{r})] = \int \rho(\vec{r}) V_{ext} d\vec{r} + F_{HK}[\rho(\vec{r})] = \int \rho(\vec{r}) V_{ext} d\vec{r} + T[\rho(\vec{r})] + J[\rho(\vec{r})] + E_{ncl}[\rho(\vec{r})] \qquad 1.5$$

Here $T[\rho(\vec{r})]$, $J[\rho(\vec{r})]$ and $E_{ncl}[\rho(\vec{r})]$ stand for the kinetic energy, classical Coulomb interaction and the non-classical effects, respectively. Unfortunately, the expressions for neither $T[\rho(\vec{r})]$ nor $E_{ncl}[\rho(\vec{r})]$ are known, making equation 1.5 in itself rather useless. Luckily, Kohn and Sham came with a highly influential solution in 1965.[129] Instead of starting with the real system of interacting particles and trying to figure out the form of $T[\rho(\vec{r})]$ and $E_{ncl}[\rho(\vec{r})]$ for that system, they decided to start from a system of non-interacting particles that has the same electron density $\rho(\vec{r})$ as the interacting system. As the kinetic energy for a non-interacting system is known, this allowed them to write the Hohenberg-Kohn functional as:

$$F_{HK}[\rho(\vec{r})] = T[\rho(\vec{r})] + J[\rho(\vec{r})] + E_{ncl}[\rho(\vec{r})] = T_S[\rho(\vec{r})] + J[\rho(\vec{r})] + E_{XC}[\rho(\vec{r})] \qquad 1.6$$

Here, $T_S[\rho(\vec{r})]$ is the kinetic energy of the non-interacting system. In essence, $E_{XC}[\rho(\vec{r})]$ is the collection of all the difficult terms we do not know, including all non-classical effects and a correction for the kinetic energy.

A salient point of this derivation is that, apart from the Born-Oppenheimer approximation, no approximations have been made, and hence, that DFT is an exact method. That is, if the exact form of the exchange-correlation functional $E_{XC}[\rho(\vec{r})]$ were known. As (alas) the exact exchange-correlation functional is not known, and the quality of a DFT calculation heavily relies on the quality of the functional, much effort has been invested in developing better functionals.[130,131] In its simplest form, called the local density approximation (LDA), the value of $E_{XC}[\rho(\vec{r})]$ at a particular position only depends on the electron density at that position. Increasing the level of detail, the generalized gradient approximation (GGA) also takes the gradient of the electron density at each position into account. Although the PBE

(Perdew-Burke-Ernzerhof) functional is probably the most widely-used GGA functional (it is also used in this thesis),[130] a multitude of other GGA functionals are available, like PBEsol, BLYP and BP86.[125,130] Meta-GGAs, like SCAN, also include the Laplacian of the electron density or kinetic energy density.[130,131] Hybrid functionals, like B3LYP, HSE06 and PBE0, include a fraction of exact exchange from Hartree-Fock theory.[125,131] Although much more can be said about the fundamental details and practical performance of these exchange-correlation functionals, a complete discussion thereof is beyond the scope of this introduction.

Lastly, in order to approximate the ground state density, we can express the electron density in terms of one-electron orbitals (using that $\rho = \sum_{i=1}^{N_e} \langle \phi_i | \phi_i \rangle$) and then calculate which set of orbitals minimizes the total energy, provided the orbitals remain orthonormal.* The derivation, which is analogous to the procedure in Hartree-Fock theory, is given in more detail in, for example, the introductory work by Jensen.[126] The final result is given by equation 1.7.

$$\hat{h}_i^{KS}\phi_i = \left(-\frac{1}{2}\nabla^2 + \int \frac{\rho(\vec{r}_2)}{r_{12}} d\vec{r}_2 + V_{XC}(\vec{r}_1) - \sum_{A=1}^{N_n} \frac{Z_A}{r_{1A}} \right) \phi_i = \epsilon_i \phi_i \qquad 1.7$$

As $\hat{h}_i^{KS}$ depends on the electron density (and by extension on the orbitals), equation 1.7 has to be solved iteratively. An initial guess for the electron density allows $\hat{h}_i^{KS}$ to be determined, after which the equations can be solved, leading to a new electron density. Once the input and output electron density are the same (or differ negligibly), self-consistency has been reached.

The last point that remains to be discussed concerns the way in which the ϕ_i orbitals are expressed. Often, this is done through an LCAO approach, using a set of L basis functions η_μ:

$$\phi_i = \sum_{\mu=1}^{L} c_{\mu i} \eta_\mu \qquad 1.8$$

A complete discussion of all the details of basis functions (e.g., Slater vs Gaussian type orbitals, contracted functions, multiple-ζ functions, polarization functions etc.) could easily double the length of this introduction. The key point is that the basis functions are a mathematical means of describing the shape of the orbitals (and hence the distribution of the electron density) in the system, which allows us to write equation 1.7 in the form of a matrix equation, consisting of the Kohn-Sham matrix F^{KS}, overlap matrix S, coefficient matrix C, and a diagonal matrix with the orbital energies ϵ:

*It must be noted that the introduction of these orbitals again increases the degrees of freedom to 3N (with N the number of orbitals). Using orbital-free DFT, it is possible to circumvent the introduction of orbitals and compute the electronic structure using functionals of the electron density. However, orbital-free DFT is generally less accurate than Kohn-Sham DFT, mainly due to difficulties in obtaining the kinetic energy from the electron density.[161,162]

$$F^{KS}C = SC\varepsilon \tag{1.9}$$

$$F_{\mu\nu}^{KS} = \int \eta_\mu(\vec{r}_1)\hat{h}^{KS}(\vec{r}_1)\eta_\nu(\vec{r}_1)d\vec{r}_1 \tag{1.10}$$

$$S_{\mu\nu} = \int \eta_\mu(\vec{r}_1)\eta_\nu(\vec{r}_1)d\vec{r}_1 \tag{1.11}$$

$$C = \begin{pmatrix} c_{11} & \cdots & c_{1L} \\ \vdots & \ddots & \vdots \\ c_{L1} & \cdots & c_{LL} \end{pmatrix} \tag{1.12}$$

$$\varepsilon = \begin{pmatrix} \varepsilon_1 & \cdots & 0 \\ \vdots & \ddots & \vdots \\ 0 & \cdots & \varepsilon_L \end{pmatrix} \tag{1.13}$$

By using the LCAO approach to describe the orbitals, the difficult problem of equation 1.7 has been transformed into the linear matrix equation of equation 1.9, which can be efficiently solved by computer programs.

1.3.2 Limitations of DFT

Despite the obvious advantages of DFT, it is no infallible panacea. Inherently to DFT, the accuracy of the calculations is determined by the choice of exchange-correlation functional, basis set, and other computational details. Moreover, in contrast to, for example, studies on small molecules, it is not exactly known what a QD looks like on an atomistic scale. Hence, certain assumptions or simplifications have to be made for the QD models that are used. This section first addresses the limitations inherent to DFT itself. Next, it discusses the accuracy of the QD model and the ways in which it may differ from real QDs under experimentally relevant conditions. It is important to note that there is a delicate balance between these two aspects and that it is of no use to calculate in tremendous detail the properties of a QD model that is entirely unrealistic.

1.3.2.1 Accuracy of the Computational Methods

In view of the large size of the QD models, and in agreement with various previous studies,[41,43,86,132] many calculations presented in this thesis make use of the relatively inexpensive PBE functional and double-ζ basis set, and neglect spin-orbit coupling. Although Azpiroz et al. showed in their benchmark study in 2014 that the hybrid PBE0 is the overall best performing functional for II-VI QDs, PBE was found to be the best GGA functional, especially for predicting geometries.[133] A well-known shortcoming of PBE (and GGA's in general), is its tendency to underestimate the bandgap of semiconductors.[134,135] Although it has been found that the use of hybrid functionals[135] (or the use of the rather prosaic "scissor operator" method)[136] can better reproduce experimental bandgaps, the trends or qualitative results that are found with GGA's can generally still be used.[110,137]

Another challenge specifically for geometry optimizations, is finding the global energy minimum.[138] Due to their large size, QDs have a complicated and often shallow potential energy surface (PES), meaning that structures will often relax to a local minimum. Although chemical intuition, realistic starting structures, and the sampling of the PES through MD simulations can help detect some local minima, finding the true global minimum is nigh impossible for these systems. However, as discussed in more detail in Chapter 4,

finding the global minimum is not as informative as it may seem. Precisely because of the shallow and complicated PES, QDs under experimental conditions are likely to sample a whole number of local minimums and related structures due to random thermal motion.

Although immensely popular, DFT is not the only computational method that can be used to study QDs. As discussed previously in Section 1.2.3, force field methods allow the simulation of larger systems at a significantly reduced computational cost.[122,123,139] For example, Cosseddu et al. used a classical force field to simulate the dynamics of a ~4 nm CdSe QD with oleate ligands in an explicit solvent.[123] However, as the force field parameters were fitted based on an ab initio MD simulation, it may not accurately describe the dynamics of the QD upon charging or excitation. For the calculation of electronic properties, tight-binding methods have been shown to be able to accurately describe experimentally measured spectra.[140–143] Although tight-binding methods can handle larger systems than DFT,[144] they do require parameters to be fitted to data from experiments or higher levels of theory.[140,145] Pseudopotential methods, in which the electron-electron and electron-nucleus interactions are replaced by atom centered pseudopotentials,[146,147] can also be used to compute the electronic structure and carrier dynamics of QDs,[83,148–150] although they again require fitting to experimental or ab initio data.[146,147] In short, whilst tight-binding and pseudopotential methods are often used for computing realistic bandgaps and optical properties, DFT is better suited to studying the surface and geometry of realistic structures.[151] As the atomistic nature of surface defects forms the center of the work presented in this thesis, all calculations have been carried out using DFT.

1.3.2.2 Accuracy of the QD Model

In addition to the computational methods, another source of uncertainty lies in the fact that it is not exactly known what the QD surface looks like, and even the things that are known cannot always be included in view of the required computational power. Nevertheless, the QD models used in this thesis are built to mirror the experimental observations as closely as possible. Based on TEM imaging, it is known that II-VI QDs are generally roughly spherical (although many different shapes are possible).[5,14,20] Moreover, they are often found to be cation-rich.[79,152] These properties are reflected in the $M_{68}C_{55}X_{26}$ (M = Zn^{2+}, Cd^{2+}; C = S^{2-}, Se^{2-}, Te^{2-}; X = Cl^-, Br^-, I^-, $HCOO^-$ etc.) model that is used throughout this thesis, and which is also shown in Figure 1.3. However, as the computational costs increase significantly with the size of the particle (most methods scale with the cube of the system size, although linear scaling is possible),[153,154] the model QD, with a diameter of ~2 nm, is quite small compared to typical QD sizes.[155]

A key assumption made for the models in this thesis is that of charge balance. This is motivated by the fact that QDs in vacuum or non-polar solvents are unlikely to be significantly charged. Approximating the QD as a metal (i.e., $\epsilon_{in} >> \epsilon_{out}$), the energy ($E_C$) required to charge a QD with N electron charges is given by:[156]

$$E_C \approx (2N-1)\frac{e^2}{8\pi\varepsilon_0\varepsilon_{out}R} \qquad 1.14$$

Thus, charging a QD of R = 1.5 nm in vacuum (ϵ_{out}=1) with 3 electron charges costs 2.4 eV, which is almost 100 k_BT at room temperature. In solvents this will be reduced, but

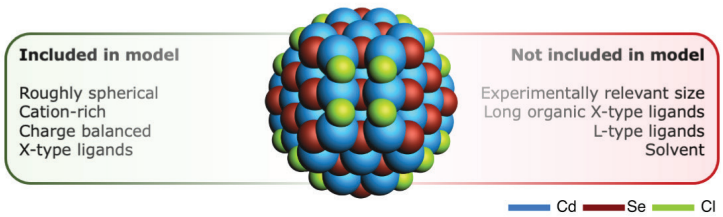

Figure 1.3. The experimental observations that are emulated by the standard QD model used in this thesis. To limit the computational costs, the model is relatively small, and does not include long organic ligands or solvent effects by default. These aspects are only included when specifically the subject of investigation, as is the case for L-type ligands and solvent in Chapter 5, and larger QDs in Chapter 7.

unless the solvent is polar (and especially if it contains an electrolyte) this reduction will be marginal and it is reasonable to assume the QD is neutral.

The distinction between charge balanced and charge unbalanced systems can be made by the model of Voznyy et al.,[157] which assumes that each QD is charge neutral. It calculates the number of excess electrons <n> through:

$$\langle n \rangle = \sum_i N_I \times q_i \qquad 1.15$$

Here, N_i is the number of atoms of type i, and q_i is the preferred oxidation state of element i (e.g., Cd^{2+}, Se^{2-}, Cl^-). If <n> > 0, the system contains excess electrons, meaning it is n-doped. A p-doped system is indicated by <n> < 0. However, note that the preferred oxidation state of an element is not always clear. For example, in InP QDs an undoped QD is obtained by taking the oxidation state of phosphorous to be P^{3-}. Subsequent oxidation of the QD can lead to the formation of PO_4^{3-} without the formation of in-gap states, implying that the oxidation state of the oxidized phosphorous has been changed to P^{5+}.[158] Hence, equation 1.15 is perhaps best regarded as a good starting point for the investigation and discussion of traps in QDs.

To compensate for the excess positive charge of the cation-rich model system, the QD is passivated by negatively charged X-type ligands. In practice, these are often long oleate ligands.[40,99] However, to limit the computational costs, usually halides[117,159] or small carboxylic acids[32,99,160] are used. To further limit the complexity of the system, L-type ligands like amines, and solvent effects are often neglected, unless their effect is directly investigated, as in Chapter 5.

1.4 Outline of this Thesis

This thesis, dedicated to the study of trap states in QDs, is subdivided into three parts and seven chapters. Part A, "Experimental studies", (Chapter 2) concerns the study of trap states via spectroelectrochemistry. In part B, "Theoretical studies", (Chapters 3-6) DFT calculations are used to understand the atomistic details of traps. Part C, "Loose ends",

(Chapter 7) is dedicated to some of the observations that remain unclear at the end of this PhD project.

In **Chapter 2**, spectroelectrochemistry is used to study the trap states in CdTe QDs before and after passivation with different metal chloride salts. $CdCl_2$ is found to bind to the QD surface as a Z-type ligand, thus passivating 2-coordinated Te^{2-} and increasing the PL by a factor of 40. In contrast, with $ZnCl_2$, only the chloride anions bind to the surface. Although these X-type ligands cannot bind to 2-coordinated Te^{2-} ions, the PL does increase 4-fold. These results therefore suggest that, although undercoordinated Te^{2-} ions form the majority of the traps in CdTe, some Cd-based traps that can be passivated by Cl^- are also likely to exist.

In **Chapter 3**, we use DFT calculations to investigate what these Cd-related traps look like on an atomistic scale. Charging a CdTe model QD with an increasing number of electrons leads to reduction of surface Cd and the formation of in-gap states when multiple electrons are added. Charging a QD where a chloride ligand has been moved to a suboptimal position leads to a trap in the form of a Cd-Cd dimer at already one extra electron. This study shows that Cd-based traps may form in negatively charged QDs.

In **Chapter 4**, we show that Cd-Cd dimers also form in charge neutral, but photoexcited QDs. Ab initio MD simulations are used to show that Cd-Cd dimers are transient in nature, appearing and disappearing on the picosecond timescale. Non-radiative decay from the trap to the VB is estimated to be much faster than radiative recombination, indicating that these traps can quench the PL.

In **Chapter 5**, we investigate the effect of ligands and solvent on the reduction of Cd in CdSe QDs. Although changing the X-type ligands or the surrounding solvent only has a small effect on the stability of n-doped QDs, binding L-type ligands directly to the most labile Cd-sites significantly enhances the stability of the QD against surface reduction.

Chapter 6 is dedicated to traps in perovskite nanocrystals (NCs). We show that the traditional picture of defect tolerance in perovskites is incomplete, and that the local electrostatic potential should also be included to explain deep Br^- traps that are shown to be present on the surface. These results suggest that traps can be passivated not only by direct covalent binding, but also by adjusting the local electrostatic environment to push the localized level out of the bandgap.

Finally, in **Chapter 7** we focus on DFT calculations on larger QDs. It has previously been observed that increasing the size of the model system leads to localization of the band edge levels on the surface. Here, we show that, although passivation with additional Z- or L-type ligands slightly improves the delocalization, surface reconstructions are required to completely delocalize the HOMO and LUMO.

References

1. Taylor, C. W. The atomists. in The Cambridge Companion to Early Greek

Philosophy (ed. Long, A. A.) 181–204 (Cambridge University Press, 1999).
2. Berryman, S. Ancient Atomism. in The Stanford Encyclopedia of Philosophy (ed. Zalta, E. N.) (Metaphysics Research Lab, Stanford University, 2016).
3. Louis, C. & Pluchery, O. Gold Nanoparticles For Physics, Chemistry And Biology. (Imperial College Press, 2021).
4. Eustis, S. & el-Sayed, M. a. Why gold nanoparticles are more precious than pretty gold: noble metal surface plasmon resonance and its enhancement of the radiative and nonradiative properties of nanocrystals of different shapes. Chem. Soc. Rev. 35, 209–217 (2006).
5. Park, J., Joo, J., Soon, G. K., Jang, Y. & Hyeon, T. Synthesis of monodisperse spherical nanocrystals. Angew. Chemie - Int. Ed. 46, 4630–4660 (2007).
6. Rogach, A. L., Talapin, D. V., Shevchenko, E. V., Kornowski, A., Haase, M. & Weller, H. Organization of matter on different size scales: Monodisperse nanocrystals and their superstructures. Adv. Funct. Mater. 12, 653–664 (2002).
7. Frey, N. A., Peng, S., Cheng, K. & Sun, S. Magnetic nanoparticles: synthesis, functionalization, and applications in bioimaging and magnetic energy storage. Chem. Soc. Rev. 38, 2532–2542 (2009).
8. Park, J., Kwon, T., Kim, J., Jin, H., Kim, H. Y., Kim, B., Joo, S. H. & Lee, K. Hollow nanoparticles as emerging electrocatalysts for renewable energy conversion reactions. Chem. Soc. Rev. 47, 8173–8202 (2018).
9. Chukwuocha, E. O., Onyeaju, M. C. & Harry, T. S. T. Theoretical Studies on the Effect of Confinement on Quantum Dots Using the Brus Equation. World J. Condens. Matter Phys. 02, 96–100 (2012).
10. Kippeny, T., Swafford, L. A. & Rosenthal, S. J. Semiconductor nanocrystals: A powerful visual aid for introducing the particle in a box. J. Chem. Educ. 79, 1094–1100 (2002).
11. Brus, L. Electronic wave functions in semiconductor clusters: Experiment and theory. J. Phys. Chem. 90, 2555–2560 (1986).
12. Pietryga, J. M., Park, Y.-S., Lim, J., Fidler, A. F., Bae, W. K., Brovelli, S. & Klimov, V. I. Spectroscopic and Device Aspects of Nanocrystal Quantum Dots. Chem. Rev. 116, 10513–10622 (2016).
13. Alivisatos, A. P. Perspectives on the physical chemistry of semiconductor nanocrystals. J. Phys. Chem. 100, 13226–13239 (1996).
14. Rogach, A. L. Semiconductor Nanocrystal Quantum Dots. (Springer Wien New York, 2008). doi:10.1007/978-3-211-75237-1.
15. Koole, R., Groeneveld, E., Vanmaekelbergh, D., Meijerink, A. & Donegá, C. de M. Size Effects on Semiconductor Nanoparticles. in Nanoparticles: Workhorses of Nanoscience (ed. Donegá, C. de M.) 13–51 (Springer, 2014). doi:10.1007/978-3-662-44823-6.
16. Shirasaki, Y., Supran, G. J., Bawendi, M. G. & Bulović, V. Emergence of colloidal quantum-dot light-emitting technologies. Nat. Photonics 7, 13 (2013).
17. Steckel, J. S., Ho, J., Hamilton, C., Xi, J., Breen, C., Liu, W., Allen, P. & Coe-Sullivan, S. Quantum dots: The ultimate down-conversion material for LCD displays. J. Soc. Inf. Disp. 23, 294–305 (2015).
18. Talapin, D. V., Lee, J.-S., Kovalenko, M. V. & Shevchenko, E. V. Prospects of Colloidal Nanocrystals for Electronic and Optoelectronic Applications. Chem.

Rev. 110, 389–458 (2010).
19. Grim, J. Q., Manna, L. & Moreels, I. A sustainable future for photonic colloidal nanocrystals. Chem. Soc. Rev. 44, 5897–5914 (2015).
20. Donegá, C. de M. Synthesis and properties of colloidal heteronanocrystals. Chem. Soc. Rev. 40, 1512–1546 (2011).
21. Talapin, D. V. & Steckel, J. Quantum dot light-emitting devices. MRS Bull. 38, 685–691 (2013).
22. Bullis, K. Quantum Dots Get Commercial Debut in More Colorful Sony TVs. MIT Technology Review https://www.technologyreview.com/2013/01/11/180532/quantum-dots-get-commercial-debut-in-more-colorful-sony-tvs/#:~:text=Technology from QD Vision replaces,LCDs%2C allowing for purer colors.&text=Sony is using nanoscale particles,its high-end Bravia televi (2013).
23. Bourzac, K. Quantum dots go on display. Nature 493, 283 (2013).
24. Hotz, C. & Yurek, J. Quantum Dot-Enabled Displays. in Advanced Display Technology: Next Generation Self-Emitting Displays 229–250 (Springer, 2021).
25. Au nanoparticles. https://commons.wikimedia.org/wiki/File:Au_nanoparticles.jpg.
26. Gold-crystals. https://commons.wikimedia.org/wiki/File:Gold-crystals.jpg.
27. Cadmium selenide 2. https://commons.wikimedia.org/wiki/File:Cadmium_selenide_2.jpg.
28. CdSe Quantum Dots. https://commons.wikimedia.org/wiki/File:CdSe_Quantum_Dots.jpg.
29. Hartley, C. L., Kessler, M. L. & Dempsey, J. L. Molecular-Level Insight into Semiconductor Nanocrystal Surfaces. J. Am. Chem. Soc. 143, 1251–1266 (2021).
30. Brown, P. R., Kim, D., Lunt, R. R., Zhao, N., Bawendi, M. G., Grossman, J. C. & Bulović, V. Energy Level Modification in Lead Sulfide Quantum Dot Thin Films through Ligand Exchange. ACS Nano 8, 5863–5872 (2014).
31. Kroupa, D. M., Vörös, M., Brawand, N. P., McNichols, B. W., Miller, E. M., Gu, J., Nozik, A. J., Sellinger, A., Galli, G. & Beard, M. C. Tuning colloidal quantum dot band edge positions through solution-phase surface chemistry modification. Nat. Commun. 8, 15257 (2017).
32. du Fossé, I., Lal, S., Hossaini, A. N., Infante, I. & Houtepen, A. J. Effect of Ligands and Solvents on the Stability of Electron Charged CdSe Colloidal Quantum Dots. J. Phys. Chem. C 125, 23968–23975 (2021).
33. Shalom, M., Rühle, S., Hod, I., Yahav, S. & Zaban, A. Energy Level Alignment in CdS Quantum Dot Sensitized Solar Cells Using Molecular Dipoles. J. Am. Chem. Soc. 131, 9876–9877 (2009).
34. Yazdani, N., Bozyigit, D., Vuttivorakulchai, K., Luisier, M., Infante, I. & Wood, V. Tuning Electron-Phonon Interactions in Nanocrystals through Surface Termination. Nano Lett. 18, 2233–2242 (2018).
35. Schnitzenbaumer, K. J. & Dukovic, G. Comparison of Phonon Damping Behavior in Quantum Dots Capped with Organic and Inorganic Ligands. Nano Lett. 18, 3667–3674 (2018).
36. Wolfbeis, O. S. An overview of nanoparticles commonly used in fluorescent bioimaging. Chem. Soc. Rev. 44, 4743–4768 (2015).
37. Wegner, K. D. & Hildebrandt, N. Quantum dots: bright and versatile in vitro and

in vivo fluorescence imaging biosensors. Chem. Soc. Rev. 44, 4792–4834 (2015).
38. Biju, V. Chemical modifications and bioconjugate reactions of nanomaterials for sensing, imaging, drug delivery and therapy. Chem. Soc. Rev. 43, 744–764 (2014).
39. Erathodiyil, N. & Ying, J. Y. Functionalization of Inorganic Nanoparticles for Bioimaging Applications. Acc. Chem. Res. 44, 925–935 (2011).
40. Boles, M. A., Ling, D., Hyeon, T. & Talapin, D. V. The surface science of nanocrystals. Nat. Mater. 15, 141–153 (2016).
41. Giansante, C. & Infante, I. Surface Traps in Colloidal Quantum Dots: A Combined Experimental and Theoretical Perspective. J. Phys. Chem. Lett. 8, 5209–5215 (2017).
42. Katsiev, K., Ip, A. H., Fischer, A., Tanabe, I., Zhang, X., Kirmani, A. R., Voznyy, O., Rollny, L. R., Chou, K. W., Thon, S. M., et al. The Complete In-Gap Electronic Structure of Colloidal Quantum Dot Solids and Its Correlation with Electronic Transport and Photovoltaic Performance. Adv. Mater. 26, 937–942 (2014).
43. Houtepen, A. J., Hens, Z., Owen, J. S. & Infante, I. On the Origin of Surface Traps in Colloidal II–VI Semiconductor Nanocrystals. Chem. Mater. 29, 752–761 (2017).
44. Reiss, P., Protière, M. & Li, L. Core/Shell Semiconductor Nanocrystals. Small 5, 154–168 (2009).
45. Kagan, C. R., Lifshitz, E., Sargent, E. H. & Talapin, D. V. Building devices from colloidal quantum dots. Science 353, aac5523–aac5523 (2016).
46. Jang, Y., Shapiro, A., Isarov, M., Rubin-Brusilovski, A., Safran, A., Budniak, A. K., Horani, F., Dehnel, J., Sashchiuk, A. & Lifshitz, E. Interface control of electronic and optical properties in IV-VI and II-VI core/shell colloidal quantum dots: a review. Chem. Commun. 53, 1002–1024 (2017).
47. Chen, O., Zhao, J., Chauhan, V. P., Cui, J., Wong, C., Harris, D. K., Wei, H., Han, H.-S. S., Fukumura, D., Jain, R. K., et al. Compact high-quality CdSe-CdS core-shell nanocrystals with narrow emission linewidths and suppressed blinking. Nat. Mater. 12, 445–451 (2013).
48. Boldt, K., Kirkwood, N., Beane, G. A. & Mulvaney, P. Synthesis of Highly Luminescent and Photo-Stable, Graded Shell CdSe/Cd x Zn 1– x S Nanoparticles by In Situ Alloying. Chem. Mater. 25, 4731–4738 (2013).
49. Kim, Y., Ham, S., Jang, H., Min, J. H., Chung, H., Lee, J., Kim, D. & Jang, E. Bright and Uniform Green Light Emitting InP/ZnSe/ZnS Quantum Dots for Wide Color Gamut Displays. ACS Appl. Nano Mater. 2, 1496–1504 (2019).
50. Ghosh, S., Mandal, S., Mukherjee, S., De, C. K., Samanta, T., Mandal, M., Roy, D. & Mandal, P. K. Near-Unity Photoluminescence Quantum Yield and Highly Suppressed Blinking in a Toxic-Metal-Free Quantum Dot. J. Phys. Chem. Lett. 12, 1426–1431 (2021).
51. Kirkwood, N., Monchen, J. O. V., Crisp, R. W., Grimaldi, G., Bergstein, H. A. C., du Fossé, I., van der Stam, W., Infante, I. & Houtepen, A. J. Finding and Fixing Traps in II–VI and III–V Colloidal Quantum Dots: The Importance of Z-Type Ligand Passivation. J. Am. Chem. Soc. 140, 15712–15723 (2018).
52. Page, R. C., Espinobarro-Velazquez, D., Leontiadou, M. A., Smith, C., Lewis, E. A., Haigh, S. J., Li, C., Radtke, H., Pengpad, A., Bondino, F., et al. Near-Unity Quantum Yields from Chloride Treated CdTe Colloidal Quantum Dots. Small

11, 1548–1554 (2015).
53. Boehme, S. C., Azpiroz, J. M., Aulin, Y. V., Grozema, F. C., Vanmaekelbergh, D., Siebbeles, L. D. A., Infante, I. & Houtepen, A. J. Density of Trap States and Auger-mediated Electron Trapping in CdTe Quantum-Dot Solids. Nano Lett. 15, 3056–3066 (2015).
54. van der Stam, W., du Fossé, I., Grimaldi, G., Monchen, J. O. V., Kirkwood, N. & Houtepen, A. J. Spectroelectrochemical Signatures of Surface Trap Passivation on CdTe Nanocrystals. Chem. Mater. 30, 8052–8061 (2018).
55. Weaver, A. L. & Gamelin, D. R. Photoluminescence Brightening via Electrochemical Trap Passivation in ZnSe and Mn2+-Doped ZnSe Quantum Dots. J. Am. Chem. Soc. 134, 6819–6825 (2012).
56. Rinehart, J. D., Weaver, A. L. & Gamelin, D. R. Redox Brightening of Colloidal Semiconductor Nanocrystals Using Molecular Reductants. J. Am. Chem. Soc. 134, 16175–16177 (2012).
57. Weber, M., Westendorf, S., Märker, B., Braun, K. & Scheele, M. Opportunities and challenges for electrochemistry in studying the electronic structure of nanocrystals. Phys. Chem. Chem. Phys. 21, 8992–9001 (2019).
58. van der Stam, W., Grimaldi, G., Geuchies, J. J., Gudjonsdottir, S., van Uffelen, P. T., van Overeem, M., Brynjarsson, B., Kirkwood, N. & Houtepen, A. J. Electrochemical Modulation of the Photophysics of Surface-Localized Trap States in Core/Shell/(Shell) Quantum Dot Films. Chem. Mater. 31, 8484–8493 (2019).
59. Zhao, J., Holmes, M. A. & Osterloh, F. E. Quantum Confinement Controls Photocatalysis: A free Energy Analysis for Photocatalytic Proton Reduction at CdSe Nanocrystals. ACS Nano 7, 4316–4325 (2013).
60. Geiregat, P., Houtepen, A. J., Sagar, L. K., Infante, I., Zapata, F., Grigel, V., Allan, G., Delerue, C., Van Thourhout, D. & Hens, Z. Continuous-wave infrared optical gain and amplified spontaneous emission at ultralow threshold by colloidal HgTe quantum dots. Nat. Mater. 17, 35–42 (2018).
61. Saniepay, M., Mi, C., Liu, Z., Abel, E. P. & Beaulac, R. Insights into the Structural Complexity of Colloidal CdSe Nanocrystal Surfaces: Correlating the Efficiency of Nonradiative Excited-State Processes to Specific Defects. J. Am. Chem. Soc. 140, 1725–1736 (2018).
62. Henglein, A. Mechanism of reactions on colloidal microelectrodes and size quantization effects. in Electrochemistry II vol. 143 113–180 (Springer-Verlag, 1988).
63. Fojtik, A., Weller, H., Koch, U. & Henglein, A. Photo-Chemistry of Colloidal Metal Sulfides 8. Photo-Physics of Extremely Small CdS Particles: Q-State CdS and Magic Agglomeration Numbers. Berichte der Bunsengesellschaft/Physical Chem. Chem. Phys. 88, 969–977 (1984).
64. Ramsden, J. J. & Grätzel, M. Photoluminescence of small cadmium sulphide particles. J. Chem. Soc. Faraday Trans. 1 Phys. Chem. Condens. Phases 80, 919–933 (1984).
65. Bawendi, M. G., Wilson, W. L., Rothberg, L., Carroll, P. J., Jedju, T. M., Steigerwald, M. L. & Brus, L. E. Electronic structure and photoexcited-carrier dynamics in nanometer-size CdSe clusters. Phys. Rev. Lett. 65, 1623–1626 (1990).
66. Heath, J. R. & Shiang, J. J. Covalency in semiconductor quantum dots. Chem. Soc.

Rev. 27, 65–71 (1998).
67. Eychmüller, A., Hässelbarth, A., Katsikas, L. & Weller, H. Fluorescence mechanism of highly monodisperse Q-sized CdS colloids. J. Lumin. 48–49, 745–749 (1991).
68. Bawendi, M. G., Carroll, P. J., Wilson, W. L. & Brus, L. E. Luminescence properties of CdSe quantum crystallites: Resonance between interior and surface localized states. J. Chem. Phys. 96, 946–954 (1992).
69. Kim, S. H., Wolters, R. H. & Heath, J. R. Photophysics of size-selected InP nanocrystals: Exciton recombination kinetics. J. Chem. Phys. 105, 7957–7963 (1996).
70. O'Neil, M., Marohn, J. & McLendon, G. Dynamics of electron-hole pair recombination in semiconductor clusters. J. Phys. Chem. 94, 4356–4363 (1990).
71. Chestnoy, N., Harris, T. D., Hull, R. & Brus, L. E. Luminescence and Photphysics of CdS Semiconductor Clusters: The Nature of the Emitting Electronic State. J. Phys. Chem. 90, 3393–3399 (1986).
72. Ramsden, J. J., Webber, S. E. & Grätzel, M. Luminescence of colloidal CdS particles in acetonitrile and acetonitrile/water mixtures. J. Phys. Chem. 89, 2740–2743 (1985).
73. Fox, M. Optical properties of solids. (Oxford University Press, 2010).
74. Knowles, K. E., Tice, D. B., McArthur, E. A., Solomon, G. C. & Weiss, E. A. Chemical Control of the Photoluminescence of CdSe Quantum Dot–Organic Complexes with a Series of Para-Substituted Aniline Ligands. J. Am. Chem. Soc. 132, 1041–1050 (2010).
75. Jasieniak, J. & Mulvaney, P. From Cd-Rich to Se-Rich - the Manipulation of CdSe Nanocrystal Surface Stoichiometry. J. Am. Chem. Soc. 129, 2841–2848 (2007).
76. Stein, J. L., Mader, E. A. & Cossairt, B. M. Luminescent InP Quantum Dots with Tunable Emission by Post-Synthetic Modification with Lewis Acids. J. Phys. Chem. Lett. 7, 1315–1320 (2016).
77. Shen, Y., Tan, R., Gee, M. Y. & Greytak, A. B. Quantum Yield Regeneration: Influence of Neutral Ligand Binding on Photophysical Properties in Colloidal Core/Shell Quantum Dots. ACS Nano 9, 3345–3359 (2015).
78. Gao, Y. & Peng, X. Photogenerated Excitons in Plain Core CdSe Nanocrystals with Unity Radiative Decay in Single Channel: The Effects of Surface and Ligands. J. Am. Chem. Soc. 137, 4230–4235 (2015).
79. Anderson, N. C., Hendricks, M. P., Choi, J. J. & Owen, J. S. Ligand Exchange and the Stoichiometry of Metal Chalcogenide Nanocrystals: Spectroscopic Observation of Facile Metal-Carboxylate Displacement and Binding. J. Am. Chem. Soc. 135, 18536–18548 (2013).
80. Puzder, A., Williamson, A. J., Gygi, F. & Galli, G. Self-healing of CdSe nanocrystals: First-principles calculations. Phys. Rev. Lett. 92, 1–4 (2004).
81. Kilina, S. V., Kilin, D. S. & Prezhdo, O. V. Breaking the phonon bottleneck in PbSe and CdSe quantum dots: Time-domain density functional theory of charge carrier relaxation. ACS Nano 3, 93–99 (2009).
82. Kamisaka, H., Kilina, S. V., Yamashita, K. & Prezhdo, O. V. Ab initio study of temperature and pressure dependence of energy and phonon-induced dephasing of electronic excitations in CdSe and PbSe quantum dots. J. Phys. Chem. C 112, 7800–7808 (2008).

83. Califano, M. & Gómez-Campos, F. M. Universal Trapping Mechanism in Semiconductor Nanocrystals. Nano Lett. 13, 2047–2052 (2013).
84. Rusishvili, M., Wippermann, S., Talapin, D. V. & Galli, G. Stoichiometry of the Core Determines the Electronic Structure of Core–Shell III–V/II–VI Nanoparticles. Chem. Mater. 32, 9798–9804 (2020).
85. Voznyy, O. & Sargent, E. H. Atomistic model of fluorescence intermittency of colloidal quantum dots. Phys. Rev. Lett. 112, 1–5 (2014).
86. Dümbgen, K. C., Zito, J., Infante, I. & Hens, Z. Shape, Electronic Structure, and Trap States in Indium Phosphide Quantum Dots. Chem. Mater. 33, 6885–6896 (2021).
87. Kilina, S., Ivanov, S. & Tretiak, S. Effect of surface ligands on optical and electronic spectra of semiconductor nanoclusters. J. Am. Chem. Soc. 131, 7717–7726 (2009).
88. Pu, C. & Peng, X. To Battle Surface Traps on CdSe/CdS Core/Shell Nanocrystals: Shell Isolation versus Surface Treatment. J. Am. Chem. Soc. 138, 8134–8142 (2016).
89. Shim, M., Wang, C., Norris, D. J. & Guyot-Sionnest, P. Doping and Charging in Colloidal Semiconductor Nanocrystals. MRS Bull. 26, 1005–1008 (2001).
90. Mocatta, D., Cohen, G., Schattner, J., Millo, O., Rabani, E. & Banin, U. Heavily Doped Semiconductor Nanocrystal Quantum Dots. Science 332, 77–81 (2011).
91. Chang, J. H., Park, P., Jung, H., Jeong, B. G., Hahm, D., Nagamine, G., Ko, J., Cho, J., Padilha, L. A., Lee, D. C., et al. Unraveling the Origin of Operational Instability of Quantum Dot Based Light-Emitting Diodes. ACS Nano 12, 10231–10239 (2018).
92. Kershaw, S. V., Jing, L., Huang, X., Gao, M. & Rogach, A. L. Materials aspects of semiconductor nanocrystals for optoelectronic applications. Mater. Horizons 4, 155–205 (2017).
93. Carey, G. H., Abdelhady, A. L., Ning, Z., Thon, S. M., Bakr, O. M. & Sargent, E. H. Colloidal Quantum Dot Solar Cells. Chem. Rev. 115, 12732–12763 (2015).
94. Gerischer, H. On the Stability of Semiconductor Electrodes Against Photodecomposition. J. Electroanal. Chem. Interfacial Electrochem. 82, 133–143 (1977).
95. Chen, S. & Wang, L.-W. Thermodynamic Oxidation and Reduction Potentials of Photocatalytic Semiconductors in Aqueous Solution. Chem. Mater. 24, 3659–3666 (2012).
96. Nadjo, L. The characterization and behaviour of n-and p-CdTe electrodes in acetonitrile solutions. J. Electroanal. Chem. Interfacial Electrochem. 108, 29–47 (1980).
97. Park, S. M. & Barber, M. E. Thermodynamic stabilities of semiconductor electrodes. J. Electroanal. Chem. 99, 67–75 (1979).
98. Hwang, G. W., Kim, D., Cordero, J. M., Wilson, M. W. B., Chuang, C.-H. M., Grossman, J. C. & Bawendi, M. G. Identifying and Eliminating Emissive Sub-bandgap States in Thin Films of PbS Nanocrystals. Adv. Mater. 27, 4481–4486 (2015).
99. Voznyy, O., Thon, S. M., Ip, A. H. & Sargent, E. H. Dynamic Trap Formation and Elimination in Colloidal Quantum Dots. J. Phys. Chem. Lett. 4, 987–992 (2013).
100. du Fossé, I., ten Brinck, S., Infante, I. & Houtepen, A. J. Role of Surface Reduction

in the Formation of Traps in n-Doped II–VI Semiconductor Nanocrystals: How to Charge without Reducing the Surface. Chem. Mater. 31, 4575–4583 (2019).
101. Hartley, C. L. & Dempsey, J. L. Electron-Promoted X-Type Ligand Displacement at CdSe Quantum Dot Surfaces. Nano Lett. 19, 1151–1157 (2019).
102. Shim, M. & Guyot-Sionnest, P. n-type colloidal semiconductor nanocrystals. Nature 407, 981 (2000).
103. Koh, W., Koposov, A. Y., Stewart, J. T., Pal, B. N., Robel, I., Pietryga, J. M. & Klimov, V. I. Heavily doped n-type PbSe and PbS nanocrystals using ground-state charge transfer from cobaltocene. Sci. Rep. 3, 2004 (2013).
104. Wang, C., Shim, M. & Guyot-Sionnest, P. Electrochromic Nanocrystal Quantum Dots. Science 291, 2390–2392 (2001).
105. Guyot-Sionnest, P. & Wang, C. Fast Voltammetric and Electrochromic Response of Semiconductor Nanocrystal Thin Films. J. Phys. Chem. B 107, 7355–7359 (2003).
106. Rinehart, J. D., Schimpf, A. M., Weaver, A. L., Cohn, A. W. & Gamelin, D. R. Photochemical Electronic Doping of Colloidal CdSe Nanocrystals. J. Am. Chem. Soc. 135, 18782–18785 (2013).
107. Tsui, E. Y., Carroll, G. M., Miller, B., Marchioro, A. & Gamelin, D. R. Extremely Slow Spontaneous Electron Trapping in Photodoped n-Type CdSe Nanocrystals. Chem. Mater. 29, 3754–3762 (2017).
108. Zherebetskyy, D., Zhang, Y., Salmeron, M. & Wang, L.-W. Tolerance of Intrinsic Defects in PbS Quantum Dots. J. Phys. Chem. Lett. 6, 4711–4716 (2015).
109. Tsui, E. Y., Hartstein, K. H. & Gamelin, D. R. Selenium Redox Reactivity on Colloidal CdSe Quantum Dot Surfaces. J. Am. Chem. Soc. 138, 11105–11108 (2016).
110. du Fossé, I., Boehme, S. C., Infante, I. & Houtepen, A. J. Dynamic Formation of Metal-Based Traps in Photoexcited Colloidal Quantum Dots and Their Relevance for Photoluminescence. Chem. Mater. 33, 3349–3358 (2021).
111. Min, J., Zhang, Y., Zhou, Y., Xu, D., Garoufalis, C. S., Zeng, Z., Shen, H., Baskoutas, S., Jia, Y. & Du, Z. Size Engineering of Trap Effects in Oxidized and Hydroxylated ZnSe Quantum Dots. Nano Lett. 22, 3604–3611 (2022).
112. Wood, B. C., Ogitsu, T. & Schwegler, E. Local structural models of complex oxygen- and hydroxyl-rich GaP/InP(001) surfaces. J. Chem. Phys. 136, 064705 (2012).
113. Zhang, X., Ogitsu, T., Wood, B. C., Pham, T. A. & Ptasinska, S. Oxidation-Induced Polymerization of InP Surface and Implications for Optoelectronic Applications. J. Phys. Chem. C 123, 30893–30902 (2019).
114. Santosh, K. C., Wang, W., Dong, H., Xiong, K., Longo, R. C., Wallace, R. M. & Cho, K. First principles study on InP (001)-(2 × 4) surface oxidation. J. Appl. Phys. 113, (2013).
115. Ghosh, D., Ivanov, S. A. & Tretiak, S. Structural Dynamics and Electronic Properties of Semiconductor Quantum Dots: Computational Insights. Chem. Mater. 33, 7848–7857 (2021).
116. Sabatini, R. P., Bappi, G., Bicanic, K. T., Fan, F., Hoogland, S., Saidaminov, M. I., Sagar, L. K., Voznyy, O. & Sargent, E. H. Temperature-Induced Self-Compensating Defect Traps and Gain Thresholds in Colloidal Quantum Dots. ACS Nano 13,

8970–8976 (2019).
117. Singh, S., Tomar, R., ten Brinck, S., De Roo, J., Geiregat, P., Martins, J. C., Infante, I. & Hens, Z. Colloidal CdSe Nanoplatelets, A Model for Surface Chemistry/ Optoelectronic Property Relations in Semiconductor Nanocrystals. J. Am. Chem. Soc. 140, 13292–13300 (2018).
118. Duke, C. B. Semiconductor surface reconstruction: The structural chemistry of two-dimensional surface compounds. Chem. Rev. 96, 1237–1259 (1996).
119. Chadi, D. J. Vacancy-induced 2×2 reconstruction of the Ga(111) surface of GaAs. Phys. Rev. Lett. 52, 1911–1914 (1984).
120. Chadi, D. J. Atomic structure of the (2×2) reconstructed GaAs(1^{-} 1^{-} 1^{-}) surface: A multivacancy model. Phys. Rev. Lett. 57, 102–105 (1986).
121. Biegelsen, D. K., Bringans, R., Northrup, J. & Swartz, L.-E. Reconstructions of GaAs(1^{-} 1^{-} 1^{-}) surfaces observed by scanning tunneling microscopy. Phys. Rev. Lett. 65, 452–455 (1990).
122. Pascazio, R., Zito, J. & Infante, I. An Overview of Computational Studies on Colloidal Semiconductor Nanocrystals. Chim. Int. J. Chem. 75, 427–434 (2021).
123. Cosseddu, S. & Infante, I. Force field parametrization of colloidal CdSe nanocrystals using an adaptive rate monte carlo optimization algorithm. J. Chem. Theory Comput. 13, 297–308 (2017).
124. Koch, W. & Holthausen, M. C. A Chemist's Guide to Density Functional Theory. (Wiley-VCH, 2001).
125. Cramer, C. J. Essentials of Computational Chemistry: Theories and Models. (Wiley, 2004).
126. Jensen, F. Introduction to Computational Chemistry. (Wiley, 2002).
127. Born, M. & Oppenheimer, R. Zur Quantentheorie der Molekeln. Ann. Phys. 389, 457–484 (1927).
128. Hohenberg, P. & Kohn, W. Inhomogeneous Electron Gas. Phys. Rev. 136, B864–B871 (1964).
129. Kohn, W. & Sham, L. J. Self-Consistent Equations Including Exchange and Correlation Effects. Phys. Rev. 140, A1133–A1138 (1965).
130. Borlido, P., Aull, T., Huran, A. W., Tran, F., Marques, M. A. L. & Botti, S. Large-Scale Benchmark of Exchange-Correlation Functionals for the Determination of Electronic Band Gaps of Solids. J. Chem. Theory Comput. 15, 5069–5079 (2019).
131. Lehtola, S., Steigemann, C., Oliveira, M. J. T. & Marques, M. A. L. Recent developments in LIBXC — A comprehensive library of functionals for density functional theory. SoftwareX 7, 1–5 (2018).
132. Ten Brinck, S. & Infante, I. Surface Termination, Morphology, and Bright Photoluminescence of Cesium Lead Halide Perovskite Nanocrystals. ACS Energy Lett. 1, 1266–1272 (2016).
133. Azpiroz, J. M., Ugalde, J. M. & Infante, I. Benchmark Assessment of Density Functional Methods on Group II-VI MX (M = Zn, Cd; X = S, Se, Te) Quantum Dots. J. Chem. Theory Comput. 10, 76–89 (2014).
134. Bagayoko, D. Understanding density functional theory (DFT) and completing it in practice. AIP Adv. 4, 127104 (2014).
135. Janesko, B. G., Henderson, T. M. & Scuseria, G. E. Screened hybrid density functionals for solid-state chemistry and physics. Phys. Chem. Chem. Phys. 11,

443–454 (2009).
136. Wang, C.-Y., Elliott, P., Sharma, S. & Dewhurst, J. K. Real time scissor correction in TD-DFT. J. Phys. Condens. Matter 31, 214002 (2019).
137. Ten Brinck, S., Zaccaria, F. & Infante, I. Defects in Lead Halide Perovskite Nanocrystals: Analogies and (Many) Differences with the Bulk. ACS Energy Lett. 4, 2739–2747 (2019).
138. Rossi, G. & Ferrando, R. Searching for low-energy structures of nanoparticles: A comparison of different methods and algorithms. J. Phys. Condens. Matter 21, (2009).
139. Pascazio, R., Zaccaria, F., van Beek, B. & Infante, I. Classical Force-Field Parameters for CsPbBr 3 Perovskite Nanocrystals. J. Phys. Chem. C 126, 9898–9908 (2022).
140. Groeneveld, E., Delerue, C., Allan, G., Niquet, Y. M. & De Mello Donegá, C. Size dependence of the exciton transitions in colloidal CdTe quantum dots. J. Phys. Chem. C 116, 23160–23167 (2012).
141. Moreels, I., Lambert, K., Smeets, D., De Muynck, D., Nollet, T., Martins, J. C., Vanhaecke, F., Vantomme, A., Delerue, C., Allan, G., et al. Size-dependent optical properties of colloidal PbS quantum dots. ACS Nano 3, 3023–3030 (2009).
142. Keuleyan, S. E., Guyot-Sionnest, P., Delerue, C. & Allan, G. Mercury Telluride Colloidal Quantum Dots: Electronic Structure, Size-Dependent Spectra, and Photocurrent Detection up to 12 μm. ACS Nano 8, 8676–8682 (2014).
143. Allan, G. & Delerue, C. Tight-binding calculations of the optical properties of HgTe nanocrystals. Phys. Rev. B - Condens. Matter Mater. Phys. 86, 1–6 (2012).
144. Pokrant, S. & Whaley, K. B. Tight-binding studies of surface effects on electronic structure of CdSe nanocrystals: The role of organic ligands, surface reconstruction, and inorganic capping shells. Eur. Phys. J. D 6, 255–267 (1999).
145. Paxton, A. T. An Introduction to the Tight Binding Approximation – Implementation by Diagonalisation. Multiscale Simul. Methods Mol. Sci. 42, 145–176 (2009).
146. Zunger, A. Pseudopotential theory of semiconductor quantum dots. Phys. Status Solidi Basic Res. 224, 727–734 (2001).
147. Rabani, E., Hetényi, B., Berne, B. J. & Brus, L. E. Electronic properties of CdSe nanocrystals in the absence and presence of a dielectric medium. J. Chem. Phys. 110, 5355–5369 (1999).
148. Gómez-Campos, F. M. & Califano, M. Hole surface trapping in CdSe nanocrystals: Dynamics, rate fluctuations, and implications for blinking. Nano Lett. 12, 4508–4517 (2012).
149. Fu, H. & Zunger, A. InP quantum dots: Electronic structure, surface effects, and the redshifted emission. Phys. Rev. B - Condens. Matter Mater. Phys. 56, 1496–1508 (1997).
150. Wang, L. W. & Zunger, A. Pseudopotential calculations of nanoscale CdSe quantum dots. Phys. Rev. B - Condens. Matter Mater. Phys. 53, 9579–9582 (1996).
151. Hens, Z. & De Roo, J. Atomically Precise Nanocrystals. J. Am. Chem. Soc. 142, 15627–15637 (2020).
152. Greaney, M. J., Couderc, E., Zhao, J., Nail, B. A., Mecklenburg, M., Thornbury, W., Osterloh, F. E., Bradforth, S. E. & Brutchey, R. L. Controlling the Trap State Landscape of Colloidal CdSe Nanocrystals with Cadmium Halide Ligands.

Chem. Mater. 27, 744–756 (2015).
153. Bowler, D. R. & Miyazaki, T. O(N) methods in electronic structure calculations. Reports Prog. Phys. 75, (2012).
154. Vandevondele, J., Krack, M., Mohamed, F., Parrinello, M., Chassaing, T. & Hutter, J. Quickstep: Fast and accurate density functional calculations using a mixed Gaussian and plane waves approach. Comput. Phys. Commun. 167, 103–128 (2005).
155. Yu, W. W., Qu, L., Guo, W. & Peng, X. Experimental Determination of the Extinction Coefficient of CdTe, CdSe, and CdS Nanocrystals. Chem. Mater. 15, 2854–2860 (2003).
156. Delerue, C. J. & Lannoo, M. Nanostructures: Theory and Modeling. vol. 59 (Springer, 2004).
157. Voznyy, O., Zhitomirsky, D., Stadler, P., Ning, Z., Hoogland, S. & Sargent, E. H. A Charge-Orbital Balance Picture of Doping in Colloidal Quantum Dot Solids. ACS Nano 6, 8448–8455 (2012).
158. Ubbink, R. F., Almeida, G., Iziyi, H., du Fossé, I., Verkleij, R., Ganapathy, S., van Eck, E. R. H. & Houtepen, A. J. A safe and water-free in-situ HF treatment for ultra-bright InP quantum dots. Submitted (2022).
159. Drijvers, E., De Roo, J., Martins, J. C., Infante, I. & Hens, Z. Ligand Displacement Exposes Binding Site Heterogeneity on CdSe Nanocrystal Surfaces. Chem. Mater. 30, 1178–1186 (2018).
160. Voznyy, O. Mobile Surface Traps in CdSe Nanocrystals with Carboxylic Acid Ligands. J. Phys. Chem. C 115, 15927–15932 (2011).
161. Xia, J., Huang, C., Shin, I. & Carter, E. A. Can orbital-free density functional theory simulate molecules? J. Chem. Phys. 136, 084102 (2012).
162. Witt, W. C., Del Rio, B. G., Dieterich, J. M. & Carter, E. A. Orbital-free density functional theory for materials research. J. Mater. Res. 33, 777–795 (2018).

Part A

Experimental studies

2

2

Spectroelectrochemical Signatures of Surface Trap Passivation on CdTe Nanocrystals

The photoluminescence (PL) quantum yield of semiconductor nanocrystals (NCs) is hampered by in-gap trap states due to dangling orbitals on the surface of the nanocrystals. While crucial for the rational design of nanocrystals, the understanding of the exact origin of trap states remains limited. Here, we treat CdTe nanocrystal films with different metal chloride salts and we study the effect on their optical properties with in situ spectroelectrochemistry, recording both changes in absorption and photoluminescence. For untreated CdTe NC films we observe a strong increase in the PL intensity as the Fermi-level is raised electrochemically and trap states in the bandgap become occupied with electrons. Upon passivation of these in-gap states we observe an increase in the steady state PL and, for the best treatments, we observe that the PL no longer depends on the position of the Fermi level in the band gap, demonstrating the effective removal of trap states. The most effective treatment is obtained for Z-type passivation with $CdCl_2$, for which the steady state PL increased by a factor 40 and the PL intensity became nearly unaffected by the applied potential. X-ray Photoelectron Spectroscopy measurements show that treatment with $ZnCl_2$ mainly leads to X-type passivation with chloride ions, which increased the PL intensity by a factor four and made the PL less susceptible to modulation by applying a potential with respect to unpassivated nanocrystal films. We elucidate the spectroelectrochemical signatures of trap states within the bandgap and conclude that undercoordinated Te at the surface constitutes the largest contribution to in-gap trap states, but that other surface states that likely originate on Cd atoms should also be considered.

This chapter is based on: Ward van der Stam, Indy du Fossé, Gianluca Grimaldi, Julius O. V. Monchen, Nicholas Kirkwood, Arjan J. Houtepen. Chemistry of Materials, 2018, 30 (21), 8052-8061

2.1 Introduction

The implementation of colloidal semiconductor nanocrystals (NCs) into optoelectronic devices is hindered by charge carrier trapping into states within the bandgap, which mainly arise due to dangling orbitals on the surface of these nanocrystals.[1–8] The passivation of these dangling orbitals has therefore been an extensive line of research.[2,5,8–12] Several strategies have been developed to understand and passivate these dangling orbitals, and hence, circumvent the nonradiative recombination pathways associated with them. For example, heteroepitaxial overgrowth of another semiconductor,[2,13] surface passivation with (in)organic ligands[10,14–17] and filling of trap states by Fermi level tuning[18] have all resulted in an increase in photoluminescence quantum yield (PL QY).[11,13,19] Interestingly, trap states are not necessarily detrimental as they can also be useful emissive centers,[20] temporarily store charge carriers for delayed luminescence,[21] or result in optical gain.[22] Therefore, improved understanding of the nature of these surface states will not only enable the rational design of passivation strategies for their removal, but may also offer new pathways to tailor the optoelectronic properties of colloidal nanomaterials.

Recently, DFT calculations have shown that the main contribution to in-gap states in Cd-chalcogenide NCs stems from undercoordinated surface chalcogen atoms (S, Se, Te).[9] Since the valence band (VB) maximum in CdTe NCs is formed predominantly by a linear combination of 5p Te orbitals, undercoordinated Te will result in trap states near the VB edge.[9] The conduction band (CB) is formed by the linear combination of the 5s Cd orbitals, which are less prone to trap state formation near the band edges due to their spherical symmetry.[9] However, the NC surface may be more complex and dynamic, which could give rise to Cd-related defect states.[17,23,24] For example, Cd–Cd dimers might form on the surface and the bonding orbital of these dimers could result in states within the bandgap, as has been suggested for Pb–Pb dimers in PbS NCs.[25] In principle, dangling orbitals on the surface can be passivated with (in)organic ligands, which are classified as L-, X-, and Z-type, depending on whether the ligands are two electron donors (L-type), one electron donors (X-type), or neutral two electron acceptors (Z-type).[10] Here, we use different trap state passivation strategies in combination with in situ spectroelectrochemistry and ex situ elemental analysis to elucidate the trap state distribution, the binding motifs of the passivating species and the effect of passivation of trap states in CdTe NC films.

Spectroelectrochemistry is a powerful tool to study important features of nanomaterials, such as the position of the band edges,[26–28] the degeneracy of the energy levels[29] and the distribution of trap states within the bandgap.[18,30,31] Since trapping of photogenerated charge carriers results in a decrease in PL QY, we use in situ photoluminescence spectroelectrochemistry to study the influence of the passivating ligands on the distribution of trap states. We correlate the observed spectroelectrochemical trends to the binding motifs of the passivating ligands with ex situ X-ray Photoelectron Spectroscopy (XPS) measurements, which suggests that X-type passivation leads to a 4-fold increase in PL intensity, whereas Z-type passivation results in almost a 40-fold increase in PL. Furthermore, after surface passivation the maximum number of injected electrons in the $1S_e$ level per nanocrystal increases, which suggests that competing surface redox reactions are slowed down. We hypothesize that X-type passivation with Cl^- occurs on Cd-related defect sites, such as Cd–Cd dimers, and Z-type passivation by $CdCl_2$ on undercoordinated

Te sites. We show that undercoordinated Te surface sites contribute the most to the presence of in-gap states, since proper passivation with Z-type $CdCl_2$ ligands results in a drastic PL increase and a decrease of the PL dependence on the applied electrochemical potential. Our results shed light on the nature of surface binding sites in CdTe NCs and on how to passivate them with inorganic ligands.

2.2 Results and Discussion

2.2.1 CdTe NC Films

Spherical zinc blende CdTe NCs (native ligands: oleic acid) were obtained with a diameter of 6.0±0.5 nm, as evidenced by Transmission Electron Microscopy (TEM, Figure 2.1A) and Electron Diffraction (ED, Figure 2.1B/C) measurements. Steady state optical measurements revealed sharp absorption features, with the $1S_{3/2}1S_e$ absorbance peak centered at 677 nm, and a narrow photoluminescence band centered at 690 nm (Figure 2.1D). The full-width-half-maximum (fwhm) was established to be 76 meV, and the photoluminescence quantum yield (PL QY) 9% (Figure A2.4). These CdTe NCs were

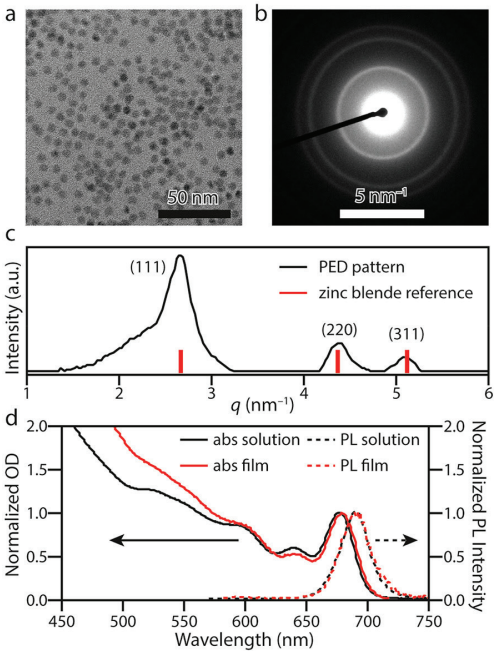

Figure 2.1. Structural and optical characterization of CdTe nanocrystals. (A) Transmission Electron Microscopy image, which reveals spherical nanocrystals (NCs) with a diameter of 6.0±0.5 nm. (B) Electron Diffraction pattern of the NCs in panel A. (C) Azimuthal integration of the 2D ED pattern in panel B results in the 1D powder ED pattern, which reveals the zinc blende CdTe crystal structure. The red bars are from reference card 1010536 for zinc blende CdTe. (D) Steady-state UV–vis absorption (solid line) and PL spectra (dashed line) of CdTe NCs in solution (black lines) and in NC films, cross-linked with octanedithiol ligands (red lines).

dip-coated, with octanedithiol as cross-linking ligands, to form NC films (see Methods), which led to a small red shift of the absorbance (to 679 nm) and PL peaks (to 691 nm, fwhm = 78 meV), as can be seen in Figure 2.1D.[32] The PL QY of the films is expected to drop below the value measured in solution due to energy-transfer.[33] These CdTe NC films are further characterized by in situ spectroelectrochemistry measurements, before and after treatment with metal chloride salt solutions, as will be described below.

2.2.2 Electrochemical Trap Filling in CdTe NC Films

The CdTe NC films were first analyzed with in situ absorbance and photoluminescence spectroelectrochemistry, prior to any passivation treatment (Figure 2.2). The potentials displayed are given with respect to a Ag pseudoreference electrode (PRE, −4.90±0.03 V vs vacuum, calibrated with ferrocene/ferrocenium, see Figure A2.2). Cyclic voltammetry (scan rate 50 mV/s) was used to monitor the current and reversibility of the charge injection. The CV scan was started at −0.5 V (the open-circuit potential, V_{OC}). Upon scanning to more negative potentials, the negative current increases at an applied potential of −1.4 V, indicating the injection of electrons into the NC film (see Figure A2.5). When the scan direction is reversed, electrons are withdrawn from the NC film, indicated by the positive measured currents. We observe a clear offset between the first scan of the CV and the subsequent second and third scan (see Figure A2.5), which is indicative of trap state filling, as will be discussed in more detail below.

The differential absorbance as a function of applied potential is measured to quantify the charge injection into the CdTe NCs. Around an applied potential of −1.4 V, the $1S_{3/2}1S_e$ transition starts to be bleached (Figure 2.2A), which is indicative of charge injection into the bottom of the CB, and the bleach increases in intensity at more negative applied potentials until it reaches a maximum at an applied potential of −1.7 V vs Ag PRE (Figure 2.2B). Further, a sub-bandgap induced absorption feature around 700 nm is observed, which is attributed to a Stark shift,[34] i.e., a change in the energy of the NC absorption feature induced by the presence of neighboring charges. As a result, the $1S_{3/2}1S_e$ absorption peak is shifted to the red, resulting in more absorption at longer wavelengths, but less at the original location of the peak. This shift can be due to the presence of $1S_e$ electrons (a trion shift) or electrostatic interactions with localized surface charges. However, as can be seen in Figure 2.2A/B, the amplitude of the bleach is larger than that of the induced absorption, indicating that part of the bleach is also caused by state-filling of the $1S_e$ level.

We separate the Stark shift from the bleach due to state filling by a fit to the signal (see Methods), from which we deduce the effective bleach ΔA due to $1S_e$ level filling (Figure 2.2C and Figure A2.6). ΔA is then converted to an average number of electrons in the $1S_e$ level per NC $\langle N_{1Se} \rangle$ (left axis Figure 2.2C), by dividing it by the steady state absorbance (A_0), taking a degeneracy g of 2 electrons for the $1S_e$ level into account:[26,35–37]

$$\langle N_{1Se} \rangle = \frac{g\Delta A}{A_0} \qquad 2.1$$

From this analysis it follows that at the most negative applied potential (−1.7 V vs Ag PRE) we inject on average 0.04 electrons/NC in the $1S_e$ level. This possibly indicates that many of the injected electrons get trapped or extracted by the reduction of impurities at the

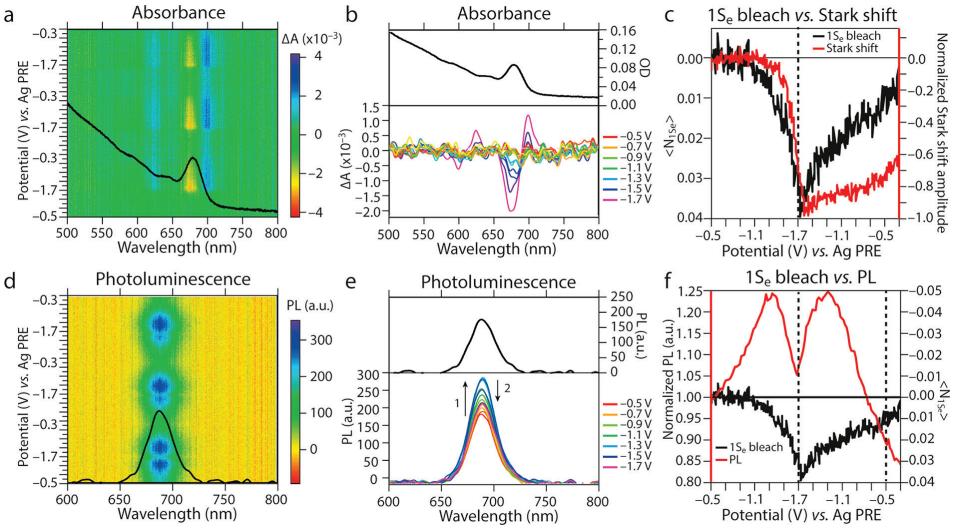

Figure 2.2. In situ spectroelectrochemistry on dithiol-capped CdTe NC films, prior to salt treatment. (A) 2D differential absorbance as a function of the applied potential for a bare CdTe NC film. A bleach of the band edge transition is observed at applied potentials below −1.4 V, indicative of electron injection into the CB edge. (B) Smoothed spectral slices at different potentials of the absorbance spectra in panel A. The steady state absorbance (A_0) is shown in black at the top. (C) Intensity of the band edge absorption bleach (at 677 nm) as a function of applied potential vs the Stark shift. On the left axis, the differential absorbance (ΔA) is divided by the steady state absorbance (A_0) and multiplied by the degeneracy of the CB edge (g = 2), which gives the average number of electrons (N_{1Se}) in the $1S_e$ level. The bleach was corrected for the Stark shift (red line, see also Figure A2.6). (D) 2D In situ PL spectra of the CdTe film as a function of applied potential. An increase in PL is clearly observed (potential range −0.5 to −1.3 V) before the PL band is quenched due to Auger recombination around −1.4 V. (E) Smoothed spectral slices of the PL spectra in panel D. The PL first increases due to trap filling (arrow 1) and then decreases due to Auger recombination (arrow 2). The steady state PL spectrum at V_{oc} is shown in black at the top. (F) Intensity of the PL as a function of applied potential vs the bleach of the $1S_e$ level. The PL is very reversible and increases first due to trap filling (above −1.4 V), after which it decreases due to efficient Auger recombination (between −1.4 V and −1.7 V, dashed line). Above V_{oc} (applied potential > −0.5 V, dashed line), the PL decreases further due to an increase in electron trap states.

NC surface, and hence do not contribute to the $1S_{3/2}1S_e$ bleach. The presence of trapped electrons is also reflected in the hysteresis of the potential dependence of the $1S_{3/2}1S_e$ bleach and the Stark shift (Figure 2.2C), which shows that the NCs are still charged (giving rise to a Stark shift) whereas no electrons are in the $1S_e$ CB edge. We conclude that the Stark shift in absence of a band edge bleach is caused by electrons that occupy trap states within the bandgap, in line with earlier suggestions that traps can cause significant Stark shifts.[38,39]

Since the PL QY of CdTe NCs depends strongly on the electron occupation of trap states,[18] the in situ PL was measured as a function of the applied potential (Figure 2.2D) for the

same CdTe NC film as described above. When the potential was scanned from −0.5 V (V_{oc}) to more negative potentials, charge injection into the CB can again be observed below −1.4 V (see CV in Figure A2.7). At these potentials a clear decrease of the PL is observed (Figure 2.2E), which we attribute to efficient Auger recombination of trions, as it coincides with the potential where the $1S_{3/2}1S_e$ absorption bleach initiates (Figure 2.2A/B). Interestingly, the PL first increases (up to an applied potential of −1.3 V, Figure 2.2D–F), before Auger recombination quenches it at lower potentials (lower than −1.4 V, Figure 2.2D–F). This PL increase is in line with our earlier observations[18] and is caused by filling of trap states as the Fermi level is raised, which reduces electron trapping and increases the PL QY (Figure 2.3A/B). The trapping rates of electrons ($\Gamma_{trap,e}$) and holes ($\Gamma_{trap,h}$) can be described as second order rate equations:

$$\Gamma_{trap,e} = k_{trap,e} N_{trap,empty} N_e \qquad 2.2$$

$$\Gamma_{trap,h} = k_{trap,h} N_{trap,full} N_h \qquad 2.3$$

The fact that trap filling leads to increased PL, shows that the electron capture rate constant $k_{trap,e}$ is much higher than the hole capture rate constant $k_{trap,h}$ in CdTe NCs (Figure 2.3A/B). We have previously argued that electron trapping is Auger assisted with the photogenerated hole being excited deeper into the valence band levels,[18] and others have seen similar effects for doped NCs[40] and core/shell heterostructures.[41]

We note that the change in PL is very reversible (Figure 2D/F). Furthermore, the PL drops below its initial value when a potential of −0.3 V is applied (i.e., a more positive potential than the V_{oc}), which can be assigned to an increase in the number of empty electron trap states, which decreases the PL QY because $\Gamma_{trap,e}$ increases. From this, the conclusion is drawn that the Fermi level in CdTe NC films at V_{oc} lies within a distribution of trap states (Figure 2.3A).

The results of the spectroelectrochemistry measurements were used to construct a model of the electron distribution in the system as a function of the Fermi-level position, depicted in Figure 2.3. From the hysteresis in potential dependence of the $1S_e$ bleach due to state filling and the Stark shift (Figure 2.2C), combined with the potential dependence of the PL intensity within the bandgap (Figure 2.2F), we argue that traps within the ensemble of CdTe NCs are quickly filled only when the Fermi level is above the $1S_e$ level. When the Fermi level is within the distribution of trap states, charge transfer between NCs has to be preceded by thermally activated detrapping to the CB (Figure 2.3C). This thermally activated detrapping (which is the rate-determining step, RDS) slows down electron transfer enormously by several orders of magnitude. If we assume an electron mobility of 10^{-2} $cm^2/(V \times s)$ for band edge electrons and thermally activated detrapping from a 0.5 eV deep trap state, then we can estimate that diffusion over the thickness d of a 100 nm thick NC film takes:

$$t = \frac{d^2 \cdot e}{k_B T \cdot \mu \cdot \exp\left(-\frac{E_a}{k_B T}\right)} = 200\ s \qquad 2.4$$

For band edge electrons (where the rate of injection is limited by cation diffusion with a

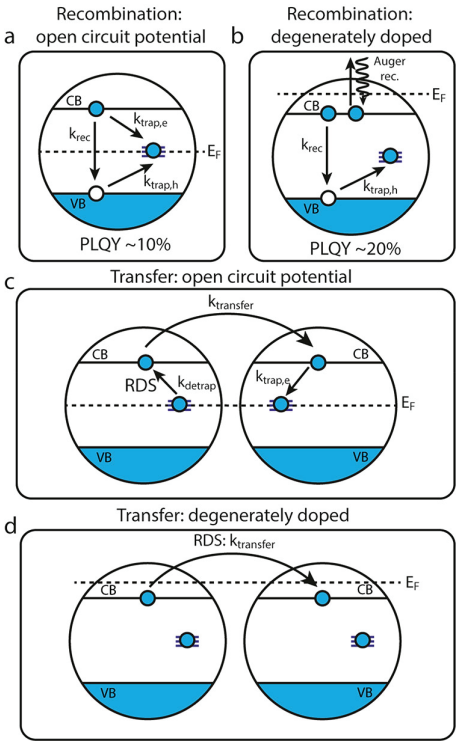

Figure 2.3. Charge carrier trapping, transfer and recombination in CdTe nanocrystals. (A) Recombination pathways in CdTe NCs. Photogenerated electrons and holes can recombine radiatively (k_{rec}), or charge carriers can get trapped (k_{trap}), which lowers the PL QY. (B) Recombination pathways in CdTe NCs with electrochemically filled trap states. Photogenerated electrons and holes can again recombine radiatively (k_{rec}), or charge carriers, in this case only holes, can get trapped ($k_{trap,h}$). Due to state filling of the CB edge, an additional nonradiative Auger recombination pathway opens up. (C) In unpassivated CdTe nanocrystals, in-gap states due to two coordinated Te (2c-Te) and Cd-related defects are present at the NC surface. Charge carriers can transfer to a neighboring NC after thermally activated detrapping of trap states, followed by transfer via the band edges ($k_{transfer}$). The thermally activated detrapping is the rate-determining step (RDS). This detrapping slows down electron transfer by several orders of magnitude. The Fermi level (E_F) lies within the distribution of trap states (dashed line). (D) The in-gap states can be filled by raising the Fermi level (E_F, dashed line) above the CB edge, thereby enhancing the charge transfer between NCs and the PL QY.

diffusion coefficient of ~10^{-7} cm^2/s)[28] charge injection over the entire film takes place on a ~1 ms time scale. So while electron injection/extraction from the conduction band may occur electrochemically reversibly, the filling/emptying of trap states is slow, resulting in the observed strong hysteresis.

This means that raising the Fermi level (E_F) above the trap states is not sufficient to fill all in-gap trap states within the NC film on a reasonable time scale, since the trap state

transfer rate is very small and hence, only the first few layers of nanocrystals will have filled in-gap trap states (Figure 2.3C). This is also reflected in the fact that the Stark shift is negligible before the $1S_e$ CB edge is filled (only the first layer of NCs will have filled traps), but is present even though the band edge is emptied when the scan direction is reversed (Figure 2.2C). Only when E_F is raised above the CB edge (Figure 2.3D), charge carriers will quickly transfer between NCs due to reduced electron trapping in the first NC layer, and as a consequence, in-gap states throughout the entire NC film will be quickly filled due to electron injection, giving rise to a substantial Stark shift (Figure 2.2C). Raising the Fermi level above the $1S_e$ level also results in CB edge state filling, giving rise to additional nonradiative Auger recombination pathways (Figure 2.3B), which eventually competes with the other radiative and nonradiative processes discussed above.

Since the PL QY of bare CdTe NCs in solution is around 9% (Figure A2.4), a substantial part of the charge carriers recombine nonradiatively via in-gap trap states (Figure 2.3A), which therefore need to be efficiently removed. As mentioned above, these trap states can be filled electrochemically (Figure 2.3B/D) or passivated chemically, as we will discuss next.

2.2.3 Metal Chloride Salt Treatments and the Effect on the Steady State Optical Properties

We now have a toolset to quantify the effect of trap states by in situ spectroelectrochemistry, which we will now discuss for CdTe NCs films that were passivated with various metal chloride salts. The CdTe NC films are placed in metal chloride salt solutions in acetone for ~16 h (see Methods). This approach differs from previous work that reports solution phase surface passivation on CdTe NCs, since we are dealing with NC films that we do not want to detach from the substrate.[42]

First, we analyze the influence of trap state passivation with different metal chloride salt solutions on the optical properties of the CdTe nanocrystal films with steady state absorption and photoluminescence spectroscopy. As can be seen in Figure 2.4A, treatment with $CdCl_2$ and $ZnCl_2$ did not change the position and width of the band edge absorption. However, treatment with $InCl_3$ resulted in a shift of the band edge absorption to a lower wavelength, indicating that the NCs have decreased in size (Figure A2.9). Since $InCl_3$ is a strong Lewis acid, it is suggested that the blue-shift is due to etching of the NCs.[17,43] There is a dramatic increase in PL intensity (by a factor ~40) after $CdCl_2$ treatment (Figure 2.4B). This observation indicates that the PL QY of bare CdTe NCs in a dense NC film cannot exceed 2.5%, and that the PL QY has dropped compared to the value found for NCs in solution (9%, Figure A2.4), possibly due to energy transfer.[33] Treatment with $ZnCl_2$ also increases the PL intensity, but only by a factor ~4. Control experiments with acetone only showed small changes in PL intensity compared to the metal chloride salt in acetone solutions (Figure A2.8). As was also observed in the absorbance measurements, $InCl_3$ slightly blue-shifted the position of the PL band, possibly due to etching of the NCs, and the PL intensity has decreased slightly (Figure A2.9). These results show that treatment with $ZnCl_2$ and $CdCl_2$ salt solutions is effective in terms of PL enhancement, but the exact binding motif and the effect on the presence of in-gap trap states, remains unclear. Therefore, we perform the same in situ absorbance and PL spectroelectrochemistry

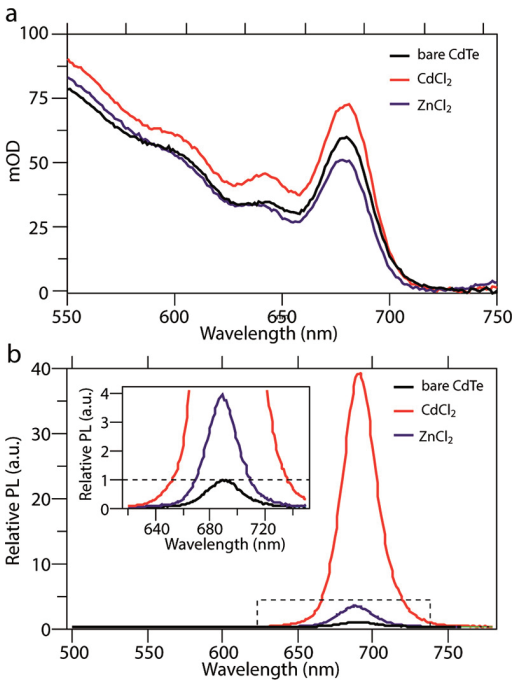

Figure 2.4. Influence of surface passivation on steady state absorbance and photoluminescence of CdTe films. (A) Absorbance and (B) photoluminescence (PL) spectra of thiol-capped CdTe NC films before and after treatment with $CdCl_2$ and $ZnCl_2$ in acetone solutions. The inset shows a zoom of the PL spectra of a bare CdTe NC film, and a film after $ZnCl_2$ treatment. The $1S_{3/2}1S_e$ absorbance does not shift after metal chloride salt treatment and a small variation in the intensity can be seen (panel A), but a much larger enhancement of the PL intensity after $ZnCl_2$ treatment (4-fold enhancement) and after $CdCl_2$ treatment (fortyfold enhancement) were observed (panel B).

measurements as discussed above for bare CdTe NC films after the metal chloride salt treatments.

2.2.4 In Situ Spectroelectrochemistry on Metal Chloride Treated CdTe Films

Figure 2.5 summarizes the in situ spectroelectrochemistry measurements after the CdTe NC films were treated with metal chloride salt solutions. The cyclic voltammograms show charge injection around −1.4 V, comparable to untreated CdTe NC films (Figure A2.10). As shown above, the PL of bare CdTe NC films depends heavily on the applied potential in the bandgap (Figure 2.2D-F), indicating the presence of in-gap trap states. Figure 2.5A-C shows that the PL of $ZnCl_2$ treated CdTe films depends only slightly on the applied potential (potential window −0.3 V until −1.4 V vs Ag PRE), although a minor increase in PL intensity is observed before efficient Auger recombination occurs around −1.4 V (vs Ag PRE). Differential absorbance measurements show that the charge injection

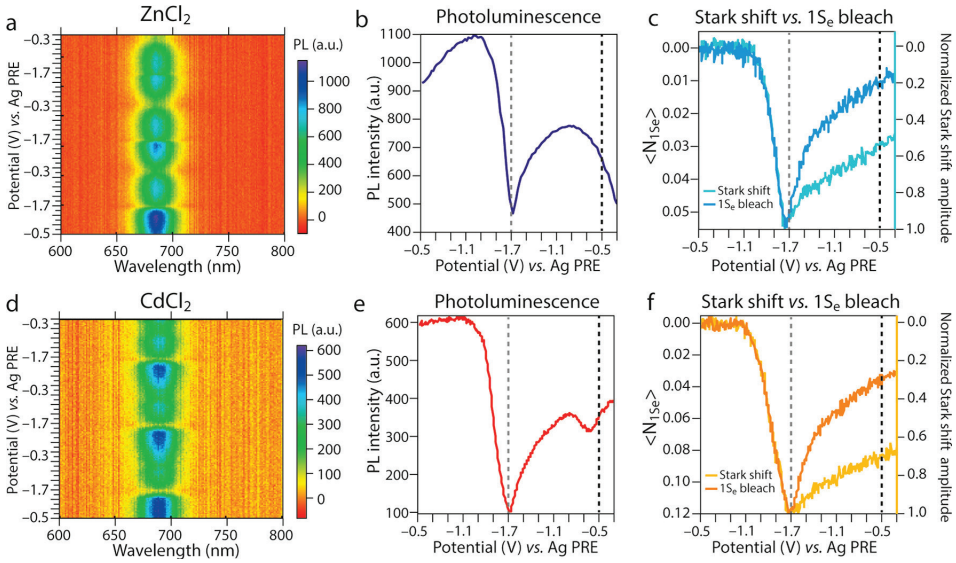

Figure 2.5. In situ photoluminescence (PL) spectroelectrochemistry on passivated CdTe NC films. (A) 2D in situ PL spectra as a function of applied potential for $ZnCl_2$ treated CdTe NC films. (B) Intensity of the PL peak (at 690 nm) as a function of applied potential of the spectra in panel A during the first cycle of the CV scan. (C) $<N_{1Se}>$ (derived from the absorption bleach at 677 nm, blue line) as a function of applied potential for $ZnCl_2$ treated CdTe NC films. The average number of electrons in the band edge is ~0.05. The bleach is corrected for the Stark shift (light blue line, Figure A2.11). (D) 2D in situ PL spectra as a function of applied potential for $CdCl_2$ treated CdTe NC films. (E) Intensity of the PL peak (at 691 nm) as a function of applied potential of the spectra in panel D during the first cycle of the CV scan. (F) $<N_{1Se}>$ (derived from the absorption bleach at 677 nm, orange line) as a function of applied potential for $CdCl_2$ treated CdTe NC films. The average number of electrons in the band edge is ~0.12. The bleach is corrected for the Stark shift (light orange line, Figure A2.12).

is very reversible (Figure 2.5C). As before, the $1S_e$ bleach was corrected for the Stark shift (Figure 2.5C and Figure A2.11), which again shows hysteresis between the $1S_e$ bleach and the Stark shift, indicative of trap states.

The same in situ photoluminescence measurements on CdTe NC films treated with $CdCl_2$ in acetone solutions show that the PL of $CdCl_2$ treated CdTe NC films is nearly independent of the applied potential within the bandgap (potential window −0.3 V until −1.4 V vs Ag PRE, Figure 2.5D–F). Furthermore, the PL is almost entirely quenched after charge injection into the CB, since all injected electrons contribute to nonradiative Auger recombination (Figure 2.5E). Again, differential absorbance measurements show that the charge injection is very reversible (Figure 2.5F). The $1S_e$ bleach was corrected for the Stark shift (Figure 2.5F and Figure A2.12), showing similar hysteresis between the $1S_e$ bleach and the Stark shift as observed above.

Figure 2.6A compares the dependence of the PL intensity on potential for the untreated

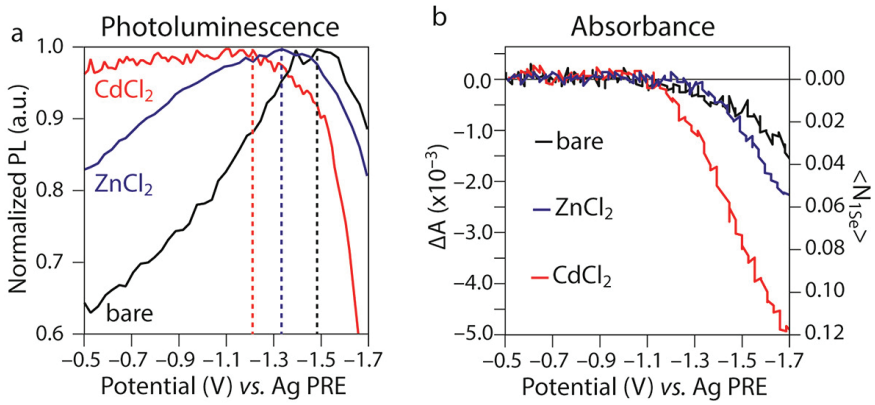

Figure 2.6. Comparison of in situ spectroelectrochemistry prior to and after metal chloride salt treatment. (A) Normalized PL intensity (at 691 nm) as a function of applied potential for CdTe NC films prior to (black line) and after metal chloride treatment (blue and red line). The PL drastically increases for untreated CdTe NCs before the band edge is reached when an electrochemical potential is applied (black line), whereas the PL is unaffected by the applied potential after $CdCl_2$ treatment (red line). The PL dependence of $ZnCl_2$ treated CdTe NC films lies in between. The onset of Auger recombination shifts to less negative potentials after treatment (indicated by the dashed lines). (B) Differential absorbance at the band edge (677 nm) as a function of applied potential for a bare CdTe NC film (black line) and CdTe NC films after $ZnCl_2$ (blue line) and $CdCl_2$ (red line) treatments. More electrons can be injected into the $1S_e$ level after metal chloride passivation, and the maximum bleach of the $1S_e$ level is not drastically shifted in potential by the treatments.

film and the $ZnCl_2$ and $CdCl_2$ treated films. In all cases the PL decreases at very negative potentials due to Auger recombination with $1S_e$ electrons. However, the potential dependence in the bandgap due to trap filling is clearly reduced by the surface treatments. The PL increases by a factor of 1.28, 1.18, and 1.02 for bare CdTe films, $ZnCl_2$ treated films and $CdCl_2$ treated films, respectively, upon the application of a potential, right before the onset of efficient Auger recombination (around −1.4 V vs Ag PRE). The trend of the dependence of the PL intensity on the applied potential is in line with the increase in the steady state PL. Overall, $CdCl_2$ treatment results in a drastic enhancement of the PL intensity, and makes the PL less susceptible to the applied potential, suggesting that in-gap states have been effectively removed. These results imply that in-gap states are partially removed upon treatment with $ZnCl_2$ and almost completely removed by $CdCl_2$.

The variation of the PL intensity as a function of applied potential shows that the onset of Auger recombination shifts to less negative potentials after metal chloride treatment (dashed lines in Figure 2.6A). This could indicate that the surface treatment induced a shift of the band edges, as observed for several II–VI nanomaterials,[24] or that the onset of Auger recombination stays constant and the apparent shift is due to the suppression of electrochemical trap filling in the treated NCs. However, limits in the potential range that can be scanned without inducing sample degradation do not allow a proper spectroelectrochemical measurement of the CB position (Figure 2.6B).

When we compare the differential absorbance as a function of applied potential for the different CdTe NC films studied here, we find that more electrons per NC can be injected in the $1S_e$ level after metal chloride treatment under otherwise identical conditions (Figure 2.6B). The increase in the maximum number of $1S_e$ electrons correlates with the increase in PL intensity and the disappearance of the PL modulation with potential in the bandgap. We consider that the maximum number of $1S_e$ electrons depends on the rate that they are injected by the potentiostat as well as the rate that they disappear via reactions with, e.g., molecular oxygen or via surface electrochemical reactions. We think that such surface electrochemical reactions likely proceed via trap states, i.e., the first step of the electrochemical reduction of surface Cd^{2+} ions is the capturing of electrons in surface traps. This would suggest that passivating surface traps could reduce the rate at which $1S_e$ electrons disappear from the NCs and hence would increase the maximum steady state occupation of the $1S_e$ levels.

2.2.5 Elemental Analysis of the CdTe Nanocrystal Surface

Although the effect of the salt treatment is clearly observed by steady-state spectroscopy and in situ spectroelectrochemistry, the exact mechanism via which the NCs are passivated remains elusive. To investigate the nature of the passivation and the binding motif on the CdTe NC surface, X-ray Photoelectron Spectroscopy (XPS) was used. As can be seen in Figure 2.7 and Table 2.1, the bare CdTe NCs are cation rich with a Cd:Te ratio of 1.35. This is in agreement with the observation that NCs are often metal rich, where negative X-type ligands (e.g., carboxylates)[16] compensate for the excess positive charge of the metal cations.[10,17,24,44,45]

After treatment with $CdCl_2$ and $ZnCl_2$, small shifts of the Cd 3d and Te 3d spectra are observed (Figure 2.7A/B). Treatment of the NCs with $CdCl_2$ gives rise to a Cl signal which was not present for the bare CdTe NCs (Figure 2.7C). Additionally, the Cd:Te ratio increased to 2.10 (Table 1), indicating that more Cd is present with respect to bare CdTe NCs. These results suggest that the NCs are passivated via $CdCl_2$ Z-type ligands. We note that the Cd:Te ratio of 2.10 is too high for solely $CdCl_2$ passivated NC surfaces, which may indicate that some free $CdCl_2$ is present in the film. Treatment of the films with $ZnCl_2$ did not drastically alter the Cd:Te ratio (1.45 after treatment vs 1.35 prior to treatment). Interestingly, a clear Cl signal was observed for $ZnCl_2$ treated films, but no Zn was detected (Figure A2.13). This suggests that treatment with $ZnCl_2$ mainly results in X-type passivation by Cl^- ligands. Possibly, charge balance is ensured by other reactions at the surface, such as the loss of thiolate ligands. When NCs were treated with $InCl_3$,

Table 2.1. Quantification of the XPS measurements.

Sample	Cadmium (%)	Tellurium (%)	Chloride (%)	Zinc/Indium (%)	Cd:Te
bare CdTe	57	43			1.35
$CdCl_2$	59	28	12		2.10
$ZnCl_2$	54	37	9		1.45
$InCl_3$	42	42	10	6	0.99

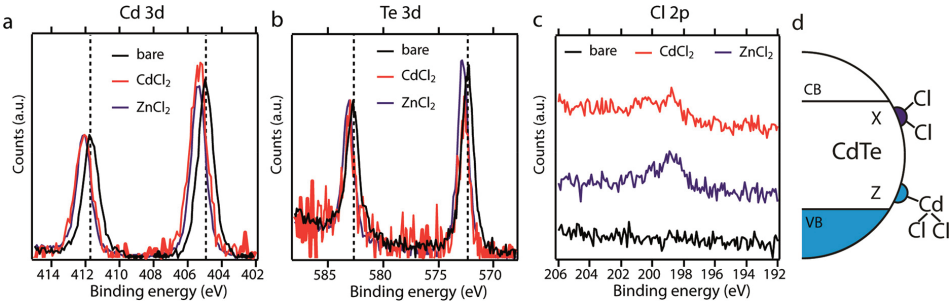

Figure 2.7. X-ray Photoelectron Spectroscopy (XPS) measurements. (A) Cd 3d, (B) Te 3d, and (C) Cl 2p XPS spectra of CdTe NC films prior to and after metal chloride treatment. The Cd and Te spectra have been normalized for the peak at a binding energy of around 412 and 583 eV, respectively. All films show the expected Cd and Te signals (slightly shifted with respect to the untreated film, panel A, B), and the metal chloride passivated films show a weak Cl peak ($ZnCl_2$, blue line, $CdCl_2$, red line), which was not present in the bare CdTe films (black line, panel C). (D) CdTe NCs contain Z- and X-type binding motifs on the surface, due to undercoordinated Te (light blue, Z-type passivation) and Cd-related defects (dark blue, X-type passivation), which therefore require different strategies for the complete passivation of the NC surface.

the Cd:Te ratio decreased to 0.99. This suggests that $InCl_3$ indeed etches the Cd-rich NCs, by stripping of $Cd(OA)_2$ Z-type ligands from the surface, as was suggested above. Furthermore, In is detected with XPS measurements, suggesting that $InCl_3$ or other In containing molecular species are adsorbed at the surface (Figure A2.14).

These results thus suggest a different type of surface passivation for the different chloride salts investigated here. Contrary to predictions that only undercoordinated Te surface atoms give rise to traps, which can be passivated with Z-type ligands,[9,42] these results suggest that X-type chloride ions can also passivate part of the traps present on the surface (Figure 2.7D). It seems likely that these chloride ions complex to surface Cd^{2+} ions and in doing so apparently passivate Cd localized trap states. While such traps were not found in recent DFT studies,[9] there could be more complicated Cd localized traps on the surface, not captured by these studies. For instance we can imagine that Cd–Cd dimers form dynamically on the surface and their bonding orbitals could act as traps, similar to suggestions of Pb–Pb dimer formation on the surface of PbS NCs.[25] Complexation of ligands (Cl^-, but perhaps also L-type ligands such as amines, which have also been shown to enhance the PL QY)[42] to surface Cd ions may prevent the formation of such Cd dimers (see also Discussion A2.1).

The different degree of passivation attained with the three metal chloride salts presented here may be partially explained by their solubility in acetone, which decreases as $ZnCl_2$ > $InCl_3$ > $CdCl_2$.[46] Since $ZnCl_2$ dissolves very well in acetone, it probably easily dissociates into Zn^{2+} and Cl^- ions, so that $ZnCl_2$ treatment will mainly passivate traps with X-type Cl^- ligands. $CdCl_2$, however, barely dissolves in acetone. As it forms complexes like $CdCl_4^{2-}$ in

aqueous solutions, $CdCl_2$ in acetone may dissolve more like complexes or molecules than by dissociation into separate ions.[46] This may facilitate its binding as Z-type $CdCl_2$ to the NC, thus passivating the majority of the undercoordinated Te traps and hence increasing the PL.

2.3 Conclusions

We have studied the effect of metal chloride salt passivation on the presence of in-gap trap states in films of CdTe NCs by in situ absorbance and photoluminescence spectroelectrochemistry. Proper passivation of undercoordinated surface Te by Z-type ligands, like $CdCl_2$, results in a 40-fold increase in PL intensity. Additionally, surface passivation by these Z-type ligands makes the PL less dependent, or even independent, on the applied potential. Both observations show that the Z-type ligands efficiently passivate the majority of in-gap trap states in CdTe NCs. Treatment with $ZnCl_2$ in acetone results in a 4-fold increase in PL intensity, and an intermediate dependence of the PL intensity on the applied potential. Interestingly, we find no evidence of Zn on the CdTe NC films, whereas a clear Cl signal is observed with XPS. It is conjectured that chloride X-type passivation occurs at Cd-related sites at the surface. Our results show a spectroelectrochemical signature of two binding motifs on the surface of CdTe NCs, which can be properly passivated by a combination of X- and Z-type ligands.

2.4 Methods

Materials. Oleic acid (OA, 90%), 1-octadecene (ODE, 90%), trioctylphosphine (TOP, 90%), 1,8-octanedithiol (8DT, ≥97%), cadmium chloride ($CdCl_2$, 99.99%), indium chloride ($InCl_3$, ≥99.999%), zinc chloride ($ZnCl_2$, 99.999%) and lithium perchlorate ($LiClO_4$, 99.99%) were purchased from Sigma-Aldrich. Cadmium oxide (CdO, 99.998%) and tellurium (Te, −18 + 60 mesh, 99.999%) were purchased from Alfa Aesar. The indium-doped tin oxide substrates (ITO, film thickness ~100 nm, $R_{sq} \leq 20\ \Omega/cm^2$) were obtained from PGO Germany. Anhydrous acetone (≥99.8%) was purchased from VWR chemicals. Anhydrous methanol (MeOH, 99.8%), 1-butanol (BuOH, 99.8%), toluene (99.8%), and acetonitrile (99.99%) were all obtained from Sigma-Aldrich. Before use, the OA was degassed at 100°C for 1 h, and the acetonitrile was dried by an Inert Technology PureSolv Micro Solvent Purification System. All other chemicals were used as-received. Cadmium and tellurium compounds are toxic and carcinogenic and should be handled with care.

Synthesis of CdTe NCs. The CdTe NCs were synthesized using the method of Kloper et al.[47] For the Cd-precursor, CdO (51.4 mg, 0.4 mmol) was mixed with OA (400 μL) and ODE (20 mL). The Te-precursor was prepared by dissolving elemental Te (51.0 mg, 0.4 mmol) in TOP (1 mL) and diluting the resulting yellow solution with ODE (4 mL). The Cd-precursor was first degassed under vacuum at 100°C for approximately 1 h. Then, the system was flushed with N_2 and heated to ca. 280°C until the red turbid mixture became a transparent colorless solution, indicating the formation of $Cd(OA)_2$. Subsequently, the temperature was raised to 310°C for roughly 30 min. When the first gray precipitate of metallic Cd^0 was observed, the Te-precursor was swiftly injected. Following the resulting nucleation, the color of the solution quickly changed from yellow to black. The NCs were allowed to grow at 260°C for 3 min, after which the mixture was quenched with 5 mL ODE. The Cd^0 was removed from the reaction mixture by centrifugation and decantation.

Subsequent washing of the NCs was carried out by precipitating the NCs with a mixture of MeOH and BuOH (NCs:MeOH:BuOH 1:1:1), and centrifugation at 3500 rpm for ca. 3 min. The supernatant was decanted, and the NCs were resuspended in 5 mL toluene. This washing procedure was then repeated once more.

Nanocrystal Film Preparation. Nanocrystal films were prepared by dip-coating, using a Nima dipcoater. First, the ITO substrates were dipped for 30 s in a concentrated NC solution (~10^{-4} M), followed by 30 s in a solution of 8DT in MeOH (0.1 M) and 30 s in MeOH to rinse off excess ligands. Using this procedure, 3–7 layers were applied to the ITO substrate. Roughly a third of the ITO was left uncoated to provide contact with the electrodes during the electrochemical measurements.

Treatment with Metal Chloride Salt Solution. The NC films were passivated by treating them with either $CdCl_2$, $InCl_3$ or $ZnCl_2$ salt solutions in acetone. For that, the films were submersed overnight (~16 h) in 2 mL of 0.1 M metal chloride salt in acetone solutions at room temperature. Due to the limited solubility of $CdCl_2$ in acetone, a saturated solution was used instead (estimated concentration <5 mM).[46] After the salt treatment, the films were rinsed with MeOH in order to remove unbound metal chloride salt.

Steady State Optical Spectroscopy. The absorbance of CdTe NC solutions and films was recorded on a PerkinElmer Lambda 900 UV/vis/NIR Spectrometer. The PL was measured on an Edinburgh Instruments FLS980 Fluorescence Spectrometer, using a 450 W xenon lamp as the excitation source. PL QY measurements were carried out in the same device, using an integrating sphere. Solutions were measured in closed quartz cuvettes (path length 10 mm). Diluted CdTe NC solutions were prepared by adding 50–100 µL of the crude NC in toluene solution (concentration ~10^{-4} M) to 3 mL toluene in quartz cuvettes, in order to reach an optical density at the $1S_{3/2}1S_e$ transition between 0.1 and 0.5.

Spectroelectrochemistry. Spectroelectrochemical experiments were carried out in a glovebox under N_2. The setup consisted of a Ag wire pseudoreference electrode (PRE), a Pt sheet counter electrode (CE) and a CdTe-ITO film as working electrode (WE) in a quartz cell (Figure A2.1). The Ag wire (−4.90±0.03 vs vacuum) was calibrated with ferrocene/ferrocenium (see Figure A2.2).[48] All potentials are given with respect to the Ag PRE. The supporting electrolyte consisted of a 0.1 M solution of $LiClO_4$ in acetonitrile. The potential was applied with an Autolab PGSTAT302N. Unless otherwise noted, a scan rate of 50 mV/s was used. Changes in absorbance were measured with a DH-2000 halogen lamp as light source, and detected with a USB2000 UV–vis spectrometer. All these components were acquired from Ocean Optics. For PL measurements, the films were excited with a 4.5 mW collimated laser diode from Thorlabs (wavelength 405 nm). The PL was detected with the same UV–vis spectrometer as used for the absorbance. For a schematic of the setup, see Figure A2.3.

Analysis of Band Edge Differential Absorption Signal. In order to separate the contributions to the spectroelectrochemical measurements arising from a bleach of the $1S_e$ transition and from a Stark shift, the signal was fitted with a sum of two components:

$$F_{Gauss}(\lambda) = A_{Gauss} \times e^{\frac{(\lambda-\lambda_0)^2}{2\times\sigma^2}} \quad 2.5$$

$$F_{Shift}(\lambda) = A_{Shift} \times \left(e^{\frac{(\lambda-\lambda_0-\lambda_{Shift})^2}{2\times\sigma^2}} - e^{\frac{(\lambda-\lambda_0)^2}{2\times\sigma^2}} \right) \quad 2.6$$

where F_{Gauss} (λ) is a Gaussian function describing the bleach due to state filling, and F_{Shift} (λ) describes the Stark shift by a difference between two Gaussians, shifted from each other by λ_{Shift}. The fit is performed keeping λ_0 and σ fixed at the values determined by the fit of a single spectral slice, and letting A_{Gauss} and A_{Shift} vary. For λ_0 and σ this choice assumes that the distribution of energies for the bandgap of the NCs does not change along the scan. The value for λ_{Shift}. is set to 17 nm, which allowed good agreement of the fitted function with the experimental data. In the Appendix we show that a small variation in the choice of λ_{Shift}. does not affect the outcome of the fit. The value of A_{Gauss} is taken as the effective bleach of the $1S_e$ transition, while A_{Shift} is proportional to the amount of trapped charges per NC, as also shown in the Appendix.

Transmission Electron Microscopy (TEM) and Electron Diffraction. TEM samples were prepared by drop-casting a dilute solution of CdTe NCs in toluene on a carbon-coated copper TEM grid (400-mesh). TEM images and electron diffraction patterns were measured on a JEOL JEM-3200 FSC cryo-TEM, operating at 300 kV. The selected area electron diffraction (SAED) pattern was radially integrated to obtain the 1D electron diffraction pattern.[49]

X-ray Photoelectron Spectroscopy (XPS). XPS measurements were conducted on the CdTe-ITO WE described above, before and after the metal chloride salt treatments. Measurements were carried out on a Thermo Fisher K-Alpha spectrometer, using an Al K_α source (1486.7 eV). The C 1s peak at 284.8 eV was used as a reference to correct for shifts due to charging. While measuring, the pressure in the analysis chamber was kept below 2×10^{-7} mbar.

References

1. Kovalenko, M. V., Manna, L., Cabot, A., Hens, Z., Talapin, D. V., Kagan, C. R., Klimov, V. I., Rogach, A. L., Reiss, P., Milliron, D. J., et al. Prospects of nanoscience with nanocrystals. ACS Nano 9, 1012–1057 (2015).
2. Donegá, C. de M. Synthesis and properties of colloidal heteronanocrystals. Chem. Soc. Rev. 40, 1512–1546 (2011).
3. Reiss, P., Protière, M. & Li, L. Core/Shell Semiconductor Nanocrystals. Small 5, 154–168 (2009).
4. Burda, C., Chen, X., Narayanan, R. & El-Sayed, M. A. Chemistry and Properties of Nanocrystals of Different Shapes. Chem. Rev. 105, 1025–1102 (2005).
5. Kagan, C. R. & Murray, C. B. Charge transport in strongly coupled quantum dot solids. Nat. Nanotechnol. 10, 1013–1026 (2015).
6. Talapin, D. V., Lee, J.-S., Kovalenko, M. V. & Shevchenko, E. V. Prospects of Colloidal Nanocrystals for Electronic and Optoelectronic Applications. Chem. Rev. 110, 389–458 (2010).
7. Kim, J. Y. & Kotov, N. A. Charge transport dilemma of solution-processed

nanomaterials. Chem. Mater. 26, 134–152 (2014).
8. Wuister, S. F., De Mello Donegá, C. & Meijerink, A. Influence of thiol capping on the exciton luminescence and decay kinetics of CdTe and CdSe quantum dots. J. Phys. Chem. B 108, 17393–17397 (2004).
9. Houtepen, A. J., Hens, Z., Owen, J. S. & Infante, I. On the Origin of Surface Traps in Colloidal II–VI Semiconductor Nanocrystals. Chem. Mater. 29, 752–761 (2017).
10. Anderson, N. C., Hendricks, M. P., Choi, J. J. & Owen, J. S. Ligand Exchange and the Stoichiometry of Metal Chalcogenide Nanocrystals: Spectroscopic Observation of Facile Metal-Carboxylate Displacement and Binding. J. Am. Chem. Soc. 135, 18536–18548 (2013).
11. Pu, C. & Peng, X. To Battle Surface Traps on CdSe/CdS Core/Shell Nanocrystals: Shell Isolation versus Surface Treatment. J. Am. Chem. Soc. 138, 8134–8142 (2016).
12. Giansante, C. & Infante, I. Surface Traps in Colloidal Quantum Dots: A Combined Experimental and Theoretical Perspective. J. Phys. Chem. Lett. 8, 5209–5215 (2017).
13. Boldt, K., Kirkwood, N., Beane, G. A. & Mulvaney, P. Synthesis of highly luminescent and photo-stable, graded shell CdSe/Cd xZn1-xS nanoparticles by in situ alloying. Chem. Mater. 25, 4731–4738 (2013).
14. Chen, P. E., Anderson, N. C., Norman, Z. M. & Owen, J. S. Tight Binding of Carboxylate, Phosphonate, and Carbamate Anions to Stoichiometric CdSe Nanocrystals. J. Am. Chem. Soc. 139, 3227–3236 (2017).
15. Drijvers, E., De Roo, J., Martins, J. C., Infante, I. & Hens, Z. Ligand Displacement Exposes Binding Site Heterogeneity on CdSe Nanocrystal Surfaces. Chem. Mater. 30, 1178–1186 (2018).
16. De Nolf, K., Cosseddu, S. M., Jasieniak, J. J., Drijvers, E., Martins, J. C., Infante, I. & Hens, Z. Binding and Packing in Two-Component Colloidal Quantum Dot Ligand Shells: Linear versus Branched Carboxylates. J. Am. Chem. Soc. 139, 3456–3464 (2017).
17. Greaney, M. J., Couderc, E., Zhao, J., Nail, B. A., Mecklenburg, M., Thornbury, W., Osterloh, F. E., Bradforth, S. E. & Brutchey, R. L. Controlling the Trap State Landscape of Colloidal CdSe Nanocrystals with Cadmium Halide Ligands. Chem. Mater. 27, 744–756 (2015).
18. Boehme, S. C., Azpiroz, J. M., Aulin, Y. V., Grozema, F. C., Vanmaekelbergh, D., Siebbeles, L. D. A., Infante, I. & Houtepen, A. J. Density of Trap States and Auger-mediated Electron Trapping in CdTe Quantum-Dot Solids. Nano Lett. 15, 3056–3066 (2015).
19. Zhou, J., Zhu, M., Meng, R., Qin, H. & Peng, X. Ideal CdSe/CdS Core/Shell Nanocrystals Enabled by Entropic Ligands and Their Core Size-, Shell Thickness-, and Ligand-Dependent Photoluminescence Properties. J. Am. Chem. Soc. 139, 16556–16567 (2017).
20. Berends, A. C., Rabouw, F. T., Spoor, F. C. M., Bladt, E., Grozema, F. C., Houtepen, A. J., Siebbeles, L. D. A. & De Mello Donegá, C. Radiative and Nonradiative Recombination in CuInS2 Nanocrystals and CuInS2-Based Core/Shell Nanocrystals. J. Phys. Chem. Lett. 7, 3503–3509 (2016).

21. Rabouw, F. T., Kamp, M., Van Dijk-Moes, R. J. A., Gamelin, D. R., Koenderink, A. F., Meijerink, A. & Vanmaekelbergh, D. Delayed Exciton Emission and Its Relation to Blinking in CdSe Quantum Dots. Nano Lett. 15, 7718–7725 (2015).
22. Geiregat, P., Houtepen, A. J., Sagar, L. K., Infante, I., Zapata, F., Grigel, V., Allan, G., Delerue, C., Van Thourhout, D. & Hens, Z. Continuous-wave infrared optical gain and amplified spontaneous emission at ultralow threshold by colloidal HgTe quantum dots. Nat. Mater. 17, 35–42 (2018).
23. Buckley, J. J., Couderc, E., Greaney, M. J., Munteanu, J., Riche, C. T., Bradforth, S. E. & Brutchey, R. L. Chalcogenol ligand toolbox for CdSe nanocrystals and their influence on exciton relaxation pathways. ACS Nano 8, 2512–2521 (2014).
24. Boles, M. A., Ling, D., Hyeon, T. & Talapin, D. V. The surface science of nanocrystals. Nat. Mater. 15, 141–153 (2016).
25. Voznyy, O., Thon, S. M., Ip, A. H. & Sargent, E. H. Dynamic Trap Formation and Elimination in Colloidal Quantum Dots. J. Phys. Chem. Lett. 4, 987–992 (2013).
26. Boehme, S. C., Vanmaekelbergh, D., Evers, W. H., Siebbeles, L. D. A. & Houtepen, A. J. In Situ Spectroelectrochemical Determination of Energy Levels and Energy Level Offsets in Quantum-Dot Heterojunctions. J. Phys. Chem. C 120, 5164–5173 (2016).
27. Chen, M. & Guyot-Sionnest, P. Reversible Electrochemistry of Mercury Chalcogenide Colloidal Quantum Dot Films. ACS Nano 11, 4165–4173 (2017).
28. Gudjonsdottir, S., van der Stam, W., Kirkwood, N., Evers, W. H. & Houtepen, A. J. The Role of Dopant Ions on Charge Injection and Transport in Electrochemically Doped Quantum Dot Films. J. Am. Chem. Soc. 140, 6582–6590 (2018).
29. Wehrenberg, B. L., Yu, D., Ma, J. & Guyot-Sionnest, P. Conduction in charged PbSe nanocrystal films. J. Phys. Chem. B 109, 20192–20199 (2005).
30. van der Stam, W., Gudjonsdottir, S., Evers, W. H. & Houtepen, A. J. Switching between Plasmonic and Fluorescent Copper Sulfide Nanocrystals. J. Am. Chem. Soc. 139, 13208–13217 (2017).
31. Pinchetti, V., Lorenzon, M., McDaniel, H., Lorenzi, R., Meinardi, F., Klimov, V. I. & Brovelli, S. Spectro-electrochemical Probing of Intrinsic and Extrinsic Processes in Exciton Recombination in I-III-VI2 Nanocrystals. Nano Lett. 17, 4508–4517 (2017).
32. Klimov, V. I., Ivanov, S. A., Nanda, J., Achermann, M., Bezel, I., McGuire, J. A. & Piryatinski, A. Single-exciton optical gain in semiconductor nanocrystals. Nature 447, 441–446 (2007).
33. Rogach, A. L., Klar, T. A., Lupton, J. M., Meijerink, A. & Feldmann, J. Energy transfer with semiconductor nanocrystals. J. Mater. Chem. 19, 1208–1221 (2009).
34. Klimov, V. I. Optical Nonlinearities and Ultrafast Carrier Dynamics in Semiconductor Nanocrystals. J. Phys. Chem. B 104, 6112–6123 (2000).
35. Puntambekar, A., Wang, Q., Miller, L., Smieszek, N. & Chakrapani, V. Electrochemical Charging of CdSe Quantum Dots: Effects of Adsorption versus Intercalation. ACS Nano 10, 10988–10999 (2016).
36. Brozek, C. K., Hartstein, K. H. & Gamelin, D. R. Potentiometric Titrations for Measuring the Capacitance of Colloidal Photodoped ZnO Nanocrystals. J. Am. Chem. Soc. 138, 10605–10610 (2016).
37. Carroll, G. M., Tsui, E. Y., Brozek, C. K. & Gamelin, D. R. Spectroelectrochemical

Measurement of Surface Electrostatic Contributions to Colloidal CdSe Nanocrystal Redox Potentials. Chem. Mater. 28, 7912–7918 (2016).

38. Houtepen, A. J. & Vanmaekelbergh, D. Orbital occupation in electron-charged CdSe quantum-dot solids. J. Phys. Chem. B 109, 19634–19642 (2005).
39. Grimaldi, G., Crisp, R. W., ten Brinck, S., Zapata, F., van Ouwendorp, M., Renaud, N., Kirkwood, N., Evers, W. H., Kinge, S., Infante, I., et al. Hot-electron transfer in quantum-dot heterojunction films. Nat. Commun. 9, 2310 (2018).
40. Brovelli, S., Galland, C., Viswanatha, R. & Klimov, V. I. Tuning Radiative Recombination in Cu-Doped Nanocrystals via Electrochemical Control of Surface Trapping. Nano Lett. 12, 4372–4379 (2012).
41. Brovelli, S., Bae, W. K., Meinardi, F., Santiago González, B., Lorenzon, M., Galland, C. & Klimov, V. I. Electrochemical control of two-color emission from colloidal dot-in-bulk nanocrystals. Nano Lett. 14, 3855–3863 (2014).
42. Kirkwood, N., Monchen, J. O. V., Crisp, R. W., Grimaldi, G., Bergstein, H. A. C., du Fossé, I., van der Stam, W., Infante, I. & Houtepen, A. J. Finding and Fixing Traps in II–VI and III–V Colloidal Quantum Dots: The Importance of Z-Type Ligand Passivation. J. Am. Chem. Soc. 140, 15712–15723 (2018).
43. Pearson, R. G. Absolute Electronegativity and Hardness: Application to Inorganic Chemistry. Inorg. Chem. 27, 734–740 (1988).
44. Luther, J. M. & Pietryga, J. M. Stoichiometry control in quantum dots: A viable analog to impurity doping of bulk materials. ACS Nano 7, 1845–1849 (2013).
45. Protesescu, L., Nachtegaal, M., Voznyy, O., Borovinskaya, O., Rossini, A. J., Emsley, L., Copéret, C., Günther, D., Sargent, E. H. & Kovalenko, M. V. Atomistic description of thiostannate-capped CdSe nanocrystals: Retention of four-coordinate SnS4 motif and preservation of Cd-rich stoichiometry. J. Am. Chem. Soc. 137, 1862–1874 (2015).
46. Vanderzee, C. E. & Dawson, H. J. The Stability Constants of Cadmium Chloride Complexes: Variation with Temperature and Ionic Strength. J. Am. Chem. Soc. 75, 5659–5663 (1953).
47. Kloper, V., Osovsky, R., Kolny-Olesiak, J., Sashchiuk, A. & Lifshitz, E. The growth of colloidal cadmium telluride nanocrystal quantum dots in the presence of Cd0 nanoparticles. J. Phys. Chem. C 111, 10336–10341 (2007).
48. Ruch, P. W., Cericola, D., Hahn, M., Kötz, R. & Wokaun, A. On the use of activated carbon as a quasi-reference electrode in non-aqueous electrolyte solutions. J. Electroanal. Chem. 636, 128–131 (2009).
49. Klinger, M. & Jäger, A. Crystallographic Tool Box (CrysTBox): Automated tools for transmission electron microscopists and crystallographers. J. Appl. Crystallogr. 48, 2012–2018 (2015).

Appendix

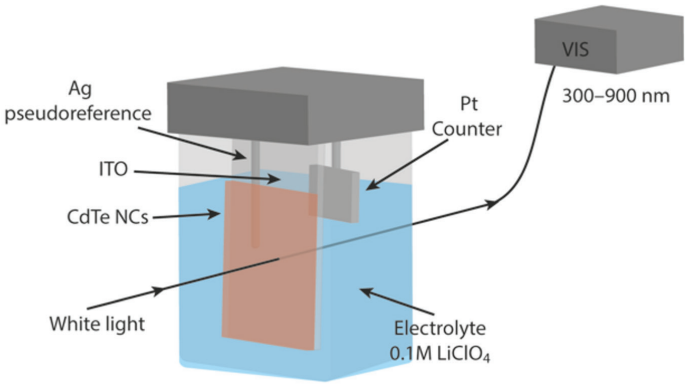

Figure A2.1. Schematic representation of the electrochemical cell.

Calibration of the Ag pseudo-reference electrode

The Ag pseudo-reference electrode used during the spectroelectrochemical experiments was calibrated with the ferrocene/ferrocenium couple. An example of a cyclic voltammogram is shown in Figure A2.2, for which the half-wave potential was determined to be +0.224 V via the equation:

$$E_{1/2} = \frac{E_{p,o} + E_{p,r}}{2} = \frac{+0.491\ V - 0.044\ V}{2} = +0.224\ V \qquad \text{A2.1}$$

The potential of the Ag pseudo-electrode can then be calculated to be -4.92 eV versus vacuum via the equation:

$$E_{vac} + E_{Ag} = -4.68\ (SCE\ vs\ vacuum) - 0.46\ (ferrocene\ vs\ SCE) + 0.224\ (ferrocene\ vs\ Ag) = -4.92\ eV \qquad \text{A2.2}$$

The ferrocene/ferrocenium couple was measured several times and subsequently averaged, which eventually resulted in a potential of -4.90 ± 0.03 eV versus vacuum.

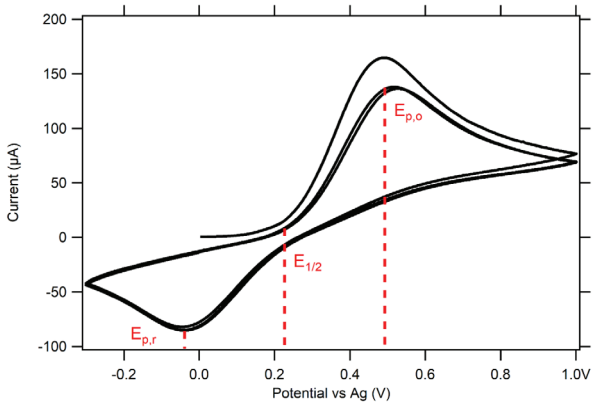

Figure A2.2. Example of a cyclic voltammogram of ferrocene in 0.1 M $LiClO_4$ in acetonitrile electrolyte solution, scanned at 50 mV/s. The oxidation and reduction peaks ($E_{p,o}$ and $E_{p,r}$ respectively) are shown, as well as the half-wave potential ($E_{1/2}$).

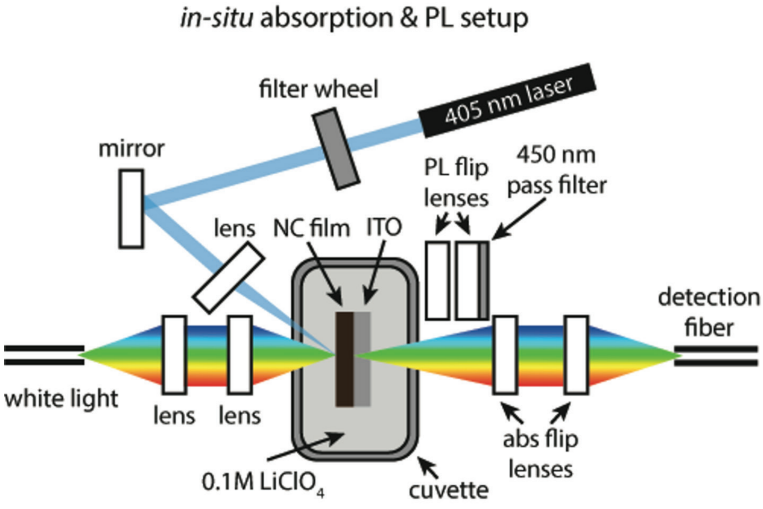

Figure A2.3. Schematic representation of the in-situ photoluminescence and absorbance setup.

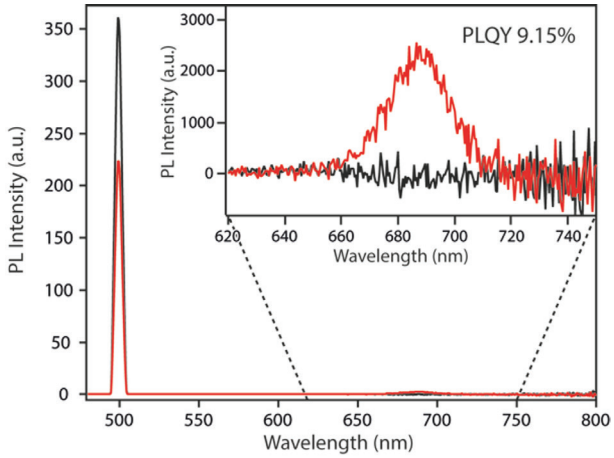

Figure A2.4. Photoluminescence quantum yield (PL QY) measurement on CdTe NCs in toluene, yielding a PL QY of 9.15%.

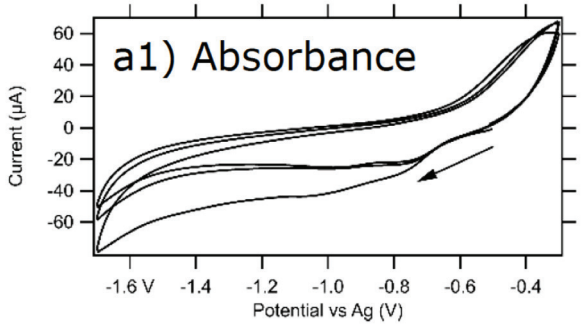

Figure A2.5. Cyclic voltammogram for a CdTe NC film during in-situ absorbance measurements.

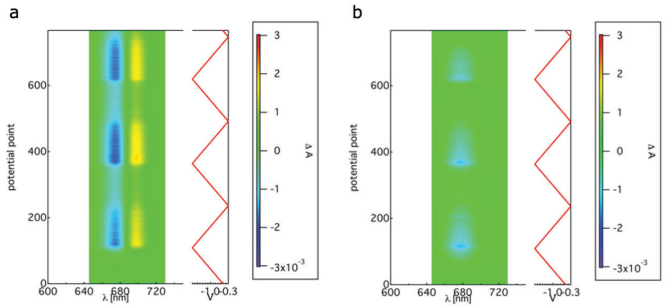

Figure A2.6. (A) Stark shift correction for untreated CdTe NC films. (B) Effective band edge bleach after Stark shift correction.

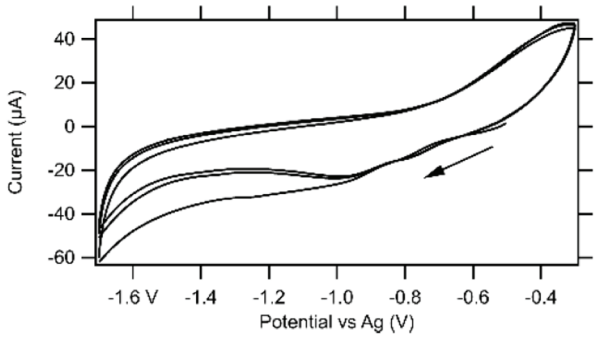

Figure A2.7. Cyclic voltammograms for a CdTe NC film during in-situ photoluminescence measurements.

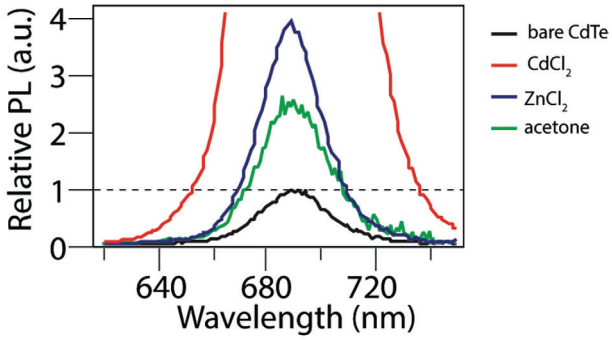

Figure A2.8. PL spectra of CdTe NC films before and after acetone-only treatment (black and green line, respectively), compared to $ZnCl_2$ and $CdCl_2$ treatment (blue and red line, respectively).

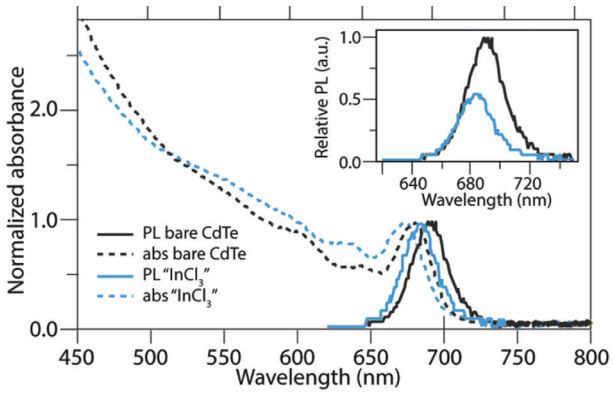

Figure A2.9. Absorbance and PL spectra of CdTe NC films after $InCl_3$ treatment.

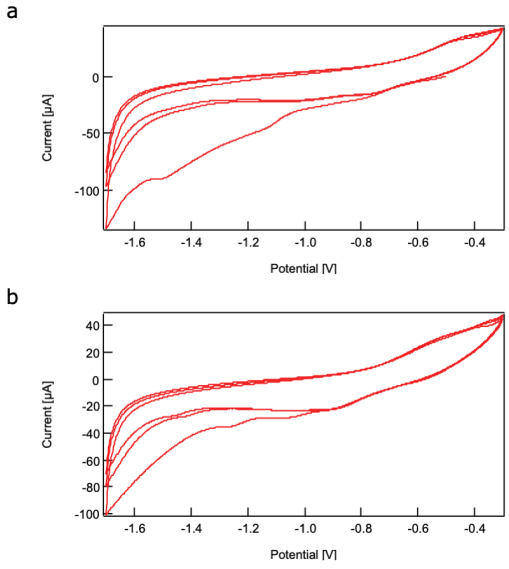

Figure A2.10. Cyclic voltammograms (CVs) after passivation with (A) $CdCl_2$ and (B) $ZnCl_2$.

Fit of the Stark shift feature in spectroelectrochemical measurements

A Stark shift of the $1S_e$ absorption shifts the energy of the transition, changing its wavelength by λ_{shift}. The differential absorbance of a Stark-shifted $1S_e$ feature, i.e. the difference between the absorbance at the currently applied potential and the absorbance at open-circuit potential in the presence of a Stark-shift, is obtained by a difference of two Gaussians:

$$F_2(\lambda) = A_2 * \left(e^{-\frac{(\lambda-\lambda_0-\lambda_{shift})^2}{2\sigma^2}} - e^{-\frac{(\lambda-\lambda_0)^2}{2\sigma^2}} \right) \quad \text{A2.3}$$

where λ_0 and σ are respectively the central wavelength and the standard deviation of the unshifted $1S_e$ feature. The parameter A_2 is the magnitude of the fitted function, related to the fraction of Stark-shifted QDs by the relation:

$$A_2 = A_0 f_{shift} \quad \text{A2.4}$$

where A_0 is the steady state absorbance of the transition.

For small values of λ_{shift}/σ, F_2 can be approximated by the linear term of the Maclaurin expansion with respect to λ_{shift}/σ:

$$F_2(\lambda) \approx A_2\, \lambda_{shift} * e^{-\frac{(\lambda-\lambda_0)^2}{2\sigma^2}} \left(\frac{\lambda - \lambda_0}{\sigma^2} \right) \quad \text{A2.5}$$

It is evident that for small values of λ_{shift}, a change in λ_{shift} and a change in A_2 produce the same variation of F_2, thus hampering extraction of reliable estimates of the two parameters from the fit (an increase in one can be compensated by a decrease in the other with negligible changes in the fitted function). It is rather their product, $A^* = A_2\lambda_{shift}$, whose best values is determined from a fit to the data.

If we assume that the amount of Stark shift is proportional to the average number of charges interacting with the Stark-shifted portion of the QD population, we obtain:

$$\lambda_{shift} = k_{shift} N_{charge} \quad \text{A2.6}$$

$$A^* = k_{shift} N_{charge} A_0 f_{shift} = k_{shift} A_0 N_{traps} \quad \text{A2.7}$$

where $N_{traps} = N_{charge} f_{shift}$ is the average number of trapped charges per QD. Thus, obtaining the potential dependence of A^* determines, within a proportionality factor, the potential dependence of the charged trap population.

In the fit to the spectroelectrochemical measurements, λ_{shift} was kept fixed and A_2 only was allowed to vary. Thus, the value of A_2 determined from the fit, $A_{2,fit}$, can be related to the charged trap population per QD via:

$$A_{2,fit} = \frac{A^*}{\lambda_{shift}} = \frac{k_{shift} A_0}{\lambda_{shift}} N_{traps} \quad \text{A2.8}$$

Thus, the fitted magnitude of the Stark shift feature is proportional to the number of trapped

charges per QD, meaning the latter can then be determined within a proportionality factor from fit of the experimental data.

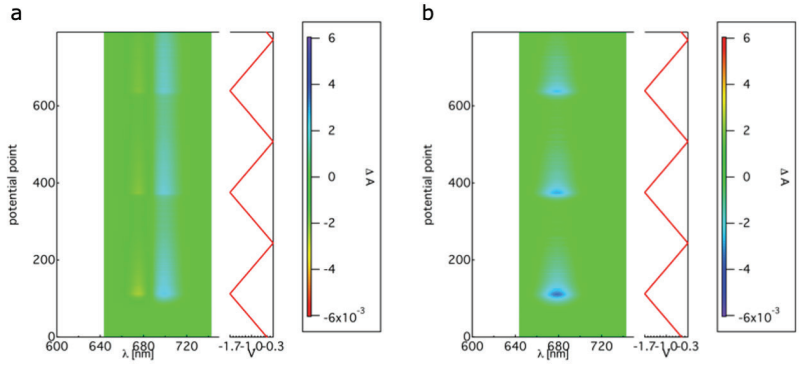

Figure A2.11. (A) Stark shift correction for $ZnCl_2$ treated CdTe NC films. (B) Effective bleach after correction.

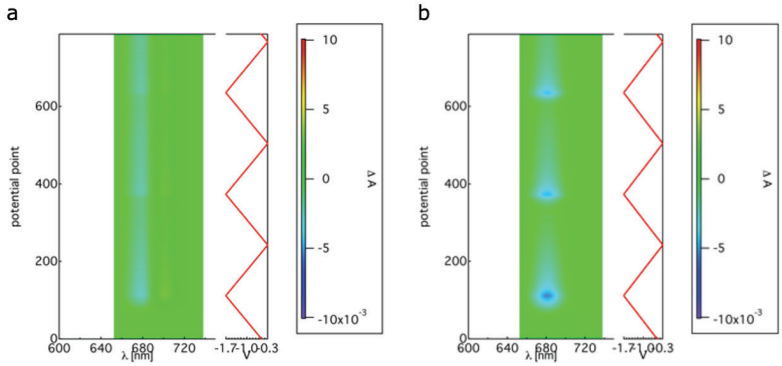

Figure A2.12. (A) Stark shift correction for $CdCl_2$ treated CdTe NC films. (B) Effective bleach after correction.

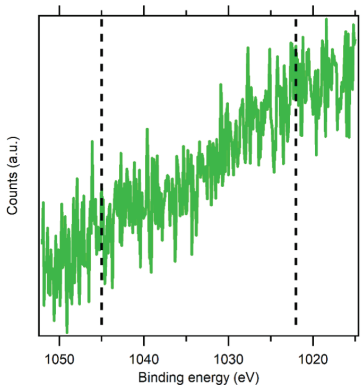

Figure A2.13. XPS characterization of the $ZnCl_2$-passivated film. The dotted lines indicate the expected positions of the Zn 2p peaks.

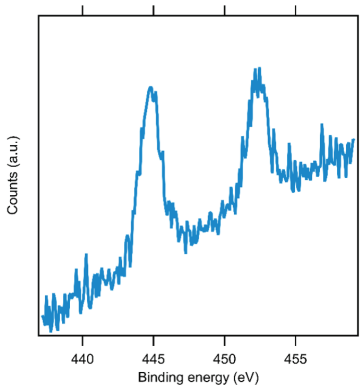

Figure A2.14. XPS characterization of the $InCl_3$-treated film. The In 3d peaks are clearly visible.

Discussion A2.1

Since the passivation of undercoordinated Te anions on neutral CdTe NCs with neutral Z-type metal chloride species will automatically retain charge balance, a balanced equation for this reaction can be easily constructed:

$$(CdTe)_{QD} + CdCl_2 \rightarrow (CdTe)_{QD}CdCl_2$$

However, since we do not exactly know what causes the Cd-related trap state, we cannot provide an unambiguous equation for the reaction with chloride anions which ensures charge balance. We can construct equations taking one of the following assumptions into account: (1) The NCs are doped after the passivation with chloride ions, due to electron

removal to ensure charge balance. (2) An ion pair is formed at the surface, possibly with protons or other cations. (3) Charge balance is not an absolute requirement at room temperature, and the NC can sustain a few charges. At this point, we cannot distinguish between these possibilities.

Part B

Theoretical studies

3

3

Role of Surface Reduction in the Formation of Traps in n-Doped II–VI Semiconductor Nanocrystals

How to Charge without Reducing the Surface

The efficiency of nanocrystal (NC)-based devices is often limited by the presence of surface states that lead to localized energy levels in the bandgap. Yet, a complete understanding of the nature of these traps remains challenging. Although theoretical modeling has greatly improved our comprehension of the NC surface, several experimental studies suggest the existence of metal-based traps that have not yet been found with theoretical methods. Since there are indications that these metal-based traps form in the presence of excess electrons, the present work uses density functional theory (DFT) calculations to study the effects of charging II–VI semiconductor NCs with either full or imperfect surface passivation. It is found that charge injection can lead to trap-formation via two pathways: metal atom ejection from perfectly passivated NCs or metal–metal dimer-formation in imperfectly passivated NCs. Fully passivated CdTe NCs are observed to be stable up to a charge of two electrons. Further reduction leads to charge localization on a surface Cd atom and the formation of in-gap states. The effects of suboptimal passivation are probed by charging NCs where an X-type ligand is removed from the (100) plane. In this case, injection of even one electron leads to Cd-dimerization and trap-formation. Addition of an L-type amine ligand prevents this dimer-formation and is suggested to also prevent trapping of photoexcited electrons in charge neutral NCs. The results presented in this work are generalized to NCs of different sizes and other II–VI semiconductors. This has clear implications for n-doping II–VI semiconductor NCs without introducing surface traps due to metal ion reduction. The possible effect of these metal ion localized traps on the photoluminescence efficiency of neutral NCs is also discussed.

This chapter is based on: Indy du Fossé, Stephanie ten Brinck, Ivan Infante, Arjan J. Houtepen. Chemistry of Materials, 2019, 31 (12), 4575-4583

3.1 Introduction

Due to their size-dependent properties and solution processability, colloidal semiconductor nanocrystals (NCs) have proven to be very interesting for application in a wide range of optoelectronic devices,[1–4] including solar cells,[5,6] light-emitting diodes,[7–9] and lasers.[10–12] However, the efficiency of these devices is often hampered by localized electronic states within the bandgap, which can trap the generated charge carriers.[13–15] Much work has been dedicated to passivating these trap states by, for example, the epitaxial growth of an inorganic shell around the NC core,[16] the addition of various ligands,[17–19] and the electrochemical filling of in-gap states.[20–22] Nevertheless, due to the complexity of the NC surface and the plethora of possible interactions between the ligands and the various binding sites on the NC, a complete understanding of the microscopic nature of these trap states remains challenging.[19,23,24]

In its simplest form, a trap can be described as a stable nonbonding orbital of an undercoordinated (and hence often surface-located) atom. This orbital usually lies deep in the bandgap, where it can act as an electron or hole trap. Surface atoms can however be fully coordinated due to the interaction with surface ligands, forming bonding and antibonding orbital energy levels, which lie within respectively the valence band (VB) and the conduction band (CB).[14,25] We recently used density functional theory (DFT) calculations to show that mostly 2-fold undercoordinated chalcogenide atoms are responsible for trap-formation in II–VI semiconductor NCs.[23] These 2-coordinated chalcogenide sites feature one nonbonding p-orbital, which remains deep in the bandgap as a trap state. In contrast, the spherical symmetry of the s-orbital of the metal ensures it is always split in states that lie outside the bandgap, regardless of coordination number.[23] In line with this description, we have recently shown that a very wide range of electron accepting Z-type ligands, which coordinate to the surface anions, can be used to increase the photoluminescence quantum yield (PL QY) of II–VI and III–V NCs.[19]

Contrary to these computational and experimental results, several experimental studies suggest that, besides the 2-coordinated chalcogenides, some traps may also be localized on the metal atoms. For instance, amine ligands have been found to increase the PL QY of NCs.[19,26–28] Since these electron donating ligands cannot passivate the undercoordinated chalcogenides,[23] amines have been suggested to passivate excess cadmium ions.[27,28] In addition, spectroelectrochemical studies of CdSe core-only and core/shell-particles have shown the existence of in-gap states near the CB that act as hole traps upon raising of the Fermi level. These traps were ascribed to undercoordinated surface Cd and could be passivated by growth of a ZnS shell.[29] Metal-based traps may be more complex and of a more dynamic nature than their chalcogenide counterparts[29] and perhaps only form in the presence of excess electrons (vide infra), which can be injected into the NCs via chemical,[30–32] electrochemical[22,33,34] or photochemical[35,36] doping but are also created upon photoexcitation of the NCs.

It is often tacitly assumed that charging NCs only leads to the filling or emptying of traps or band edge states, without affecting the structure of the NC. Yet, it is well-known that there are limits to charging of bulk semiconductor materials due to electrochemical degradation or photodecomposition,[37–39] meaning that metal (chalcogenide) atoms can be reduced

(oxidized) at certain electrochemical potentials. These effects will be strongly modified in NCs due to the high surface-to-volume ratio and the presence of stabilizing ligands. Yet it is to be expected that, even with full NC passivation, charging will eventually lead to degradation and consequent trap-formation; this process will likely be enhanced for imperfectly passivated NCs.

To study the effect of excess electrons on the NC surface, this work will focus on charge unbalanced NCs. To make a clear distinction between charge-balanced and charge unbalanced NCs, the number of excess electrons in this work is determined using the model of Voznyy et al., which has as its basic underlying assumption that each entire NC is charge neutral:[40]

$$\langle n \rangle = \sum_i N_i \times q_i \qquad 3.1$$

Here, <n> is the number of excess electrons, N_i the number of chemical species of type i, and q_i the oxidation state of species i. In this work it is assumed that the oxidation states of the constituents of the NCs are M^{2+} (M = Cd, Zn), X^{2-} (X = S, Se, Te), K^+ and Cl^-. If <n> = 0, the NC is charge-balanced. If <n> > 0, electrons are injected in the CB, while holes occupy the VB when <n> < 0. Previous theoretical works have shown that making PbS NCs charge unbalanced can lead to traps localized on (partially) reduced surface Pb[41,42] or on Pb–Pb dimers,[43,44] which are different from the 2-fold undercoordinated chalcogenides found for charge-balanced NCs.

Although these previous studies show that disrupting the charge balance of NCs in different ways can lead to different surface states, no theoretical study has given a structured overview of what happens to the NC when it becomes increasingly charged. Yet, investigating the traps that form upon electron charging can be relevant for various fields of research that involve the redox chemistry of NCs. First of all, a better comprehension of the stability of charged NCs can open up new pathways to prevent trap-formation, which will be essential for the controllable doping of NCs that is required for NC-based optoelectronic devices.[45,46] Defects in charged NCs are also relevant for NC-based catalysis, where reduction of surface Cd^{2+} to Cd^0 has been found to create catalytically active metal sites.[47,48] Understanding the surface of charged NCs may lead to the design of better NC-catalysts. Lastly, this work may help to explain the photoinstability and lower-than-unity PL QY of charge-balanced NCs. If injection of electrons can lead to trap-formation (as will be shown in this work), it is conceivable that a photoexcited electron in the CB could also lead to the formation of new surface states. Such a mechanism would lower the PL QY of uncharged NCs, without the need of (electro)chemical charge injection or doping.

The aim of the current work is to provide an atomistic picture of what happens to the NC surface upon negative charging (<n> > 0) and to show that, depending on the NC passivation, injection of electrons can lead to the formation of new surface states within the bandgap. DFT calculations are used to charge both fully passivated CdTe NCs and NCs with missing ligands. In the former case, the complete passivation prevents the occurrence of surface reorganization. Instead, it probes the maximum stability of the NCs. It is shown

that, for small, perfectly passivated NCs, charging with more than two electrons will cause the (partial) reduction of surface Cd^{2+} to Cd^0, leading to localized in-gap states that can act as hole-traps. However, if the NC is not perfectly passivated, charging with only one electron already leads to surface reconstruction in the form of Cd–Cd dimers, which manifest themselves as traps within the bandgap that are half-filled and hence can trap both electrons and holes. While both these results can be generalized to other Cd-chalcogenide materials, the increased electrochemical stability of zinc causes fully passivated Zn-chalcogenide to be significantly more stable upon electron injection. Upon ligand removal, Zn–Zn dimer-formation also leads to trap states in Zn-chalcogenide NCs. Lastly, it is shown that addition of L-type ligands can stabilize the surface and prevent dimerization, which may explain the positive effect of amines on the PL QY of charge-balanced NCs.

3.2 Results and Discussion

3.2.1 Model System

Following the example of Houtepen et al.,[23] a zincblende $Cd_{68}Te_{55}Cl_{26}$ NC of ca. 1.9 nm in diameter (see Figure 3.1A-i) was used as the model system for the calculations presented here. As also often found experimentally,[49,50] the NC is cation-rich with a Cd/Te ratio of 1.24. Chloride anions were added to preserve charge balance, since they are electronically similar to the experimentally frequently employed oleate ligands[43] but are computationally less demanding.[51,52] Figure 3.1B shows the electronic structure of these model NCs, computed at the DFT level (see Methods for further technical details). For these systems, the so-called PBE exchange-correlation functional was employed, which provides reliable geometrical structures and the composition of the molecular orbitals (MOs) [i.e., the density of states (DOS)]. On the other hand, the bandgap tends to be underestimated.[53] For the purpose of this work, one should keep in mind that the absolute energy of the calculated MOs may differ significantly from experimentally found values. Although energy levels can therefore not be directly related to, for example, electrochemical potentials, trends between different systems can still easily be observed. Also, for charged NCs, the energetic position of the trap state in the bandgap versus the CB and VB can only be qualitatively reproduced.

3.2.2 Charging of Perfectly Passivated NCs

Perfectly passivated CdTe NCs were charged with up to four extra electrons, as shown in Figure 3.1. For this, neutral potassium atoms were added to the NC structure. Subsequent geometry optimization resulted in an overall charge neutral system, where one electron per potassium atom is donated to the NC. This gives an effectively negative NC, compensated by positive potassium ions. Since different counterions can be used to compensate for the negatively charged NCs,[54] it was verified that the same results are obtained for other cations, as shown for Li^+ and Cs^+ in Figure A3.1. Throughout this work, the number of excess electrons in a NC is denoted by <n>, as defined in the introduction.

Figure 3.1A shows that charging the NCs with up to two electrons results in no major structural changes. As indicated by the DOS in Figure 3.1B, the electrons are simply injected into the CB edge and no states are formed in the bandgap. Note that for <n> =

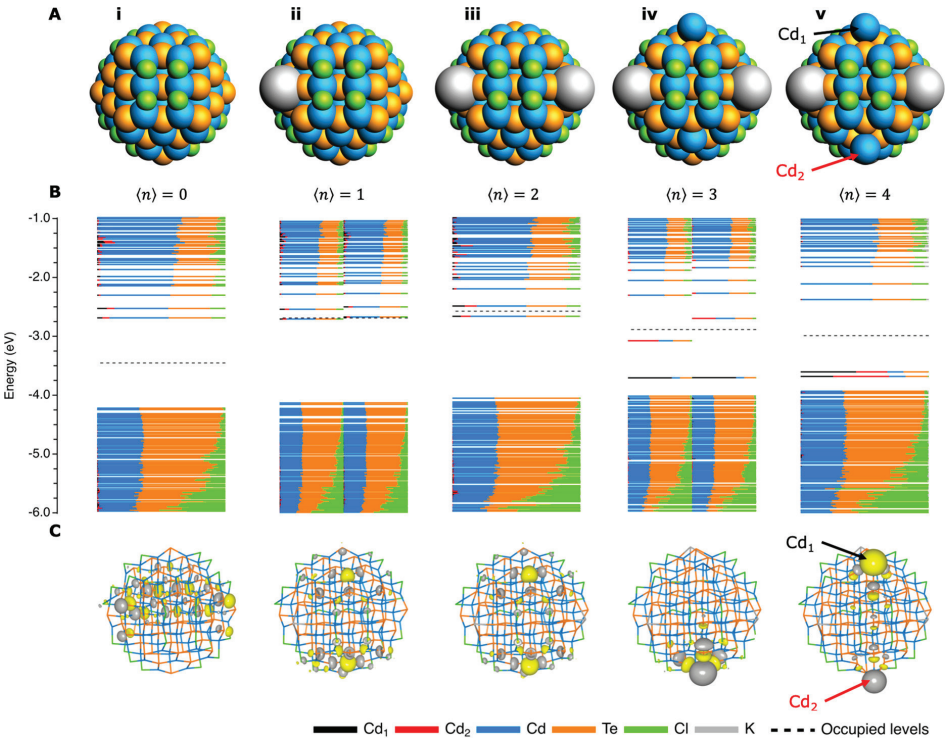

Figure 3.1. Effect of charging fully passivated CdTe NCs on their structure and DOS. (A) Structure of the NCs when 0, 1, 2, 3, and 4 electrons are injected, respectively. The total system is kept neutral by the addition of a potassium cation for each added electron. (B) DOS for each of the NCs, where every line corresponds to an MO. The length of a colored line segment indicates the contribution of the corresponding atom or element to that MO. MOs below the dotted line are occupied, whereas the ones above are unoccupied. If the total number of electrons is even (i.e., for <n> = 0, 2, 4), every MO is occupied by two electrons with opposing spin. If the total number of electrons is odd (<n> = 1, 3), the unrestricted calculation leads to a splitting of the spin-up and spin-down orbitals, which are plotted separately on the left- and right-hand side of the graph. As a result, each MO is only occupied by a single electron. (C) Contour plots of the HOMO level of each of the NCs.

1, the odd total number of electrons in the system necessitates the use of an unrestricted DFT calculation, so that each MO holds only one electron (either spin-up or spin-down). This approach breaks the spatial symmetry between alpha and beta electrons, providing two distinct densities of states, a difference that is more pronounced near the band edge region. Apart from this, the unrestricted calculation for odd numbers of electrons does not lead to significantly different results compared to the restricted calculation for an even number of electrons. In Figure 3.1B and in all of the ensuing figures with an odd total number of electrons, the MOs belonging to the alpha electrons are displayed on the left half of the graph, while the beta electrons are plotted on the right half. For <n> = 2, the total number of electrons is even, so that no unrestricted calculation is required and each

MO holds two electrons. Plotting the HOMO level for <n> = 1 and <n> = 2, as done in Figure 3.1C-ii and 3.1C-iii, respectively, shows that the electrons are delocalized over the NC. However, when three electrons are added to the NC, a Cd^0 is ejected from the (111) plane (designated by Cd_1 in Figure 3.1), which leads to the formation of multiple in-gap states (see Figure 3.1B-iv). Two electrons are injected into two closely spaced MOs around −3.7 eV. The black line segment in Figure 3.1B-iv indicates that these levels are mainly localized on the ejected Cd_1. The third electron occupies the HOMO localized on a Cd from another (111) plane (Cd_2 in Figure 3.1), as can be clearly seen in the contour plot of Figure 3.1C-iv. The MO localized on Cd_1 is full and can hence act as a hole trap, while the MO on Cd_2 is half-filled and can trap both electrons and holes. If four electrons are added to the NC (Figure 3.1-v), Cd_2 will also be expelled from its facet (as Cd^0), resulting in two filled in-gap states that are highly localized on the two ejected Cd^0 atoms.

These results can be interpreted as the gradual reduction of surface Cd^{2+} and illustrate the instability of the fully chloride-passivated CdTe surface against negative charging. It shows that a limited number of electrons can be injected into the CB of the NCs without significant structural changes. However, if too many electrons are injected, localization of the excess charge on certain Cd^{2+} sites can lead to their reduction to Cd^0. It should be noted that not all of the excess charge is localized on the Cd^{2+} sites and that the Cd is therefore not completely reduced to Cd^0 but to a small noninteger oxidation state. However, for simplicity, the oxidation states of Cd will be limited to integers in this discussion. Since the CB consists of antibonding Cd 5s orbitals,[55] charge localization will probably weaken the Cd–Te bonds of the Cd^0 sites, thus leading to expulsion of the Cd^0 from the lattice. This is in agreement with previous theoretical studies, which have shown that addition of ligands can lead to the ejection of Cd atoms from certain facets.[56,57]

It may be possible that the weakening of the Cd–Te bonds can cause Cd^0 to entirely leave the NC. With the removal of the Cd^0 atoms, the in-gap states would also be removed (see Figure A3.2), suggesting that the traps presented in this section are only transient. We performed molecular dynamics simulations that show that the Cd^0 atoms are highly mobile. However, experimentally there are various factors that influence the stability of the Cd^0, like the presence of L-type ligands on the surface and solvent effects, that are not considered in the current work and make it difficult to predict theoretically if the Cd^0 remains bound to the surface. Spectroelectrochemical experiments show an induced sub-bandgap absorbance at negative potentials, which is attributed to the formation of metallic Cd^0, and which disappears again at more positive potentials.[29] This chemical reversibility suggests that the Cd^0 remains on the NC surface, where it can be oxidized back upon application of more anodic potentials. In addition, stable surface Cd^0 is suggested to play an important role in NC-based catalysis.[47,48] On the basis of these experimental results, we conjecture that at least part of the Cd^0 remains on the NC surface.

The reduction of Cd^{2+} has already been suggested in various previous experimental works on NCs that were chemically,[30,58,59] photochemically,[36] or electrochemically[21,22,29,60] n-doped. The results presented in this section are in line with these experimental observations and provide the first atomistic picture of the surface during increasing reduction of the NC.

The results presented in this section can be generalized to charging with a different counterion (see Figure A3.1) and to certain larger NC sizes (see Figure A3.3). Interestingly, upon charging $Cd_{152}Te_{135}Cl_{34}$ NCs with up to four electrons, no in-gap states are formed, whereas charging of $Cd_{176}Te_{147}Cl_{58}$ NCs does lead to expulsion of Cd^0 and trap-formation (see Figure A3.3). This suggests that the stability of the NCs also depends on the local coordination of the surface atoms. Only if suitable surface sites are present, does it become energetically favorable to expel one or multiple atoms from the lattice.

Lastly, the findings presented in this section can also be generalized to other II–VI NCs. Figure 3.2 shows the structures and DOS of six different $M_{68}X_{55}Cl_{26}$ (M = Cd, Zn; X = S, Se, Te) zincblende semiconductor NCs after injection of four electrons (see Figure A3.4 for the structures and trap-free DOS of the uncharged NCs). It shows that the stability of a NC is highly dependent on the nature of the metal cation. While injection of four electrons leads to expulsion of surface Cd^0 in the CdX NCs, the electrons in the ZnX NCs remain completely delocalized in the CB. This is in line with the thermodynamic reduction potentials of the bulk materials, which show that the Zn-chalcogenides are generally more stable against reduction than the Cd-based compounds.[39] Although these potentials are based on aqueous media and neglect the details of the surface and surface passivation, they give an indication on why the injected charges are less prone to localize on Zn sites.

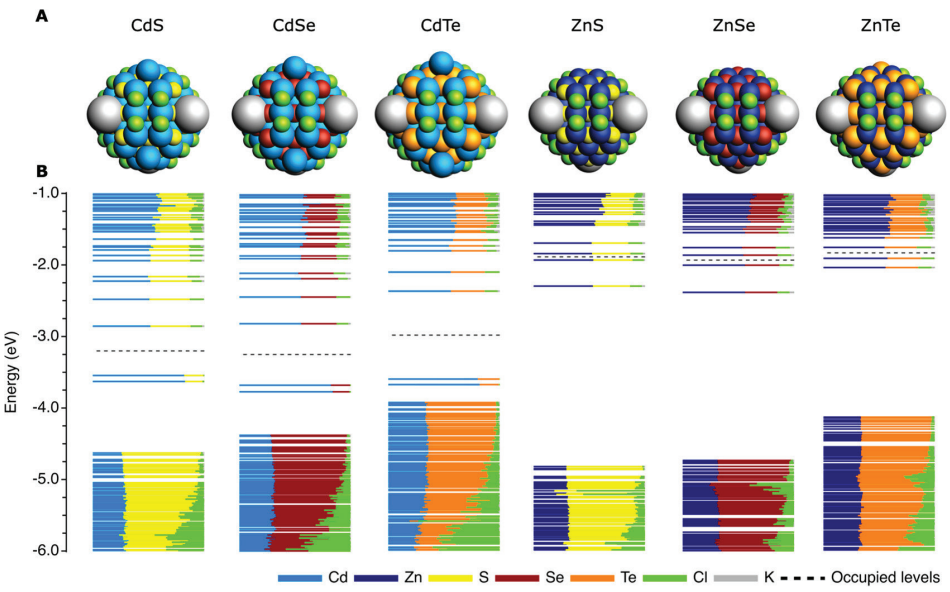

Figure 3.2. Effect of charging different $M_{68}X_{55}Cl_{26}$ (M = Cd, Zn; X = S, Se, Te) zincblende NCs on their structure and DOS. (A) Structure and (B) DOS of the NCs when charged with four electrons. The total system is kept neutral by the addition of a potassium cation for each added electron. The structure and DOS of the uncharged NCs are given in Figure A3.4.

We note that contrary to the observation presented here that ZnX NCs are more stable than CdX, charge injection into CdX NCs has been shown to be reversible,[33,34] while reports on charging ZnX NCs are scarce. We conjecture that this may be due to the energetic position of the CB edge of the materials. Since the CB of ZnX lies higher than that of CdX,[39,61] electrons injected into the CB of the Zn-based compounds have a higher electrochemical potential than electrons in the Cd-based materials. While the ZnX material would remain stable according to our calculations, the high energy of CB electrons could more easily lead to side-reactions with ligands, solvent, or impurities, which could consume the electrons. Lastly, as will be shown in the ensuing section, ligand passivation has a large influence on the stability of the NC and may also explain some of the differences found between charging Cd- and Zn-based NCs.

3.2.3 Charging of Imperfectly Passivated NCs

So far, perfectly passivated NCs have been considered. However, NCs often have some form of surface imperfections, like incomplete ligand passivation. Surface states resulting from such imperfections do not necessarily act as traps themselves (vide infra), but they can provide a pathway to the formation of trap states. Any ligand on the surface will stabilize the ions it is coordinated to and will hence make it harder for them to be reduced. Inversely, removing such ligands will lead to more facile reduction of the same ions.

To investigate the effects of imperfect passivation, Figure 3.3 shows the results of charging a NC when a chloride ligand has either been removed from a (100) surface or moved to another facet. If a chloride is moved from a (100) to the neighboring (111) facet, as shown in Figure 3.3A-i, it can no longer stabilize Cd_1 and Cd_2. As a result, the structure will adapt a new geometry to minimize its energy. In Figure 3.3A-i, it can be seen that Cd_1 moves deeper into the NC, so that its distance from Cd_2 is increased to 4.98 Å (as compared to a distance of 3.95 Å for the perfectly passivated NC in Figure 3.1-i). Still, the bandgap remains clean (see Figure 3.3B-i). If, simultaneously with the displacement of this Cl^-, the NC is charged with one electron (Figure 3.3-ii), Cd_1 and Cd_2 form a dimer that gives an energy state within the bandgap. We confirmed with molecular dynamics simulations that this dimer is stable (i.e., it is not removed by surface reconstruction). The same dimer-formation is observed when a chloride is removed as Cl^- and an electron is injected into the NC (which is isoelectric with removing a chlorine, Cl^0), as shown in Figure 3.3-iii. Further charging of this NC (Figure 3.3-iv) reduces the Cd_1–Cd_2 distance to 2.75 Å (as compared to a Cd_1–Cd_2 distance of 2.97 Å for the NC in Figure 3.3-iii).

These results can be explained by considering the 5s orbitals of the Cd^{2+} ions, which could in theory overlap to form a Cd–Cd sigma-bond. However, this surface configuration is prevented by two factors. First of all, the stabilizing influence of the X-type ligands prevents the Cd^{2+} sites from moving closer to each other. Additionally, the 5s orbitals of Cd^{2+} are empty. As a result, even if the Cd^{2+} ions would be able to approach each other close enough to form a bond, there would be no electrons to populate the bonding MO. Thus, there would be no energetic gain by bond formation. If a chloride is moved from the (100) plane to the adjacent (111) facet (Figure 3.3-i), there is room for the Cd^{2+} ions to move toward each other. Yet, no extra electrons are present to occupy the bonding MO and no dimer is therefore formed. Only if the NC is charged (Figure 3.3-ii) can the

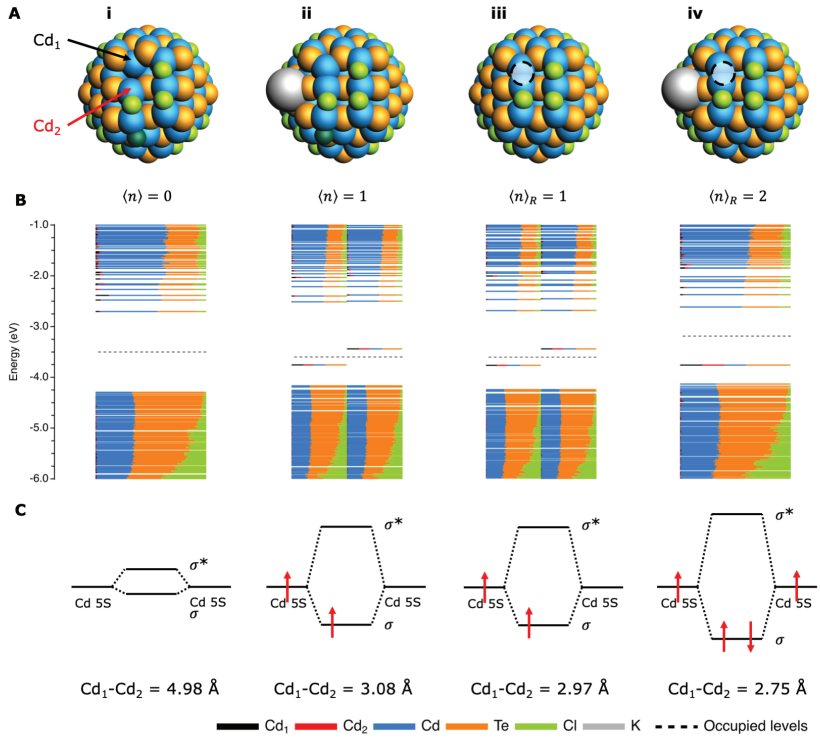

Figure 3.3. Cd–Cd dimerization upon charging of imperfectly passivated NCs. (A) Structure of the NCs when (i) a chloride (indicated in dark green) is moved from a (100) to an adjacent (111) facet (<n> = 0); (ii) the NC is charged simultaneously with moving the chloride (<n> = 1); (iii) a chloride is removed from the (100) facet (from the position indicated with the black circle) while an electron is injected, which is isoelectric with removing a Cl^0 ligand ($\langle n \rangle_R = 1$); and (iv) when the same chloride is removed and two electrons are injected ($\langle n \rangle_R = 2$). Note that the R in $\langle n \rangle_R$ indicates that a Cl^0 has been removed from the NC. For <n> = 1 and $\langle n \rangle_R = 2$ a potassium cation has been added to keep the total system charge neutral. (B) The DOS for each of the NCs. (C) Simplified MO diagram, which shows that a Cd–Cd dimer is only formed when an extra electron is available to occupy the bonding MO, which in turn forms a trap state in the bandgap. The distance between Cd_1 and Cd_2 has been given for each of the structures to show the significant reduction in bond length upon dimerization (the Cd_1–Cd_2 distance for the fully passivated NC in Figure 3.1-i is 3.95 Å).

extra electron occupy the bonding orbital and thus lead to dimerization. This bonding MO is then pushed out of the CB into the bandgap, where it forms a half-filled trap state, meaning that it can trap both holes and electrons. The same reasoning applies to the NC where a chlorine (Cl^0) ligand has been removed (see Figure 3.3-iii). Charging this NC further (Figure 3.3-iv) will lead to the injection of a second electron in the bonding orbital, thus shortening the Cd–Cd bond, as shown in Figure 3.3C. Since the in-gap state is now completely filled, it can only lead to hole-trapping.

These results show that the passivation of the NC surface plays an important role in the stability of the NC in the presence of extra electrons. If the NC is perfectly passivated (as discussed in the previous section) the NC is initially stable upon reduction, with electrons occupying the CB. However, since ligands like acetates[57] and Z-type complexes[24] have been found to be mobile on the NC surface, there is a possibility of charging NCs with a suboptimal distribution of ligands on the surface. If a ligand diffuses from the (100) surface to another facet, injection of one electron (Figure 3.3-ii) can lead to the formation of a trap. Moreover, charging of NCs could force X-type ligands off the surface to retain charge neutrality[58] and thus enable the formation of Cd–Cd dimers.

The results presented in this section can be generalized to larger NCs (see Figure A3.5) and other II–VI materials (see Figure A3.6). Figure A3.5 shows that the removal of chloride from certain sites on the (100) facet actually does not lead to dimer-formation. It is conjectured that dimerization on those specific sites may induce too high a strain on the surrounding structure to be energetically favorable.[43] Figure A3.6 shows that, contrary to the stable charging of fully passivated NCs, all singly charged Cd- and Zn-chalcogenide NCs form trap states when a chloride ligand is missing from the (100) facet, again emphasizing the importance of surface passivation for the NC stability.

Although various studies have shown that L-type amine ligands can increase the PL QY of NCs,[19,26–28] this cannot be properly explained by the hypothesis that only undercoordinated chalcogenides can lead to trap states, as passivating those traps requires electron accepting Z-type ligands instead of electron donating L-type ligands.[23] The atomistic picture of dimer-formation given in this section, however, may help to understand a possible mechanism of L-type passivation. Figure 3.4 shows that, if a Cl^0 atom is replaced by an L-type methylamine ligand, Cd–Cd dimerization is prevented, even though the NC is effectively negatively charged (<n> = 1). Instead, the extra electron remains delocalized in the CB (see Figure 3.4C), indicating that amines can stabilize NCs against surface reduction of metal ions.

An interesting open question is whether the formation of traps on reduced surface metal ions is only relevant for charged NCs, or whether it also plays a role in neutral, photoexcited NCs and may explain a suboptimal PL QY in absence of stabilizing amine ligands. Here, we conjecture that if the time scale of dimer-formation is similar to the radiative lifetime of the photoexcited electron–hole pair, the electron could be trapped in the bonding MO of the Cd–Cd dimer before it recombines with the hole. If the time scale of dimer-formation is slow compared to the radiative lifetime, the event can still happen once in a while, and as long as the dimer exists (i.e., before recombining with a hole) it will act as a trap state, thus decreasing the PL of the NC. If an amine is now present to block the Cd-dimerization, as shown in Figure 3.4A, the photoexcited electron can no longer be trapped in the dimer and the PL QY remains unaffected. Although more research is required to test this hypothesis, such a mechanism may eventually help to understand not only the PL-increasing effect of amines[19,26–28] but also perhaps processes like blinking and delayed photoluminescence.[62]

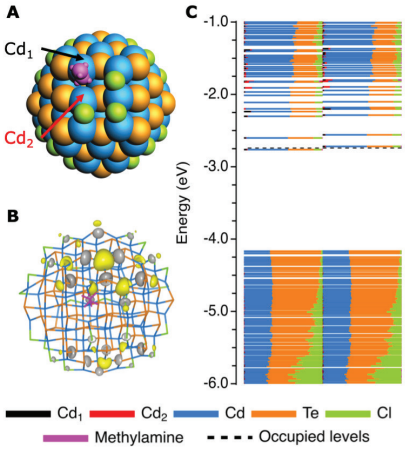

Figure 3.4. Influence of methylamine on the formation of Cd–Cd dimers. (A) Structure of the NC when a Cl^0 is replaced by a methylamine ligand (this is isoelectric to removing a chloride and injecting one extra electron into the NC). (B) Contour plot of the HOMO level of the NC, indicating that the electron is delocalized over the NC. (C) DOS of the NC, showing a clean bandgap and one electron in the CB.

3.3 Conclusions

In conclusion, DFT calculations have been used to study the effects of charging fully and imperfectly passivated CdTe NCs on their electronic structure. It is shown that charge injection can lead to trap-formation via two pathways: metal atom ejection from perfectly passivated NCs or metal–metal dimer-formation in imperfectly passivated NCs. The small, fully passivated model NCs used here were found to be stable up to a charge of two electrons. Further charge injection led to charge localization and consequent reduction of Cd^{2+} ions. The resulting Cd^0 atoms were ejected from the lattice and acted as localized in-gap states. The effects of surface passivation were probed by charging NCs with missing or displaced ligands. It was found that, if NCs miss an X-type ligand from a (100) facet, injection of one electron can already lead to Cd-dimerization and trap-formation. Addition of L-type ligands can prevent dimer-formation and is suggested to also prevent trapping of photoexcited electrons in charge neutral NCs, which emphasizes the importance of surface passivation for the stability of NCs. The results presented in this work can be generalized to NCs of different sizes and other Cd- and Zn-based zincblende chalcogenide NCs. They show that excess charges can lead to the formation of new surface defects and can therefore help to gain a better understanding of trap-formation during (electro) chemical doping or illumination of NCs.

3.4 Methods

All calculations have been carried out at the DFT level with a PBE exchange-correlation function[63] and double-ζ basis set, as used in the CP2K quantum chemistry software package.[64] Relativistic effects have been taken into account by means of effective

core-potentials. All structures have been optimized to the lowest energy in the gas phase at 0 K. Unrestricted calculations were used for all systems with an odd total number of electrons. Further details are given in the main text.

References

1. Talapin, D. V., Lee, J.-S., Kovalenko, M. V. & Shevchenko, E. V. Prospects of Colloidal Nanocrystals for Electronic and Optoelectronic Applications. Chem. Rev. 110, 389–458 (2010).
2. Donegá, C. de M. Synthesis and properties of colloidal heteronanocrystals. Chem. Soc. Rev. 40, 1512–1546 (2011).
3. Shirasaki, Y., Supran, G. J., Bawendi, M. G. & Bulović, V. Emergence of colloidal quantum-dot light-emitting technologies. Nat. Photonics 7, 13 (2013).
4. Grim, J. Q., Manna, L. & Moreels, I. A sustainable future for photonic colloidal nanocrystals. Chem. Soc. Rev. 44, 5897–5914 (2015).
5. Carey, G. H., Abdelhady, A. L., Ning, Z., Thon, S. M., Bakr, O. M. & Sargent, E. H. Colloidal Quantum Dot Solar Cells. Chem. Rev. 115, 12732–12763 (2015).
6. Ganesan, A., Houtepen, A. & Crisp, R. Quantum Dot Solar Cells: Small Beginnings Have Large Impacts. Appl. Sci. 8, 1867 (2018).
7. Dai, X., Deng, Y., Peng, X. & Jin, Y. Quantum-Dot Light-Emitting Diodes for Large-Area Displays: Towards the Dawn of Commercialization. Adv. Mater. 29, 1607022 (2017).
8. Li, X., Zhao, Y.-B., Fan, F., Levina, L., Liu, M., Quintero-Bermudez, R., Gong, X., Quan, L. N., Fan, J. Z., Yang, Z., et al. Bright colloidal quantum dot light-emitting diodes enabled by efficient chlorination. Nat. Photonics 12, 159 (2018).
9. Choi, M. K., Yang, J., Kim, D. C., Dai, Z., Kim, J., Seung, H., Kale, V. S., Sung, S. J., Park, C. R., Lu, N., et al. Extremely Vivid, Highly Transparent, and Ultrathin Quantum Dot Light-Emitting Diodes. Adv. Mater. 30, 1703279 (2018).
10. Wu, K., Park, Y.-S., Lim, J. & Klimov, V. I. Towards zero-threshold optical gain using charged semiconductor quantum dots. Nat. Nanotechnol. 12, 1140 (2017).
11. Geiregat, P., Houtepen, A. J., Sagar, L. K., Infante, I., Zapata, F., Grigel, V., Allan, G., Delerue, C., Van Thourhout, D. & Hens, Z. Continuous-wave infrared optical gain and amplified spontaneous emission at ultralow threshold by colloidal HgTe quantum dots. Nat. Mater. 17, 35–42 (2018).
12. Lim, J., Park, Y.-S. & Klimov, V. I. Optical gain in colloidal quantum dots achieved with direct-current electrical pumping. Nat. Mater. 17, 42 (2018).
13. Katsiev, K., Ip, A. H., Fischer, A., Tanabe, I., Zhang, X., Kirmani, A. R., Voznyy, O., Rollny, L. R., Chou, K. W., Thon, S. M., et al. The Complete In-Gap Electronic Structure of Colloidal Quantum Dot Solids and Its Correlation with Electronic Transport and Photovoltaic Performance. Adv. Mater. 26, 937–942 (2014).
14. Boles, M. A., Ling, D., Hyeon, T. & Talapin, D. V. The surface science of nanocrystals. Nat. Mater. 15, 141–153 (2016).
15. Kagan, C. R., Lifshitz, E., Sargent, E. H. & Talapin, D. V. Building devices from colloidal quantum dots. Science 353, aac5523–aac5523 (2016).
16. Reiss, P., Protière, M. & Li, L. Core/Shell Semiconductor Nanocrystals. Small 5, 154–168 (2009).

17. Jasieniak, J. & Mulvaney, P. From Cd-Rich to Se-Rich - the Manipulation of CdSe Nanocrystal Surface Stoichiometry. J. Am. Chem. Soc. 129, 2841–2848 (2007).
18. Page, R. C., Espinobarro-Velazquez, D., Leontiadou, M. A., Smith, C., Lewis, E. A., Haigh, S. J., Li, C., Radtke, H., Pengpad, A., Bondino, F., et al. Near-Unity Quantum Yields from Chloride Treated CdTe Colloidal Quantum Dots. Small 11, 1548–1554 (2015).
19. Kirkwood, N., Monchen, J. O. V., Crisp, R. W., Grimaldi, G., Bergstein, H. A. C., du Fossé, I., van der Stam, W., Infante, I. & Houtepen, A. J. Finding and Fixing Traps in II–VI and III–V Colloidal Quantum Dots: The Importance of Z-Type Ligand Passivation. J. Am. Chem. Soc. 140, 15712–15723 (2018).
20. Weaver, A. L. & Gamelin, D. R. Photoluminescence Brightening via Electrochemical Trap Passivation in ZnSe and Mn2+-Doped ZnSe Quantum Dots. J. Am. Chem. Soc. 134, 6819–6825 (2012).
21. Boehme, S. C., Azpiroz, J. M., Aulin, Y. V., Grozema, F. C., Vanmaekelbergh, D., Siebbeles, L. D. A., Infante, I. & Houtepen, A. J. Density of Trap States and Auger-mediated Electron Trapping in CdTe Quantum-Dot Solids. Nano Lett. 15, 3056–3066 (2015).
22. van der Stam, W., du Fossé, I., Grimaldi, G., Monchen, J. O. V., Kirkwood, N. & Houtepen, A. J. Spectroelectrochemical Signatures of Surface Trap Passivation on CdTe Nanocrystals. Chem. Mater. 30, 8052–8061 (2018).
23. Houtepen, A. J., Hens, Z., Owen, J. S. & Infante, I. On the Origin of Surface Traps in Colloidal II–VI Semiconductor Nanocrystals. Chem. Mater. 29, 752–761 (2017).
24. Saniepay, M., Mi, C., Liu, Z., Abel, E. P. & Beaulac, R. Insights into the Structural Complexity of Colloidal CdSe Nanocrystal Surfaces: Correlating the Efficiency of Nonradiative Excited-State Processes to Specific Defects. J. Am. Chem. Soc. 140, 1725–1736 (2018).
25. Knowles, K. E., Tice, D. B., McArthur, E. A., Solomon, G. C. & Weiss, E. A. Chemical Control of the Photoluminescence of CdSe Quantum Dot–Organic Complexes with a Series of Para-Substituted Aniline Ligands. J. Am. Chem. Soc. 132, 1041–1050 (2010).
26. Shen, Y., Tan, R., Gee, M. Y. & Greytak, A. B. Quantum Yield Regeneration: Influence of Neutral Ligand Binding on Photophysical Properties in Colloidal Core/Shell Quantum Dots. ACS Nano 9, 3345–3359 (2015).
27. Gao, Y. & Peng, X. Photogenerated Excitons in Plain Core CdSe Nanocrystals with Unity Radiative Decay in Single Channel: The Effects of Surface and Ligands. J. Am. Chem. Soc. 137, 4230–4235 (2015).
28. Pu, C. & Peng, X. To Battle Surface Traps on CdSe/CdS Core/Shell Nanocrystals: Shell Isolation versus Surface Treatment. J. Am. Chem. Soc. 138, 8134–8142 (2016).
29. van der Stam, W., Grimaldi, G., Geuchies, J. J., Gudjonsdottir, S., van Uffelen, P. T., van Overeem, M., Brynjarsson, B., Kirkwood, N. & Houtepen, A. J. Electrochemical Modulation of the Photophysics of Surface-Localized Trap States in Core/Shell/(Shell) Quantum Dot Films. Chem. Mater. 31, 8484–8493 (2019).
30. Shim, M. & Guyot-Sionnest, P. n-type colloidal semiconductor nanocrystals. Nature 407, 981 (2000).

31. Koh, W., Koposov, A. Y., Stewart, J. T., Pal, B. N., Robel, I., Pietryga, J. M. & Klimov, V. I. Heavily doped n-type PbSe and PbS nanocrystals using ground-state charge transfer from cobaltocene. Sci. Rep. 3, 2004 (2013).
32. Garcia, G., Buonsanti, R., Runnerstrom, E. L., Mendelsberg, R. J., Llordes, A., Anders, A., Richardson, T. J. & Milliron, D. J. Dynamically Modulating the Surface Plasmon Resonance of Doped Semiconductor Nanocrystals. Nano Lett. 11, 4415–4420 (2011).
33. Wang, C., Shim, M. & Guyot-Sionnest, P. Electrochromic Nanocrystal Quantum Dots. Science 291, 2390–2392 (2001).
34. Guyot-Sionnest, P. & Wang, C. Fast Voltammetric and Electrochromic Response of Semiconductor Nanocrystal Thin Films. J. Phys. Chem. B 107, 7355–7359 (2003).
35. Rinehart, J. D., Schimpf, A. M., Weaver, A. L., Cohn, A. W. & Gamelin, D. R. Photochemical Electronic Doping of Colloidal CdSe Nanocrystals. J. Am. Chem. Soc. 135, 18782–18785 (2013).
36. Tsui, E. Y., Carroll, G. M., Miller, B., Marchioro, A. & Gamelin, D. R. Extremely Slow Spontaneous Electron Trapping in Photodoped n-Type CdSe Nanocrystals. Chem. Mater. 29, 3754–3762 (2017).
37. Gerischer, H. On the Stability of Semiconductor Electrodes Against Photodecomposition. J. Electroanal. Chem. Interfacial Electrochem. 82, 133–143 (1977).
38. Nadjo, L. The characterization and behaviour of n-and p-CdTe electrodes in acetonitrile solutions. J. Electroanal. Chem. Interfacial Electrochem. 108, 29–47 (1980).
39. Chen, S. & Wang, L.-W. Thermodynamic Oxidation and Reduction Potentials of Photocatalytic Semiconductors in Aqueous Solution. Chem. Mater. 24, 3659–3666 (2012).
40. Voznyy, O., Zhitomirsky, D., Stadler, P., Ning, Z., Hoogland, S. & Sargent, E. H. A Charge-Orbital Balance Picture of Doping in Colloidal Quantum Dot Solids. ACS Nano 6, 8448–8455 (2012).
41. Zherebetskyy, D., Zhang, Y., Salmeron, M. & Wang, L.-W. Tolerance of Intrinsic Defects in PbS Quantum Dots. J. Phys. Chem. Lett. 6, 4711–4716 (2015).
42. Hwang, G. W., Kim, D., Cordero, J. M., Wilson, M. W. B., Chuang, C.-H. M., Grossman, J. C. & Bawendi, M. G. Identifying and Eliminating Emissive Sub-bandgap States in Thin Films of PbS Nanocrystals. Adv. Mater. 27, 4481–4486 (2015).
43. Voznyy, O., Thon, S. M., Ip, A. H. & Sargent, E. H. Dynamic Trap Formation and Elimination in Colloidal Quantum Dots. J. Phys. Chem. Lett. 4, 987–992 (2013).
44. Giansante, C. & Infante, I. Surface Traps in Colloidal Quantum Dots: A Combined Experimental and Theoretical Perspective. J. Phys. Chem. Lett. 8, 5209–5215 (2017).
45. Shim, M., Wang, C., Norris, D. J. & Guyot-Sionnest, P. Doping and Charging in Colloidal Semiconductor Nanocrystals. MRS Bull. 26, 1005–1008 (2001).
46. Mocatta, D., Cohen, G., Schattner, J., Millo, O., Rabani, E. & Banin, U. Heavily Doped Semiconductor Nanocrystal Quantum Dots. Science 332, 77–81 (2011).
47. Shiragami, T., Ankyu, H., Fukami, S., Pac, C. & Yanagida, S. Semiconductor

Photocatalysis: Visible Light lnduced Photoreduction of Aromatic Ketones and Electron-deficient Alkenes Catalysed by Quantised Cadmium Sulfide. J. Chem. Soc. Faraday Trans. 88, 1055–1061 (1992).

48. Zhao, J., Holmes, M. A. & Osterloh, F. E. Quantum Confinement Controls Photocatalysis: A free Energy Analysis for Photocatalytic Proton Reduction at CdSe Nanocrystals. ACS Nano 7, 4316–4325 (2013).
49. Anderson, N. C., Hendricks, M. P., Choi, J. J. & Owen, J. S. Ligand Exchange and the Stoichiometry of Metal Chalcogenide Nanocrystals: Spectroscopic Observation of Facile Metal-Carboxylate Displacement and Binding. J. Am. Chem. Soc. 135, 18536–18548 (2013).
50. Greaney, M. J., Couderc, E., Zhao, J., Nail, B. A., Mecklenburg, M., Thornbury, W., Osterloh, F. E., Bradforth, S. E. & Brutchey, R. L. Controlling the Trap State Landscape of Colloidal CdSe Nanocrystals with Cadmium Halide Ligands. Chem. Mater. 27, 744–756 (2015).
51. Drijvers, E., De Roo, J., Martins, J. C., Infante, I. & Hens, Z. Ligand Displacement Exposes Binding Site Heterogeneity on CdSe Nanocrystal Surfaces. Chem. Mater. 30, 1178–1186 (2018).
52. Singh, S., Tomar, R., ten Brinck, S., De Roo, J., Geiregat, P., Martins, J. C., Infante, I. & Hens, Z. Colloidal CdSe Nanoplatelets, A Model for Surface Chemistry/ Optoelectronic Property Relations in Semiconductor Nanocrystals. J. Am. Chem. Soc. 140, 13292–13300 (2018).
53. Azpiroz, J. M., Ugalde, J. M. & Infante, I. Benchmark Assessment of Density Functional Methods on Group II-VI MX (M = Zn, Cd; X = S, Se, Te) Quantum Dots. J. Chem. Theory Comput. 10, 76–89 (2014).
54. Gudjonsdottir, S., van der Stam, W., Kirkwood, N., Evers, W. H. & Houtepen, A. J. The Role of Dopant Ions on Charge Injection and Transport in Electrochemically Doped Quantum Dot Films. J. Am. Chem. Soc. 140, 6582–6590 (2018).
55. Fox, M. Optical properties of solids. (Oxford University Press, 2010).
56. Manna, L., Wang, L. W., Cingolani, R. & Alivisatos, A. P. First-Principles Modeling of Unpassivated and Surfactant-Passivated Bulk Facets of Wurtzite CdSe: A Model System for Studying the Anisotropic Growth of CdSe Nanocrystals. J. Phys. Chem. B 109, 6183–6192 (2005).
57. Voznyy, O. Mobile Surface Traps in CdSe Nanocrystals with Carboxylic Acid Ligands. J. Phys. Chem. C 115, 15927–15932 (2011).
58. Hartley, C. L. & Dempsey, J. L. Electron-Promoted X-Type Ligand Displacement at CdSe Quantum Dot Surfaces. Nano Lett. 19, 1151–1157 (2019).
59. Shim, M., Wang, C. & Guyot-Sionnest, P. Charge-Tunable Optical Properties in Colloidal Semiconductor Nanocrystals. J. Phys. Chem. B 105, 2369–2373 (2001).
60. Haram, S. K., Quinn, B. M. & Bard, A. J. Electrochemistry of CdS Nanoparticles: A Correlation between Optical and Electrochemical Band Gaps. J. Am. Chem. Soc. 123, 8860–8861 (2001).
61. Norris, D. J., Efros, A. L. & Erwin, S. C. Doped Nanocrystals. Science 319, 1776–1779 (2008).
62. Rabouw, F. T., Kamp, M., Van Dijk-Moes, R. J. A., Gamelin, D. R., Koenderink, A. F., Meijerink, A. & Vanmaekelbergh, D. Delayed Exciton Emission and Its Relation to Blinking in CdSe Quantum Dots. Nano Lett. 15, 7718–7725 (2015).

63. Perdew, J. P., Burke, K. & Ernzerhof, M. Generalized Gradient Approximation Made Simple. Phys. Rev. Lett. 77, 3865–3868 (1996).
64. Hutter, J., Iannuzzi, M., Schiffmann, F. & VandeVondele, J. cp2k: atomistic simulations of condensed matter systems. Wiley Interdiscip. Rev. Comput. Mol. Sci. 4, 15–25 (2014).

Appendix

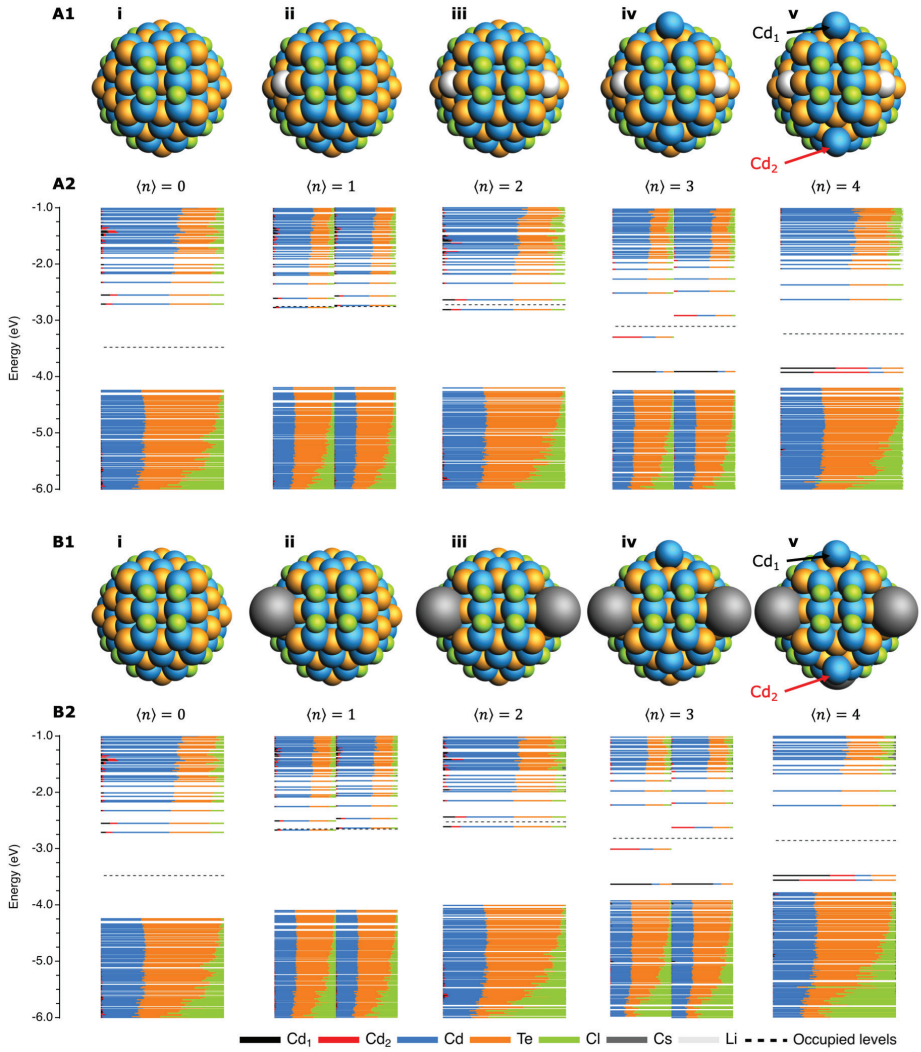

Figure A3.1. The effect of charging fully passivated CdTe nanocrystals (NCs) on their structure and density of states (DOS), using (A) Li^+ and (B) Cs^+ as counterion. (A1) and (B1) Structure of the NCs when respectively 0, 1, 2, 3 and 4 electrons are injected. The total system is kept neutral by the addition of (A1) a lithium or (B1) a cesium cation for each added electron. (A2) and (B2) DOS for each of the NCs, where every line corresponds to a molecular orbital (MO). The length of a colored line segment indicates the contribution of the corresponding atom or element to that MO. MOs above the dotted line are empty, whereas the ones below are occupied. In this and the ensuing figures, if the total number of electrons is odd (<n> = 1, 3), the spin-up and spin-down orbitals are plotted separately on the left- and right-hand side of the graph. Each MO is then occupied by a single electron.

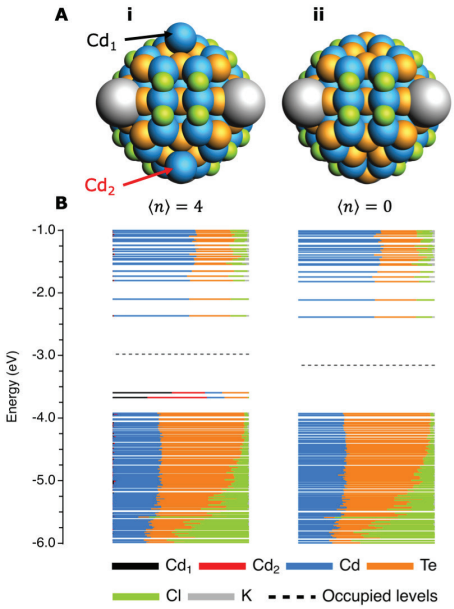

Figure A3.2. The effect of removing the Cd^0 atoms from a charged NC on its structure and DOS. (A) Structure of the NCs. i) The NC is charged with four electrons, which is compensated by the presence of four potassium cations. As also shown in Figure 3.1-v in the main text, Cd_1 and Cd_2 are reduced to Cd^0 and ejected from the lattice. ii) The Cd^0 sites (Cd_1 and Cd_2) are removed from the structure. (B) DOS of the two NCs. The DOS in i) shows two in-gap levels that are highly localized on Cd_1 and Cd_2. Removal of these two Cd^0 atoms in ii) also removes the related trap states.

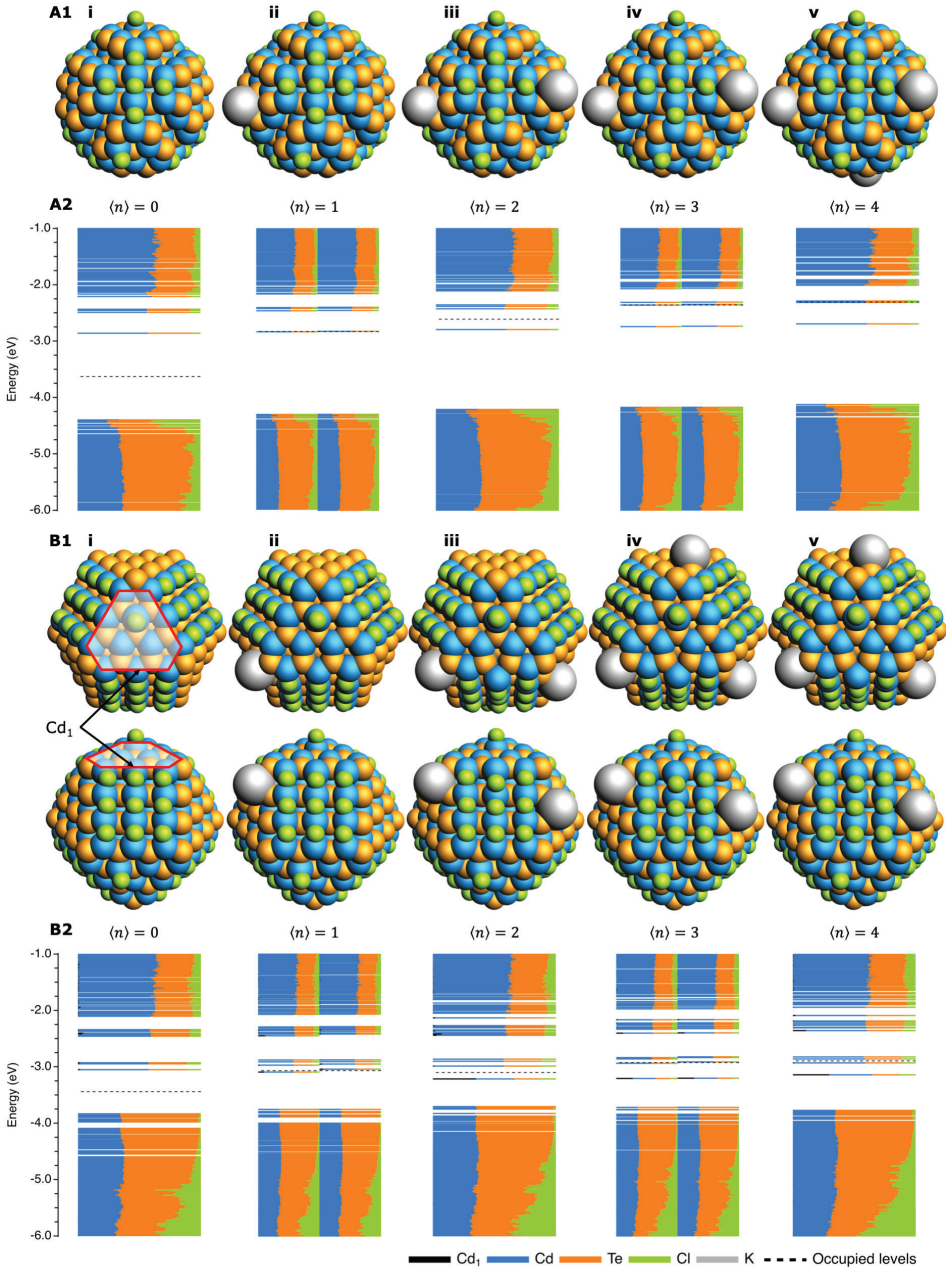

Figure A3.3. The effect of charging larger fully passivated NCs of different sizes. (A1) Structure and (A2) DOS of $Cd_{152}Te_{135}Cl_{34}$ NCs when respectively 0, 1, 2, 3 and 4 electrons are injected. Note that the NCs are stable under these conditions and that no trap states are formed. (B1) Structure of $Cd_{176}Te_{147}Cl_{58}$ NCs when 0 to 4 electrons are injected. The top row shows the top-view of the

(111) facet indicated in the lower row. Note that here, charging leads to the expulsion of Cd_1 from the (111) plane. (B2) DOS for each of the NCs. In all cases, the total system is kept neutral by the addition of a potassium cation for each added electron.

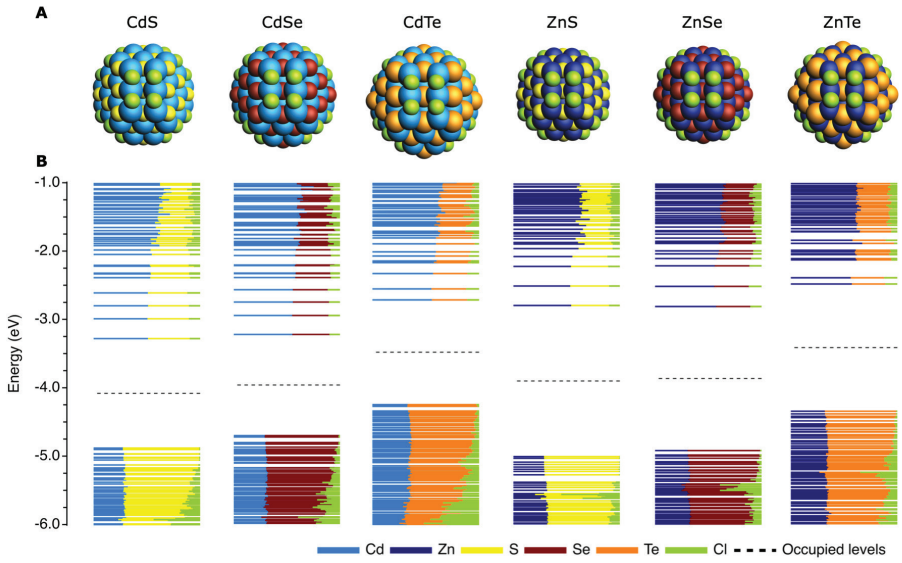

Figure A3.4. The structure and DOS of different fully passivated neutral $M_{68}X_{55}Cl_{26}$ (M = Cd, Zn; X = S, Se, Te) zincblende NCs. (A) Structure and (B) DOS of the NCs.

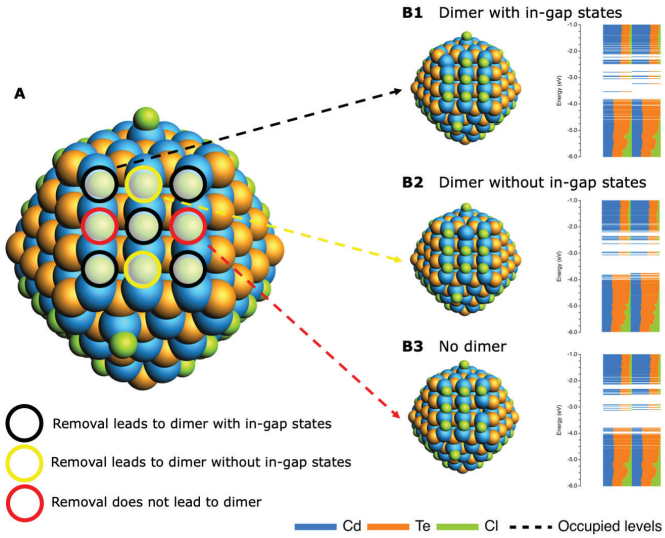

Figure A3.5. The effect of charging with one electron when a chloride (Cl^-) has been removed from different sites on the (100) plane of a larger CdTe NC on its structure and DOS. Note that this is isoelectric with removing a chlorine, Cl^0. (A) Structure of the NC and the different chlorine atoms that have been removed. A black circle indicates that removal of the chlorine leads to Cd-Cd dimerization and trap-formation. Yellow circles indicate that removing the chlorine leads to the formation of a dimer, but that no new state in the bandgap is formed. Removal of the chlorine atoms that are circled in red does not lead to a dimer. (B1-3) gives the structure and DOS of the NCs in these respective cases and shows the heterogeneity of the sites on the (100) facet. The DOS of the perfectly passivated NC can be seen in Figure A3.3B2-i.

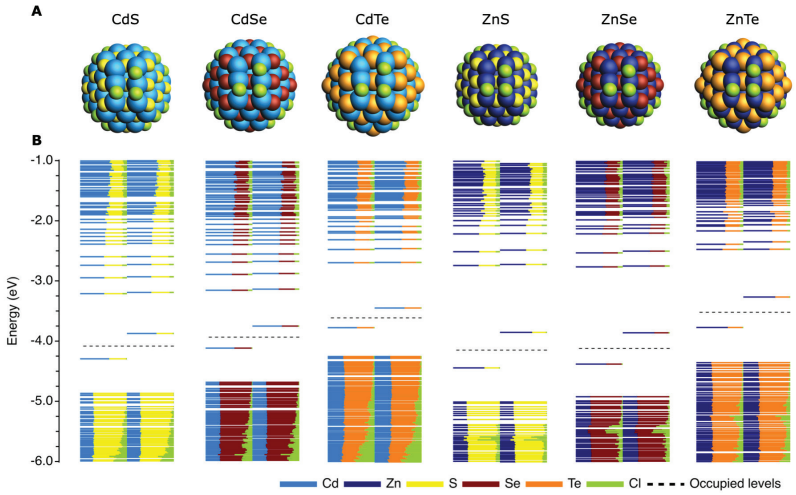

Figure A3.6. The effect of charging different $M_{68}X_{55}Cl_{26}$ (M = Cd, Zn; X = S, Se, Te) zincblende NCs with one electron, when a chloride (Cl^-) has been removed from the (100) surface. (A) Structure and (B) DOS of the NCs. The perfectly passivated NCs were already shown in Figure A3.4.

4

Dynamic Formation of Metal-Based Traps in Photoexcited Colloidal Quantum Dots and Their Relevance for Photoluminescence

Trap states play a crucial role in the design of colloidal quantum dot (QD)-based technologies. The presence of these in-gap states can either significantly limit the efficiency of devices (e.g., in solar cells or LEDs) or play a pivotal role in the functioning of the technology (e.g., in catalysis). Understanding the atomistic nature of traps is therefore of the highest importance. Although the mechanism through which undercoordinated chalcogenide atoms can lead to trap states in II–VI QDs is generally well understood, the nature of metal-based traps remains more elusive. Previous research has shown that reduction of metal sites in negatively charged QDs can lead to in-gap states. Here, we use density functional theory to show that metal-based traps are also formed in charge-neutral but photoexcited CdSe QDs. It is found that Cd–Cd dimers and the concomitant trap states are transient in nature and appear and disappear on the picosecond time scale. Subsequent nonradiative recombination from the trap is shown to be much faster than radiative recombination, indicating that dimer-related trap states can quench the photoluminescence. These results are expected to be transferable to other II–VI materials and highlight the importance of surface redox reactions for the optical properties of QDs. Moreover, they show that photoexcitation can lead to atomic rearrangements on the surface and thus create transient in-gap states.

This chapter is based on: Indy du Fossé, Simon C. Boehme, Ivan Infante, Arjan J. Houtepen. Chemistry of Materials, 2021, 33 (9), 3349-3358

4.1 Introduction

Colloidal quantum dots (QDs) possess unique characteristics like solution processability and size-dependent optical and electronic properties, which make them of particular interest for application in optoelectronic devices.[1,2] QD-based technologies have developed quickly over the past few decades,[3] leading to the incorporation of QDs in solar cells,[4,5] displays,[6–8] light-emitting diodes (LEDs),[9–11] transistors,[12,13] and lasers.[14–16] For many of these applications, it is of paramount importance that the band gap remains clear of localized energy levels, as these states can lead to unwanted charge carrier trapping.[17,18] Consequently, many methods of removing the influence of trap states have been developed, including the epitaxial growth of an inorganic shell,[19,20] the addition of various ligands,[21–26] and the electrochemical filling of in-gap states.[27–30] However, trap states have also been shown to play an essential role in, for example, optical gain[31] or catalytic activity,[32] indicating that for certain applications the presence of specific types of traps can be highly advantageous. Thus, a better understanding of the atomistic nature of these trap states may lead not only to more efficient approaches to passivate traps but also to novel strategies aimed at engineering the in-gap states with the desired properties.

Trap states are usually ascribed to the nonbonding orbitals of undercoordinated, often surface-situated atoms.[33,34] Density functional theory (DFT) calculations have refined this picture for II–VI semiconductor QDs by showing that in-gap states mainly arise from undercoordinated chalcogenide atoms[35] or from reduced metal sites,[36] as summarized in Figure 4.1A. Chalcogenide-based traps (indicated in white in Figure 4.1A) can be understood in terms of the shape of the orbitals that contribute to the valence band (VB) and conduction band (CB) in II–VI materials. Since the chalcogenide p orbitals mainly constitute the VB, each chalcogenide atom has to be at least 3-fold coordinated to split each of the 3 orthogonal p orbitals. Displacement of Z-type ligands can lead to chalcogenide sites with only two neighboring atoms, causing one of the three p orbitals to remain in the band gap as a nonbonding trap state.[35] In contrast, metal atoms mainly contribute to the CB with s orbitals. The spherical symmetry of the s orbital ensures that it is split into bonding and antibonding orbitals, even when the Cd atom is undercoordinated.[35] In line with this description, it has been shown experimentally that addition of Z-type ligands, which bind to undercoordinated chalcogenide sites, can indeed increase the photoluminescence quantum yield (PL QY) to near unity.[23] Lastly, chalcogenides can also lead to trap states through the formation of chalcogenide dimers upon oxidation (indicated in beige in Figure 4.1A), as has been shown both experimentally[37] and computationally.[29,38,39]

The existence of metal-based traps is suggested by several experimental studies, which found that both L-type ligands like amines[23–25,40] and phosphines[24,41] and anionic X-type ligands can increase the PL QY.[23,30] These electron-donating ligands cannot passivate undercoordinated chalcogenide atoms and have therefore been proposed to passivate cadmium sites.[23,25,30,40] Moreover, spectroelectrochemical studies have found in-gap states near the CB edge of CdSe core-only and core/shell particles, which were ascribed to undercoordinated surface cadmium.[42] In our previous computational work,[36] it was shown that metal-based traps in II–VI semiconductor QDs can be formed in the presence of excess electrons. It was found that charging trap-free QDs with multiple electrons leads to charge localization on Cd atoms in (111) facets and their subsequent ejection from the

lattice (indicated in black in Figure 4.1A, see also Figure A4.1 for the different facets in the model QD). If an X-type ligand from the (100) facet is moved to a different position, charging with one excess electron already creates a trap in the form of a Cd–Cd dimer. During the formation of this dimer, which is shown in orange in Figure 4.1A, the Cd atoms move closer to each other, causing their orbitals to overlap and pushing a bonding Cd–Cd molecular orbital (MO) into the band gap. The injected electron occupies this state, thus stabilizing the Cd–Cd dimer.[36]

Although the trap formation in charged QDs can be relevant for catalysis[32] or QDs in optoelectronic devices,[43,44] the question remains how important these metal-based traps are for charge-neutral QDs. The formation of the metal-based traps described in the previous paragraph is essentially a reduction reaction in which electrons in the CB (i.e., with a high electrochemical potential) localize on surface cadmium. It may therefore be possible that also photoexcited electrons can cause the formation of such surface states, leading to a trapping process, in which the trap state itself is formed by the presence of an excited CB electron. Such a trap state would remain in the band gap until the electron

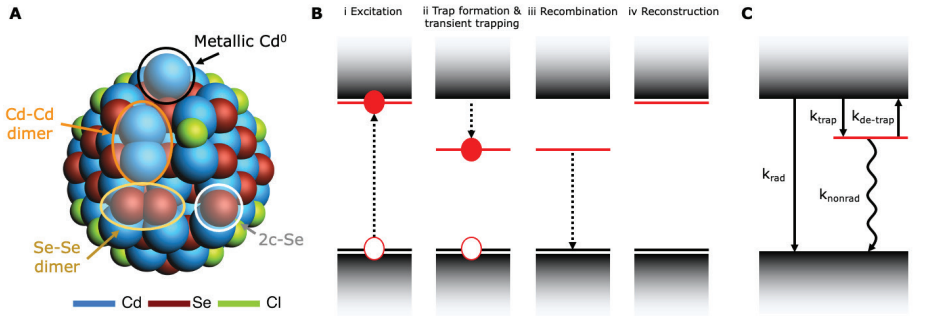

Figure 4.1. Overview of the different traps and trapping mechanisms in CdSe QDs considered in this work. (A) Model of a CdSe QD, showing the surface configurations that can lead to in-gap states. In line with the model system used in this work, the experimentally often employed oleate ligands have been replaced with chloride ions to limit the computational costs of the DFT calculations. Note that the structure shown here is only for illustrative purposes and not the result of a geometry optimization. Two-coordinated Se (2c-Se, white circle) can be formed in charge-balanced QDs,[35] while Se–Se dimers (beige oval) may be present in oxidized systems.[29,37–39] Cd–Cd dimers (orange oval) can both be formed in negatively doped and charge-neutral but photoexcited QDs (vide infra). Metallic Cd^0 (black circle) has so far only been reported for negatively charged QDs[36] but is also expected to form upon creation of multiple excitons. (B) Summary of the different steps of trapping an electron in a transient trap state. VB and CB edges are indicated by the black and red horizontal lines, respectively. (i) Excitation of a trap-free QD leads to a CB electron and a VB hole; (ii) presence of this electron in the CB leads to the formation of a trap state that simultaneously traps the electron; (iii) trapped electron recombines with the VB hole; (iv) trap is no longer stabilized by the electron and therefore disappears, leaving the band gap free of in-gap states. (C) Overview of the main recombination pathways in a QD with trapping to a transient surface state: radiative band edge recombination (k_{rad}), creation of the trap that captures the electron (k_{trap}), removal of the trap and simultaneous detrapping of the electron to the CB (k_{detrap}), and nonradiative decay from the trap to the VB (k_{nonrad}).

recombines with a VB hole or gets detrapped and the transient surface state disappears again, as schematically shown in Figure 4.1B.

For this type of trap to be relevant for the PL QY, it should form on a time scale comparable to or shorter than the lifetime of the excited state (ES). If trap formation is much slower than that (i.e., $k_{trap} << k_{rad} \approx 10^8\ s^{-1}$,[45,46] see Figure 4.1C), it is unlikely for a CB electron to be trapped in a transient surface state. If trapping is much faster than radiative decay ($k_{trap} >> k_{rad}$), two main scenarios are possible. In the first scenario, the nonradiative recombination of the trapped electron to the VB is much slower than the removal of the transient trap ($k_{nonrad} << k_{detrap}$). Here, the trapping of an electron to a transient surface state does not necessarily reduce the PL QY, but it can lead to long-time tails of PL decay traces[47] or result in delayed fluorescence if the detrapping rate is slower than the radiative rate ($k_{detrap} < k_{rad}$).[45] The second scenario arises when the nonradiative recombination is much faster than the detrapping rate ($k_{nonrad} >> k_{detrap}$). Now, nearly every trapped electron will decay nonradiatively to the VB, thus quenching the PL.

Here, we use DFT calculations to investigate both the energetics and the dynamics of Cd–Cd dimers in charge-neutral but photoexcited QDs. Our model QD was constructed in such a way that none of the trap states shown in Figure 4.1A are present in the ground state (GS). Due to the computational challenges of optimizing singlet ES geometries of large systems, we decided to approximate the ES potential energy surface by a triplet state, as it describes similar orbital features to the lowest singlet ES within the single-particle approximation. This approach ensures that one electron is promoted from the top of the VB to the lowest CB level and makes it possible to carry out ab initio molecular dynamics (AIMD) at limited computational costs. First, geometry optimization will be used to show that given a suboptimal surface passivation, where a chloride ligand has been moved from the (100) to the adjoining (111) facet (see Figure A4.1), it is energetically favorable for a CB electron to induce Cd–Cd dimer formation, as was previously observed only for negatively charged QDs.[36] Next, the time scale on which these dimers form is investigated with AIMD. It is found that when the ligand coverage is already suboptimal, excitation of the QD leads to a Cd–Cd dimer that is both formed and broken up in a period on the order of a picosecond (k_{trap}, $k_{detrap} \approx 10^{12}\ s^{-1}$). Lastly, we draw the configuration coordinate diagrams of the GS and ES for both a trap-free QD and a QD with a Cd–Cd dimer. The nonradiative recombination rate from the trap to the VB (k_{nonrad}) is found to be very high, and it is therefore expected that the dynamic formation of Cd–Cd traps can quench the PL QY of photoexcited QDs. These results show that photoexcitation can affect the optical properties of QDs by inducing atomic rearrangements that lead to the creation of transient in-gap states.

4.2 Results and Discussion

4.2.1 Model System

For the calculations presented here, a zincblende $Cd_{68}Se_{55}Cl_{26}$ QD with a diameter of ca. 1.9 nm (see Figure 4.2A-i) was used as a model system. It is charge balanced as defined by the model of Voznyy et al.[48] and contains none of the trap states shown in Figure 4.1A. It replicates the cation-rich nature of most QDs[49,50] but replaces the experimentally often used oleate ligands with computationally less demanding chlorides.[51,52] Of the 26 chloride

ligands, 24 have been placed on the Cd-terminated (100) facets, as these comprise the Cd atoms with the lowest coordination. The two remaining chlorides have been placed on Cd-terminated (111) facets (see Figure A4.1 for the different facets of the model QD). This ligand configuration ensures the highest possible coordination of the surface atoms while using a minimum number of ligands (meaning that L-type ligands are not included). During this work, we will therefore refer to this ligand configuration as "perfectly passivated". Further details of this model system have been discussed previously.[35,36] Although we will look at CdSe QDs throughout this work, we expect that the results can be generalized to other zincblende II–VI QDs (vide infra).

4.2.2 Energetics of Dimer Formation

The first step in determining the relevance of Cd–Cd dimer formation for charge-neutral but photoexcited QDs consists of investigating the energetics of the dimerization. If the energy of the QD significantly increases upon dimer formation, the event is unlikely to happen and the trapping rate (k_{trap}) will be low. Due to the large computational cost of optimizing ES geometries for these systems, we will approximate the photoexcited QD by calculating the GS of the lowest triplet state. This results in a situation where there is a hole in the top of the VB and an electron in the CB edge, thus in a first approximation mimicking the singlet ES. In the ensuing sections, calculations on the QD in its lowest singlet state will therefore be referred to as the GS and calculations on the lowest triplet state as the ES. By extension, "excitation" of a QD indicates its properties are computed for the lowest triplet state.

Figure 4.2B-i shows the density of states (DOS) of the perfectly passivated model QD in the GS. Here, every horizontal line corresponds to a MO, where the length of each colored line segment indicates the contribution of the corresponding element or atom. The MOs are filled up to the dotted line, indicating that the entire VB is filled with electrons and that the CB is empty. Figure 4.2B-ii shows the DOS for the perfectly passivated QD in the ES. All of the ES calculations in this work are computed as spin unrestricted, so that the α and β orbitals are allowed to relax independently from each other as a consequence of their different occupation. This approach results in two distinct densities of states: the DOS for the α-electrons is displayed on the left of Figure 4.2B-ii, while the DOS for β-electrons is given on the right. The dotted lines show that one α electron occupies the CB, whereas the top level of the VB is empty in the β-DOS. The dotted lines thus represent the quasi-Fermi levels of electrons (α electrons, left) and holes (β electrons, right) in the ES. Although the true lowest singlet ES will be a linear combination of different many-electron excitations with the same spin, for the remainder of this work we will approximate the lowest singlet ES by only considering a single electronic transition, i.e., the HOMO-LUMO transition. This approach has been proved to be valid in several works on QDs, in particular, by Prezhdo et al.[53] As can be seen by comparing Figure 4.2A-i and 4.2A-ii, exciting the QD does not significantly alter its structure. Comparison of Figure 4.2B and 2C for the perfectly passivated QDs shows that the ES does not lead to new localized in-gap states and that the HOMO remains delocalized over the entire QD. However, note that the shape of the orbitals in Figure 4.2C changes, since the HOMO is shifted from a VB state consisting mainly of Se 4p orbitals in Figure 4.2C-i to a CB state consisting mainly of Cd 5s orbitals in Figure 4.2C-ii.

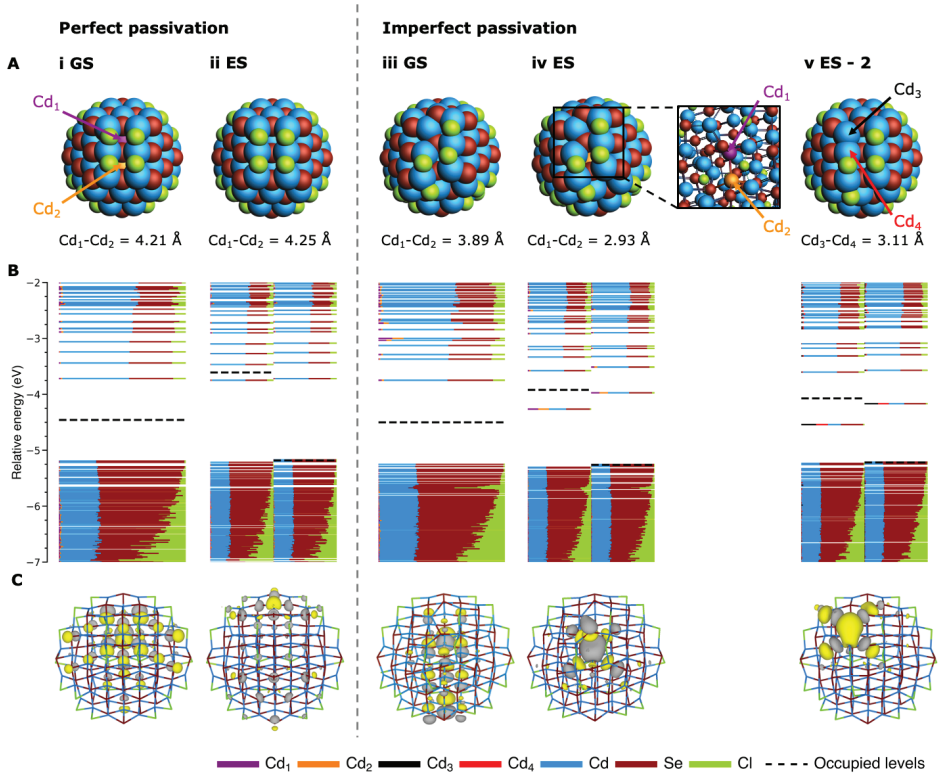

Figure 4.2. Cd–Cd dimer formation in excited, charge-neutral QDs with imperfect passivation. (A) Structure of the QD when perfectly passivated (left of dashed line) or imperfectly passivated (right of dashed line). Title above each structure indicates whether the respective QD was in the GS or ES. Columns iv and v show that excitation can lead to dimerization between different cadmium atoms. Cd_1–Cd_2 or Cd_3–Cd_4 distance, as indicated by the arrows, is given below each structure. For clarity, Cd_1 and Cd_2 are colored purple and orange, respectively, in panels A-i and A-iv. (B) DOS for each of the QDs. Here, every line corresponds to a MO. Relative contributions of specific atoms or elements to each MO are indicated by the length of the colored line segments. MOs are occupied below the dotted line and empty above it. All ES calculations are unrestricted, meaning that the spin-up (α) and spin-down (β) orbitals are allowed to relax independently (see main text for more details). This results in two distinct densities of states, which are plotted separately on the left and right side of the graph, respectively. (C) Contour plots of the HOMO of each QD.

Figure 4.2A-iii shows the structure obtained after moving one of the chloride ligands from the (100) to the adjacent (111) facet. Such a surface configuration, which we will refer to as "imperfectly passivated", may be formed due to random diffusion of ligands over the QD surface, as acetate ligands[54] and Z-type complexes[55] have been found to be mobile on the QD surface. Since simulating ligand diffusion, which typically occurs on a much longer time scale than that investigated here, is beyond the scope of the current work, the chloride atom was moved to the (111) facet prior to geometry optimization. Moving the chloride to the position shown in Figure 4.2A-iii increases the energy of the system by roughly 0.47

eV (~18 k_BT) but does not significantly alter the electronic structure (see Figure 4.2B-iii). The band gap remains free of localized states, and although the HOMO changes in shape, it is still delocalized over the entire QD, as shown in Figure 4.2C-iii. However, exciting this imperfectly passivated QD reduces the distance between two specific Cd atoms (indicated as Cd_1 and Cd_2 in Figure 4.2A-iv) from 3.89 Å for the QD in the GS to 2.93 Å in the ES. At the same time, two in-gap states appear which are ~30% localized on Cd_1 and Cd_2. Both of these observations are indicative of the formation of a Cd–Cd dimer.

Figure 4.2A-v shows that dimerization is not limited to specifically Cd_1 and Cd_2. The system can also relax to another local minimum that is roughly 0.02 eV (0.9 k_BT) higher in energy than the system in Figure 4.2A-iv and in which a different dimer is obtained. In this case, two Cd atoms at the surface (indicated by Cd_3 and Cd_4 in Figure 4.2A-v, see Figure A4.2 for more details) move closer to each other and form an in-gap state, which is localized ~40% on those two atoms. The small energy difference between the two systems with the different Cd–Cd dimers indicates that both structures are likely to be sampled under ambient conditions. Indeed, both dimers are found in the AIMD runs discussed in the ensuing section (vide infra).

To summarize, Figure 4.2 shows that given a suboptimal ligand passivation, the CB electron in photoexcited QDs can energetically lead to the formation of a Cd–Cd dimer and the associated in-gap state. In the Appendix we show that CdTe and ZnS QDs exhibit the same dimer formation in the ES (see Figure A4.3). Therefore, we expect that the traps described in this work can be generalized to zincblende II–VI semiconductor materials in general and potentially also to zincblende III–V QDs, such as InP. As discussed before, whether dimer formation is relevant for excited QDs depends also on the time scale of the dimerization, which will be discussed in the ensuing section.

It must be noted that in real CdSe QDs undercoordinated Cd atoms may not be the only sites that can be reduced by photoexcited electrons. An excited electron may possibly also reduce oxidized selenium sites, like Se–Se dimers or SeO_x surface moieties.[37,51] Such oxidized selenium sites can be formed by reactions with ambient oxygen or by (unintentional) p-doping (to form Se–Se dimers) and as such represent extrinsic surface effects that were not included in the current calculations, although transient Se–Se dimer formation will be discussed below. In addition, there have been reports on surface Cd reduction and resulting X-type ligand displacement.[56] This effect is not seen in the current calculations. However, the free energy change of this reaction will strongly depend on the solvation energy of the displaced X-type ligands, and no solvent is included in our DFT calculations.

4.2.3 Dynamics of Dimer Formation

In this section, AIMD is used to investigate the time scale on which Cd–Cd dimerization occurs. Given the computational costs of AIMD, simulations can only run for a few picoseconds. Therefore, in this section we will assume that random ligand diffusion has already led to the imperfect ligand configuration shown in Figure 4.2A-iii, and we will investigate how long after excitation the Cd atoms move close enough to each other to form an in-gap state.

As a reference, we first perform an AIMD simulation starting with the GS of the perfectly passivated structure shown in Figure 4.2A-i (see Methods for further technical details). During the simulation, the DOS is calculated every 20 fs, as shown in Figure 4.3A-i. At time = 3 ps, the QD is excited, i.e., a triplet is enforced. As discussed in the preceding section for the geometry optimizations, this leads to one α-electron in the CB, while the top of the VB is empty in the β-DOS. Apart from a slight splitting of the α and β levels and a reorganization of the VB levels, no significant changes to the DOS occur. This is corroborated by the contour plots given in Figure 4.3B-i, which show that the HOMO, at three different times after excitation, remains delocalized over the QD.

Figure 4.3A-ii shows the DOS and Cd_1–Cd_2 distance during an AIMD simulation starting with the GS of the imperfectly passivated QD. During the first 3 ps of the simulation, the DOS shows a clean band gap similar to that of the perfectly passivated QD. Likewise, the average Cd_1–Cd_2 distance of 3.9 Å is comparable to the value of 4.2 Å found for the perfectly passivated QD. However, when the QD is excited at time = 3 ps, the energy of the lowest α and β CB levels is lowered significantly (see the first blue shaded area) and the Cd_1–Cd_2 distance decreases to around 3.0 Å. The contour plot of Figure 4.3B-ii shows that at time = 4.0 ps (i.e., 1.0 ps after excitation), the HOMO is localized on Cd_1 and Cd_2, indicating that Cd–Cd dimerization has taken place. Around time = 5.3 ps, the in-gap states disappear, accompanied by an increase in the Cd_1–Cd_2 distance, which then remains stable for approximately 2.2 ps (until time = 7.5 ps). The contour plot shown in Figure 4.3B-ii at time = 6.0 ps shows that the HOMO has become delocalized during this period, indicating that the Cd–Cd dimer has temporarily been broken up. Around time = 7.5 ps, the Cd_1–Cd_2 distance decreases again significantly to 3.0 Å and the in-gap state reappears (see the second blue shaded area). This indicates that the Cd–Cd dimer has formed again, as supported by the contour plot at time = 9.0 ps, which shows the localization of the wave function around Cd_1 and Cd_2. In Figure A4.4, which shows the same AIMD run extended to ~21 ps, it can be seen that the Cd_1–Cd_2 dimer is eventually broken up again, followed by the formation of a dimer between Cd_3 and Cd_4, similar to the structure found in the geometry optimization in Figure 4.2-v.

Interesting to note is the VB level that extends far into the band gap at time = 7.0 ps (see the gray shaded area), which we ascribe to an antibonding Se–Se orbital that has also been reported previously.[38,57] While in this manuscript we mostly focus on metal-based traps, we note that Se–Se dimer formation appears to be entirely analogous to Cd–Cd dimer formation: oxidation of a QD with undercoordinated Se surface atoms results in Se–Se dimers by depopulating one of the antibonding Se–Se orbitals (see Figure A4.5),[29] analogous to the formation of Cd–Cd dimers upon reduction.[36] In addition, photoexcitation can result in transient Cd–Cd dimer formation by electron trapping in the Cd–Cd bonding orbital as well as transient Se–Se dimer formation by hole trapping in the Se–Se antibonding orbital (see Figure A4.6). Both Cd–Cd dimers and Se–Se dimers lead to trap states in the band gap, formed by the bonding orbital of the Cd–Cd dimer (electron trap) and the antibonding orbital of the Se–Se dimer (hole trap).

From the results presented in this section, we conclude that, upon excitation of an

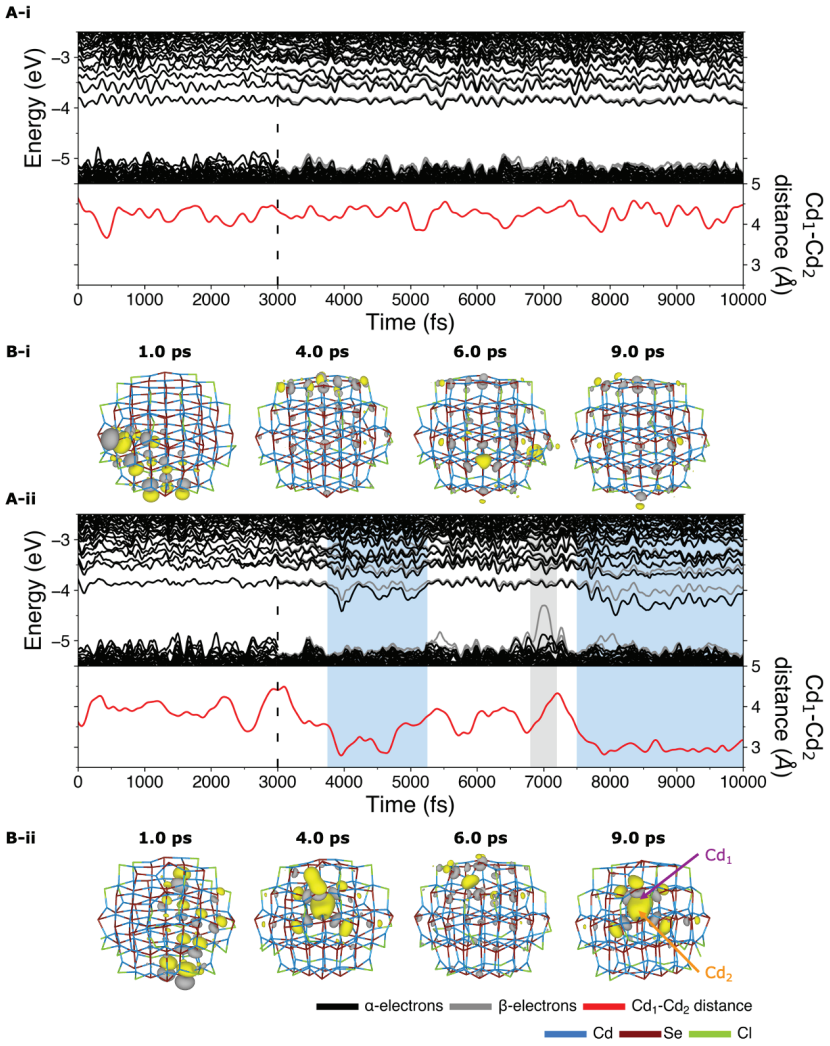

Figure 4.3. Time-dependent Cd–Cd dimerization in AIMD simulations. (A) DOS as a function of time for (i) a perfectly and (ii) an imperfectly passivated QD. AIMD runs start in the GS but sample the ES after the excitation event at time = 3 ps (see dashed vertical line). Red line in the lower part of the graph shows the distance between Cd_1 and Cd_2 over time. Blue or gray shaded areas serve as a guide to the eye to indicate the times when a Cd–Cd or Se–Se dimer is present, respectively. (B) Contour plots of the HOMO level at time = 1.0, 4.0, 6.0, and 9.0 ps for (i) the perfectly and (ii) the imperfectly passivated QD.

imperfectly passivated QD, the Cd–Cd dimer is formed and broken up again and that both the Cd_1–Cd_2 and the Cd_3–Cd_4 dimers are sampled at room temperature. As shown in Figure A4.4C, the QD is in the dimer configuration for ~60% of the time, indicating that the rates of trapping and detrapping are roughly equal. As the dimer is formed or broken

up every few picoseconds, the (de)trapping rates must hence be on the order of 1 ps^{-1}: k_{trap}, $k_{detrap} \approx 10^{12}\ s^{-1}$. By running the AIMD for a much longer time than the ~21 ps used here, it would in principle be possible to accurately determine the average lifetime of the Cd–Cd dimer and find more precise values for k_{trap} and k_{detrap}. However, this is prohibited by the computational costs of the calculation. Therefore, we will limit our conclusion to stating that both forming and breaking of the Cd–Cd dimers take place on a ~1 ps time scale (i.e., k_{trap}, $k_{detrap} \approx 10^{12}\ s^{-1}$).

The high rate at which the dimerization takes place suggests that the process occurs with a very small activation energy. To probe the energy of the system as a function of Cd–Cd distance, we carried out constrained geometry optimizations, where the structure is allowed to relax, under the constraint that the coordinates of two selected Cd atoms are frozen to their initial position. First, the structure obtained at time = 3.0 ps in Figure 4.3A-ii (when no dimer has formed yet) was allowed to relax in the ES while freezing the coordinates of Cd_1 and Cd_2 so that the Cd_1–Cd_2 distance remained constant at 4.41 Å. In this way, the most stable configuration at that point without dimer was obtained. Next, the structure around time = 4.0 ps in Figure 4.3A-ii (when the dimer has just formed) was relaxed in the ES with frozen positions for Cd_1 and Cd_2 (Cd_1–Cd_2 distance = 2.87 Å) to obtain the most stable configuration with dimer. The positions of Cd_1 and Cd_2 were subsequently varied between these two configurations, leading to structures where the Cd_1–Cd_2 distance ranges from 4.41 to 2.21 Å (structures with a Cd_1–Cd_2 distances shorter than 2.87 Å were obtained through linear extrapolation). The energy of the relaxed structures (under the aforementioned constraint of freezing the positions of Cd_1 and Cd_2) are plotted in Figure 4.4A as a function of Cd_1–Cd_2 distance (see Figure A4.7 for the DOS).

In Figure 4.4A (black trace, solid markers), it can be seen that starting from the maximal Cd_1–Cd_2 separation in the ES, reducing the Cd_1–Cd_2 distance also reduces the total energy of the system. When the Cd atoms are close enough, the initially delocalized HOMO level gradually starts to localize on the Cd–Cd dimer that is being formed (see Figure 4.4B). After reaching the equilibrium bond length, further reduction of the Cd_1–Cd_2 distance significantly increases the energy again. As shown by the solid line that is fitted to the data in Figure 4.4A, the data can be described well with a Morse potential of the form:

$$V(r) = D_e\left(1 - e^{-a(r-r_e)}\right)^2 - C \qquad 4.1$$

Here, D_e is the depth of the energy well, a determines the width of the well, r_e is the equilibrium bond length, and C is a constant that determines the (arbitrary) point of zero potential energy. From the fit, the dissociation energy of the Cd_1–Cd_2 dimer (i.e., the depth of the potential energy well D_e) is estimated to be 0.16 eV (~6.0 k_BT at room temperature), indicating that the dimer may be broken up by random thermal fluctuations. One would expect that due to the energetic gain related to dimerization, the system would spend more time in the dimer state than shown in Figure A4.4C, where the dimer configuration is present for only ~60% of the time. To give a possible explanation for this, we approximate the QD as a two-level system, where p_{dimer} and $p_{no\text{-}dimer}$ are the probability that the QD is in a nuclear configuration with and without a Cd–Cd dimer, respectively. Boltzmann statistics state that:

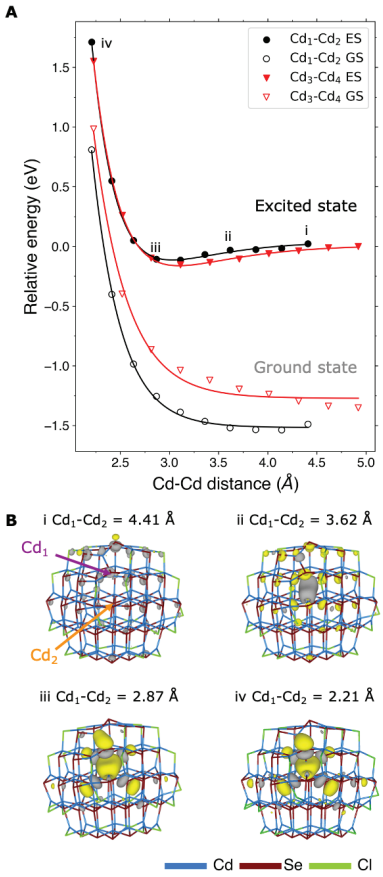

Figure 4.4. Energy change as a function of Cd–Cd distance. (A) Energy of the QD as a function of the distance between either Cd_1 and Cd_2 or Cd_3 and Cd_4 in both the GS (open markers) and the ES (solid markers). Energy of the QD at maximum Cd_3–Cd_4 separation has been arbitrarily set to zero to facilitate comparison. (B) Contour plots of the HOMO level of the QD in the ES at different Cd_1–Cd_2 distances.

$$\frac{p_{no-dimer}}{p_{dimer}} = \frac{g_{no-dimer}}{g_{dimer}} e^{-\frac{\Delta E}{k_B T}} \qquad 4.2$$

Here, ΔE is the energy difference between the dimer and no-dimer states and g_{dimer} and $g_{no\text{-}dimer}$ are the number of nuclear configurations the QD can sample in the absence and presence of a Cd–Cd dimer, respectively (i.e., the degeneracy of each state). This suggests that there is a higher number of configurations without a dimer, compensating for the energy gain due to dimerization.

The same trends can be observed when changing the distance between two different Cd atoms. Figure 4.4A (red trace, solid markers) shows the energy changes that are obtained

when varying the distance between Cd_3 and Cd_4 (see also Figures A4.2A-iii/iv) in the ES. Although the exact shape of the curve is different from the curve obtained for the Cd_1–Cd_2 dimer (i.e., the dissociation energy is now 0.17 eV (~6.7 k_BT) and the equilibrium bond length is 3.1 instead of 3.0 Å), there is no activation energy required for the formation of the dimer in either case, which is in agreement with the high rate of dimerization found during the AIMD simulations. In the absence of an activation barrier, we can estimate the dimer formation time from the Cd–Cd oscillation frequency. To this end, we treat the dimer as a harmonic oscillator, of which the frequency is given by:

$$\nu = \frac{1}{2\pi}\sqrt{\frac{k}{\mu}} = k_{trap} \qquad 4.3$$

Here, k is the spring constant and μ the reduced mass of the two Cd atoms. To determine the spring constant, we fit a parabola to the right side of the black ES curve in Figure 4.4A (see Figure A4.8 for details) and obtain k = 0.31 eV/Å^2. Using μ = 56.2 u, we find that dimerization occurs in ~860 fs ($\nu = k_{trap} = 1.2 \times 10^{12}$ s^{-1}), which is in good agreement with the AIMD runs. We note that the Cd–Cd dimerization is a complex process and that by manually varying the Cd–Cd distance we may not probe along the exact reaction coordinate. Nevertheless, since we find that the reaction is barrierless along this suboptimal pathway, it must be barrierless along the optimal reaction coordinate as well.

Figure 4.4A (black and red traces with open markers) also shows that dimerization is only energetically favorable in the ES. A geometry optimization of the GS, with the same constraints on Cd_1/Cd_2 or Cd_3/Cd_4 as imposed previously for the ES, does not lead to an energy well at reduced Cd–Cd distances. Instead, the energy increases with decreasing Cd–Cd distance, in agreement with the geometry optimizations of the preceding section, which showed that dimerization only takes place in the ES.

4.2.4 Nonradiative Recombination from Dimer States

In the preceding section, it was shown that Cd–Cd dimerization takes place on the picosecond time scale and is hence much faster than the radiative lifetime in CdSe QDs ($k_{trap} >> k_{rad}$). In order to decide whether this trapping process also quenches the PL QY, an estimate must be made of the nonradiative recombination rate of the trapped electron and the VB hole (k_{nonrad}, see Figure 4.1C). In this section, we construct the configuration coordinate diagrams for the GS and ES of both the perfectly and the imperfectly passivated QDs. Although it is difficult to extract a quantitative estimate of k_{nonrad} from these diagrams, it does provide an intuitive picture on why a Cd–Cd dimer is expected to lead to significantly faster nonradiative decay.

In order to draw the configuration coordinate diagrams, we again adopt the harmonic approximation and emulate the potential energy surfaces of the GS and ES by one-dimensional parabolas. In addition, we approximate the reaction coordinate by the Cd_1–Cd_2 distance, so that the potential energy of the GS and ES can be expressed as, respectively:

$$E_0 = \frac{1}{2}k_0\left(d_{Cd} - d_{Cd,0}\right)^2 \qquad 4.4$$

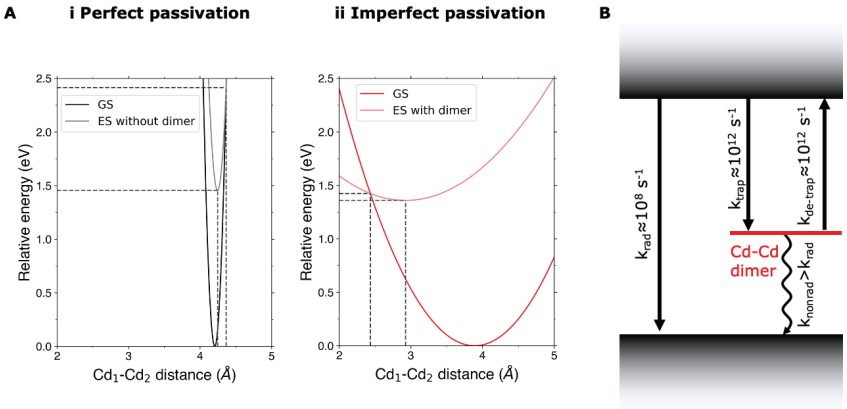

Figure 4.5. Estimation of k_{nonrad} by constructing configuration coordinate diagrams. (A) Configuration coordinate diagrams for (i) a perfectly passivated QD and (ii) an imperfectly passivated QD with a Cd–Cd dimer in the ES. (B) Schematic overview of the main recombination pathways in a QD with a Cd–Cd dimer.

$$E_1 = E + \frac{1}{2}k_1\left(d_{Cd} - d_{Cd,1}\right)^2 \qquad 4.5$$

Here, d_{Cd} is the Cd_1–Cd_2 distance, with $d_{Cd,0}$ and $d_{Cd,1}$ being the Cd_1–Cd_2 distance at the equilibrium configuration of the GS and ES, respectively. E is the energy difference between the minima of the two parabolas, while k_0 and k_1 refer to the spring constant of the GS and ES, respectively. Using Nelson's four-point method,[58,59] the parabolas can be drawn by calculating four points along the potential energy surfaces. First, the energies and Cd_1–Cd_2 distances at the minima of the parabola were determined by the geometry optimizations shown in Figure 4.2A-i-iv. For the vertical transition from the GS minimum to the ES, a single-point calculation was carried out in which the triplet state wave function was solved for the nuclear coordinates at the GS minimum. The vertical transition between the minimum of the ES and the GS parabola was calculated analogously. Further details regarding the computational methods are given in the discussion of Figure A4.9.

Figure 4.5A compares the configuration coordinate diagrams of a perfectly passivated QD, where the ES remains delocalized over the QD, and an imperfectly passivated QD, where the ES parabola refers to the electron trapped in a Cd–Cd dimer. Comparison of the two figures shows that the bottom of the ES parabola is lower in energy for the imperfectly passivated QD, which is in agreement with the first section of this paper and Figure 4.4A, where it was shown that the QD can lower its energy in the ES by forming a Cd–Cd dimer. Another difference lies in the horizontal shift of the ES parabola. For the perfectly passivated QD, the parabolas are only slightly shifted, meaning that excitation leads to only minor changes in the Cd_1–Cd_2 distance, as also shown previously in Figure 4.2A. In contrast, the large shift of the parabolas in Figure 4.5A-ii indicates that the Cd_1–Cd_2 distance reduces significantly upon excitation of the imperfectly passivated QD due to formation of the Cd–Cd dimer. Lastly, the imperfectly passivated QD was created by

moving a chloride ligand from the (100) facet (see Figure A4.1). This causes the QD structure to become less rigid, allowing for the facile formation and dissociation of Cd–Cd dimers that we have seen throughout this work. This is reflected by the shallower shape of the ES parabola in Figure 4.5A-ii, which indicates that the QD can sample multiple configurations (i.e., Cd–Cd distances) without significantly increasing its energy.

Due to both the larger displacement and the shallower potential well of the ES in the QD with the dimer (see Figure 4.5A), the activation energy required to nonradiatively cross from the ES minimum to the GS parabola (E_{act} = 0.06 eV) is significantly lower than that for the perfectly passivated QD (E_{act} = 0.96 eV). From this decrease in activation energy we can infer an estimate for the acceleration of the nonradiative decay according to:[60–62]

$$k_{nonrad} = \frac{2\pi}{\hbar}\frac{|V|^2}{\sqrt{4\pi\lambda k_B T}} e^{-E_{act}/k_B T} \quad 4.6$$

Here, V is the electronic coupling between the GS and the ES, estimated from calculating the absorption spectrum of the QD in the relaxed ES configuration within the single-orbital approximation, as implemented in the Nano-QMFlows package.[63] Taking λ as the total reorganization energy (see Figure A4.9) yields the decay rates $k_{nonrad,perf} \approx 10^{-1}$ s^{-1} and $k_{nonrad,imp} \approx 10^{13}$ s^{-1} for the perfectly and imperfectly passivated QD, respectively. While we stress that these values must be seen as rough estimates only, due to both the one-dimensional parabolic approximation and the exponential dependence of the decay rate on the activation barrier, the order-of-magnitude disparity in both rates undoubtedly shows that dimer formation greatly accelerates nonradiative decay. Furthermore, the nonradiative decay from the trap state is also expected to be much faster than radiative recombination ($k_{nonrad,imp} > k_{rad} \approx 10^8$ s^{-1},[45,46] as summarized in Figure 4.5B), indicating that dimer formation efficiently quenches the PL. As shown in Figure A4.10, this result is robust even when accounting for the known underestimation of the band gap in DFT/PBE (see Methods).[64]

An interesting question concerns the frequency with which these dimers form in practice. As has just been shown, dimer formation is a very rapid process given imperfect surface passivation. Yet, as discussed at the start of the Results and Discussion, for the current work it was assumed that the surface ligands were already in such a suboptimal configuration. How often these imperfect surface configurations occur will depend on how the ligands diffuse over the surface or possibly desorb from the surface followed by resorption from the solution at a different site. These processes are expected to take place on a much longer time scale than investigated here. Moreover, for a realistic simulation of these processes, in addition to the X-type ligands employed here, L-type ligands and solvent molecules must be taken into account explicitly, as they will significantly influence the way ligands move across the QD surface. Although beyond the scope of the current work, such calculations may give great insight into how often surface configurations appear that allow for Cd–Cd dimer formation and if that time scale agrees with, for example, QD blinking.

4.3 Conclusions

In conclusion, DFT calculations have been used to study the formation of Cd–Cd dimers and the concomitant traps in charge-neutral but photoexcited CdSe QDs. We showed

that for suboptimal surface passivation, the formation of Cd–Cd dimers is energetically favorable in a photoexcited QD. Ab initio molecular dynamics simulations show that the formation of the trap is a dynamic process and that the in-gap state appears and disappears in a period on the order of 1 ps as a result of a barrierless reaction with a relatively shallow potential well. Lastly, construction of configuration coordinate diagrams shows that nonradiative recombination from the trapped state is much faster than radiative recombination, which leads us to conclude that these transient Cd–Cd dimer traps strongly reduce the PL QY. These results show that photoexcitation can lead to atomic rearrangements and thus create transient in-gap states. Finally, we find that a similar metal-based dimer formation occurs in the excited state of other II–VI semiconductor QDs, suggesting that this type of trap may be important for the reduction of the PL QY in a broad range of semiconductor nanomaterials.

4.4 Methods

Geometry optimizations and AIMD simulations have been carried out at the DFT level with a PBE exchange-correlation functional[65] and double-ζ basis set, as implemented in the CP2K quantum chemistry software package.[66] Relativistic effects have been taken into account through the use of effective core potentials. The ES calculations were performed without spin restrictions. Geometry optimizations were carried out at 0 K in the gas phase. AIMD simulations were performed in the canonical (NVT) ensemble at a constant temperature of 300 K using a velocity rescaling thermostat.[67] MD simulations of QDs in the GS were typically run for ≥12 ps, of which the first 2 ps were discarded as an equilibration step. MD runs of the QDs in the ES were restarted from the atomic positions and velocities as obtained from the GS MD simulations. Further details are given in the main text and, for the construction of the configuration coordinate diagrams, in the Appendix.

References

1. Talapin, D. V., Lee, J.-S., Kovalenko, M. V. & Shevchenko, E. V. Prospects of Colloidal Nanocrystals for Electronic and Optoelectronic Applications. Chem. Rev. 110, 389–458 (2010).
2. Donegá, C. de M. Synthesis and properties of colloidal heteronanocrystals. Chem. Soc. Rev. 40, 1512–1546 (2011).
3. Litvin, A. P., Martynenko, I. V., Purcell-Milton, F., Baranov, A. V., Fedorov, A. V. & Gun'Ko, Y. K. Colloidal quantum dots for optoelectronics. J. Mater. Chem. A 5, 13252–13275 (2017).
4. Carey, G. H., Abdelhady, A. L., Ning, Z., Thon, S. M., Bakr, O. M. & Sargent, E. H. Colloidal Quantum Dot Solar Cells. Chem. Rev. 115, 12732–12763 (2015).
5. Ganesan, A., Houtepen, A. & Crisp, R. Quantum Dot Solar Cells: Small Beginnings Have Large Impacts. Appl. Sci. 8, 1867 (2018).
6. Jang, E., Jun, S., Jang, H., Lim, J., Kim, B. & Kim, Y. White-light-emitting diodes with quantum dot color converters for display backlights. Adv. Mater. 22, 3076–3080 (2010).
7. Kim, Y., Ham, S., Jang, H., Min, J. H., Chung, H., Lee, J., Kim, D. & Jang, E. Bright and Uniform Green Light Emitting InP/ZnSe/ZnS Quantum Dots for Wide Color Gamut Displays. ACS Appl. Nano Mater. 2, 1496–1504 (2019).

8. Ziegler, J., Xu, S., Kucur, E., Meister, F., Batentschuk, M., Gindele, F. & Nann, T. Silica-coated InP/ZnS nanocrystals as converter material in white LEDs. Adv. Mater. 20, 4068–4073 (2008).
9. Shirasaki, Y., Supran, G. J., Bawendi, M. G. & Bulović, V. Emergence of colloidal quantum-dot light-emitting technologies. Nat. Photonics 7, 13 (2013).
10. Lim, J., Park, Y.-S., Wu, K., Yun, H. J. & Klimov, V. I. Droop-Free Colloidal Quantum Dot Light-Emitting Diodes. Nano Lett. 18, 6645–6653 (2018).
11. Kim, S., Kim, J., Kim, D., Kim, B., Chae, H., Yi, H. & Hwang, B. High-Performance Transparent Quantum Dot Light-Emitting Diode with Patchable Transparent Electrodes. ACS Appl. Mater. Interfaces 11, 26333–26338 (2019).
12. Chung, D. S., Lee, J. S., Huang, J., Nag, A., Ithurria, S. & Talapin, D. V. Low voltage, hysteresis free, and high mobility transistors from all-inorganic colloidal nanocrystals. Nano Lett. 12, 1813–1820 (2012).
13. Balazs, D. M., Rizkia, N., Fang, H. H., Dirin, D. N., Momand, J., Kooi, B. J., Kovalenko, M. V. & Loi, M. A. Colloidal Quantum Dot Inks for Single-Step-Fabricated Field-Effect Transistors: The Importance of Postdeposition Ligand Removal. ACS Appl. Mater. Interfaces 10, 5626–5632 (2018).
14. Kovalenko, M. V., Manna, L., Cabot, A., Hens, Z., Talapin, D. V., Kagan, C. R., Klimov, V. I., Rogach, A. L., Reiss, P., Milliron, D. J., et al. Prospects of nanoscience with nanocrystals. ACS Nano 9, 1012–1057 (2015).
15. Geiregat, P., Van Thourhout, D. & Hens, Z. A bright future for colloidal quantum dot lasers. NPG Asia Mater. 11, 41 (2019).
16. Pietryga, J. M., Park, Y.-S., Lim, J., Fidler, A. F., Bae, W. K., Brovelli, S. & Klimov, V. I. Spectroscopic and Device Aspects of Nanocrystal Quantum Dots. Chem. Rev. 116, 10513–10622 (2016).
17. Katsiev, K., Ip, A. H., Fischer, A., Tanabe, I., Zhang, X., Kirmani, A. R., Voznyy, O., Rollny, L. R., Chou, K. W., Thon, S. M., et al. The Complete In-Gap Electronic Structure of Colloidal Quantum Dot Solids and Its Correlation with Electronic Transport and Photovoltaic Performance. Adv. Mater. 26, 937–942 (2014).
18. Kagan, C. R., Lifshitz, E., Sargent, E. H. & Talapin, D. V. Building devices from colloidal quantum dots. Science 353, aac5523–aac5523 (2016).
19. Reiss, P., Protière, M. & Li, L. Core/Shell Semiconductor Nanocrystals. Small 5, 154–168 (2009).
20. Jang, Y., Shapiro, A., Isarov, M., Rubin-Brusilovski, A., Safran, A., Budniak, A. K., Horani, F., Dehnel, J., Sashchiuk, A. & Lifshitz, E. Interface control of electronic and optical properties in IV-VI and II-VI core/shell colloidal quantum dots: a review. Chem. Commun. 53, 1002–1024 (2017).
21. Page, R. C., Espinobarro-Velazquez, D., Leontiadou, M. A., Smith, C., Lewis, E. A., Haigh, S. J., Li, C., Radtke, H., Pengpad, A., Bondino, F., et al. Near-Unity Quantum Yields from Chloride Treated CdTe Colloidal Quantum Dots. Small 11, 1548–1554 (2015).
22. Stein, J. L., Mader, E. A. & Cossairt, B. M. Luminescent InP Quantum Dots with Tunable Emission by Post-Synthetic Modification with Lewis Acids. J. Phys. Chem. Lett. 7, 1315–1320 (2016).
23. Kirkwood, N., Monchen, J. O. V., Crisp, R. W., Grimaldi, G., Bergstein, H. A. C., du Fossé, I., van der Stam, W., Infante, I. & Houtepen, A. J. Finding and Fixing

Traps in II–VI and III–V Colloidal Quantum Dots: The Importance of Z-Type Ligand Passivation. J. Am. Chem. Soc. 140, 15712–15723 (2018).
24. Shen, Y., Tan, R., Gee, M. Y. & Greytak, A. B. Quantum Yield Regeneration: Influence of Neutral Ligand Binding on Photophysical Properties in Colloidal Core/Shell Quantum Dots. ACS Nano 9, 3345–3359 (2015).
25. Gao, Y. & Peng, X. Photogenerated Excitons in Plain Core CdSe Nanocrystals with Unity Radiative Decay in Single Channel: The Effects of Surface and Ligands. J. Am. Chem. Soc. 137, 4230–4235 (2015).
26. Fan, J. Z., Andersen, N. T., Biondi, M., Todorović, P., Sun, B., Ouellette, O., Abed, J., Sagar, L. K., Choi, M. J., Hoogland, S., et al. Mixed Lead Halide Passivation of Quantum Dots. Adv. Mater. 31, 1904304 (2019).
27. Weaver, A. L. & Gamelin, D. R. Photoluminescence Brightening via Electrochemical Trap Passivation in ZnSe and Mn2+-Doped ZnSe Quantum Dots. J. Am. Chem. Soc. 134, 6819–6825 (2012).
28. Rinehart, J. D., Weaver, A. L. & Gamelin, D. R. Redox Brightening of Colloidal Semiconductor Nanocrystals Using Molecular Reductants. J. Am. Chem. Soc. 134, 16175–16177 (2012).
29. Boehme, S. C., Azpiroz, J. M., Aulin, Y. V., Grozema, F. C., Vanmaekelbergh, D., Siebbeles, L. D. A., Infante, I. & Houtepen, A. J. Density of Trap States and Auger-mediated Electron Trapping in CdTe Quantum-Dot Solids. Nano Lett. 15, 3056–3066 (2015).
30. van der Stam, W., du Fossé, I., Grimaldi, G., Monchen, J. O. V., Kirkwood, N. & Houtepen, A. J. Spectroelectrochemical Signatures of Surface Trap Passivation on CdTe Nanocrystals. Chem. Mater. 30, 8052–8061 (2018).
31. Geiregat, P., Houtepen, A. J., Sagar, L. K., Infante, I., Zapata, F., Grigel, V., Allan, G., Delerue, C., Van Thourhout, D. & Hens, Z. Continuous-wave infrared optical gain and amplified spontaneous emission at ultralow threshold by colloidal HgTe quantum dots. Nat. Mater. 17, 35–42 (2018).
32. Zhao, J., Holmes, M. A. & Osterloh, F. E. Quantum Confinement Controls Photocatalysis: A free Energy Analysis for Photocatalytic Proton Reduction at CdSe Nanocrystals. ACS Nano 7, 4316–4325 (2013).
33. Knowles, K. E., Tice, D. B., McArthur, E. A., Solomon, G. C. & Weiss, E. A. Chemical Control of the Photoluminescence of CdSe Quantum Dot–Organic Complexes with a Series of Para-Substituted Aniline Ligands. J. Am. Chem. Soc. 132, 1041–1050 (2010).
34. Boles, M. A., Ling, D., Hyeon, T. & Talapin, D. V. The surface science of nanocrystals. Nat. Mater. 15, 141–153 (2016).
35. Houtepen, A. J., Hens, Z., Owen, J. S. & Infante, I. On the Origin of Surface Traps in Colloidal II–VI Semiconductor Nanocrystals. Chem. Mater. 29, 752–761 (2017).
36. du Fossé, I., ten Brinck, S., Infante, I. & Houtepen, A. J. Role of Surface Reduction in the Formation of Traps in n-Doped II–VI Semiconductor Nanocrystals: How to Charge without Reducing the Surface. Chem. Mater. 31, 4575–4583 (2019).
37. Tsui, E. Y., Hartstein, K. H. & Gamelin, D. R. Selenium Redox Reactivity on Colloidal CdSe Quantum Dot Surfaces. J. Am. Chem. Soc. 138, 11105–11108 (2016).

38. Sabatini, R. P., Bappi, G., Bicanic, K. T., Fan, F., Hoogland, S., Saidaminov, M. I., Sagar, L. K., Voznyy, O. & Sargent, E. H. Temperature-Induced Self-Compensating Defect Traps and Gain Thresholds in Colloidal Quantum Dots. ACS Nano 13, 8970–8976 (2019).
39. Hartley, C. L., Kessler, M. L. & Dempsey, J. L. Molecular-Level Insight into Semiconductor Nanocrystal Surfaces. J. Am. Chem. Soc. 143, 1251–1266 (2021).
40. Pu, C. & Peng, X. To Battle Surface Traps on CdSe/CdS Core/Shell Nanocrystals: Shell Isolation versus Surface Treatment. J. Am. Chem. Soc. 138, 8134–8142 (2016).
41. Kalyuzhny, G. & Murray, R. W. Ligand effects on optical properties of CdSe nanocrystals. J. Phys. Chem. B 109, 7012–7021 (2005).
42. van der Stam, W., Grimaldi, G., Geuchies, J. J., Gudjonsdottir, S., van Uffelen, P. T., van Overeem, M., Brynjarsson, B., Kirkwood, N. & Houtepen, A. J. Electrochemical Modulation of the Photophysics of Surface-Localized Trap States in Core/Shell/(Shell) Quantum Dot Films. Chem. Mater. 31, 8484–8493 (2019).
43. Shim, M., Wang, C., Norris, D. J. & Guyot-Sionnest, P. Doping and Charging in Colloidal Semiconductor Nanocrystals. MRS Bull. 26, 1005–1008 (2001).
44. Mocatta, D., Cohen, G., Schattner, J., Millo, O., Rabani, E. & Banin, U. Heavily Doped Semiconductor Nanocrystal Quantum Dots. Science 332, 77–81 (2011).
45. Rabouw, F. T., Kamp, M., Van Dijk-Moes, R. J. A., Gamelin, D. R., Koenderink, A. F., Meijerink, A. & Vanmaekelbergh, D. Delayed Exciton Emission and Its Relation to Blinking in CdSe Quantum Dots. Nano Lett. 15, 7718–7725 (2015).
46. Efros, A. L. & Nesbitt, D. J. Origin and control of blinking in quantum dots. Nat. Nanotechnol. 11, 661 (2016).
47. Bodunov, E. N. & Simões Gamboa, A. L. Photoluminescence Decay of Colloidal Quantum Dots: Reversible Trapping and the Nature of the Relevant Trap States. J. Phys. Chem. C 123, 25515–25523 (2019).
48. Voznyy, O., Zhitomirsky, D., Stadler, P., Ning, Z., Hoogland, S. & Sargent, E. H. A Charge-Orbital Balance Picture of Doping in Colloidal Quantum Dot Solids. ACS Nano 6, 8448–8455 (2012).
49. Anderson, N. C., Hendricks, M. P., Choi, J. J. & Owen, J. S. Ligand Exchange and the Stoichiometry of Metal Chalcogenide Nanocrystals: Spectroscopic Observation of Facile Metal-Carboxylate Displacement and Binding. J. Am. Chem. Soc. 135, 18536–18548 (2013).
50. Greaney, M. J., Couderc, E., Zhao, J., Nail, B. A., Mecklenburg, M., Thornbury, W., Osterloh, F. E., Bradforth, S. E. & Brutchey, R. L. Controlling the Trap State Landscape of Colloidal CdSe Nanocrystals with Cadmium Halide Ligands. Chem. Mater. 27, 744–756 (2015).
51. Voznyy, O., Thon, S. M., Ip, A. H. & Sargent, E. H. Dynamic Trap Formation and Elimination in Colloidal Quantum Dots. J. Phys. Chem. Lett. 4, 987–992 (2013).
52. Drijvers, E., De Roo, J., Martins, J. C., Infante, I. & Hens, Z. Ligand Displacement Exposes Binding Site Heterogeneity on CdSe Nanocrystal Surfaces. Chem. Mater. 30, 1178–1186 (2018).
53. Neukirch, A. J., Hyeon-Deuk, K. & Prezhdo, O. V. Time-domain ab initio modeling of excitation dynamics in quantum dots. Coord. Chem. Rev. 263, 161–181 (2014).
54. Voznyy, O. Mobile Surface Traps in CdSe Nanocrystals with Carboxylic Acid

Ligands. J. Phys. Chem. C 115, 15927–15932 (2011).
55. Saniepay, M., Mi, C., Liu, Z., Abel, E. P. & Beaulac, R. Insights into the Structural Complexity of Colloidal CdSe Nanocrystal Surfaces: Correlating the Efficiency of Nonradiative Excited-State Processes to Specific Defects. J. Am. Chem. Soc. 140, 1725–1736 (2018).
56. Hartley, C. L. & Dempsey, J. L. Electron-Promoted X-Type Ligand Displacement at CdSe Quantum Dot Surfaces. Nano Lett. 19, 1151–1157 (2019).
57. Baturin, V., Lepeshkin, S., Bushlanova, N. & Uspenskii, Y. Atomistic Origins of Charge Traps in CdSe Nanoclusters. Phys. Chem. Chem. Phys. 22, 26299–26305 (2020).
58. Nelsen, S. F., Blackstock, S. C. & Kim, Y. Estimation of Inner Shell Marcus Terms for Amino Nitrogen Compounds by Molecular Orbital Calculations. J. Am. Chem. Soc. 109, 677–682 (1987).
59. López-Estrada, O., Laguna, H. G., Barrueta-Flores, C. & Amador-Bedolla, C. Reassessment of the Four-Point Approach to the Electron-Transfer Marcus-Hush Theory. ACS omega 3, 2130–2140 (2018).
60. Jortner, J. Dynamics of Electron Transfer in Bacterial Photosynthesis. Biochim. Biophys. Acta (BBA)- Rev. Bioenerg. 594, 193–230 (1980).
61. Marcus, R. A. & Sutin, N. Electron Transfers in Chemistry and Biology. Biochim. Biophys. Acta (BBA)-Reviews Bioenerg. 811, 265–322 (1985).
62. Benniston, A. C. & Harriman, A. Charge on the move: How electron-transfer dynamics depend on molecular conformation. Chem. Soc. Rev. 35, 169–179 (2006).
63. Zapata, F., Ridder, L., Hidding, J., Jacob, C. R., Infante, I. & Visscher, L. QMflows: A Tool Kit for Interoperable Parallel Workflows in Quantum Chemistry. J. Chem. Inf. Model. 59, 3191–3197 (2019).
64. Azpiroz, J. M., Ugalde, J. M. & Infante, I. Benchmark Assessment of Density Functional Methods on Group II-VI MX (M = Zn, Cd; X = S, Se, Te) Quantum Dots. J. Chem. Theory Comput. 10, 76–89 (2014).
65. Perdew, J. P., Burke, K. & Ernzerhof, M. Generalized Gradient Approximation Made Simple. Phys. Rev. Lett. 77, 3865–3868 (1996).
66. Hutter, J., Iannuzzi, M., Schiffmann, F. & VandeVondele, J. cp2k: atomistic simulations of condensed matter systems. Wiley Interdiscip. Rev. Comput. Mol. Sci. 4, 15–25 (2014).
67. Bussi, G., Donadio, D. & Parrinello, M. Canonical sampling through velocity rescaling. J. Chem. Phys. 126, 014101 (2007).

Appendix

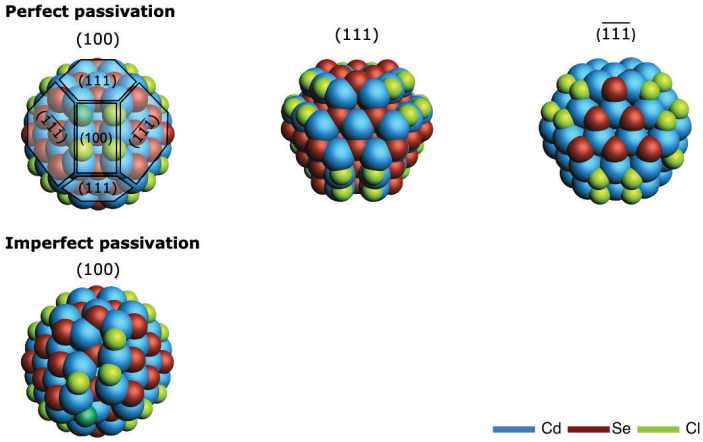

Figure A4.1. Overview of the different facets of the $Cd_{68}Se_{55}Cl_{26}$ model used in the current work. The top row shows the perfectly passivated QD, as viewed perpendicular to the (100), (111) and ($\overline{111}$) facets, respectively. The bottom figure shows the imperfectly passivated QD. The chloride ligand that has been moved from the (100) to the (111) facet has been indicated in dark green.

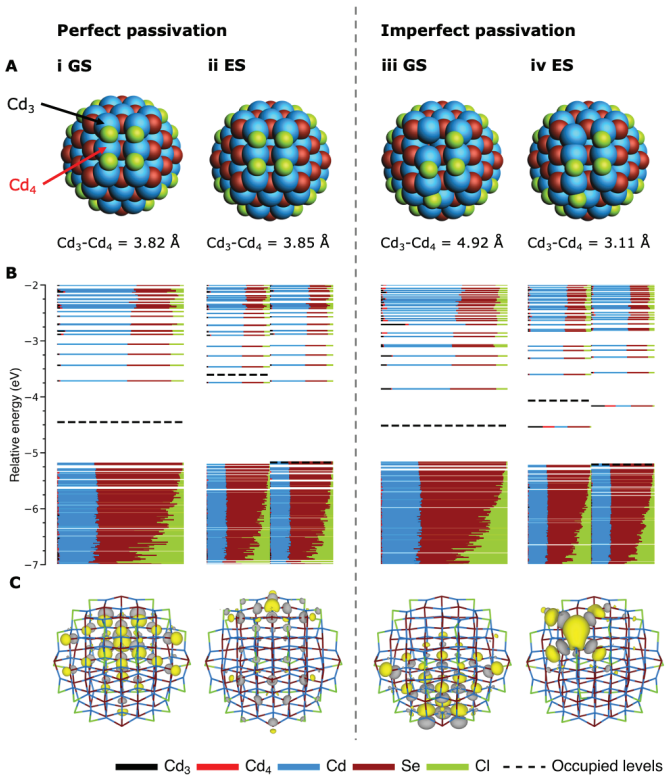

Figure A4.2. Cd-Cd dimer formation in excited, charge-neutral QDs with imperfect passivation. (A) Structure of the QD when perfectly passivated (left of dashed line), or imperfectly passivated (right of dashed line). The imperfectly passivated QD was optimized from a slightly different starting geometry than used in Figure 4.2 in the main text. As a result, the dimer forms between two different Cd atoms, indicated by Cd_3 and Cd_4. The Cd_3-Cd_4 distance is given below each structure. (B) DOS for each of the QDs. (C) Contour plots of the HOMO of each QD.

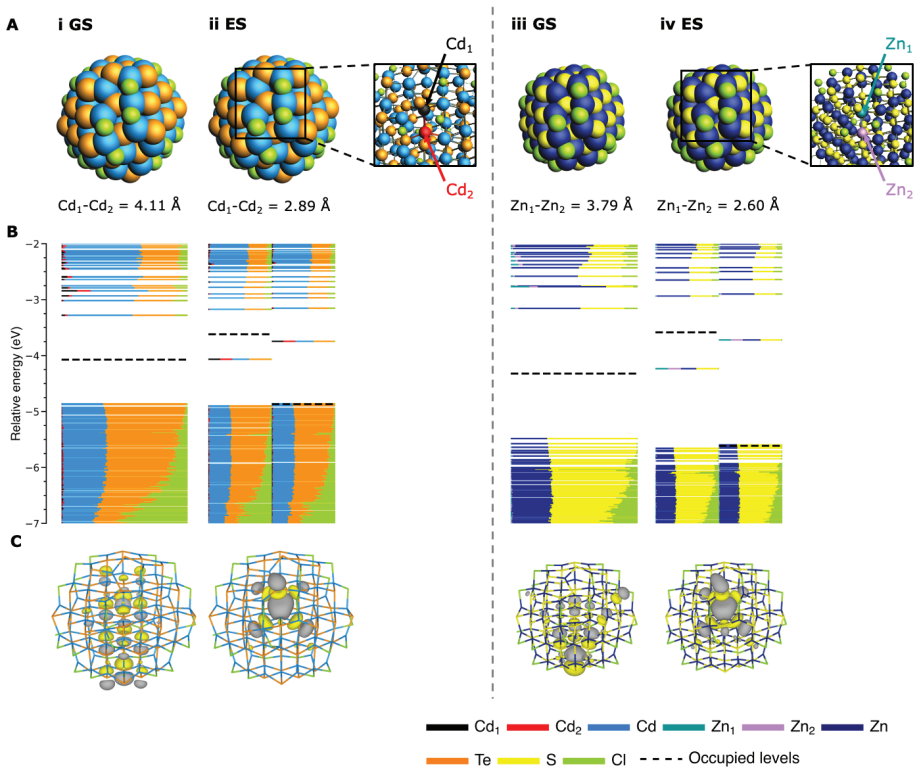

Figure A4.3. Metal dimer formation in excited, charge-neutral CdTe and ZnS QDs with imperfect passivation. (A) Structure of the CdTe (left of dashed line) and the ZnS QD (right of dashed line). The M_1-M_2 distance is given below each structure. (B) DOS for each of the QDs. (C) Contour plots of the HOMO of each QD.

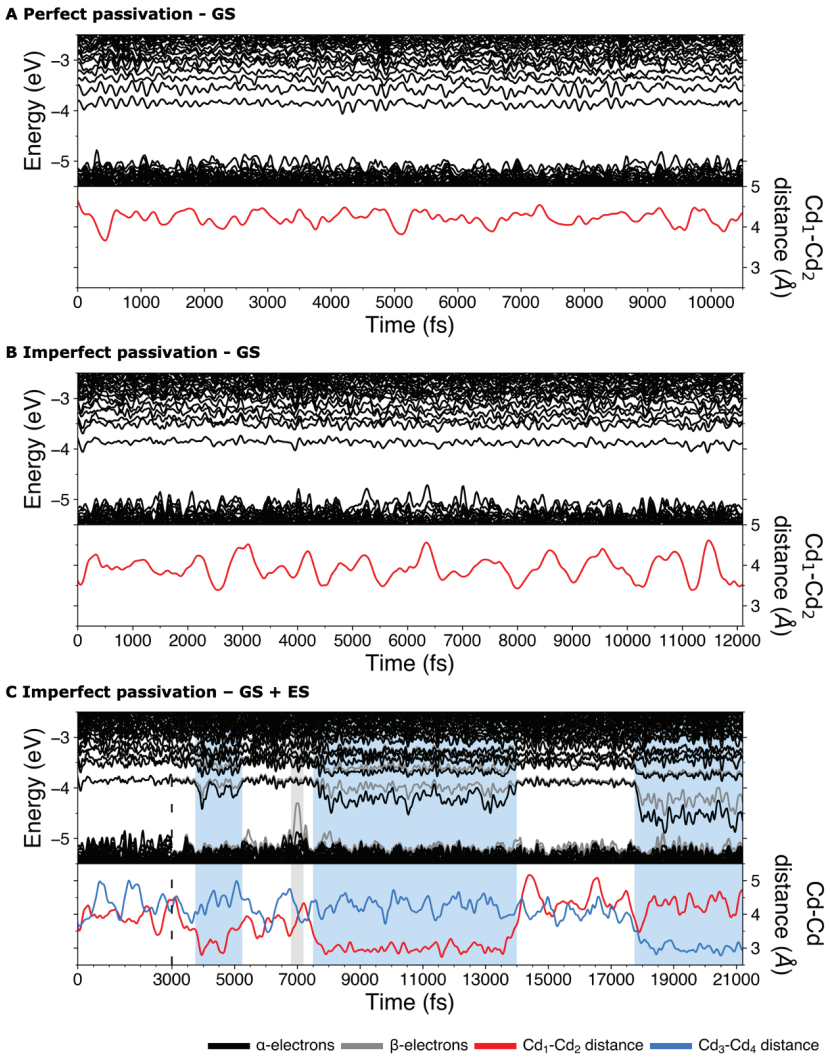

Figure A4.4. Time-dependent Cd-Cd dimerization in AIMD simulations covering longer time scales than shown in Figure 4.3 of the main text. DOS and Cd-Cd distance for (A) the perfectly passivated QD in the GS, i.e. the same as in Figure 4.3A-i of the main text, but without excitation to the ES; (B) the imperfectly passivated QD in the GS, i.e. the same as in Figure 4.3A-ii, but without excitation to the ES; and (C) the imperfectly passivated QD, starting in the GS and promoted to the ES at time = 3.0 ps (see vertical dashed line), i.e. with the first 10 ps being identical to those shown in Figure 4.3A-ii. The blue and grey shaded areas serve as a guide to the eye to indicate the times when a Cd-Cd or Se-Se dimer is present, respectively.

Se-Se dimers. As discussed in the main text, Se-Se dimers appear to form entirely analogously to Cd-Cd dimers. Cd-Cd dimers form upon the reduction of a QD with undercoordinated Cd sites, where the excess electron stabilizes the dimer by occupying the Cd-Cd bonding orbital.[36] Se-Se dimers form upon the oxidation of a QD with undercoordinated Se sites by depopulating one of the anti-bonding Se-Se orbitals.[29] Following the model by Voznyy et al.,[48] we assume that the oxidation states of the elements are Cd^{2+}, Se^{2-} and Cl^{-}. As a result, in a charge balanced (i.e. not oxidized) QD the chalcogenide p orbitals are full. Se-Se dimerization would therefore lead to a fully occupied anti-bonding MO, making the process energetically unfavorable. Upon oxidation of the QD, one of the electrons is removed from the anti-bonding MO (oxidizing one Se^{2-} site to Se^{-}), making it possible to form the Se-Se dimer.[29]

In order to study the effect of Se-Se dimers, we start with our perfectly passivated model QD (see Figure A4.5A-i). First, we move one chloride from the (100) to the adjacent (111) facet, as also done in the main text to create the imperfectly passivated QD. In addition, we remove a $CdCl^{+}$ unit from the (100) facet and inject an extra hole into the QD (this is isoelectronic with removing $CdCl^{0}$). This p-dopes the QD and additionally leaves the underlying Se atoms undercoordinated. In line with the preceding discussion, optimization of the structure leads to the formation of a Se-Se dimer and a localized state in the bandgap (see Figure A4.5-ii).

In Figure A4.5-iii, we charge this QD with one extra electron, adding a K^{+} counterion to keep the overall system charge neutral. We note that, for simplicity, instead of exciting an electron from the VB to the CB, we add one electron to the system. Based on the results on Cd-Cd dimers presented in this work, we expect that the results shown here for added CB electrons can be extended to excited CB electrons. In Figure A4.5-iii, the extra electron fills the anti-bonding Se-Se MO, breaking up the dimer and increasing the Se_1-Se_2 distance from 3.08 Å (in Figure A4.5A-ii) to 3.83 Å. At the same time, the HOMO is no longer localized on both Se atoms, but only on the two-coordinated Se on the right (Se_2, as indicated by the green arrow in Figure A4.5A-ii). Now that the Se-Se dimer is broken up, addition of a second electron (Figure A4.5-iv) leads to the formation of a Cd-Cd dimer, as evinced by the reduced Cd_3-Cd_4 distance and the appearance of a new in-gap state.

In Figure A4.5-v, the QD is charged with one excess electron (as was the case for Figure A4.5-iii). However, here we simulate the situation where the CB electron has not (yet) relaxed to the Se-Se anti-bonding MO, by enforcing a triplet state. As a result, the electron cannot relax to the Se-Se MO, and instead leads to the formation of the Cd-Cd dimer. The energy of this structure (see Figure A4.5A-v) is roughly 0.23 eV (9.1 k_BT) higher than the structure shown in Figure A4.5A-iii, indicating that it is more favorable for the system to reduce and break up the Se-Se dimer, than to retain the Se-Se dimer and additionally form the Cd-Cd dimer. Translating this to an electrochemical interpretation, it means that the standard reduction potential of breaking the Se-Se dimer is less negative than the standard reduction potential of forming the Cd-Cd dimer.

We note that, in Figure A4.5, we have added electrons by charging the QDs. In Figure A4.6 below, we show that Se-Se dimers may also form transiently upon photoexcitation

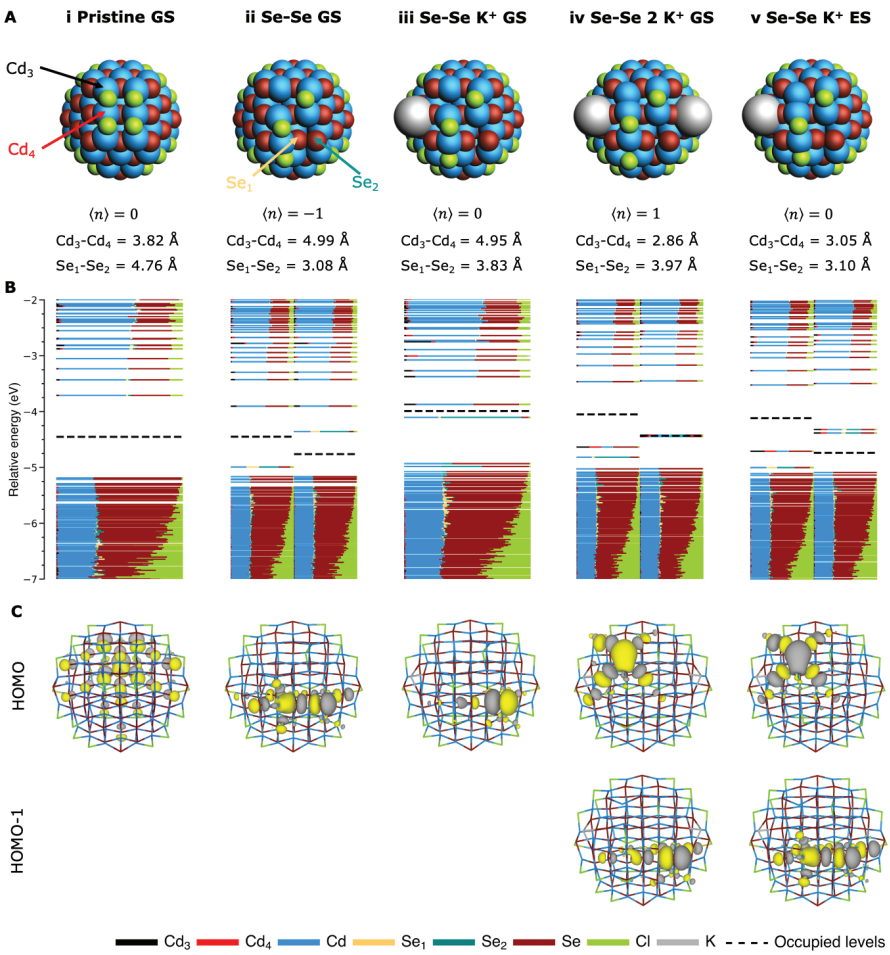

Figure A4.5. Se-Se and Cd-Cd dimer formation in charged QDs. (A) Structure of the QD when (i) perfectly passivated; (ii) with a Se-Se dimer due to removal of a $CdCl^0$ moiety; (iii) with a broken-up Se-Se dimer due to the addition of an extra electron; (iv) with a Cd-Cd dimer due to the addition of two electrons; (v) with both a Se-Se and a Cd-Cd dimer by adding an extra electron and enforcing a triplet state. The number of excess electrons <n> is indicated below each structure. <n> = 0 indicates a charge neutral system, whereas <n> < 0 and <n> > 0 refer to p- and n-doped structures, respectively. The distance between Cd_3-Cd_4 and Se_1-Se_2, as indicated by the arrows, is given below each QD. (B) DOS for each structure. (C) Contour plots of the α HOMO of each QD. For structures (iv) and (v), the HOMO-1 is also shown.

of charge neutral QDs. As also discussed in the main text, a VB level briefly extends far into the bandgap around time = 7.0 ps in the AIMD run of the imperfectly passivated QD (see Figure A4.6A or Figure 4.3A-ii in the main text). Further inspection of this state, as summarized in Figure A4.6 below, suggests that the level is due to an anti-bonding Se-Se orbital (note that the Se atoms involved here are different from those in Figure A4.5), which

has also been reported previously.[38,57] In line with the discussion above, we interpret this as the trapping of the VB hole in the excited QD to the anti-bonding Se-Se MO, causing the dimer-bond to be energetically more favorable. This is also reflected by the Se-Se bond length, which briefly decreases to ~3 Å at time = 7.0 ps, compared to an average bond length of ~4.5 Å during the rest of the run (see also Figure A4.6A). Excitation of a QD is thus expected to lead to the formation of both Cd-Cd and Se-Se dimers through similar mechanisms. In our AIMD runs, the Cd-Cd dimers are observed much more frequently than the Se-Se dimers, which suggests that the stabilization of the former is larger.

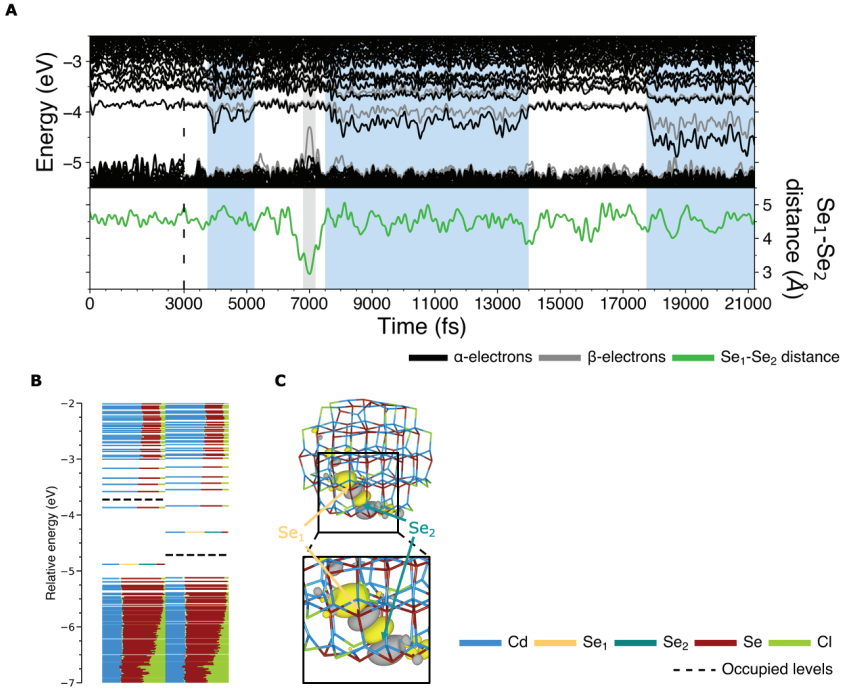

Figure A4.6. The formation of a Se-Se dimer during the AIMD simulation. (A) DOS and Se_1-Se_2 distance for the imperfectly passivated QD (i.e. the same system as shown in Figure A4.4C), starting in the GS and promoted to the ES at time = 3.0 ps (see vertical dashed line). The blue and grey shaded areas serve as a guide to the eye to indicate the times when a Cd-Cd or Se-Se dimer is present, respectively. (B) DOS of the QD in the ES at time = 7.0 ps. It can be seen that the in-gap states are localized for ~59% on the two Se-atoms indicated with Se_1 and Se_2. (C) Contour plot of the α HOMO-1, showing the anti-bonding character of the Se_1-Se_2 orbital.

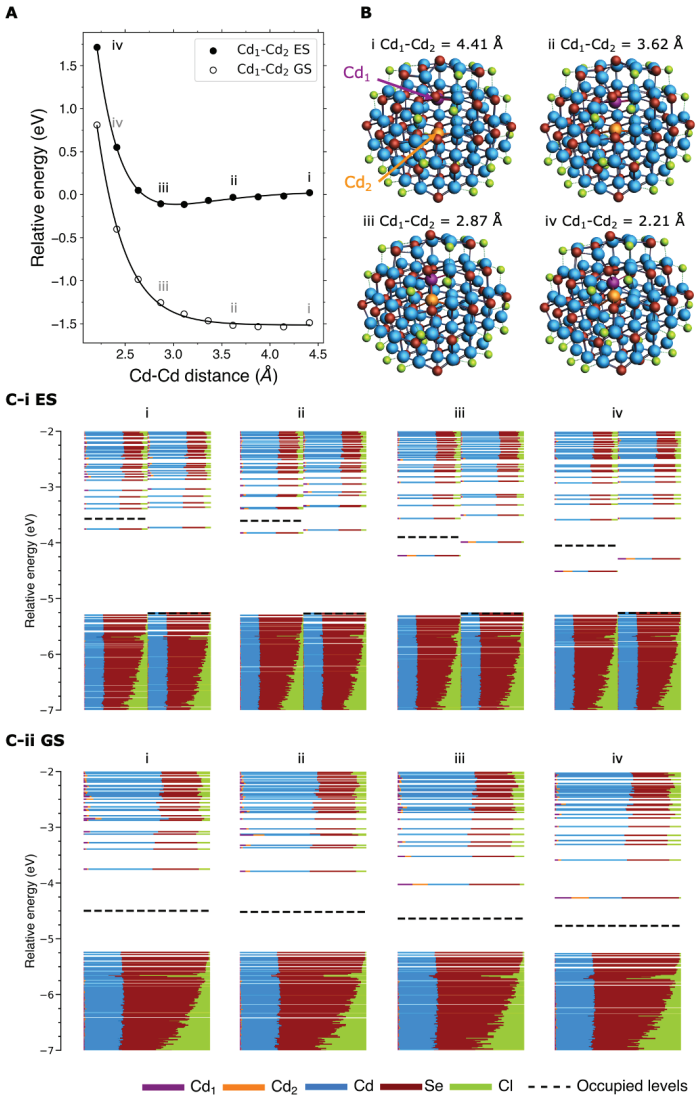

Figure A4.7. Comparison of the energy and DOS as function of the Cd-Cd distance in both the GS and ES. (A) Energy of the QD as function of the Cd_1-Cd_2 distance, in both the GS and ES (this figure shows the same data as Figure 4.4A in the main text). (B) Structure of the QD in the ES at varying Cd_1-Cd_2 distance. (C) The DOS for the same four Cd_1-Cd_2 distances, for both (i) the ES and (ii) GS. It can be seen that similar energy levels are pushed into the bandgap in both cases, but that there is no electron to occupy and thus stabilize the Cd-Cd level in the GS.

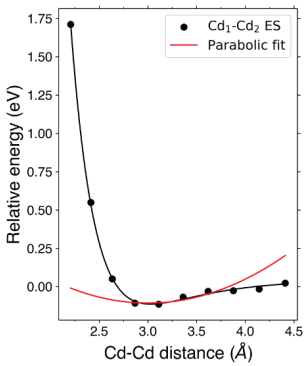

Figure A4.8. Estimating the rate of Cd-Cd dimer formation from the potential energy landscape. The energy of the QD as function of the Cd_1-Cd_2 distance is given by the black dots, and the fitted Morse potential is shown by the black line. As discussed in the main text, we treat the dimer as a harmonic oscillator with frequency:

$$\nu = \frac{1}{2\pi}\sqrt{\frac{k}{\mu}} = k_{trap} \qquad \text{A4.1}$$

Here, k is the spring constant and μ the reduced mass of two Cd atoms. In order to obtain k, the right side of the Morse potential ($2.85 \leq x \leq 3.75$, with x being the Cd-Cd distance) is approximated by a parabolic energy well (shown in red):

$$E(x) = \frac{1}{2}k(x - r_e)^2 - C \qquad \text{A4.2}$$

This gives k = 0.31 eV/Å^2. Using that μ = 56.2 u, we find that $k_{trap} = \nu = 1.2 \cdot 10^{12}$ s^{-1}, or ~860 fs, which is in agreement with the rates found in the AIMD runs (see Figure A4.4).

Constructing the configuration coordinate diagrams. The rate of non-radiative recombination of the trapped electron with the VB hole is estimated by the construction of configuration coordinate diagrams, for which we approximate the potential energy surfaces of the GS and ES by one-dimensional parabolas. In addition, we approximate the reaction coordinate by the Cd_1-Cd_2 distance, so that the potential energy of the GS and ES can be expressed by:

$$E_0 = \frac{1}{2}k_0\left(d_{Cd} - d_{Cd,0}\right)^2 \quad \text{A4.3}$$

$$E_1 = E + \frac{1}{2}k_1\left(d_{Cd} - d_{Cd,1}\right)^2 \quad \text{A4.4}$$

As also discussed in the main text, d_{Cd} is the Cd_1-Cd_2 distance, with $d_{Cd,0}$ and $d_{Cd,1}$ the Cd_1-Cd_2 distance at the equilibrium configuration of the GS and ES, respectively. E is the energy difference between the minima of the two parabolas, while k_0 and k_1 refer to the spring constant of the GS and ES, respectively. Using Nelson's four-point method,[58,59] the parabolas can be drawn by calculating four points along the potential energy surfaces, which are indicated with the terms SS, TS, TT and ST in Figure A4.9. The energy at the minimum of the GS parabola was calculated by optimizing the geometry of the QD in the singlet state (a singlet wavefunction on a singlet atomic configuration, SS). The energy on the ES parabola that is obtained by a vertical transition from the GS minimum was calculated by carrying out a single point calculation, in which a triplet state wavefunction was optimized for the atomic configuration at point SS (a triplet wavefunction on a singlet atomic configuration, TS). In the same way, the minimum of the ES parabola was computed by optimizing the geometry in the triplet state (TT). The energy at point ST was obtained by a single point calculation in which a singlet state wavefunction was optimized for the nuclear configuration at point TT. These four points were calculated both for the perfectly passivated QDs (by taking the energies of the structures in Figures 4.2A-i/ii in the main text) and the imperfectly passivated QDs (by using the structures in Figures 4.2A-iii/iv in the main text), as summarized in the table of Figure A4.9B (note that the values are reported relative to the SS energy). Next, the different excitation and reorganization energies, as summarized in Figure A4.9B, can be calculated by:

$$E = TT - SS \quad \text{A4.5}$$

$$\lambda_0 = ST - SS \quad \text{A4.6}$$

$$\lambda_1 = TS - TT \quad \text{A4.7}$$

$$\lambda = \lambda_0 + \lambda_1 \quad \text{A4.8}$$

Lastly, the spring constants of the parabolas (k_0 and k_1) can be determined via:

$$k_0 = \frac{2 \cdot ST}{\left(d_{Cd,0} - d_{Cd,1}\right)^2} \quad \text{A4.9}$$

$$k_1 = \frac{2 \cdot (TS - E)}{\left(d_{Cd,0} - d_{Cd,1}\right)^2} \quad \text{A4.10}$$

A

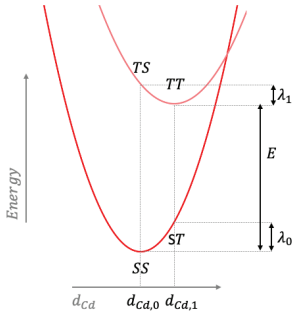

B

	Perfect passivation	Imperfect passivation
$SS\ (eV)$	0.00	0.00
$TS\ (eV)$	1.56	1.61
$TT\ (eV)$	1.45	1.36
$ST\ (eV)$	0.15	0.62
$E\ (eV)$	1.45	1.36
$\lambda_0\ (eV)$	0.15	0.62
$\lambda_1\ (eV)$	0.10	0.25
$\lambda\ (eV)$	0.25	0.87
$d_{Cd,0}\ (Å)$	4.21	3.89
$d_{Cd,1}\ (Å)$	4.25	2.93
$k_0\ (eV/Å^2)$	189.95	1.35
$k_1\ (eV/Å^2)$	133.06	0.54
$E_{act}\ (eV)$	0.96	0.06
$\lvert V\rvert\ (eV)$	0.26	0.09

Figure A4.9. Overview of the energies required for constructing the configuration coordinate diagrams. (A) Schematic overview of the different (reorganization) energies. (B) Summary of the values obtained for the different (reorganization) energies.

Now that all the parameters in equations (A4.3) and (A4.4) are known, the parabolas of both the perfectly passivated QD and the imperfectly passivated QD with the Cd-Cd dimer can be constructed, as shown in Figure 4.5A in the main text. Subsequently, simple algebra can be used to extract the intersection point of the two parabolas that is lowest in energy. From this, the activation energy E_{act} can be determined, which is defined as the difference in energy at the intersection point and the minimum of the ES parabola. Lastly, the rate of non-radiative decay was calculated from:[60–62]

$$k_{nonrad} = \frac{2\pi}{\hbar}\frac{|V|^2}{\sqrt{4\pi\lambda k_B T}} \cdot e^{-\frac{E_{act}}{k_B T}} \qquad \text{A4.11}$$

As also discussed in the main text, V is the electronic coupling between the GS and ES, which is estimated from calculating the absorption spectrum of the QD in the relaxed ES configuration, using the single-orbital approximation, as implemented in the Nano-QMFlows package.[63] For λ we use the total reorganization energy (see Figure A4.9). This gives a decay rate of $k_{nonrad} \approx 10^{-1}\ s^{-1}$ and $k_{nonrad} \approx 10^{13}\ s^{-1}$ for the perfectly and imperfectly passivated QD, respectively. It must be noted that these values are only rough estimates. Due to the shallow energy minimum of the model QDs, it remains challenging to find the exact energy at the minimum of the parabolas in the configuration coordinate diagrams. This influences the value of the activation barrier (E_{act}), which in turn can significantly affect the non-radiative decay rate, as $k_{nonrad} \sim e^{-Eact}$. This effect can be especially pronounced for the pristine QD in Figure 4.5A-i, where the intersection point lies at the steep part of the parabolas. As a result, small changes in the minima of the parabolas can lead to large differences in E_{act}. The parabolas of the imperfectly passivated QD (Figure 4.5A-ii) are much less affected by variations in energy, as the intersection point lies in the flat region of the ES parabola. Therefore, the general conclusion, that k_{nonrad} is much faster in the presence of a Cd-Cd dimer and also faster than k_{rad}, still holds.

Effect of the bandgap on the non-radiative decay rate. As the PBE functional used in this work has been shown to underestimate the bandgap,[64] the vertical separation of the parabolas, constructed in the preceding section and shown in Figure 4.5A in the main text, is also underestimated. In order to estimate the effect of a larger bandgap on the non-radiative decay rate, we rigidly shift the ES parabola up by $TT_{new} = TT + \alpha$ and $TS_{new} = TS + \alpha$ for $0 \leq \alpha \leq 0.8$ eV (see Figure A4.9A for the definitions of TT and TS). Figure A4.10 shows the activation energy (E_{act}) and non-radiative recombination rate (k_{nonrad}) as a function of the bandgap, which is defined as bandgap = TT_{new} - SS. It can be seen that increasing the bandgap by 0.8 eV reduces k_{nonrad} for the perfectly passivated QD by ~17 orders of magnitude. In contrast, due to the shallower shape of the ES parabola, k_{nonrad} only decreases by ~3 orders of magnitude for the QD with the Cd-Cd dimer. These results show that the underestimation of the bandgap does not qualitatively affect our conclusions, i.e. that the non-radiative decay from the dimer trap state is expected to be much faster than the radiative recombination.

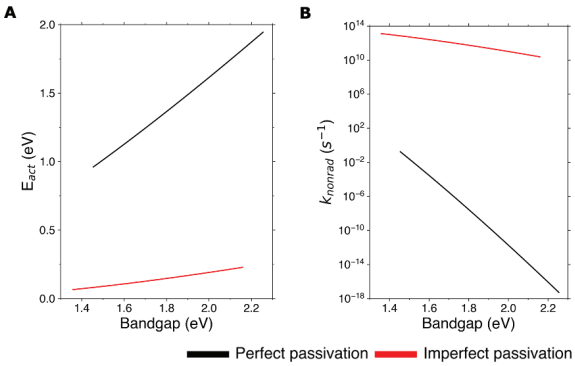

Figure A4.10. The effect of the bandgap on the non-radiative decay rate. (A) The activation energy (E_{act}) and (B) the non-radiative recombination rate (k_{nonrad}) as function of the bandgap.

5

Effect of Ligands and Solvents on the Stability of Electron Charged CdSe Colloidal Quantum Dots

Many colloidal quantum dot (QD)-based devices involve charging of the QD, either via intentional electronic doping or via electrical charge injection or photoexcitation. Previous research has shown that this charging can give rise to undesirable electrochemical surface reactions, leading to the formation of localized in-gap states. However, little is known about the factors that influence the stability of charged QDs against surface oxidation or reduction. Here, we use density functional theory to investigate the effect of various ligands and solvents on the reduction of surface Cd in negatively charged CdSe QDs. We find that X-type ligands can lead to significant shifts in the energy of the band edges but that the in-gap state related to reduced surface Cd is shifted in the same direction. As a result, shifting the band edges to higher energies does not necessarily lead to less stable electron charging. However, subtle changes in the local electrostatic environment lead to a clear correlation between the position of the in-gap state in the bandgap and the energy gained upon surface reduction. Binding ligands directly to the Cd sites most prone to reduction was found to greatly enhance the stability of the electron charged QDs. We find that ligands bind much more weakly after reduction of the Cd site, leading to a loss in binding energy that makes charge localization no longer energetically favorable. Lastly, we show that increasing the polarity of the solvent also increases the stability of QDs charged with electrons. These results highlight the complexity of surface reduction reactions in QDs and provide valuable strategies for improving the stability of charged QDs.

This chapter is based on: Indy du Fossé, Snigdha Lal, Aydin Najl Hossaini, Ivan Infante, Arjan J. Houtepen. Journal of Physical Chemistry C, 2021, 125 (43), 23968-23975

5.1 Introduction

Because of their high surface-to-volume ratio, colloidal quantum dots (QDs) have properties that are significantly influenced by the nature of the surface.[1,2] As atoms at the surface typically have a lower coordination than in the bulk, the QD surface often gives rise to localized energy levels in the bandgap.[2–4] These in-gap states can trap generated charge carriers, leading to reduced radiative recombination[5] or hindered charge transport,[6,7] which limits the efficiency of QD devices.[8] Much of the study geared toward improving the performance of these devices has been focused on reducing the density of surface traps via ligand capping[5,9–11] or core/shell synthesis.[12,13]

Many QD devices involve charging of the QD, be it via intentional electronic doping,[14,15] or via electrical charge injection[16–18] or photoexcitation and subsequent charge separation.[19–22] However, this charging can lead to the unwanted formation of new surface defects.[23] In bulk systems, the degradation of semiconductor materials through reduction of the metal cations or oxidation of the anions has long been known.[24,25] In contrast, our understanding of surface electrochemical reactions in charged QDs remains limited. In a previous computational study, we used density functional theory (DFT) calculations to show that electron charging of II–VI semiconductor QDs can lead to the formation of in-gap states due to the reduction of metal atoms. Upon addition of multiple electrons to a CdTe model QD, charge localization on Cd atoms in the (111) facets was found to create metal-based in-gap states.[26] We later showed that surface reduction can also occur upon photoexcitation of charge neutral QDs with suboptimal ligand coverage.[27]

However, these initial studies only start to scratch the surface of the problem. For instance, the energetics of surface reduction are expected to be significantly affected by the ligands present on the surface and the solvent surrounding the QD. In addition to the passivating effect discussed above, ligands can have an electrostatic effect that leads to an energetic shift of the band edges.[28–32] The dielectric constant of the surrounding solvent has been reported to influence the charge distribution over the QD.[33] Moreover, solvent molecules can essentially be seen as weakly binding ligands and may hence bind directly to the QD surface, an effect that is expected to be more pronounced for solvents with a lone electron pair, like acetonitrile or propylene carbonate.

The aim of the current work is to look closer at the influence of ligand passivation and solvent interaction on the stability of electron charged CdSe QDs. We use DFT calculations to model the effect of different X- and L-type ligands as well as solvents on the localization of charge on surface Cd sites. We show that X-type ligands can lead to significant shifts of the band edge energies but that the in-gap state related to reduced Cd largely shifts in the same direction. As a result, X-type ligands only weakly affect the energetics of surface reduction. In contrast, L-type ligands, binding directly to the Cd sites that are most prone to reduction, can greatly stabilize the QD and thus prevent surface reduction. Finally, polar solvents stabilize the delocalized charges in the CB more than in localized surface states, resulting in a further stabilization of the charged QD. These results can be used to design QDs and QD environments with strongly increased stability against surface reduction.

5.2 Results and Discussion

5.2.1 Model System

This study uses a zincblende $Cd_{68}Se_{55}Cl_{26}$ QD model that has been used as a basis for previous DFT studies.[26,27,34] In accordance with experiments, it contains an excess of cations,[35,36] compensated by the presence of 26 X-type chloride ligands, so that the complete system is charged balanced as defined by Voznyy et al.[37] Details regarding the substitution of different X-type ligands or addition of L-type ligands are given throughout the text where relevant for the discussion. The QDs were charged with extra electrons by adding neutral potassium atoms. Because of the very negative reduction potential, each potassium will inject one electron into the QD and then remain as a K^+ counterion.[26] Throughout this work, the number of excess electrons in the QD will be indicated by <n>. Further details of the model system have been reported previously.[34]

5.2.2 Energetics of Reduction

To introduce the problem of surface reduction,[26] Figure 5.1 shows the charging of the CdSe model system with an increasing amount of electrons. Figure 5.1B-i shows the density of states (DOS) at <n> = 1. Here, each horizontal line indicates a molecular orbital (MO). The length of each colored segment indicates the contribution of a specific element or atom.

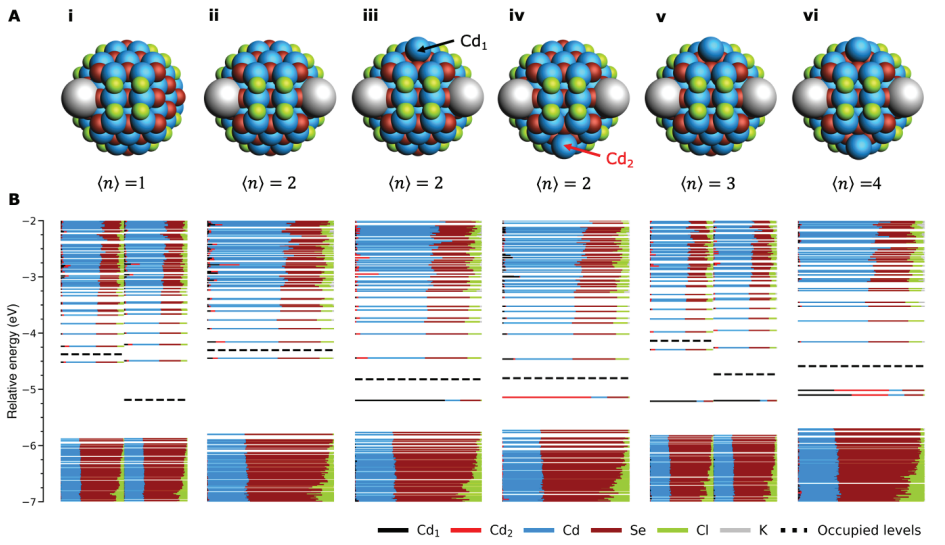

Figure 5.1. Reduction of a CdSe QD as a result of increasing electron charging. (A) Structure of the QD when 1–4 electrons are injected. The addition of one K^+ counterion per injected electron ensures the total system remains uncharged. For <n> = 3 and <n> = 4 the additional K^+ ions are not visible as they are located on the backside of the QD. (B) DOS for each of the structures. Each horizontal line corresponds to an MO. The length of each colored line segment indicates the relative contribution of an element or specific atom to that MO. For systems with an odd total number of electrons, unrestricted calculations were used. This results in two distinct densities of states for spin-up and spin-down orbitals, which are shown on the left and right side of the graph, respectively. MOs below the dashed line are filled, and MOs above the line do not contain electrons.

The levels above the dashed line are empty, whereas they are filled below the line. For all calculations with an odd total number of electrons (i.e., <n> = 1, 3, ...), spin-unrestricted calculations have been carried out. This allows the spin-up (α) and spin-down (β) orbitals to relax independently from each other, resulting in two distinct densities of states that are shown on the left and right side of Figure 5.1B-i, respectively. It can be seen that at <n> = 1 the electron remains delocalized in the conduction band (CB) and that no charge localization takes place. At <n> = 3 (see Figure 5.1A-v, we will discuss the effects at <n> = 2 soon), a Cd atom (indicated in black as Cd_1) is ejected from the (111) facet at the top of the QD. At the same time, an in-gap state appears in the bandgap, which is localized for ~75% on Cd_1 (see Figure 5.1B-v). This indicates that the excess electrons have localized on Cd_1, thus reducing it from $Cd^{\sim 2+}$ to $Cd^{\sim 0}$. At <n> = 4 (Figure 5.1-vi), a second Cd atom (indicated in red as Cd_2) is ejected from an (111) facet at the bottom of the QD, and a second in-gap state appears.

From these results, it becomes clear that a limited number of electrons can remain delocalized in the CB (<n> ≤ 1 for our model system) but that injection of too many charges (n ≥ 3) will result in charge localization and concomitant surface reduction and trap formation. For our model system, the transition between these two effects occurs at <n> = 2. We previously reported that two electrons still remain delocalized in the CB edge,[26] as also shown in Figure 5.1-ii. Here, we report that the system, after overcoming an energy barrier of ~0.07 eV (~2.9 k_BT at room temperature, see Figure A5.1), can lower its energy further by ~0.09 eV (~3.4 k_BT) by reduction and ejection of Cd_1 (see Figure 5.1-iii). Reduction of Cd_2, as show in Figure 5.1-iv, lowers the energy ~0.03 eV (1.1 k_BT). Throughout this paper, we will refer to the structure with two electrons delocalized in the CB as the QD in its "nonreduced" configuration. The structure with either of the Cd atoms ejected and the concomitant trap will be termed the "reduced" conformation of the QD. The energy change of the system upon its moving from the nonreduced to the reduced configuration will be defined as $\Delta E_R = E_{red} - E_{nonred}$, where E_{red} and E_{nonred} are the energies of the optimized QD in the reduced and nonreduced configuration, respectively.

We note that due to its complex potential energy surface, a QD can further lower its energy upon reduction through ensuing surface reconstructions. Ligand diffusion and subsequent formation of a Cd–Cd dimer or the diffusion of an ejected Cd over the (111) facet can both lower the energy of the QD in Figure 5.1 even further. Indeed, it is also expected that upon further charging of a QD, reduced Cd atoms will diffuse together and form metallic Cd clusters. However, the ejection of Cd from the (111) facet shown in Figure 5.1 constitutes the first step in surface reduction. Hence, throughout this paper we will use this surface configuration as a measure of the energetics of surface reduction.

Figure 5.2 shows the main processes and related energy changes that occur upon surface reduction: (i) ΔE_{trap}: trapping of the two CB electrons into an in-gap state; (ii) ΔE_{bind}: ejection of a Cd atom from the (111) facet; and (iii) ΔE_{solv}: readjustment of the surrounding solvent. As the two CB electrons lower their energy by moving from the CB to a lower-lying in-gap state, we define $\Delta E_{trap} = 2(E_{trap\text{-}state} - E_{CB})$, where $E_{trap\text{-}state}$ and E_{CB} are the energies of the in-gap level and CB, respectively. We posit that the ejection of the Cd atom from the surface has two main contributions: the energy penalty related to expulsion of the Cd from its lattice

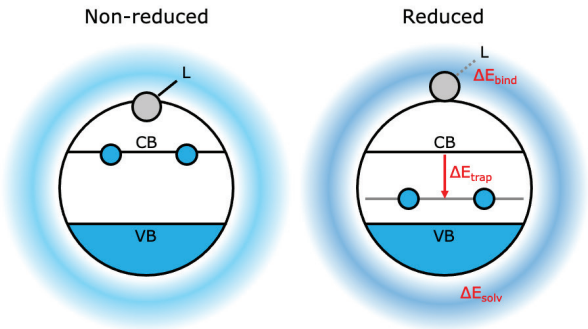

$$\Delta E_R = \Delta E_{trap} + \Delta E_{bind} + \Delta E_{solv} + \Delta E_{rest}$$

Figure 5.2. Summary of the main processes and related energy changes that occur upon charge localization to surface Cd in an electron charged CdSe QD. (i) ΔE_{trap}: during charge localization, the two CB electrons can lower their energy by falling into the Cd-localized in-gap state. (ii) ΔE_{bind}: concomitant ejection of the reduced Cd atom from the (111) facet will cost energy by disrupting the surrounding CdSe lattice and weakening the binding to ligands (here indicated as "L"). (iii) ΔE_{solv}: lastly, localization to surface Cd will change the charge distribution, leading to readjustments of the solvent interaction.

and the change in binding strength between the Cd atom and the surrounding ligands. As the ejection of the Cd atom is accompanied by subtle rearrangements of the surrounding CdSe lattice, an exact value for the first contribution is difficult to give. Throughout this work, we will therefore focus on the change in ligand binding. ΔE_{solv} refers to any dielectric effect or reorganization of the solvent that may occur when reduction leads to a different charge distribution over the QD.

We note that these energy terms are not entirely independent of each other and that more processes will influence ΔE_R. However, we will use the energy contributions specified above as handles, with which we can explain the complex effects seen in the DFT calculations in a chemically intuitive manner. Therefore, any other effects not specifically studied here, like subtle reorganizations of the ligand shell or slight changes in the valence band (VB) DOS, will be grouped into the term ΔE_{rest}. Hence, the final equation which we will use to interpret the results becomes $\Delta E_R = E_{red} - E_{nonred} = \Delta E_{trap} + \Delta E_{bind} + \Delta E_{solv} + \Delta E_{rest}$.

5.2.3 X-Type Ligand Induced Energy Shifts

To assess the effect of changing the X-type ligands on the stability of electron charged CdSe QDs, we successively change the 26 chloride ligands of the model system at <n> = 2 for bromide, iodide, formate, acetate, methanethiolate (which we will refer to as "thiolate" throughout the paper), and thiophenolate. In agreement with previous experimental and theoretical studies,[29,30] the ligand-dependent surface dipoles lead to energy shifts of the CB and VB edges, as shown in Figure 5.3A. We observe a downward shift of the energy levels of halogen X-type ligands compared to thiolate ligands, which is similar in trend and magnitude to the shifts reported by Brown et al. for these ligands on PbS QDs.[29] At first glance, one may expect that the QDs with higher-lying CB edges (i.e., the QDs with

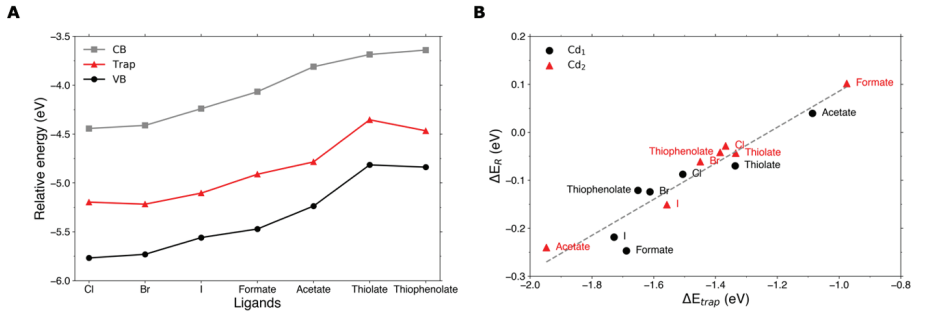

Figure 5.3. Effect of X-type ligands on the stability of electron charged CdSe QDs. (A) Energies of CB edge, in-gap level, and VB edge of $Cd_{68}Se_{55}X_{26}$ QDs in the reduced configuration at <n> = 2, with X = Cl, Br, I, etc., as indicated on the x-axis. (B) Correlation between ΔE_R and ΔE_{trap} with reduction of Cd_1 (black circles) or Cd_2 (red triangles). The gray dashed line is a linear fit to the data points.

5

thiolate ligands) are more prone to surface reduction than QDs with lower CB energies (i.e., the QDs with halide passivation). After all, the higher the CB energy, the higher the electrochemical potential of electrons in the CB edge and the easier it should become to reduce surface Cd. However, as shown in Figure A5.2, there is no clear correlation between CB energy and the energy gain upon reduction (ΔE_R). The reason for this, as also shown in Figure 5.3A, is that the energy of the in-gap state due to localization on surface Cd is shifted in the same direction as the band edges. We attribute this effect to the ligand-induced surface dipoles. Although localized, the electrons in the in-gap state will still feel the electrostatic effect of the ligands, and their energy will hence be pushed in the same direction as the band edges.

Yet, whereas the CB edge is completely delocalized over the entire QD and will hence be affected by an average of all ligands, the in-gap state is localized and will hence be mainly influenced by nearby ligands. This results in the energy of the in-gap state not exactly following the CB energy and hence in small differences in ΔE_{trap} (as defined in the previous section). Figure 5.3B shows there is a linear correlation between ΔE_{trap} and ΔE_R. The larger ΔE_{trap} and hence the more the CB electrons can lower their energy by relaxing into the in-gap state, the more favorable reduction becomes (i.e., ΔE_R becomes more negative). Figure 5.3B also shows that due to the local effects that influence ΔE_{trap}, there can be a significant energy difference between reducing and ejecting Cd_1 (black circles) and Cd_2 (red triangles). For acetate and formate, the effect of local electrostatics is even large enough to make reduction unfavorable (i.e., $\Delta E_R \geq 0$) for Cd_2, whereas $\Delta E_R < 0$ for reduction of Cd_1. Nevertheless, both the data sets of Cd_1 and Cd_2 reduction follow the linear correlation between ΔE_{trap} and ΔE_R. Lastly, it should be noted that the slope of the trend in Figure 5.3B is not 1, as one would expect from the definition of ΔE_R given in the introduction, but 0.38. This indicates that as ΔE_{trap} changes as a function of ligand or ejected Cd atom, other effects take place (which we have grouped under ΔE_{rest} in the previous section) in parallel, which changes the slope of the correlation between ΔE_R and ΔE_{trap}. These effects could be related to the reorganization of the CdSe lattice near

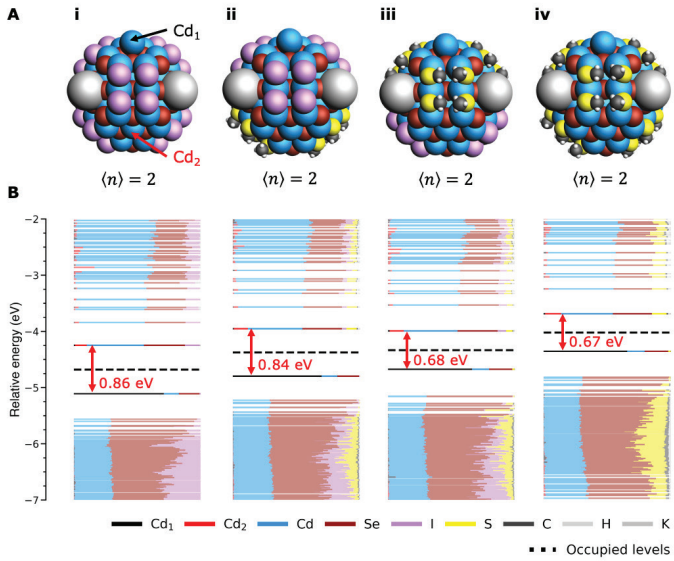

Figure 5.4. In-gap formation in QDs with mixed passivation. (A) Structure of QDs with (i) complete iodide passivation, (ii) iodide:thiolate = 50:50 passivation with the iodide ligands closest to Cd_1 (indicated in black), (iii) iodide:thiolate = 50:50 passivation with the thiolate ligands closest to Cd_1, and (iv) complete thiolate passivation. (B) DOS of each system. The energy difference between the CB edge and the in-gap state is indicated in red.

the reduced Cd, as the atoms closest to the ejected Cd are likely to experience a similar electrostatic effect of the ligands.

To further investigate the local effects of the ligand shell on ΔE_{trap}, we compare the DOS of fully iodide and thiolate passivated QDs with mixed iodide/thiolate systems in Figure 5.4. Figure 5.4-i shows the structure of a fully iodide passivated QD in the reduced configuration at <n> = 2. Analogous to Figure 5.1-iii, an in-gap state is present that is largely localized on Cd_1. Figure 5.4-iv shows the same behavior for a fully thiolate-capped QD, with the difference that the CB edges lies higher and the energy difference between the CB and the in-gap state is smaller than in Figure 5.4-i. Figures 5.4-ii/iii both show a QD with a mixed ligand passivation consisting of iodide:thiolate = 50:50. In Figure 5.4-ii the ligands closest to Cd_1 are iodides. In Figure 5.4-iii the thiolate ligands lie closest to Cd_1. A comparison of the two mixed-ligand systems shows that the CB edge has the same energy in both cases, indicating that the shift of the band edges depends on the average electrostatic effect of all the ligands. In contrast, the energy difference between the CB edge and the in-gap state is different in Figures 5.4B-ii and 5.4B-iii. In Figure 5.4B-ii, where Cd_1 is surrounded by iodide ligands, the in-gap state lies 0.84 eV below the CB edge, which is very similar to the value of 0.86 eV for the fully iodide passivated QD. In Figure 5.4B-iii, in which Cd_1 is surrounded by thiolates, the trap lies 0.68 eV below the CB, which closely resembles the 0.67 eV for the fully thiolate passivated system. This shows that the shift of the in-gap state is mainly influenced by the ligands that are close to the site where the wave

function localizes. These trends can be generalized to other mixed-passivated systems, as shown for Cl/I in Figure A5.3.

To summarize, X-type ligand exchange causes the band edges and the in-gap state to move largely in parallel. Only subtle changes in the local environment of the trap state influence ΔE_{trap} and by extension ΔE_R. Although X-type ligands can hence only play a minor role in making electron charged QDs more stable against intrinsic reduction (i.e., reduction of surface Cd), they are expected to have a large effect on the importance of reduction reactions with external impurities. Contrary to the in-gap states, the reduction potentials of external impurities (e.g., O_2 or H_2O)[23,38,39] are not expected to shift along with the band edge energies. Hence, X-type ligands that lead to a lower CB edge (higher VB edge) may still lead to the more stable electron charging (hole charging) of the QDs.

5.2.4 Direct Ligand Binding

Next, we investigate the effect of ligands directly binding to Cd_1 or Cd_2 on the energetics of surface reduction. For that we bind a range of L-type ligands (aniline, methylamine, and acetonitrile) as well as hexane and toluene directly to Cd_1 and Cd_2. As argued in the introduction, compounds commonly considered as solvent can also be seen as weakly binding ligands. Although hexane and toluene do not have a lone pair and hence are not L-type ligands, they can still interact, albeit weakly, with the QD surface through dispersion forces. As summarized in Figure A5.4, we assess the effect of direct ligand binding to the QD by adding one ligand to both Cd_1 and Cd_2. By removing one of the ligands, we can compute the binding energy to the Cd atom by using that $\Delta E_{bind} = E_{QD\text{-}2L} - E_{QD\text{-}1L} - E_L$, where $E_{QD\text{-}2L}$ stands for the energy of the QD with one ligand to both Cd_1 and Cd2, $E_{QD\text{-}1L}$ for the QD with one ligand attached to either Cd_1 or Cd_2, and E_L for the energy of a loose ligand. We passivate both Cd sites at the same time to prevent the situation where passivation of one Cd site will simply lead to the CB electrons localizing on the other Cd atom.

As summarized in Table A5.1, the binding energy of the ligands to the nonreduced QD ranges from ~0.1 eV (hexane) to ~0.7 eV (methylamine), with no significant differences between the binding to Cd_1 and Cd_2. As defined by Green,[40] L-type ligands (a Lewis base) bind to Cd (a Lewis acid) by donation of an electron pair.[35] If a Cd atom is reduced from $Cd^{\sim 2+}$ to $Cd^{\sim 0}$, this interaction becomes much less favorable. Indeed, upon reduction of the surface Cd sites, the binding energy decreases with an average of ~90% for the three L-type ligands tested here. In contrast, the binding energy of hexane and toluene, which could only bind to Cd with weak dispersion forces from the start, is on average reduced by ~65% (see Table A5.1).

Clearly, the reduction in binding strength with the ligands forms an energy penalty the system has to pay to localize charge on surface Cd. To quantify this effect, we define $\Delta E_{bind} = E_{bind,red} - E_{bind,nonred}$, where $E_{bind,red}$ and $E_{bind,nonred}$ are the binding energy of the ligands to the QD in its reduced and nonreduced configuration, respectively. Figure 5.5 shows that there is a linear correlation between ΔE_{bind} and ΔE_R. Although hexane and toluene bind only weakly to the QD and hence increase ΔE_R by a relatively small amount, it is already enough to ensure that $\Delta E_R \geq 0$ and hence make charge localization unfavorable. The L-type amine ligands bind stronger and hence increase ΔE_R even further. The linear

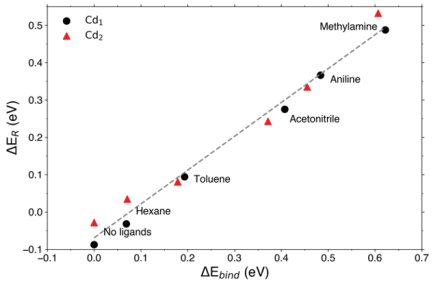

Figure 5.5. Correlation between ΔE_R and ΔE_{bind} for electron charged CdSe QDs with different ligands binding directly to Cd_1 and Cd_2, as determined with the reduction of Cd_1 (black circles) and Cd_2 (red triangles). The gray dashed line is a linear fit to the data points.

fit to the data indicated by the dashed gray line in Figure 5.5 has a slope of 0.91, indicating that the direct binding of ligands has a larger effect on ΔE_R than changing the X-type ligands (as shown in Figure 5.3B). However, as the slope is not 1, other effects must take place in parallel. For instance, as shown in Figure A5.5, we found that ΔE_{trap} becomes less negative with increasing ΔE_{bind}. We conclude that the addition of L-type ligands to the surface is a powerful tool to enhance the stability of electron charged QDs and that even weakly binding solvent molecules can help stabilize the system.

Although no direct experimental evidence is available for the relation between surface reduction and L-type ligand passivation, there are various observation in the literature that support this conclusion. First, it is well-known that addition of L-type ligands can enhance the PL QY of II–VI QDs[5] and that L-type ligands in the form of amines or phosphines are required for near-unity PL QY, even in core–shell QDs.[41,42] There is, however, no clear atomistic picture of the trap level that is passivated by L-type ligands, since these should bind to undercoordinated surface Cd ions, which should theoretically not expose states in the bandgap.[34] One explanation is that the photoexcitation of CdSe QDs results in surface reduction unless L-type ligands are employed to stabilize the surface Cd ions.[27]

Perhaps more direct evidence could come from electrochemical studies of CdSe QD films. It is well-known that treatment of films of CdSe QDs with molecules like 1,7-heptanediamine increases the stability and reversibility in electrochemical measurements. Yu et al.[43] showed in a comparison of various surface treatments that cyclic voltammograms of CdSe QD films treated with 1-butylamine, and especially 1,7-heptanediamine, exhibit more reversible electron charging and discharging than films treated in other ways. This could reflect the higher stability of amine passivated CdSe QDs against surface reduction, although it is difficult to draw hard conclusions, since such treatments will also change other properties of the QD films, including an increase in the electron mobility which will also affect the shape of the cyclic voltammograms. In addition, the addition of ligands like 1,7-heptanediamine will result in the stripping of Z-type ligands, in addition to adding L-type ligands, changing the surface composition in multiple ways.[35,44]

5.2.5 Solvent Effects

In the previous section, we discussed the direct bonding interaction between solvent molecules and the QD. However, solvents also screen the charge distribution of the QD. In this section, we model this dielectric effect by adding an implicit solvent as implemented in the COSMO model in ADF.[45] Inclusion of the solvent lowers the energy of the system by the solvation energy E_{solv} (i.e., with $E_{solv} < 0$). Following the definition used in the COSMO model,[45] E_{solv} includes the stabilizing contribution of the electrostatic interaction between the QD and the solvent, as well as the energy penalty of creating a solute cavity in the continuum, but excludes changes in the energy of the solute (i.e., the QD itself). To quantify the change in E_{solv} upon charge localization and assess its effect on ΔE_R, we define $\Delta E_{solv} = E_{solv,red} - E_{solv,nonred}$, where $E_{solv,red}$ and $E_{solv,nonred}$ are the solvation energy of the QD in its reduced and nonreduced conformation, respectively. As can be seen in Figure 5.6A, in all solvents the QD is stabilized more in its nonreduced form ($E_{solv,nonred}$) than in its reduced configuration ($E_{solv,red}$). Moreover, ΔE_{solv} becomes more positive with increasing dielectric constant of the solvent. We infer that the solvation effect of delocalized CB electrons is larger than of electrons localized on surface Cd. This can be understood by considering that the CB wave function extends over more of the QD surface than the localized trap level, causing a larger solvation effect in the former case.

Figure 5.6B shows the correlation between ΔE_{solv} and ΔE_R for a chloride passivated QD in increasingly polar solvents. It can be seen that for more positive values of ΔE_{solv} reduction becomes less favorable (i.e., ΔE_R increases), a trend which also holds for various X-type ligands (see Figure A5.6B). However, as was the case for the effect of X-type ligands discussed previously, the slope of the linear fit is not 1, as one would expect. Moreover, although the reduction of Cd_1 and Cd_2 depends on ΔE_{solv} in the same way (with slopes of 0.28 and 0.26, respectively), the trends do show an offset that was not present in Figures 5.3B and 5.5. This shows that while the change in ΔE_{solv} clearly affects ΔE_R, there are additional energy terms that partially compensate for the effect. For instance, we found for the chloride passivated QD that ΔE_{trap} is not constant when changing the solvent but changes with ΔE_{solv} (see Figure A5.6A). This partially explains the small slope in Figure 5.6B, although there must be additional effects that are currently not completely understood. The overall trend, however, clearly shows that the stability of electron-charged QDs increases with the dielectric constant of the solvent.

The calculations presented here were performed on CdSe QDs only. In a previous paper,[26] we showed results for charging of various II–VI QDs (CdS, CdSe, CdTe, ZnS, ZnSe, and ZnTe) using a single type of surface coverage and without any solvent interaction. We showed that charging of Zn chalcogenide QDs is stable up to at least four electrons, while for none of the Cd-chalcogenide QDs this is the case. This is attributed to the higher intrinsic stability of Zn^{2+} against reduction (E° in water is −0.76 V vs NHE) than of Cd^{2+} against reduction (E° = −0.40 V vs NHE). We expect that the trends reported here for X- and L-type ligands and solvent polarity also hold for other II–VI QDs, on top of the differences in intrinsic stability against surface reduction.

5.3 Conclusions

In conclusion, DFT calculations have been used to study the effects of ligand passivation

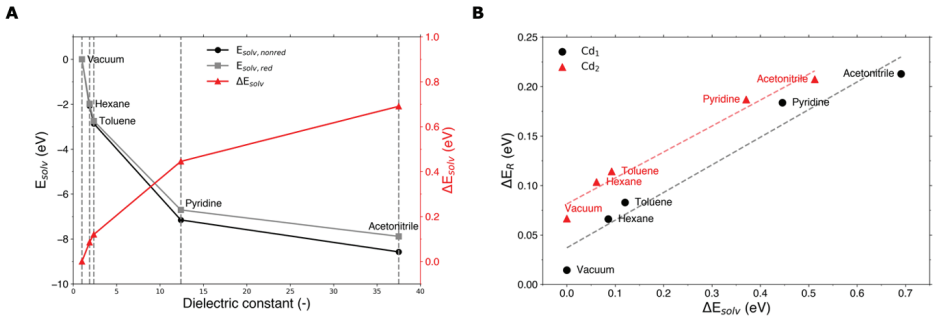

Figure 5.6. Effects of inclusion of implicit solvents on electron charged CdSe QDs. (A) Relation between the dielectric constant of the solvent and $E_{solv,nonred}$, $E_{solv,red}$, and ΔE_{solv}. (B) Relation between ΔE_R and ΔE_{solv} when changing the solvent for a chloride passivated QD at <n> = 2, when reducing Cd_1 (black circles) and Cd_2 (red triangles). The gray and light red dashed lines are linear fits to the data points.

and solvent interaction on the stability of electron charged CdSe QDs. We show that X-type ligands can lead to significant shifts of the band edges. However, as the in-gap state related to metallic Cd moves largely in parallel with the band edges, X-type ligands only have a minor effect on the energetics of surface reduction. Binding L-type ligands directly to the most labile Cd sites was found to greatly enhance the stability of the electron charged QDs. The loss in binding energy upon reduction of the surface creates an energy penalty that is larger than the energy gain related to charge localization, meaning that reduction of the Cd atom is no longer favorable. Lastly, we show that electron charged QDs can be further stabilized by increasing the polarity of the solvent. These results show that the nature of the ligand shell and the surrounding solvent significantly affect the energetics of surface reduction reactions, providing valuable strategies for improving the stability of charged QDs.

5.4 Methods

Calculations on systems with different X-type ligands or explicit ligand binding were performed at the DFT level by using a PBE exchange-correlation functional[46] and double-ζ basis set, as implemented in the CP2K quantum chemistry software package.[47] GTH pseudopotentials incorporate the effective core potentials to account for scalar relativistic effects. Geometry optimizations were performed at 0 K in the gas phase. We use the following criteria of convergence for the optimizations: max_force: 4.50×10^{-4} Ha/Bohr; rms_force: 3.0×10^{-4} Ha/Bohr; max_dr: 3.0×10^{-3} Bohr; rms_dr: 1.5×10^{-3} Bohr. Unrestricted spin calculations were used for systems with an odd total number of electrons (i.e., <n> = 1, 3, ...). Solvation effects were studied with the COSMO model[45] as implemented in the ADF package[48] by using a TZP basis set and PBE exchange-correlation functional in combination with a large frozen core. Scalar relativistic effects were included through the zeroth-order regular approximation (ZORA).[49–51] Predefined solvents are used within the COSMO model with the default parameters.

References

1. Hartley, C. L., Kessler, M. L. & Dempsey, J. L. Molecular-Level Insight into Semiconductor Nanocrystal Surfaces. J. Am. Chem. Soc. 143, 1251–1266 (2021).
2. Donegá, C. de M. Synthesis and properties of colloidal heteronanocrystals. Chem. Soc. Rev. 40, 1512–1546 (2011).
3. Giansante, C. & Infante, I. Surface Traps in Colloidal Quantum Dots: A Combined Experimental and Theoretical Perspective. J. Phys. Chem. Lett. 8, 5209–5215 (2017).
4. Boles, M. A., Ling, D., Hyeon, T. & Talapin, D. V. The surface science of nanocrystals. Nat. Mater. 15, 141–153 (2016).
5. Kirkwood, N., Monchen, J. O. V., Crisp, R. W., Grimaldi, G., Bergstein, H. A. C., du Fossé, I., van der Stam, W., Infante, I. & Houtepen, A. J. Finding and Fixing Traps in II–VI and III–V Colloidal Quantum Dots: The Importance of Z-Type Ligand Passivation. J. Am. Chem. Soc. 140, 15712–15723 (2018).
6. Katsiev, K., Ip, A. H., Fischer, A., Tanabe, I., Zhang, X., Kirmani, A. R., Voznyy, O., Rollny, L. R., Chou, K. W., Thon, S. M., et al. The Complete In-Gap Electronic Structure of Colloidal Quantum Dot Solids and Its Correlation with Electronic Transport and Photovoltaic Performance. Adv. Mater. 26, 937–942 (2014).
7. Ip, A. H., Thon, S. M., Hoogland, S., Voznyy, O., Zhitomirsky, D., Debnath, R., Levina, L., Rollny, L. R., Carey, G. H., Fischer, A., et al. Hybrid passivated colloidal quantum dot solids. Nat. Nanotechnol. 7, 577–582 (2012).
8. Kagan, C. R., Lifshitz, E., Sargent, E. H. & Talapin, D. V. Building devices from colloidal quantum dots. Science 353, aac5523–aac5523 (2016).
9. Knowles, K. E., Tice, D. B., McArthur, E. A., Solomon, G. C. & Weiss, E. A. Chemical Control of the Photoluminescence of CdSe Quantum Dot–Organic Complexes with a Series of Para-Substituted Aniline Ligands. J. Am. Chem. Soc. 132, 1041–1050 (2010).
10. Tang, J., Kemp, K. W., Hoogland, S., Jeong, K. S., Liu, H., Levina, L., Furukawa, M., Wang, X., Debnath, R., Cha, D., et al. Colloidal-quantum-dot photovoltaics using atomic-ligand passivation. Nat. Mater. 10, 765–771 (2011).
11. Calvin, J. J., Swabeck, J. K., Sedlak, A. B., Kim, Y., Jang, E. & Alivisatos, A. P. Thermodynamic Investigation of Increased Luminescence in Indium Phosphide Quantum Dots by Treatment with Metal Halide Salts. J. Am. Chem. Soc. 142, 18897–18906 (2020).
12. van der Stam, W., Grimaldi, G., Geuchies, J. J., Gudjonsdottir, S., van Uffelen, P. T., van Overeem, M., Brynjarsson, B., Kirkwood, N. & Houtepen, A. J. Electrochemical Modulation of the Photophysics of Surface-Localized Trap States in Core/Shell/(Shell) Quantum Dot Films. Chem. Mater. 31, 8484–8493 (2019).
13. Reiss, P., Protière, M. & Li, L. Core/Shell Semiconductor Nanocrystals. Small 5, 154–168 (2009).
14. Shim, M., Wang, C., Norris, D. J. & Guyot-Sionnest, P. Doping and Charging in Colloidal Semiconductor Nanocrystals. MRS Bull. 26, 1005–1008 (2001).
15. Mocatta, D., Cohen, G., Schattner, J., Millo, O., Rabani, E. & Banin, U. Heavily Doped Semiconductor Nanocrystal Quantum Dots. Science 332, 77–81 (2011).
16. Pietryga, J. M., Park, Y.-S., Lim, J., Fidler, A. F., Bae, W. K., Brovelli, S. & Klimov, V. I. Spectroscopic and Device Aspects of Nanocrystal Quantum Dots. Chem.

Rev. 116, 10513–10622 (2016).
17. Lim, J., Park, Y.-S., Wu, K., Yun, H. J. & Klimov, V. I. Droop-Free Colloidal Quantum Dot Light-Emitting Diodes. Nano Lett. 18, 6645–6653 (2018).
18. Chang, J. H., Park, P., Jung, H., Jeong, B. G., Hahm, D., Nagamine, G., Ko, J., Cho, J., Padilha, L. A., Lee, D. C., et al. Unraveling the Origin of Operational Instability of Quantum Dot Based Light-Emitting Diodes. ACS Nano 12, 10231–10239 (2018).
19. Ganesan, A., Houtepen, A. & Crisp, R. Quantum Dot Solar Cells: Small Beginnings Have Large Impacts. Appl. Sci. 8, 1867 (2018).
20. Kershaw, S. V., Jing, L., Huang, X., Gao, M. & Rogach, A. L. Materials aspects of semiconductor nanocrystals for optoelectronic applications. Mater. Horizons 4, 155–205 (2017).
21. Carey, G. H., Abdelhady, A. L., Ning, Z., Thon, S. M., Bakr, O. M. & Sargent, E. H. Colloidal Quantum Dot Solar Cells. Chem. Rev. 115, 12732–12763 (2015).
22. Liu, M., Yazdani, N., Yarema, M., Jansen, M., Wood, V. & Sargent, E. H. Colloidal quantum dot electronics. Nat. Electron. 4, 548–558 (2021).
23. Schimpf, A. M., Gunthardt, C. E., Rinehart, J. D., Mayer, J. M. & Gamelin, D. R. Controlling Carrier Densities in Photochemically Reduced Colloidal ZnO Nanocrystals: Size Dependence and Role of the Hole Quencher. J. Am. Chem. Soc. 135, 16569–16577 (2013).
24. Gerischer, H. On the Stability of Semiconductor Electrodes Against Photodecomposition. J. Electroanal. Chem. Interfacial Electrochem. 82, 133–143 (1977).
25. Nadjo, L. The characterization and behaviour of n-and p-CdTe electrodes in acetonitrile solutions. J. Electroanal. Chem. Interfacial Electrochem. 108, 29–47 (1980).
26. du Fossé, I., ten Brinck, S., Infante, I. & Houtepen, A. J. Role of Surface Reduction in the Formation of Traps in n-Doped II–VI Semiconductor Nanocrystals: How to Charge without Reducing the Surface. Chem. Mater. 31, 4575–4583 (2019).
27. du Fossé, I., Boehme, S. C., Infante, I. & Houtepen, A. J. Dynamic Formation of Metal-Based Traps in Photoexcited Colloidal Quantum Dots and Their Relevance for Photoluminescence. Chem. Mater. 33, 3349–3358 (2021).
28. Grimaldi, G., van den Brom, M. J., du Fossé, I., Crisp, R. W., Kirkwood, N., Gudjonsdottir, S., Geuchies, J. J., Kinge, S., Siebbeles, L. D. A. & Houtepen, A. J. Engineering the Band Alignment in QD Heterojunction Films via Ligand Exchange. J. Phys. Chem. C 123, 29599–29608 (2019).
29. Brown, P. R., Kim, D., Lunt, R. R., Zhao, N., Bawendi, M. G., Grossman, J. C. & Bulović, V. Energy Level Modification in Lead Sulfide Quantum Dot Thin Films through Ligand Exchange. ACS Nano 8, 5863–5872 (2014).
30. Kroupa, D. M., Vörös, M., Brawand, N. P., McNichols, B. W., Miller, E. M., Gu, J., Nozik, A. J., Sellinger, A., Galli, G. & Beard, M. C. Tuning colloidal quantum dot band edge positions through solution-phase surface chemistry modification. Nat. Commun. 8, 15257 (2017).
31. Yang, S., Prendergast, D. & Neaton, J. B. Tuning Semiconductor Band Edge Energies for Solar Photocatalysis via Surface Ligand Passivation. Nano Lett. 12, 383–388 (2012).

32. Shalom, M., Rühle, S., Hod, I., Yahav, S. & Zaban, A. Energy Level Alignment in CdS Quantum Dot Sensitized Solar Cells Using Molecular Dipoles. J. Am. Chem. Soc. 131, 9876–9877 (2009).
33. Liu, H., Brozek, C. K., Sun, S., Lingerfelt, D. B., Gamelin, D. R. & Li, X. A Hybrid Quantum-Classical Model of Electrostatics in Multiply Charged Quantum Dots. J. Phys. Chem. C 121, 26086–26095 (2017).
34. Houtepen, A. J., Hens, Z., Owen, J. S. & Infante, I. On the Origin of Surface Traps in Colloidal II–VI Semiconductor Nanocrystals. Chem. Mater. 29, 752–761 (2017).
35. Anderson, N. C., Hendricks, M. P., Choi, J. J. & Owen, J. S. Ligand Exchange and the Stoichiometry of Metal Chalcogenide Nanocrystals: Spectroscopic Observation of Facile Metal-Carboxylate Displacement and Binding. J. Am. Chem. Soc. 135, 18536–18548 (2013).
36. Greaney, M. J., Couderc, E., Zhao, J., Nail, B. A., Mecklenburg, M., Thornbury, W., Osterloh, F. E., Bradforth, S. E. & Brutchey, R. L. Controlling the Trap State Landscape of Colloidal CdSe Nanocrystals with Cadmium Halide Ligands. Chem. Mater. 27, 744–756 (2015).
37. 3oznyy, O., Zhitomirsky, D., Stadler, P., Ning, Z., Hoogland, S. & Sargent, E. H. A Charge-Orbital Balance Picture of Doping in Colloidal Quantum Dot Solids. ACS Nano 6, 8448–8455 (2012).
38. Gudjonsdottir, S., Koopman, C. & Houtepen, A. J. Enhancing the stability of the electron density in electrochemically doped ZnO quantum dots. J. Chem. Phys. 151, 144708 (2019).
39. Rinehart, J. D., Schimpf, A. M., Weaver, A. L., Cohn, A. W. & Gamelin, D. R. Photochemical Electronic Doping of Colloidal CdSe Nanocrystals. J. Am. Chem. Soc. 135, 18782–18785 (2013).
40. Green, M. L. H. A new approach to the formal classification of covalent compounds of the elements. J. Organomet. Chem. 500, 127–148 (1995).
41. Pu, C. & Peng, X. To Battle Surface Traps on CdSe/CdS Core/Shell Nanocrystals: Shell Isolation versus Surface Treatment. J. Am. Chem. Soc. 138, 8134–8142 (2016).
42. Zhou, J., Zhu, M., Meng, R., Qin, H. & Peng, X. Ideal CdSe/CdS Core/Shell Nanocrystals Enabled by Entropic Ligands and Their Core Size-, Shell Thickness-, and Ligand-Dependent Photoluminescence Properties. J. Am. Chem. Soc. 139, 16556–16567 (2017).
43. Yu, D., Wehrenberg, B. L., Jha, P., Ma, J. & Guyot-Sionnest, P. Electronic transport of n-type CdSe quantum dot films: Effect of film treatment. J. Appl. Phys. 99, 104315 (2006).
44. Sandeep, C. S. S., Azpiroz, J. M., Evers, W. H., Boehme, S. C., Moreels, I., Kinge, S., Siebbeles, L. D. A., Infante, I. & Houtepen, A. J. Epitaxially connected PbSe quantum-dot films: Controlled neck formation and optoelectronic properties. ACS Nano 8, 11499–11511 (2014).
45. Pye, C. C. & Ziegler, T. An implementation of the conductor-like screening model of solvation within the Amsterdam density functional package. Theor. Chem. Acc. 101, 396–408 (1999).
46. Perdew, J. P., Burke, K. & Ernzerhof, M. Generalized Gradient Approximation

Made Simple. Phys. Rev. Lett. 77, 3865–3868 (1996).
47. Hutter, J., Iannuzzi, M., Schiffmann, F. & VandeVondele, J. cp2k: atomistic simulations of condensed matter systems. Wiley Interdiscip. Rev. Comput. Mol. Sci. 4, 15–25 (2014).
48. te Velde, G., Bickelhaupt, F. M., Baerends, E. J., Fonseca Guerra, C., van Gisbergen, S. J. A., Snijders, J. G. & Ziegler, T. Chemistry with ADF. J. Comput. Chem. 22, 931–967 (2001).
49. van Lenthe, E., Ehlers, A. & Baerends, E.-J. Geometry optimizations in the zero order regular approximation for relativistic effects. J. Chem. Phys. 110, 8943–8953 (1999).
50. Lenthe, E. van, Baerends, E. J. & Snijders, J. G. Relativistic regular two-component Hamiltonians. J. Chem. Phys. 99, 4597–4610 (1993).
51. van Lenthe, E., Baerends, E. J. & Snijders, J. G. Relativistic total energy using regular approximations. J. Chem. Phys. 101, 9783–9792 (1994).

Appendix

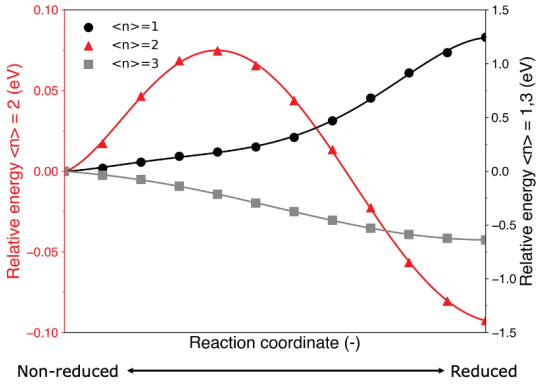

Figure A5.1. Total energy of a CdSe QD at <n> = 1, 2, 3 when moving from the non-reduced (left) to the reduced configuration (right). The non-reduced configurations for <n> = 1, 2 are obtained from a geometry optimization. As the non-reduced configuration at <n> = 3 is not stable (i.e., its optimization immediately leads to the reduced configuration), it was estimated using the coordinates of the non-reduced QD at <n> = 2. Likewise, the reduced configuration at <n> = 1 was estimated from the reduced configuration at <n> = 2. The intermediate states were produced by linear interpolation of the coordinates of all the atoms between the non-reduced and reduced geometry. It can be seen that moving to the reduced configuration leads to a monotonic energy increase for <n> = 1, and a monotonic decrease for <n> = 3. Although reduction also lowers the total energy at <n> = 2, an activation barrier of ~0.07 eV (~2.9 k_BT) prevents a geometry optimization started from the non-reduced configuration from finding the reduced structure.

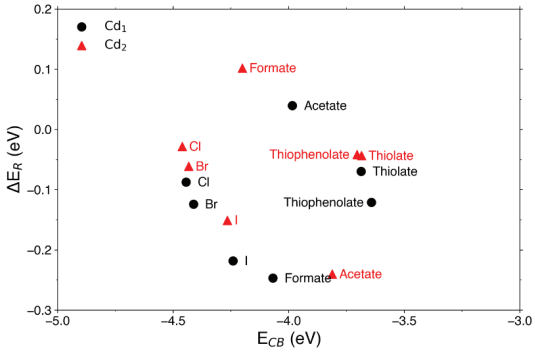

Figure A5.2. Correlation between ΔE_R and the position of the CB edge (E_{CB}) with reduction of Cd_1 (black circles) or Cd_2 (red triangles). Contrary to the linear trend between ΔE_R and ΔE_{trap} as shown in Figure 5.3B in the main text, no clear trend can be observed between ΔE_R and E_{CB}.

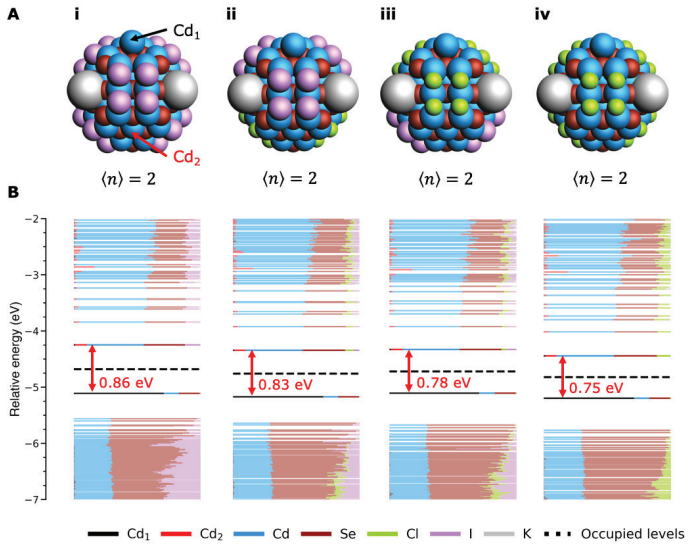

Figure A5.3. In-gap formation in QDs with mixed passivation. (A) Structure of QDs with (i) complete iodide passivation, (ii) iodide:chloride = 50:50 passivation with the iodide ligands closest to Cd_1 (indicated in black), (iii) iodide:chloride = 50:50 passivation with the chloride ligands closest to Cd_1, and (iv) complete chloride passivation. (B) DOS of each system. The energy difference between the CB edge and the in-gap state has been indicated in red.

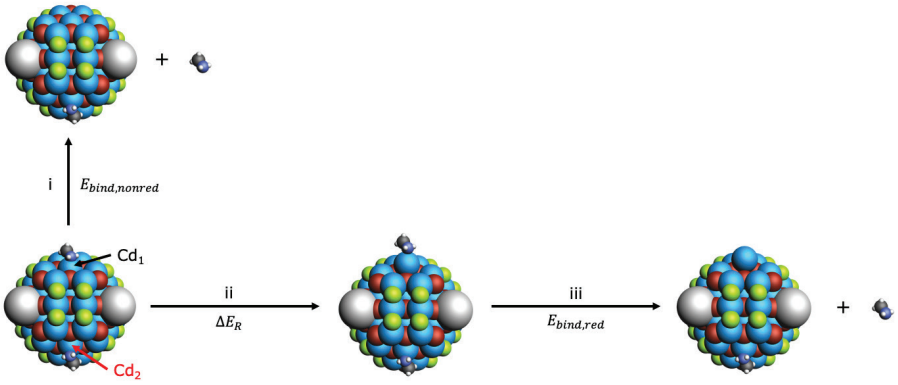

Figure A5.4. Schematic overview of how the binding energy was calculated. As shown in the bottom left corner, both Cd_1 and Cd_2 (indicated with the black and red arrows, respectively) are passivated by direct binding of a ligand. (i) The binding energy of the ligand to Cd_1 ($E_{bind,nonred}$) is computed by calculating the energy of the separate ligand and QD. (ii) The energy difference upon reduction of Cd_1 (ΔE_R) is calculated by optimizing the QD in its reduced structure. (iii) Computation of the energy of the separate ligand and reduced QD gives the binding energy to the reduced Cd_1 site ($E_{bind,red}$). A completely analogous procedure was used to compute the binding energies to Cd_2.

Table A5.1. Overview of the binding energy (in eV) of each ligand to Cd_1 and Cd_2 before and after reduction.

	Cd_1			Cd_2		
Ligand	$E_{bind,nonred}$	$E_{bind,red}$	ΔE_{bind}	$E_{bind,nonred}$	$E_{bind,red}$	ΔE_{bind}
Hexane	-0.12	-0.06	0.07	-0.13	-0.06	0.07
Toluene	-0.24	-0.05	0.19	-0.24	-0.07	0.18
Acetonitrile	-0.43	-0.02	0.41	-0.43	-0.05	0.37
Aniline	-0.50	-0.02	0.48	-0.50	-0.04	0.46
Methylamine	-0.68	-0.06	0.62	-0.69	-0.08	0.61

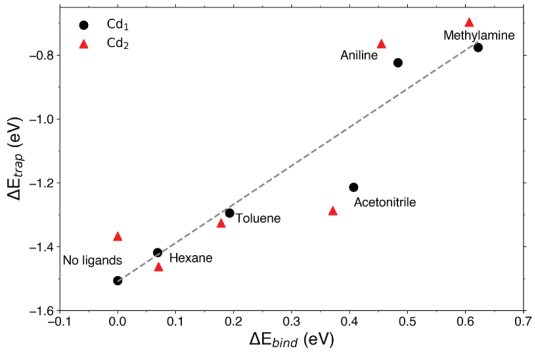

Figure A5.5. Correlation between ΔE_{trap} and ΔE_{bind} for electron charged CdSe QDs with different ligands binding directly to Cd_1 and Cd_2, as determined with the reduction of Cd_1 (black circles) and Cd_2 (red triangles). The grey dashed line is a linear fit to the data points. The linear correlation between ΔE_{trap} and ΔE_{bind} suggests that both factors influence the overall ΔE_R.

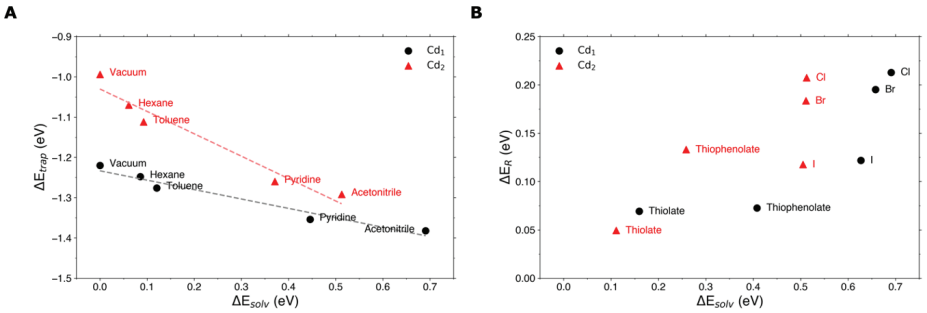

Figure A5.6. Effects of inclusion of implicit solvents on electron charged CdSe QDs. (A) Relation between ΔE_{trap} and ΔE_{solv} when changing the solvent of a chloride passivated QD at <n> = 2, when reducing Cd_1 (black circles) and Cd_2 (red triangles). The grey and light red dashed lines are linear fits to the data points. As in Figure A5.5, the linear correlation suggests that both ΔE_{trap} and ΔE_{solv} influence the overall ΔE_R. (B) Relation between ΔE_R and ΔE_{solv} in acetonitrile for different X-type ligand passivations.

6

Limits of Defect Tolerance in Perovskite Nanocrystals

Effect of Local Electrostatic Potential on Trap States

One of the most promising properties of lead halide perovskite nanocrystals (NCs) is their defect tolerance. It is often argued that, due to the electronic structure of the conduction and valence bands, undercoordinated ions can only form localized levels inside or close to the band edges (i.e., shallow traps). However, multiple studies have shown that dangling bonds on surface Br^- can still create deep trap states. Here, we argue that the traditional picture of defect tolerance is incomplete and that deep Br^- traps can be explained by considering the local environment of the trap states. Using density functional theory calculations, we show that surface Br^- sites experience a destabilizing local electrostatic potential that pushes their dangling orbitals into the bandgap. These deep trap states can be electrostatically passivated through the addition of ions that stabilize the dangling orbitals via ionic interactions without covalently binding to the NC surface. These results shed light on the formation of deep traps in perovskite NCs and provide strategies to remove them from the bandgap.

This chapter is based on: Indy du Fossé, Jence T. Mulder, Guilherme Almeida, Anne G. M. Spruit, Ivan Infante, Ferdinand C. Grozema, Arjan J. Houtepen. Journal of the American Chemical Society, 2022, 144 (25), 11059-11063

6.1 Introduction

As a result of their high photoluminescence quantum yield, facile synthesis, narrow emission width, and tunable bandgap across the visible spectrum depending on the halide composition,[1,2] lead halide perovskite nanocrystals (NCs) are of great interest for application in devices.[3–5] For instance, they can be used as a color-converting phosphor,[1,6] lasing material,[7–9] absorber layer in solar cells,[10–13] and emitter in light-emitting diodes.[1,6,14] The high performance of lead halide perovskite-based materials is often linked to their defect tolerance, which is attributed to a combination of the high formation energy of defects[15,16] and the electronic structure of the conduction (CB) and valence bands (VB).[1,2,17] The latter point is illustrated in Figure 6.1, where the electronic structure of perovskites is compared with that of common "defect-intolerant" semiconductors, which include II–VI (e.g., CdSe) and III–V (e.g., InP) materials. Taking CdSe as an example, as shown in Figure 6.1, the bandgap is formed between bonding states (the VB) and antibonding states (the CB). As a result, nonbonding orbitals from undercoordinated atoms are likely to lie in the bandgap. This has indeed been shown to be the case for two-coordinated chalcogenides.[18–20] However, the spherical symmetry of the s orbital of the metal ensures it is split out of the bandgap, even if the metal is undercoordinated.[18] In lead halide

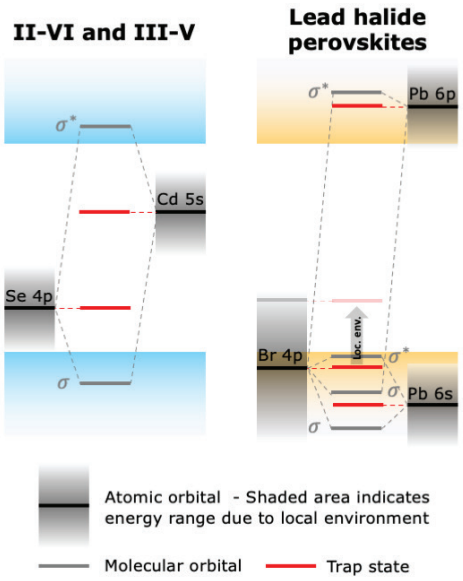

Figure 6.1. Electronic structure of (left) defect-intolerant materials, such as CdSe, and (right) defect-tolerant materials, like $CsPbBr_3$. In defect-intolerant materials, the VB and CB are respectively composed of bonding and antibonding orbitals, causing nonbonding atomic orbitals (AOs, black) to form deep trap states (red). In defect-tolerant materials, both the VB and CB are formed by antibonding orbitals, so that nonbonding AOs are expected to lie close to or in the bands. However, differences in the local environment of each atom can lead to shifts of the energy of the AOs (gray-shaded areas), thus pushing trap states into the bandgap even in defect-tolerant materials, as illustrated by the gray arrow.

perovskites (see the example of $CsPbBr_3$ in Figure 6.1), the top of the VB consists of the antibonding interaction between the Br 4p and the Pb 6s orbitals, while the antibonding interaction between Br 4p and Pb 6p orbitals forms the CB edge. As both band edges consist of antibonding orbitals, nonbonding orbitals are expected to either lie within the bands or form shallow traps.[1,2,17]

However, computational studies on perovskite NCs show that excess surface halide ions[16,21] or stripping of the perovskite surface[22] can still create deep trap states in the form of undercoordinated surface Br^-, suggesting that the above description of defect tolerance is incomplete. In the current work, we use density functional theory (DFT) calculations on $CsPbBr_3$ NCs to show that this apparent discrepancy can be understood by taking the local environment of the undercoordinated halide ions into account. Although the energy of the Br 4p orbitals lies within the VB in the perovskite bulk, a Br^- ion at the surface experiences a different local electrostatic potential. If the electrostatic potential is destabilizing, it can push the nonbonding Br^- orbitals into the bandgap; if it is stabilizing, for instance due to the presence of ionic species, dangling orbitals can be pushed further into the VB. The resulting spread in the energy of atomic orbitals (AOs) is schematically illustrated in Figure 6.1 by the gray-shaded areas.

6.2 Results and Discussion

From TEM images and X-ray diffraction, it is known that as-synthesized $CsPbBr_3$ NCs present a cubic shape and an orthorhombic crystal structure.[23,24] They are typically capped by oleylammonium and oleate ligands[25,26] and have excess Br^- and Cs^+ (some of which may be replaced by oleylammonium cations) at the surface.[21,22,27] These characteristics suggest a CsBr-terminated NC, and, in line with previous computational works,[21,22,28,29] we decided to construct a cubic $Cs_{324}Pb_{216}Br_{756}$ NC model system (see Figure A6.1). After this step, we followed the approach of Bodnarchuk et al. (see Methods for computational details)[22] to simulate the variation of the NC surface by the stepwise removal of the outer CsBr layer (models M1–M5, see Figure A6.2), followed by the gradual removal of the underlying $PbBr_2$ layer (models M6–M10, see Figure 6.2). The highest occupied molecular orbital (HOMO) of each model is shown in Figure 6.2B. We further calculate the density of states (DOS), inverse participation ratio (IPR), and crystal orbital overlap population (COOP) for the Pb–Br interaction for all models, as shown in Figure 6.2C (see Methods for more details on these analyses).

As reported previously,[22] Figure A6.2 shows that, although removal of the CsBr layer leads to more localized levels (i.e., with a higher IPR) near the VB edge, no deep traps are created, which is in line with the concept of defect tolerance. Upon removal of the $PbBr_2$ shell, Br^-–localized levels start to appear in model M7 (with 25% of the $PbBr_2$ removed). As predicted by Figure 6.1, these Br^- levels still largely lie at the VB edge (see Figure A6.3 for details). However, upon removal of 50% of the $PbBr_2$ shell in model M8, many highly localized trap states (IPR ≈ 1) appear in the middle of the bandgap, as shown in Figure 6.2C. Inspection of the shape of the trap states (Figure 6.2B, see Figure A6.4 for more details) and the COOP analysis (COOP ≈ 0, see Figure 6.2C) reveals that these states are formed by the nonbonding p orbitals of surface Br^-. Model M8 contains five such Br^- sites, each of which creates three trap states with its orthogonal p orbitals, leading to a total of

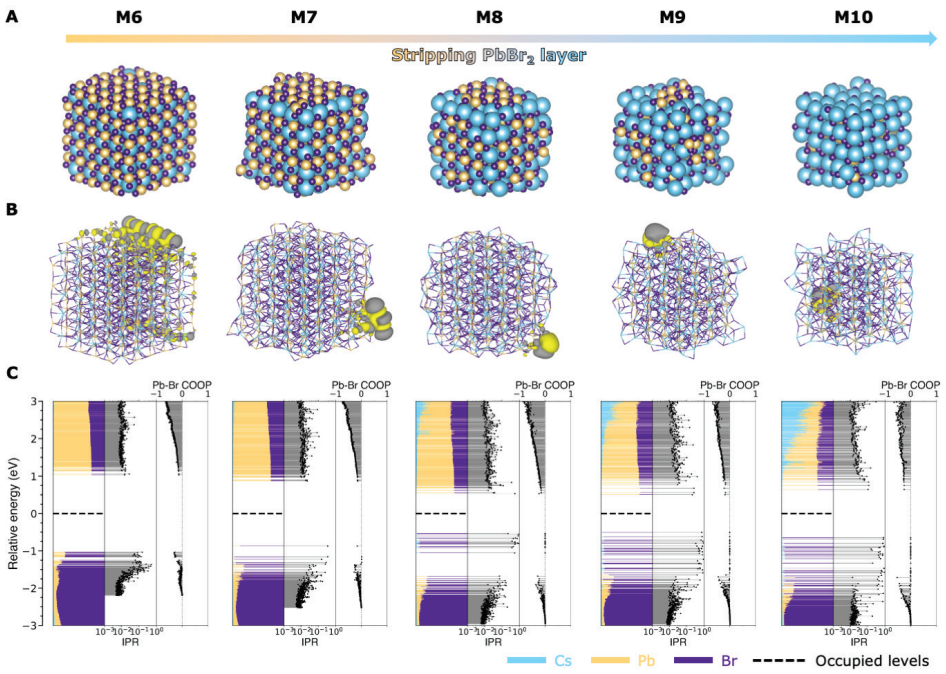

Figure 6.2. Formation of deep traps upon stripping of the $PbBr_2$ layer. (A) Structure, (B) isosurface plot of the HOMO, and (C) density of states (DOS), inverse participation ratio (IPR), and crystal orbital overlap population (COOP) of each model upon gradual stripping of the $PbBr_2$ layer. As shown in Figure A6.2 (models M1–M5), gradual stripping of the outer CsBr layer of our $CsPbBr_3$ model system does not create any trap states in the bandgap. However, upon removal of the underlying $PbBr_2$ layer (models M6–M10, shown here), deeper states start to appear. From model M8 onward, multiple deep traps, localized on surface Br^-, are present.

15 deep traps in Figure 6.2C.

The models shown in Figures 6.2 and A6.2 are constructed by removing CsBr or $PbBr_2$ units first from corners and edges, since they possess the lowest binding energy. In reality, removal of $PbBr_2$ can lead to a great number of surface compositions. To test that the occurrence of deep traps localized on Br^- ions is not specific to the structure of model M8 in Figure 6.2, we performed additional calculations where $PbBr_2$ moieties are either removed from the middle of the facets (Figure A6.5, models M8-ii and M8-iii) or randomly removed (Figure A6.5, models M8-iv and M8-v). The observation from these additional calculations is that the formation of deep Br^- traps can be generalized to many different $PbBr_2$ configurations, as long as Br^- ions with only Cs^+ neighbors are present. Changes in the surface configuration lead to changes in the total energy, but the creation of a Br^- trap does not necessarily lead to a significant increase of the energy of the system. Due to the dynamic nature of NC surfaces, many of these configurations will be sampled at room

temperature, including configurations that expose uncoordinated surface Br^- ions that form deep traps.

Clearly, these trap states are not consistent with the picture of defect tolerance expounded in the first paragraph, which would expect the nonbonding p orbitals to lie in or close to the VB. This suggests that the traditional picture of defect tolerance is incomplete. This picture assumes that the energy of a molecular orbital (MO) only depends on the interaction (be it bonding, antibonding, or nonbonding) between AOs. However, the energy of an AO can also be significantly influenced by its surroundings. For example, crystal field theory describes how the electrostatic field created by the surrounding ligands lifts the degeneracy of d orbitals in metal complexes.[30] We therefore hypothesize that the appearance of deep trap states can be explained by including the effects of the local electrostatic potential in the description of defect tolerance.

To test this hypothesis, we now take a closer look at model M8, as this is the first model with multiple deep traps. In Figure 6.3A-ii, we plot the potential energy (in eV), as generated by both the nuclei and electrons, of an electron at the surface of model M8. A blue color in Figure 6.3A-ii corresponds to a low potential energy, while a red color indicates a high potential energy. Figure 6.3A-ii shows that the potential energy is significantly higher at five points on the NC surface. These points correspond to the location of the aforementioned five surface Br^- sites that are responsible for the 15 deep traps in Figure 6.3A-iii. What sets these five Br^- apart from the other Br^- ions in the NC is that they have no direct bonds to Pb^{2+}. Instead, their nearest neighbors solely comprise Cs^+, with which there is little interaction. Whereas all other Br^- sites in the bulk and on the surface are stabilized by Pb^{2+}, these five surface Br^- sites in Figure 6.3A-ii can practically be seen as loose Br^- in vacuum. The absence of Pb^{2+} neighbors means that they experience a significantly higher local potential energy, which pushes their AOs from the VB into the bandgap. The same trends are observed for the models with different $PbBr_2$ configurations in Figure A6.5. There, moving a Br^- away from its Pb^{2+} neighbors is also found to significantly raise the potential energy around the Br^- ion, thus creating deep traps.

This reasoning implies that it should also be possible to push deep trap states back into the VB by changing the local potential. In Figure 6.3B-i we apply an artificial external stabilizing potential (see Methods for computational details) around one specific Br^- (indicated in red as Br_1 in Figure 6.3). As shown in Figure 6.3B-ii, this lowers the potential energy around Br_1 and consequently pushes the states related to Br_1 into the VB, leaving 12 instead of 15 deep traps (see Figure 6.3B-iii). Figure A6.6 shows that by varying the magnitude of the external potential, the energy of the trap states can be shifted across the bandgap.

These results clearly show that the position of localized MOs depends both on (the absence of) bonds formed with neighboring atoms, as expressed by Figure 6.1, and on the local electrostatic environment. This conclusion does not depend on the exact surface configuration, but holds generally for undercoordinated Br^- ions on the surface, as similar results are obtained on various other surface compositions (see Figure A6.5). Therefore, one can distinguish two main pathways via which traps may be passivated: (1) the covalent

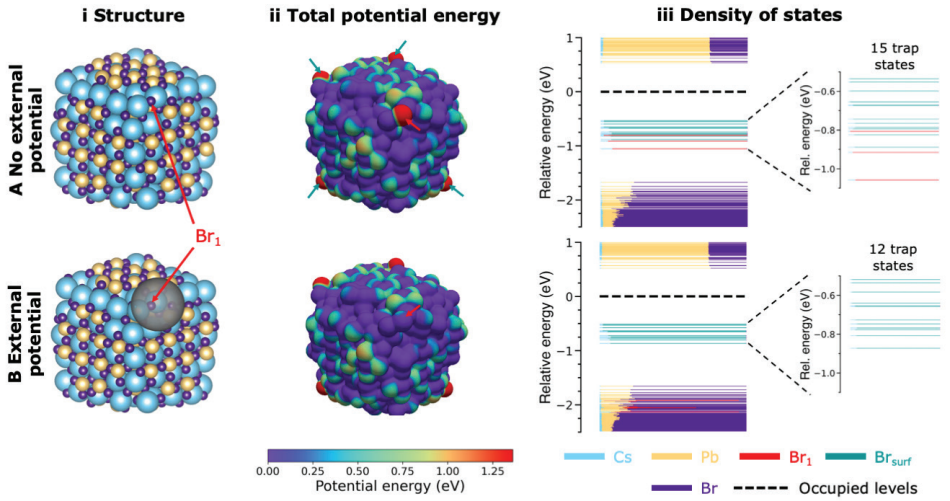

Figure 6.3. Effect of local potential on the energy of trap states (A) without and (B) with the application of an external potential. (i) Structure of model M8 and the location of the applied external potential around one of the five Br^- sites that give a deep trap, indicated as Br_1. (ii) Total potential energy (i.e., the electrostatic potential generated by the nuclei and electrons plus the external potential, see Methods for details) of an electron at the NC surface (in eV). Blue colors correspond to a low potential energy, while red indicates a high potential energy. The location of Br_1 is indicated by the red arrow. The turquoise arrows indicate the other four Br^- sites that give rise to deep trap states. (iii) DOS, showing the contribution of the surface Br^- to the deep traps. Application of an external potential shifts the states from Br_1 into the VB, leaving 12 instead of 15 traps in the bandgap.

binding of ligands to the surface to split nonbonding trap states and (2) the electrostatic interaction between the NC surface and electrolytes that do not covalently bind to the surface but influence the energy of surface-localized MOs via ionic interactions. In the Appendix we show in two ways how traps can be removed through the electrostatic interaction with charges that do not bind covalently to the surface. In Figure A6.7, we created a core/shell structure, where a $CsPbBr_3$ core is surrounded by Cs^+, Pb^{2+}, and Br^- like charges to mimic the perovskite bulk potential at the surface of the core. Although these charges do not bind covalently to the surface, Figure A6.7 shows that the bandgap has become completely trap free, with both the VB and CB edge delocalized over the NC. In Figure A6.8, we show that states localized on a Br^- ion can be removed from the bandgap by addition of a nearby proton (H^+)-like charge.

6.3 Conclusions

In conclusion, we have used DFT calculations to show that the general picture of defect tolerance in cesium lead halide perovskite NCs is incomplete and that the local environment of trap states should also be considered. Br^- sites on the surface can experience such a different local potential compared to the bulk that their nonbonding orbitals are pushed

into the bandgap and form deep trap states. These results not only give insight into the formation of traps in perovskites but also provide novel approaches for removing these states from the bandgap.

6.4 Methods

Geometry optimizations were carried out at the DFT level with a PBE exchange-correlation functional[31] and double-ζ basis set, as implemented in the CP2K quantum chemistry software package.[32] Relativistic effects were taken into account using effective core potentials. Due to the large size of the systems, spin-orbit coupling was not included.

The inverse participation ratio (IPR) and crystal orbital overlap population (COOP) were computed for the 500 highest occupied and 500 lowest unoccupied orbitals of each model. The IPR was calculated via:

$$IPR_i = \sum_\alpha |P_{\alpha,i}|^4 \Big/ \left(\sum_\alpha |P_{\alpha,i}|^2\right)^2 \qquad 6.1$$

Here, IPR_i is the IPR of the ith molecular orbital (MO) and $P_{\alpha,i}$ the weight of the MO on atom α. The IPR ranges from 1/N (with N the total number of atoms in the system) for a completely delocalized MO, to 1 for complete localization on one atom. The COOP between Pb and Br was computed through:

$$COOP_i^{Pb-Br} = \sum_{n\in Pb} \sum_{m\in Br} S_{nm} \cdot c_{n,i} \cdot c_{m,i} \qquad 6.2$$

Here, $COOP_i^{Pb\text{-}Br}$ is the COOP of the ith MO and S_{nm} the overlap between atomic orbitals (AOs) n and m, with coefficients $c_{n,i}$ and $c_{m,i}$, respectively. n loops over the AOs of all Pb atoms, m loops over the AOs of all Br. A negative COOP value indicates that an MO is of an overall anti-bonding character, while positive COOP values indicate an overall bonding MO. COOP values close to zero are indicative of a non-bonding MO. Both the IPR and the COOP were calculated using the workflows implemented in the Nano-QMFlows package.[33]

The external potential, mentioned in the main text during the discussion of Figure 6.3, was applied using the "EXTERNAL_POTENTIAL" keyword in CP2K. We introduced a Gaussian potential, centered 3.3 Å away from Br_1 (see Figure 6.3 in the main text), and described by:

$$V_{ext} = A \cdot \exp\left(-\frac{(x-39.32286428)^2 + (y-8.17028545)^2 + (z-34.22436985)^2}{2\cdot 3.0^2}\right) \qquad 6.3$$

Here, A is the maximal amplitude of the external potential (which we varied between -0.1 and 0.1 Ha in Figure A6.6) and x, y, z are the spatial coordinates in Å. This potential is added as an extra term to the Hamiltonian. As a result, a positive external potential (i.e., A>0) lowers the energy of the electrons.

The total potential energy experienced per MO (as plotted in Figures A6.3C, A6.4C and A6.6A) was calculated via:

$$V_{total,i} = \frac{\langle \psi_i | V_{ion} - V_{ext} | \psi_i \rangle}{\langle \psi_i | \psi_i \rangle} \quad 6.4$$

Here, V_{ion} is the electrostatic potential generated by all the electrons and nuclei, V_{ext} the external potential (if applied) and ψ_i the wavefunction of the ith MO. Note that we subtract V_{ext} from V_{ion} to correct for the opposite sign of V_{ext}.

References

1. Kovalenko, M. V., Protesescu, L. & Bodnarchuk, M. I. Properties and potential optoelectronic applications of lead halide perovskite nanocrystals. *Science* 358, 745–750 (2017).
2. Akkerman, Q. A., Rainò, G., Kovalenko, M. V. & Manna, L. Genesis, challenges and opportunities for colloidal lead halide perovskite nanocrystals. *Nat. Mater.* 17, 394–405 (2018).
3. Shamsi, J., Rainò, G., Kovalenko, M. V. & Stranks, S. D. To nano or not to nano for bright halide perovskite emitters. *Nat. Nanotechnol.* 16, 1164–1168 (2021).
4. Dey, A., Ye, J., De, A., Debroye, E., Ha, S. K., Bladt, E., Kshirsagar, A. S., Wang, Z., Yin, J., Wang, Y., et al. State of the Art and Prospects for Halide Perovskite Nanocrystals. *ACS Nano* 15, 10775–10981 (2021).
5. Protesescu, L., Yakunin, S., Bodnarchuk, M. I., Krieg, F., Caputo, R., Hendon, C. H., Yang, R. X., Walsh, A. & Kovalenko, M. V. Nanocrystals of Cesium Lead Halide Perovskites (CsPbX3, X = Cl, Br, and I): Novel Optoelectronic Materials Showing Bright Emission with Wide Color Gamut. *Nano Lett.* 15, 3692–3696 (2015).
6. Yan, F., Tan, S. T., Li, X. & Demir, H. V. Light Generation in Lead Halide Perovskite Nanocrystals: LEDs, Color Converters, Lasers, and Other Applications. *Small* 15, 1902079 (2019).
7. Yakunin, S., Protesescu, L., Krieg, F., Bodnarchuk, M. I., Nedelcu, G., Humer, M., De Luca, G., Fiebig, M., Heiss, W. & Kovalenko, M. V. Low-threshold amplified spontaneous emission and lasing from colloidal nanocrystals of caesium lead halide perovskites. *Nat. Commun.* 6, 8056 (2015).
8. Chen, J., Du, W., Shi, J., Li, M., Wang, Y., Zhang, Q. & Liu, X. Perovskite quantum dot lasers. *InfoMat* 2, 170–183 (2020).
9. Wang, Y., Li, X., Nalla, V., Zeng, H. & Sun, H. Solution-Processed Low Threshold Vertical Cavity Surface Emitting Lasers from All-Inorganic Perovskite Nanocrystals. *Adv. Funct. Mater.* 27, 1605088 (2017).
10. Yuan, J., Hazarika, A., Zhao, Q., Ling, X., Moot, T., Ma, W. & Luther, J. M. Metal Halide Perovskites in Quantum Dot Solar Cells: Progress and Prospects. *Joule* 4, 1160–1185 (2020).
11. Zhou, F., Li, Z., Chen, H., Wang, Q., Ding, L. & Jin, Z. Application of perovskite nanocrystals (NCs)/quantum dots (QDs) in solar cells. *Nano Energy* 73, 104757 (2020).
12. Hao, M., Bai, Y., Zeiske, S., Ren, L., Liu, J., Yuan, Y., Zarrabi, N., Cheng, N., Ghasemi, M., Chen, P., et al. Ligand-assisted cation-exchange engineering for high-efficiency colloidal Cs1−xFAxPbI3 quantum dot solar cells with reduced phase segregation. *Nat. Energy* 5, 79–88 (2020).

13. Liu, L., Najar, A., Wang, K., Du, M. & Liu, S. (Frank). Perovskite Quantum Dots in Solar Cells. *Adv. Sci.* 9, 2104577 (2022).
14. Wang, N., Liu, W. & Zhang, Q. Perovskite-Based Nanocrystals: Synthesis and Applications beyond Solar Cells. *Small Methods* 2, 1700380 (2018).
15. Kang, J. & Wang, L.-W. High Defect Tolerance in Lead Halide Perovskite CsPbBr3. *J. Phys. Chem. Lett.* 8, 489–493 (2017).
16. Ten Brinck, S., Zaccaria, F. & Infante, I. Defects in Lead Halide Perovskite Nanocrystals: Analogies and (Many) Differences with the Bulk. *ACS Energy Lett.* 4, 2739–2747 (2019).
17. Huang, H., Bodnarchuk, M. I., Kershaw, S. V., Kovalenko, M. V. & Rogach, A. L. Lead Halide Perovskite Nanocrystals in the Research Spotlight: Stability and Defect Tolerance. *ACS Energy Lett.* 2, 2071–2083 (2017).
18. Houtepen, A. J., Hens, Z., Owen, J. S. & Infante, I. On the Origin of Surface Traps in Colloidal II–VI Semiconductor Nanocrystals. *Chem. Mater.* 29, 752–761 (2017).
19. Boehme, S. C., Azpiroz, J. M., Aulin, Y. V., Grozema, F. C., Vanmaekelbergh, D., Siebbeles, L. D. A., Infante, I. & Houtepen, A. J. Density of Trap States and Auger-mediated Electron Trapping in CdTe Quantum-Dot Solids. *Nano Lett.* 15, 3056–3066 (2015).
20. Kirkwood, N., Monchen, J. O. V., Crisp, R. W., Grimaldi, G., Bergstein, H. A. C., du Fossé, I., van der Stam, W., Infante, I. & Houtepen, A. J. Finding and Fixing Traps in II–VI and III–V Colloidal Quantum Dots: The Importance of Z-Type Ligand Passivation. *J. Am. Chem. Soc.* 140, 15712–15723 (2018).
21. Ten Brinck, S. & Infante, I. Surface Termination, Morphology, and Bright Photoluminescence of Cesium Lead Halide Perovskite Nanocrystals. *ACS Energy Lett.* 1, 1266–1272 (2016).
22. Bodnarchuk, M. I., Boehme, S. C., Ten Brinck, S., Bernasconi, C., Shynkarenko, Y., Krieg, F., Widmer, R., Aeschlimann, B., Günther, D., Kovalenko, M. V., et al. Rationalizing and Controlling the Surface Structure and Electronic Passivation of Cesium Lead Halide Nanocrystals. *ACS Energy Lett.* 4, 63–74 (2019).
23. Cottingham, P. & Brutchey, R. L. On the crystal structure of colloidally prepared CsPbBr3 quantum dots. *Chem. Commun.* 52, 5246–5249 (2016).
24. Swarnkar, A., Chulliyil, R., Ravi, V. K., Irfanullah, M., Chowdhury, A. & Nag, A. Colloidal CsPbBr3 Perovskite Nanocrystals: Luminescence beyond Traditional Quantum Dots. *Angew. Chemie* 127, 15644–15648 (2015).
25. De Roo, J., Ibáñez, M., Geiregat, P., Nedelcu, G., Walravens, W., Maes, J., Martins, J. C., Van Driessche, I., Kovalenko, M. V. & Hens, Z. Highly Dynamic Ligand Binding and Light Absorption Coefficient of Cesium Lead Bromide Perovskite Nanocrystals. *ACS Nano* 10, 2071–2081 (2016).
26. Maes, J., Balcaen, L., Drijvers, E., Zhao, Q., De Roo, J., Vantomme, A., Vanhaecke, F., Geiregat, P. & Hens, Z. Light Absorption Coefficient of CsPbBr3 Perovskite Nanocrystals. *J. Phys. Chem. Lett.* 9, 3093–3097 (2018).
27. Zhang, F., Zhong, H., Chen, C., Wu, X. G., Hu, X., Huang, H., Han, J., Zou, B. & Dong, Y. Brightly luminescent and color-tunable colloidal CH3NH3PbX3 (X = Br, I, Cl) quantum dots: Potential alternatives for display technology. *ACS Nano* 9, 4533–4542 (2015).

28. Giansante, C. & Infante, I. Surface Traps in Colloidal Quantum Dots: A Combined Experimental and Theoretical Perspective. *J. Phys. Chem. Lett.* 8, 5209–5215 (2017).
29. Boehme, S. C., Brinck, S. Ten, Maes, J., Yazdani, N., Zapata, F., Chen, K., Wood, V., Hodgkiss, J. M., Hens, Z., Geiregat, P., et al. Phonon-Mediated and Weakly Size-Dependent Electron and Hole Cooling in CsPbBr 3 Nanocrystals Revealed by Atomistic Simulations and Ultrafast Spectroscopy. *Nano Lett.* 20, 1819–1829 (2020).
30. Crabtree, R. H. *The Organometallic Chemistry of the Transition Metals.* (John Wiley & Sons, Inc., 2014).
31. Perdew, J. P., Burke, K. & Ernzerhof, M. Generalized Gradient Approximation Made Simple. *Phys. Rev. Lett.* 77, 3865–3868 (1996).
32. Hutter, J., Iannuzzi, M., Schiffmann, F. & VandeVondele, J. cp2k: atomistic simulations of condensed matter systems. *Wiley Interdiscip. Rev. Comput. Mol. Sci.* 4, 15–25 (2014).
33. Zapata, F., Ridder, L., Hidding, J., Jacob, C. R., Infante, I. & Visscher, L. QMflows: A Tool Kit for Interoperable Parallel Workflows in Quantum Chemistry. *J. Chem. Inf. Model.* 59, 3191–3197 (2019).

Appendix

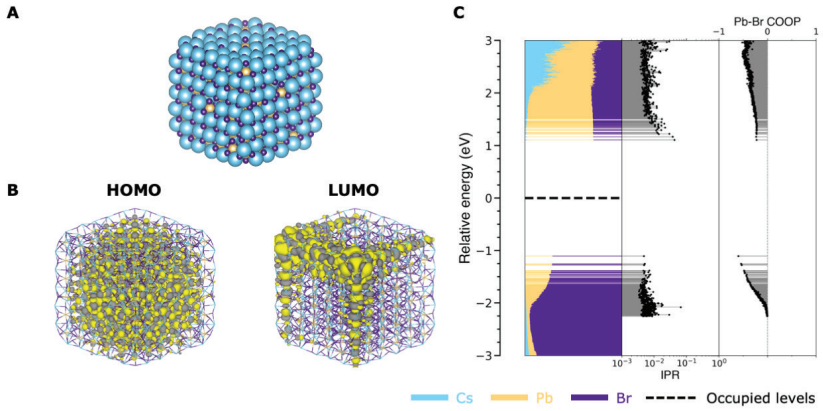

Figure A6.1. Details of the $Cs_{324}Pb_{216}Br_{756}$ model system M1. (A) Structure, (B) HOMO and LUMO and (C) density of states (DOS), IPR and COOP of the NC.

Ligand stripping. Following the method by Bodnarchuk et al.,[22] we remove the outer CsBr layer of the model system M1 (shown in Figure A6.1) in four consecutive steps, in which we remove 25%, 50%, 75% and 100% of the CsBr units. This is shown in models M2-M5 in the first half of Figure A6.2. After removal of all CsBr units, the NC is terminated by a layer of $PbBr_2$, with some loose Br^- left on the NC surface. These loose Br^- are removed in model M6. Subsequently, in four consecutive steps, we again remove 25%, 50%, 75% and 100% of the $PbBr_2$ shell (models M7-M10, shown in the second half of Figure A6.2 on the next page).

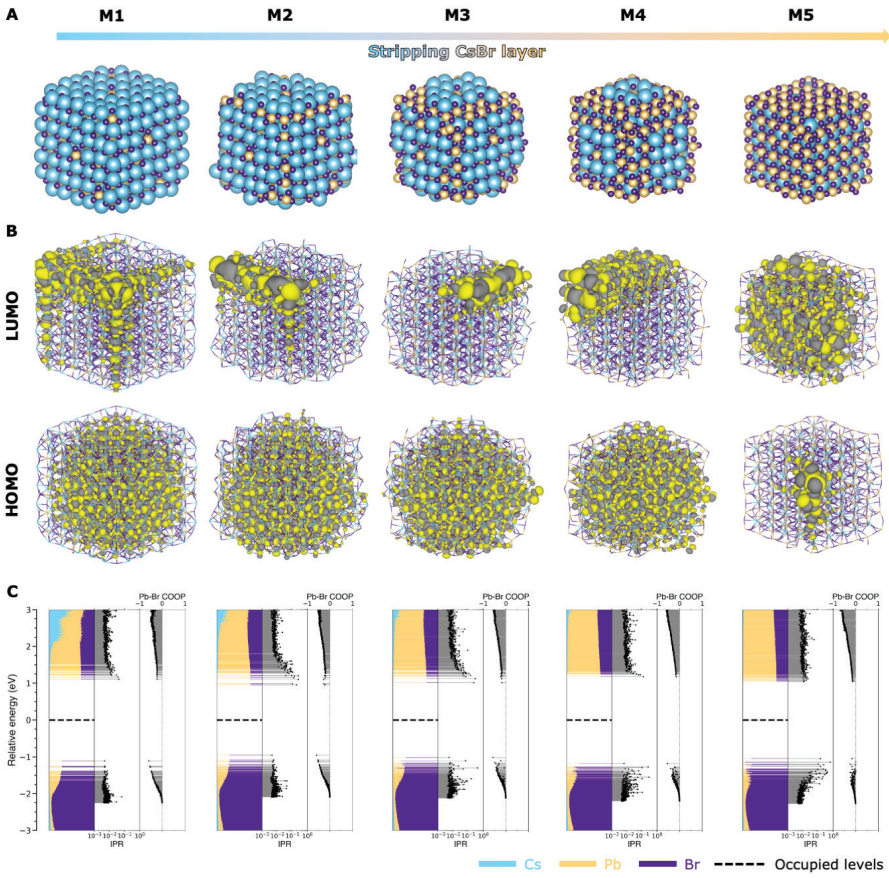

Figure A6.2. Stepwise removal of CsBr and $PbBr_2$ layers from model system M1. (A) Structure, (B) HOMO and LUMO, and (C) DOS, IPR and COOP of each NC.

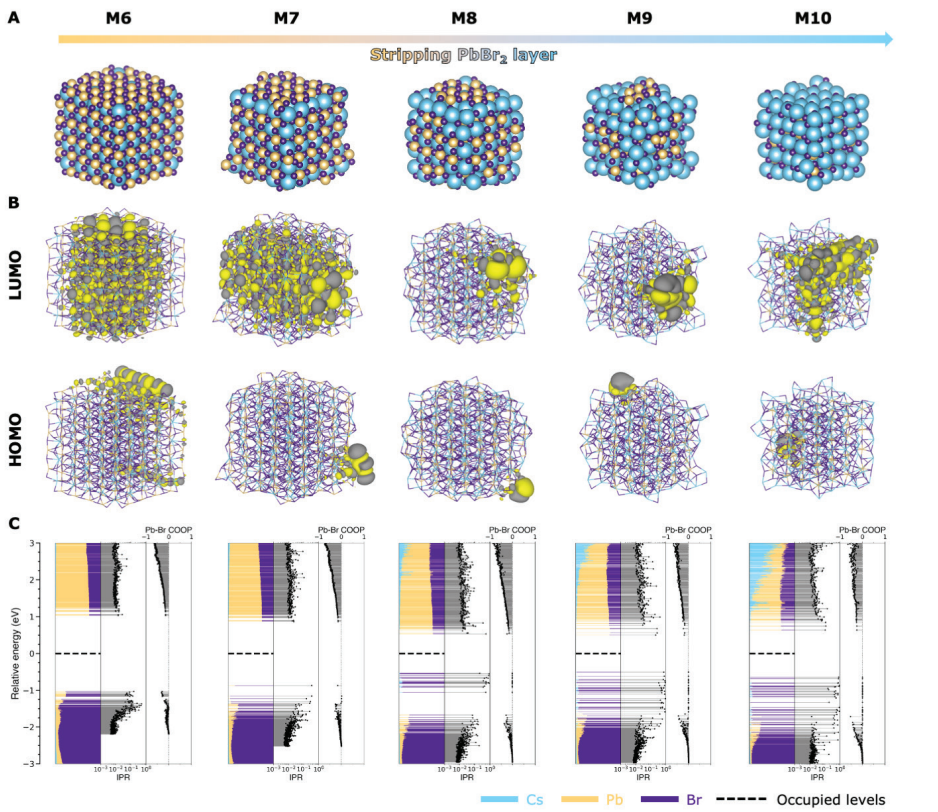

Figure A6.2 (continued). Stepwise removal of CsBr and $PbBr_2$ layers from model system M1. (A) Structure, (B) HOMO and LUMO, and (C) DOS, IPR and COOP of each NC.

Shallow traps in model M7. As discussed in the main text, removal of 25% of the $PbBr_2$ layer leads to the creation of Br^--localized levels at the VB edge, which are shown in more detail in Figure A6.3. The highest five occupied levels are located on the $PbBr_2$ unit indicated in turquoise in Figure A6.3A. In the HOMO, there is a slight anti-bonding interaction between the Br^- and Pb^{2+}, as indicated by the small Pb-contribution in the DOS and the negative COOP-value in Figure A6.3C. The four levels below the HOMO (i.e., HOMO-1 through HOMO-4) do not interact with Pb^{2+}, as evinced by the COOP values of ~0. However, as can be seen in Figure A6.3B, the two Br^- ions do interact with each other, forming π and π* bonds. As the π- and π*-like orbitals lie very close in energy, the Br^--Br^- interaction is expected to be small. Since the trap levels are close to the VB edge, these results are still in agreement with the concept of defect tolerance as discussed in the main text. However, further stripping of the $PbBr_2$ layer creates Br^--localized levels that do lie in the middle of the bandgap (see Figure A6.4 and the main text).

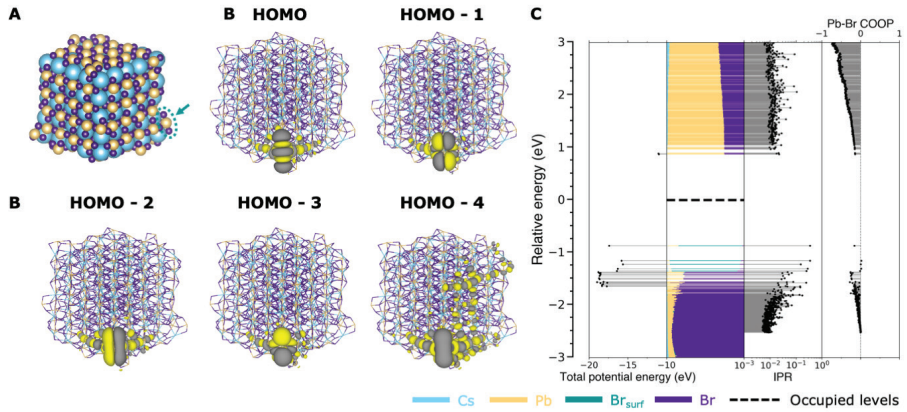

Figure A6.3. Details of the shallow traps formed in model M7. (A) Structure of model M7. The five highest occupied levels are localized on the two Br^- ions indicated by the turquoise arrow. (B) Shape of the five highest occupied MOs. (C) DOS, IPR and COOP of the NC. The contribution of the two Br^- ions are shown in turquoise. The leftmost panel shows the total potential energy for each MO around the bandgap (see Methods for computational details).

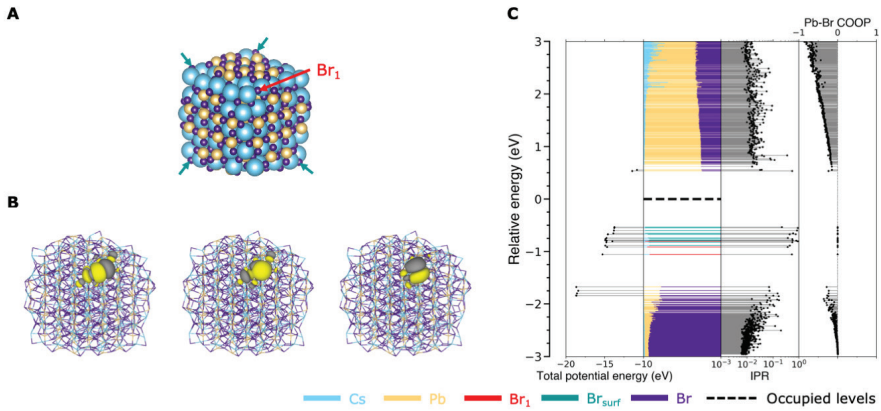

Figure A6.4. Details of the deep traps formed in model M8. (A) Structure of model M8. The deep traps are localized on five Br^- ions. Four are indicated by the turquoise arrows, while Br_1 is indicated in red (as also done in Figure 6.3 in the main text). (B) Shape of the three traps localized on Br_1. Each Br^- site creates three trap states, formed by three orthogonal p-orbitals. (C) DOS, IPR and COOP of the NC. The contribution of the five Br^- ions are shown in turquoise and red. The leftmost panel shows the total potential energy for each MO around the bandgap (see Methods for computational details).

Effect of removing $PbBr_2$ in different configurations. As discussed in the main text, the occurrence of deep Br^- traps in model M8 is not linked to the specific structure of M8. Instead, it can be generalized to many different surface configurations, as long as Br^- ions with only Cs^+ neighbors are present. To show Br^- traps are not unique to model M8, we demonstrate in Figure A6.5 that removing 50% of the $PbBr_2$ moieties from different surface sites can also lead to the formation of deep traps.

Model M8, which is used in the main text (and also plotted in Figure A6.2), is shown in the leftmost column. Following the approach of Bodnarchuk et al.,[22] $PbBr_2$ moieties were removed first from the corners and edges of the NC. In model M8-ii, $PbBr_2$ was first removed from the center of each facet. As shown in Figure A6.5A, this surface configuration is less favorable, increasing the total energy by 1.0 eV (compared to model M8). Moreover, all Br^- are coordinated to Pb^{2+}, so that no traps are present in Figure A6.5D, confirming our interpretation of the traps as arising from Br^- with no coordination to Pb^{2+}. Moving one Br^- from model M8-ii away from its Pb^{2+} neighbors results in structure M8-iii (the red circle indicates which Br^- has been moved). In line with the results shown in the main text, this Br^-, which now only has Cs^+ neighbors, experiences a significantly higher potential energy (see Figure A6.5C). As also described in the main text, this leads to the formation of three deep traps, which are indicated in turquoise in Figure A6.5D. Yet, note that displacing the Br^- increases the energy of the system by 0.4 eV, which makes the formation of this specific trap energetically unfavorable. In model M8-iv, surface $PbBr_2$ moieties have been removed from random positions. No traps are found due to the coordination of all surface Br^- to Pb^{2+}. Again, moving one Br^- (indicated by the orange circle) away from Pb^{2+} causes the Br^- to experience a higher local potential energy, leading to the formation of three traps. However, in contrast to model M8-iii, there is only a negligible change in the total energy, indicating that both systems are roughly equally likely to be sampled at room temperature.

These results show that, although model M8 as used in the main text is not the lowest energy configuration, the formation of deep Br^- traps can be generalized to many different $PbBr_2$ configurations, as long as Br^- ions with only Cs^+ neighbors are present. Changes in the surface configuration can also lead to changes in the total energy, but the creation of a Br^- trap does not necessarily lead to a significant increase of the energy of the system. Hence, thermal motion will cause the NC to sample a great number of surface compositions, with varying numbers of Br^- traps.

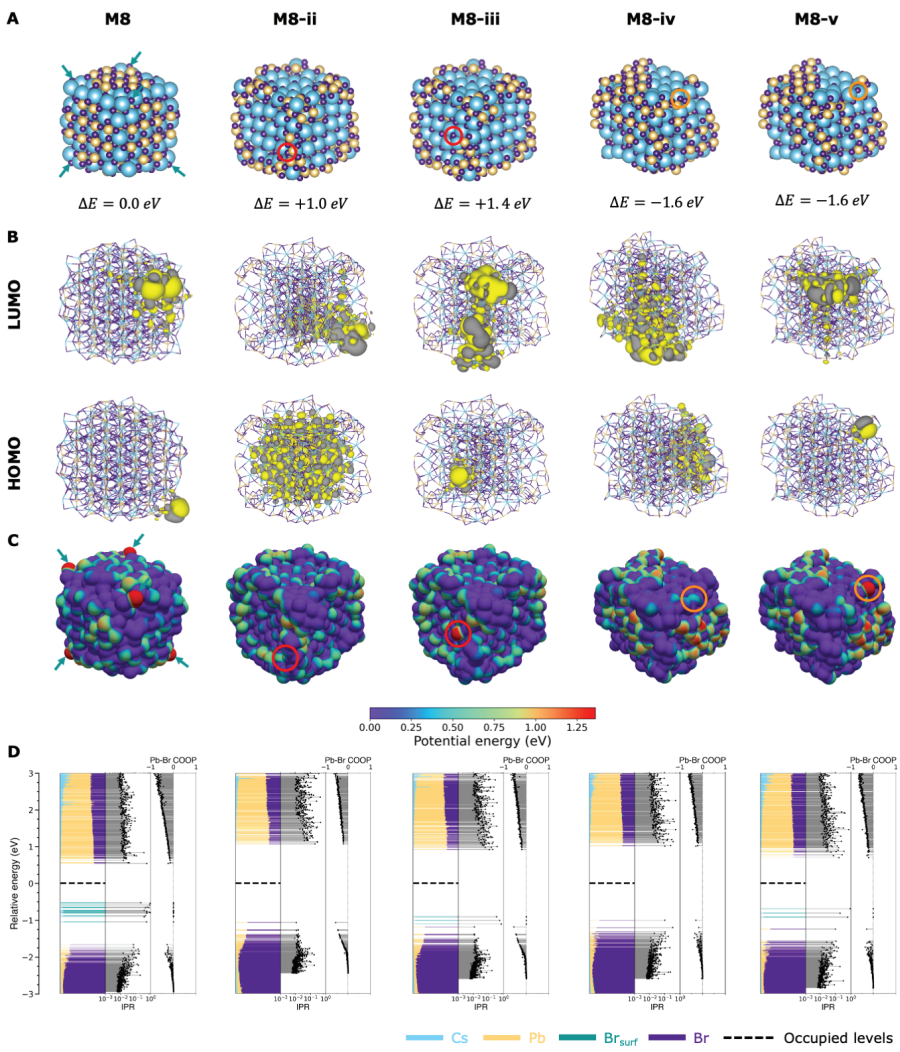

Figure A6.5. Effect of stripping the $PbBr_2$ layer in different configurations. Model M8 (used in the main text): $PbBr_2$ first removed from corners and edges. Model M8-i: $PbBr_2$ first removed from the middle of each facet. Model M8-iii: Same as model M8-ii, but one Br^- has been moved (see red circle). Model M8-iv: $PbBr_2$ removed from random surface sites. Model M8-v: Same as Model M8-iv, but one Br^- has been moved (see orange circle). (A) Structure and energy (relative to model M8 as used in the main text), (B) HOMO and LUMO, (C) the potential energy (in eV) of an electron at the NC surface, and (D) DOS, IPR and COOP of each NC. The contribution of surface Br^- ions (which are either indicated by the turquois arrows or the red or orange circles) is given in turquois.

Shifting energy of traps. As discussed in the main text and shown in Figure 6.3B, application of a stabilizing external potential around Br_1 can push the energy of the traps back into the VB. Figure A6.6 shows that by varying the magnitude of the applied potential, the traps localized on Br_1 can be shifted through the entire bandgap. Figure A6.6A plots the energy (relative to the VB edge) of the three traps localized on Br_1 (shown in black, red, and blue) against the total potential energy experienced by those traps (see Methods for computational details). It can be seen that a more negative total potential energy lowers the energy of the trap with respect to the VB, and eventually pushes the trap below the VB edge (as indicated by the negative energy in Figure A6.6A). Conversely, a less negative total potential energy increases the energy of the traps with respect to the VB, and pushes them towards the CB, as also illustrated in Figure A6.6B.

The fits in Figure A6.6A show a strong linear correlation between the energy of the traps vs the VB edge and their total potential energy, with a slope in the range of 0.8-1.0. This suggests that the shift in energy is largely caused by the change in total potential energy, but that small additional effects take place in parallel, leading to a slope of not exactly 1. One significant outlier, in red at a total potential energy of -17 eV, may be explained by the fact that this trap, which lies in the VB, is slightly mixed with other VB levels. This is expected to lead to additional energy effects that break up the linear correlation.

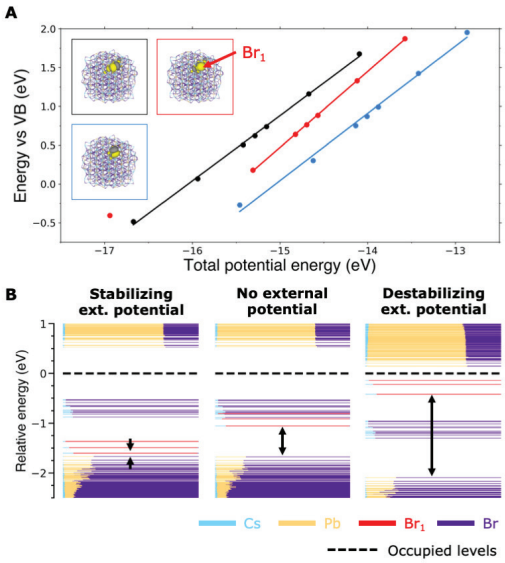

Figure A6.6. Shifting the energy of the traps located on Br_1 by application of an external potential. (A) Energy of the trap (relative to the VB edge) against the total potential energy, as experienced by the three trap states localized on Br_1. The fits show a linear correlation, with the exclusion of the outlier in red at a total potential energy of -17 eV. (B) DOS, showing the location of the Br_1 traps upon application of a stabilizing ($V_{ext} > 0$, see Methods) and destabilizing ($V_{ext} < 0$) external potential.

Electrostatic trap passivation. In order to investigate if deep traps can be removed solely through the electrostatic effect of ligands (i.e., without covalent binding to, and splitting of the non-bonding Br^--orbital), we carried out two types of calculations. In the first, we constructed a sort of core/shell structure, based on model M1, as shown in Figure A6.7A. Here, the shell (indicated in gray) consists of all the atoms of model M1 that are removed during the stripping procedure (Figure A6.2) to create model M8. The core (indicated with the standard colors for Cs, Pb and Br) comprises the same atoms that are in model M8. However, note that the coordinates of the core atoms in Figure A6.7A are not exactly the same as in model M8, since the coordinates of the former are extracted from the geometry optimization of model M1 in Figure A6.2. As a result, the atoms at the surface of the core (in Figure A6.7A) still have the same configuration as they had in the bulk of model M1. Carrying out a single point calculation on the core atoms only, as shown in Figure A6.7D "without shell", indicates that this type of NC termination leads to many trap states and virtually no bandgap.

In the main text, we argued that the different potential experienced at the surface, causes Br^- dangling bonds to end up in the bandgap. By extension, one would expect that the traps in Figure A6.7D will be pushed out of the bandgap if the potential experienced at the core surface is equal to the potential experienced in the bulk. To simulate this effect, we removed the basis functions and electrons of all the atoms in the shell (gray in Figure A6.7A), leaving only the effective core potentials (see Methods). We corrected the charge of the core potentials so that the atoms in the shell have a charge of Cs^+, Pb^{2+} and Br^-. As a result, the atoms in the shell mimic the perovskite bulk potential at the surface of the core, without forming any covalent bonds with the core surface. Figure A6.7D shows that addition of this "point charge" shell effectively removes all traps from the bandgap. Figures A6.7B and A6.7C show that the band edges are delocalized over the entire core. Note that the MOs do not delocalize over the shell, as these atoms do not have basis functions.

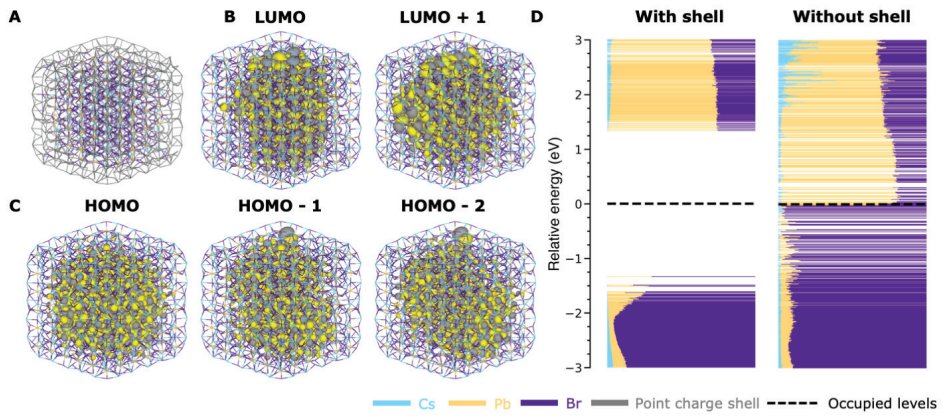

Figure A6.7. Electrostatic trap passivation by addition of a "point charge" shell. (A) Structure of the core/shell structure. The shell is indicated in gray. (B) Shape of the CB edge levels and (C) the VB edge levels. (D) DOS of the core with and without the shell.

In the second calculation, the traps related to Br_1 were pushed out of the bandgap by placing a proton (H^+)-like charge in the vicinity of Br_1 (see Figure A6.8A). To ensure no covalent binding to Br_1 takes place, we removed the basis functions of the proton. In addition, we removed the electron of the H^+ by setting the charge of the overall system (i.e., NC + proton) to +1, leaving only the effective core potential of the proton (with a total charge of +1). Figure A6.8B shows that the addition of the H^+ lowers the potential energy around Br_1, which pushes the trap states on Br_1 back into the VB, as shown in red in Figure A6.8C. As the H^+ is only placed in the vicinity of Br_1, the other four Br^- sites (indicated in turquoise in Figure A6.8A) still experience a high potential energy, which leaves their traps in the bandgap.

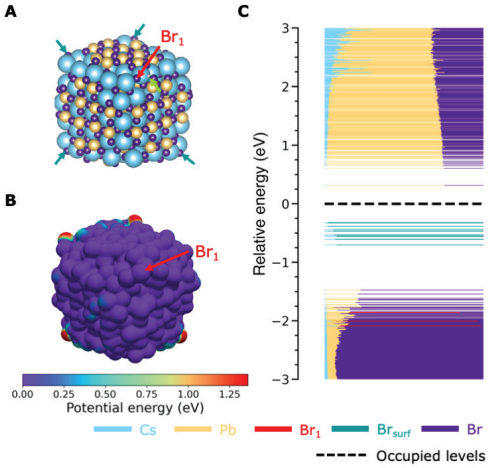

Figure A6.8. Electrostatic trap passivation by addition of a proton (H^+)-like charge. (A) Location of the H^+ (indicated by the light green arrow), which is placed 6.5 Å away from Br_1 (indicated in red). (B) The potential energy (in eV) of an electron at the NC surface. (C) DOS, showing the contribution of Br_1 and the other four Br^- sites (indicated in turquoise) that give deep traps.

Part C

Loose ends

7

Role of Surface Reconstructions in the Charge Delocalization in CdSe Quantum Dots

Although density functional theory (DFT) calculations have been crucial in our understanding of colloidal quantum dots (QDs), simulations are commonly carried out on QD models that are significantly smaller than generally found in experiment. While smaller models allow the efficient study of local surface configurations, increasing the size of the QD model will increase the size and/or number of facets, which can in turn influence the energetics and characteristics of trap formation. Moreover, core/shell structures can only be studied with QD models that are large enough to accommodate the different layers with the correct thickness. Here, we use DFT calculations to study the electronic properties of QDs as a function of size (up to a diameter of ~4.5 nm). We show that increasing the size of the QD model leads to the disappearance of the bandgap and the localization of the HOMO and LUMO levels on the QD surface. Addition of L-type or Z-type ligands leads to a slightly better delocalization of the LUMO and HOMO, respectively, but fail to open up the bandgap. In contrast, the introduction of surface reconstructions significantly increases the bandgap and delocalizes both the HOMO and LUMO. The surface reconstructions may be interpreted as a Jahn-Teller distortion, where reorganization of the QD facets converts a metallic system (i.e., bandgap ≈ 0) into a semiconducting one. These results show that not only the presence of (in)organic ligands, but also the surface geometry of the facets play a pivotal role in the electronic properties of the QD.

7.1 Introduction

Computational studies have been indispensable for increasing our understanding of colloidal quantum dots (QDs).[1–4] In the past decade, it has become feasible to use density functional theory (DFT) calculations to study QD models with realistic structures and ligand-terminated surfaces that are in line with experimental observations.[1,5] However, although computational power has vastly increased since the first DFT calculations on small QD clusters,[1,6–8] calculations are still commonly carried out on model systems that are significantly smaller than real QDs as found in experiment. A spherical CdSe QD with a diameter of 5 nm contains ~2400 atoms (excluding ligands), yet the number of atoms in the models used in DFT studies rarely exceeds 500 (~3 nm diameter).[9–14] While local surface configurations can be studied well with these smaller models,[13–15] larger QDs will have larger and/or different facets, which can influence the energetics and consequences of trap formation. Moreover, for an accurate description of core/shell(/shell) particles, it is imperative that the QD model is of (almost) the experimental size, as it will have to accommodate the core and shell(s) with the correct thickness.

Larger QD systems (i.e., diameter ≥ 5 nm) have been investigated previously using tight-binding methods, pseudopotential calculations and classical force fields. While tight-binding calculations can accurately reproduce experimentally observed spectra,[16–19] and pseudopotential methods are used to study carrier dynamics and the electronic structure of QDs,[20–23] both methods are less suited to predicting the geometry of the surface.[5] Moreover, these calculations often passivate the surface by binding pseudo-hydrogen atoms to all undercoordinated atoms.[17,18,20,21,24] Yet, such pseudo-hydrogen passivation does not resemble the experimentally present carboxylate or amine ligands and is hence not suitable for an accurate description of the QD surface.[5] Recent developments in classical force fields that are specifically tailored to QDs have made it possible to study the dynamics of large QDs with realistic ligand capping at a fraction of the computational cost.[25,26] However, these force fields cannot predict if a certain atomic configuration leads to charge localization or what the effect would be of changing the electronic state of the QD (e.g., by excitation or charging of the system). For such detailed analyses of surface states and their influence on the electronic properties of the QD, DFT remains the best choice.[5]

As mentioned previously, the literature on DFT studies on models with ≥500 atoms is relatively scarce. As with the pseudopotential and tight-binding studies, some reports passivate the QD with pseudo-hydrogen atoms.[27,28] Although this approach can reproduce the expected trends in bandgap and the delocalization of the HOMO and LUMO levels, it again fails to accurately describe the nature of the surface. In 2014, Voznyy et al. presented a CdSe QD model, comprising ~1200 atoms (excluding the ligands), that was passivated with chloride ions.[29] However, in contrast to the pseudo-hydrogen passivated models, the Cl-passivation resulted in the disappearance of the bandgap and the localization of the valence band (VB) and conduction band (CB) edge on the QD surface. Comparable surface localization has been observed for CdSe nanoplatelets.[30] These results are incompatible with the traditional particle-in-a-box description of QDs,[31,32] which accurately predicts, for example, the delocalized orbitals that are observed with scanning tunneling microscopy,[33–35] or the size-tunable bandgap of QDs.[36,37] Voznyy et al. solved this

problem by introducing a number of surface vacancies, leading to a slightly n-doped QD.[29]

Here, we study the electronic properties of model QDs as a function of QD size. While the HOMO and LUMO are still delocalized for small models, increasing the size of the system gradually leads to charge localization on surface facets. These results suggest that the surface of real QDs deviates from the model systems investigated here. Therefore, we systematically modify the QD surface to investigate what causes the localization of the HOMO and LUMO level on the surface. It is found that ligand passivation can only partly alleviate the problem. L-type amine ligands mainly lead to a slight delocalization of the LUMO, and Z-type $CdCl_2$ ligands mainly delocalize the HOMO, but neither can efficiently open up the bandgap. Only the introduction of surface reconstructions as known from literature on flat semiconductor surfaces,[38–41] leads to delocalization of both the HOMO and the LUMO, and a significant increase of the bandgap for systems of all sizes. These results suggest that real QD surfaces, even in the presence of surface ligands, may also exhibit such surface reconstructions.

7.2 Results and Discussion

7.2.1 Problems of Larger QDs

Figure 7.1A shows the zincblende $Cd_{68}Se_{55}Cl_{26}$ model system that has been used as the basis of multiple previous studies.[13,15,42,43] As it contains 68 cadmium atoms, it will henceforth be referred to as Cd_{68}. In accordance with experimental observations, it is roughly spherical, cation-rich,[44,45] and charge balanced[46] by the passivation with chloride ligands (in lieu of the experimentally employed oleate ligands).[14,47] However, with a diameter of ~1.8 nm (as measured from one corner of a (111) facet to the furthest corner of the (111) facet on the opposite side of the QD) it is significantly smaller than typical experimental CdSe QDs. The density of states (DOS) and the shape of the HOMO and LUMO are shown in Figures 7.1B and 7.1C, respectively. Both the HOMO and the LUMO are delocalized over the entire QD and separated by a clear bandgap of 1.5 eV. Further details of the system have been discussed previously.[13]

As predicted by a simple particle-in-a-box model, increasing the QD diameter to 2.7 nm (Cd_{176}) leads to a decrease in the bandgap. However, Figure 7.1C shows that the HOMO is no longer equally spread over the entire QD and instead localizes at certain points in the particle. Increasing the QD size further to 3.6 (Cd_{360}) or 4.5 nm (Cd_{640}) results in a bandgap-less (i.e., metallic) system, where both the HOMO and LUMO are clearly located on the QD surface, specifically on the Se-terminated ($\overline{111}$) and Cd-terminated (111) facets.

The inverse participation ratio (IPR) is commonly used to quantify the degree of localization of the wavefunction. The IPR ranges from 1 for complete localization to $1/N_{atoms}$ (with N_{atoms} the number of atoms in the system) for complete delocalization. Thus, for a system of 100 atoms IPR = 0.01 would correspond to complete delocalization, whereas for a QD of 1000 atoms it would be IPR = 0.001. As this would complicate comparison between the different QD sizes, we instead plot 1/IPR, i.e., the "participation ratio" (PR), expressed as a fraction of the number of Cd and Se atoms in the system:

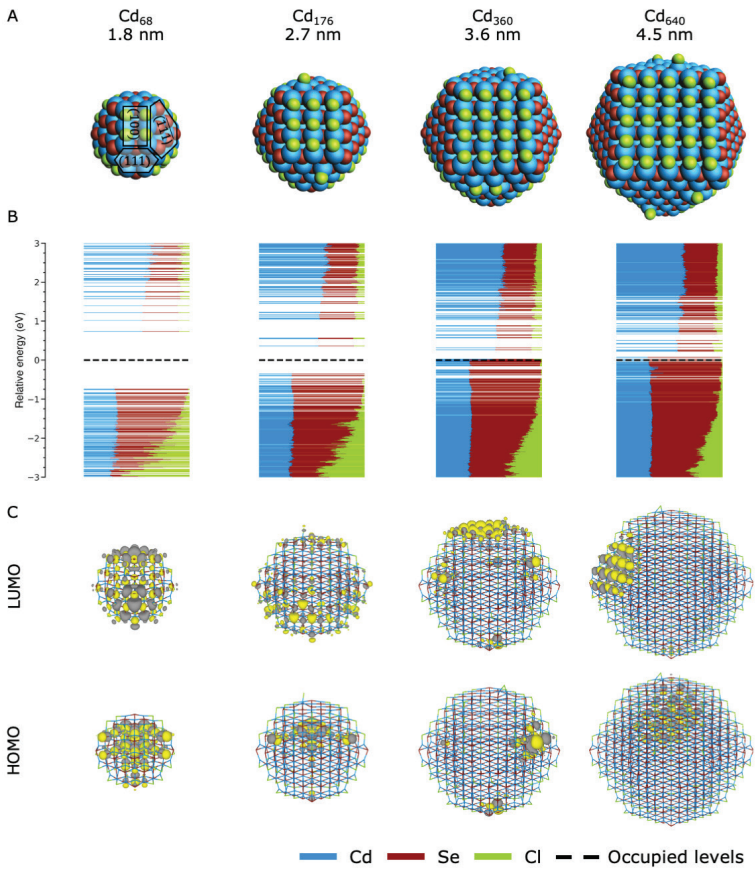

Figure 7.1. Effect of increasing the size of the QD model. (A) Structure of CdSe QD models with a composition of $Cd_{68}Se_{55}Cl_{26}$, $Cd_{176}Se_{147}Cl_{58}$, $Cd_{360}Se_{309}Cl_{102}$, and $Cd_{640}Se_{561}Cl_{158}$, respectively. (B) DOS for each QD. Every horizontal line corresponds to an MO. The length of the colored line segments indicates the contribution of each element to an MO. Levels below the dotted line are filled with two electrons, levels above the line are empty. (C) Contour plots of the HOMO and LUMO of each system.

$$PR_i = \frac{1}{IPR_i} \times \frac{100\%}{N_{Cd} + N_{Se}} = \frac{\left(\sum_\alpha |P_{\alpha,i}|^2\right)^2}{\sum_\alpha |P_{\alpha,i}|^4} \times \frac{100\%}{N_{Cd} + N_{Se}} \qquad 7.1$$

Here, (I)PR_i is the (I)PR of molecular orbital (MO) i, $P_{\alpha,i}$ the weight of MO i on atom α, and N_{Cd} and N_{Se} the number of Cd and Se atoms in the inorganic QD core, respectively. Note that the number of ligand atoms (e.g., N_{Cl^-}, N_{CH3NH2} or N_{CdCl2}) is specifically not included as the contribution of the ligands to the HOMO and LUMO is generally small. Using the given expression for the PR, complete delocalization over the inorganic QD core corresponds to a value of 100%, whereas low values correspond to localized states.

Figure 7.2A shows that both the VB and CB levels of Cd_{68} are delocalized over ~10-60% of the CdSe QD. The HOMO and LUMO levels have similar PR-values, as indicated by the black horizontal lines, which shows that no localization occurs for this QD size. For Cd_{640}, shown in green in Figure 7.2A, the PR-values of the levels deep inside the VB and CB are similar to that of Cd_{68}. However, the PR significantly decreases near the HOMO and LUMO, indicating that the band edges are localized at the QD surface (as shown in Figure 7.1C). Figure 7.2C plots the PR of the HOMO and LUMO for all four QD sizes. It can be seen that the PR of the HOMO drops from ~13% for Cd_{68} to ~1-2% for the three bigger QDs. Likewise, the PR of the LUMO monotonically decreases from ~47% to 1.5%. Figure 7.2B shows that the bandgap decreases with increasing QD size, until the system becomes metallic for Cd_{360} and Cd_{640}. These results confirm and quantify the conclusion, previously based on Figure 7.1C, that increasing the size of the QD leads to surface localization of the band edges.

The disappearance of the bandgap and the localization of the HOMO and LUMO on the QD surface do not agree with multiple experimental findings. The possibility of attaining near-unity photoluminescence quantum yield (PL QY),[48,49] the size-tuneability of the bandgap,[36,37] and the delocalized orbitals as measured by scanning tunneling microscopy[33–35] are all consistent with the traditional description of the band edges as a particle-in-a-box, which predicts that the bandgap > 0 and that the HOMO and LUMO levels are delocalized.[31,32] Hence, we presume that these computational results represent a situation that is not found in real QDs. This can have two possible causes: 1) the computational method is wrong, or 2) the atomistic structure of the modeled QD is wrong.

As further detailed in the Methods, the calculations shown in Figures 7.1 and 7.2 are obtained with a double-ζ basis set and the PBE functional. As shown in Figure A7.1, switching to the larger triple-ζ basis set has no significant effect on either the bandgap or the shape of the HOMO and LUMO. Although it is well known that the PBE functional underestimates the bandgap,[50] it still predicts a bandgap of ~0.5 eV for bulk CdSe, which should hence be the limit for large QDs. Changing to the hybrid PBE0 exchange-correlation functional increases the bandgap of Cd_{176} and Cd_{360} to 1.6 and 0.2 eV, respectively, but does not affect the surface localization (see Figure A7.1). Likewise, switching to ADF[51] instead of CP2K[52] has no significant effect.

As the choice of basis set, functional or software does not qualitatively affect the results, we can conclude that the computational method is not at fault here. Instead, the atomistic structure of our model QD must fail to reproduce key characteristics of QDs in experiment. One possible explanation is that ligands play a pivotal role in the electronic properties of QDs. In experiment, QDs are often completely covered with X-type oleate ligands, L-type ligands like amines or phosphines, and Z-type ligands like $CdCl_2$ or $Cd(RCOO)_2$.[44,53] Yet, for computational efficiency usually only chloride X-type ligands are included as they ensure the QD remains charge balanced. It was previously shown that, for the small Cd_{68} model, the addition of L-type ligands, or the replacement of the chloride X-type ligands with thiolates has little effect on the electronic structure.[13] However, these calculations were not explored for larger QDs. Figure A7.2, shows that for the large Cd_{360} model, exchanging the chlorides for formate ligands has no significant effect on the electronic

structure, in line with the earlier conclusion for Cd_{68}. However, as shown below, differences are observed for the addition of L-type and Z-type ligands to larger QD models. Section 7.2.2 therefore investigates the effect of adding L-type (methylamine) and Z-type ligands ($CdCl_2$) to the (111) facets and to the ($\overline{111}$) facets, respectively.

A second possibility is that the facets of the QD, which are obtained by cutting the QD from the bulk and hence have the same atomic structure as the bulk CdSe crystal, are not stable and will reconstruct under experimental conditions, as has indeed been observed for various bulk surfaces.[41] The effect of surface reconstruction is assessed in section 7.2.3.

7.2.2 Addition of Ligands

In the model structures shown in Figure 7.1A, the Cd-terminated (111) facets are completely unpassivated, save for the incidental chloride ligand that is placed there for charge balance. In experiment, these facets are likely to be passivated by electron donating L-type ligands. To investigate the effect of these ligands, we passivate all Cd atoms on the (111) facets with methylamine, as shown for Cd_{640} in Figure 7.2D. As indicated by the blue data points in Figure 7.2B, the amine ligands have little effect on the bandgap of the QDs. Although the bandgap of Cd_{176} is slightly larger than without amine ligands, both Cd_{360} and Cd_{640} have virtually no bandgap.

Figure 7.2C shows the effect on the PR of the HOMO and LUMO. Although the amines have no systematic effect on the delocalization of the HOMO, they consistently increase the PR of the LUMO. This may be explained by the electronic structure of the CB and VB in CdSe (and II-VI materials in general). As the CB is mainly composed of Cd 5s orbitals and as the amines bind directly to the Cd atoms on the (111) facets, their effect on the LUMO is expected to be greater than on the HOMO. The remarkably large PR of the HOMO of Cd_{640} may be because the lowest of these partly delocalized Cd 5s-derived levels have dropped below the Fermi level (as in a semimetal). Inspection of the contour plot and the DOS near the Fermi level (see Figure A7.3) indeed shows that the HOMO is mainly localized on (111) facets with a large contribution of Cd to the DOS.

As the ($\overline{111}$) facets are terminated by the Lewis base Se, they cannot be passivated by electron donating L-type ligands. Instead, they require electron accepting Z-type ligands. As shown in Figure 7.2D for Cd_{640}, we passivate ~1/3 of the surface Se atoms with a $CdCl_2$ ligand. Figure 7.2B shows that the addition of Z-type ligands, like the addition of amines, has only a moderate effect on the bandgap, giving a bandgap of 0.3 eV for Cd_{640}. The $CdCl_2$ ligands barely affect the PR of the LUMO, but do increase the delocalization of the HOMO. Analogously to the amine ligands, this can be explained by the electronic structure of the QD: the $CdCl_2$ directly binds to the Se atoms, of which the 4p orbitals form the VB, and will hence affect the HOMO more than the LUMO. As shown for Cd_{176} in Figure A7.4, adding more $CdCl_2$ ligands can further improve the delocalization of the HOMO. However, as the anion:cation ratio for $CdCl_2$ is larger than for CdSe (i.e., 2:1 vs 1:1), passivating all Se-sites is expected to lead to significant steric hindrance. Moreover, as will be discussed in the next section, surface reconstruction leads to more delocalization and a larger bandgap than observed for the model with 7 $CdCl_2$ ligands per facet in Figure A7.4.

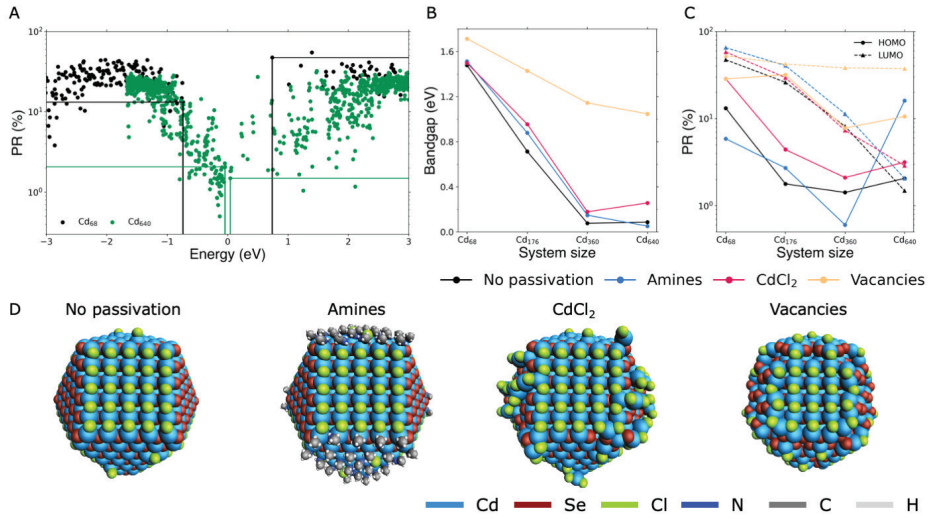

Figure 7.2. Effect of ligand addition and surface reconstructions. (A) PR (i.e., 1/IPR) of Cd_{68} and Cd_{640}. Each data point corresponds to an MO. The horizontal and vertical lines indicate the PR and energy of the HOMO and LUMO of each system. (B) Bandgap as function of the QD size (on the x-axis) and the passivation (indicated by the different colors). (C) PR of the HOMO and LUMO as function of the QD size and passivation. (D) Structures of Cd_{640} with no passivation, L-type methylamine ligands, Z-type $CdCl_2$ ligands, and surface vacancies.

Lastly, as shown in Figure A7.5 for Cd_{640}, the addition of both amines and $CdCl_2$ does not lead to a significant improvement of the electronic properties of the QD. The HOMO and LUMO remain localized on surface facets, while the size of the bandgap is comparable to that of Cd_{640} with only Z-type ligand passivation.

To summarize, although the HOMO and LUMO are slightly delocalized by the $CdCl_2$ and amine ligands, respectively, neither results in complete delocalization of the band edges. Hence, we conclude that the absence of L- and Z-type ligands in Figure 7.1 cannot account for the observed surface localization.

7.2.3 Surface Reconstruction

It is well known from studies on the surfaces of bulk semiconductors, that facets as obtained by cutting the bulk are not always stable and can hence reconstruct.[41] As indicated in Figure 7.1A, our model QDs exhibit (100), (111) and ($\overline{111}$) facets. If only X-type ligands are included in the model, the (100) facets are completely passivated with those ligands. In contrast, the (111) and ($\overline{111}$) facets are almost completely unpassivated, so that they are expected to reconstruct more readily than the (100) facets. Hence, although all three surfaces have been shown to reconstruct,[41] the current study will focus on the behavior of the (111) and ($\overline{111}$) facets.

Although much of the previous research on surface reconstructions of compound

semiconductors has been carried out on GaAs surfaces, it is expected that the findings can be largely transferred to II-VI compounds.[41] In the most commonly observed reconstruction of GaAs (111) surfaces, as shown in Figure 7.3A, 25% of the surface cations is replaced with a vacancy.[38,41,54] The same reconstruction has been predicted for ZnSe,[55] and similar results have been calculated for wurtzite CdSe.[56] For the ($\overline{111}$) surface, multiple structures have been proposed. In 1986 Chadi proposed a multivacancy model, in which both cation and anion vacancies lead to the ring-structure displayed in Figure 7.3B.[39] Subsequently, Biegelsen et al. used scanning tunneling microscopy to demonstrate that the structure shown in Figure 7.3C, where a trimer of anion-adatoms forms on the surface, occurs on the GaAs ($\overline{111}$) surface. Annealing was observed to lead to the structure in Figure 7.3D. Note that the structure of Figure 7.3B can be obtained from Figure 7.3D by shifting the hexagonal structures of the latter such that the protruding cations are turned into bridging atoms.[40]

When introducing surface reconstructions into our model QDs, the cation vacancy reconstruction (Figure 7.3A) is the clear choice for the (111) facets. For the ($\overline{111}$) facets, three options are available. The trimer-structure (Figure 7.3C) is discarded based on charge balance. Introducing so many anions on the ($\overline{111}$) would necessitate the removal of chloride ligands from the (100) facets to retain charge balance, which would significantly destabilize those facets. It is possible that the (100) facets would then also reconstruct,[41] but this possibility is beyond the scope of the current study. Due to the large unit cell of the reconstruction shown in Figure 7.3D, it is difficult to fit it onto a QD facet. Moreover, as the cation/anion ratio is higher than for the structure in Figure 7.3B, more chloride ligands have to be placed on the (111) facets. As shown for Cd_{640} in Figure A7.5, this leads to the formation of unwanted localized states. We therefore chose to continue with the reconstruction of Figure 7.3B.

As shown in Figure 7.2B, introduction of the surface reconstructions increases the bandgap for all QD sizes. The effect is especially pronounced for Cd_{360} and Cd_{640} where the bandgap increases to >1.0 eV. Similar improvements can be seen in the delocalization as plotted in Figure 7.2C. Regardless of the QD size, the LUMO remains delocalized at a PR value of ~40%. Although the PR of the HOMO varies more between the QD systems, the HOMO of the larger QDs is more delocalized than with the ligand passivations. Note that, due to the introduction of vacancies, the number of Cd atoms is slightly lower than indicated by the name (i.e., 68, 176, 360 and 640), the total compositions being $Cd_{56}Se_{43}Cl_{26}$, $Cd_{152}Se_{123}Cl_{58}$, $Cd_{324}Se_{281}Cl_{86}$, and $Cd_{592}Se_{517}Cl_{150}$, respectively.

Figure 7.4 shows the characteristics of Cd_{640} before and after surface reconstruction in more detail. The DOS in Figure 7.4B shows that the system has a bandgap, in contrast to the metallic behavior of the un-reconstructed QD (also shown previously in Figure 7.1B). Instead of the surface localized HOMO and LUMO levels, the reconstructed system has band edges that are delocalized over the entire QD (see Figure 7.4C). Note that, due to the extensive delocalization in Figure 7.4C, there are few areas with high electron density. The iso-surface value has therefore been decreased from |0.01| in Figure 7.1C, to |0.005| $(e^-/bohr^3)^{1/2}$ in Figure 7.4C.

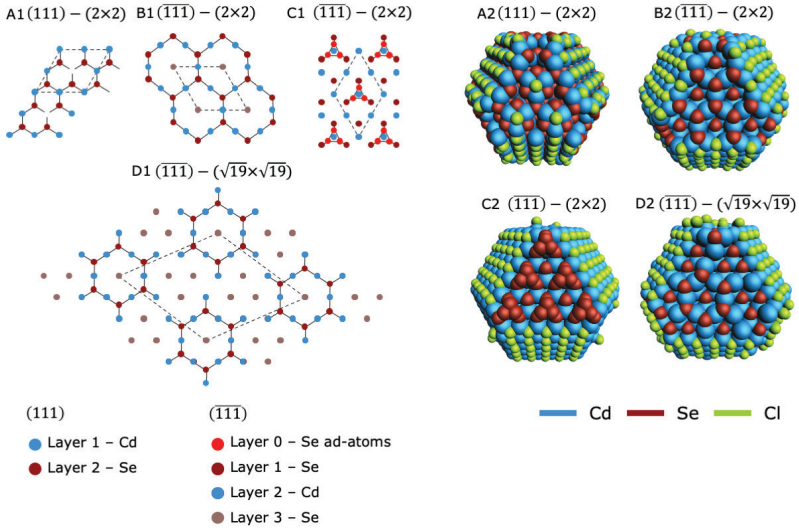

Figure 7.3. Possible reconstructions of (111) and ($\overline{111}$) facets. (A1) Reconstruction of the (111) facet based on a cation vacancy. (B1) Reconstruction of the ($\overline{111}$) facet as proposed by Chadi.[39] (C1/D1) Reconstructions of the ($\overline{111}$) facet as observed by Biegelsen et al.[40] Although these structures have been proposed or observed for GaAs, it is likely that they can be transferred to CdSe surfaces, and they are therefore shown here for CdSe. The layers are counted starting from the surface. For example, the ($\overline{111}$) facet is terminated by a layer of Se atoms (layer 1), with directly below that a layer of Cd atoms (layer 2), followed by another layer of Se (layer 3). Adatoms (layer 0) are located on top of the normal Se-terminated surface. (A2-D2) The reconstructions of panels A1-D1 applied to Cd_{640}. For clarity, the structures have not been optimized (which can lead to small distortions of the reconstructions near edge or corner sites). Note that no attempt has been made to make structure (C2) charge balanced.

As reconstruction of the QD surface makes it possible to create larger QD models that still show the expected behavior (i.e., a bandgap and delocalized band edges), the reconstructed model of Cd_{640} can now also be used to create core/shell structures. Figure 7.4 compares the Cd_{640} model with a CdSe/ZnS core/shell QD, both with and without vacancies. The core/shell model consists of a $Cd_{68}Se_{55}$ core (i.e., the smallest QD model in Figure 7.1) and ~3 layers of ZnS shell, leading to a total composition of $Cd_{68}Se_{55}Zn_{572}S_{506}Cl_{158}$ and $Cd_{68}Se_{55}Zn_{524}S_{462}Cl_{150}$ for the unreconstructed and reconstructed models, respectively (see Figure A7.6 for a view of the inside of the reconstructed core/shell QD). Inspection of Figures 7.4B/C shows that the introduction of reconstructions on the outer ZnS surface of the core/shell structure has a similar effect as for the large core-only QD. Without these vacancies, the HOMO and LUMO levels localize on the surface, rather than in the core of the QD, thus preventing any discussion on the band offset or the distribution of the orbitals. Figure 7.4B also shows that the reconstructed core/shell QD has a larger bandgap than the reconstructed core-only model, reflecting the smaller CdSe core. Comparison of the DOS with the HOMO and LUMO of the core/shell model shows that the HOMO is mainly localized on the core, while the LUMO is more delocalized over the entire system,

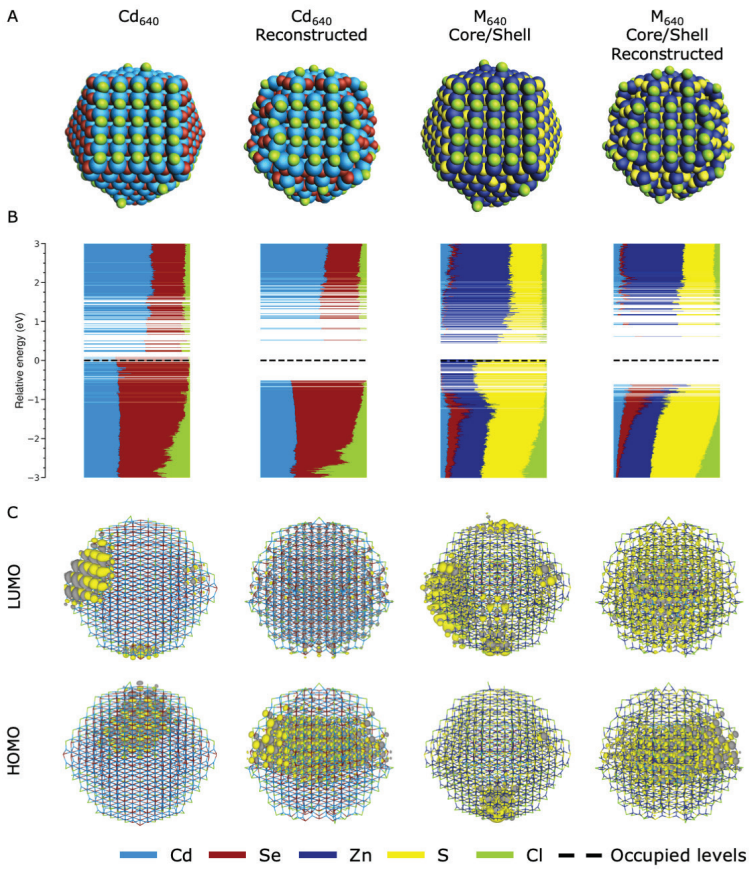

Figure 7.4. Comparison of the Cd_{640} model with the CdSe/ZnS core/shell system, both with and without surface reconstructions. (A) Structure of both the unreconstructed $Cd_{640}Se_{561}Cl_{158}$ (as shown previously in Figure 7.1) and reconstructed $Cd_{592}Se_{517}Cl_{150}$ core-only models; and the unreconstructed $Cd_{68}Se_{55}Zn_{572}S_{506}Cl_{158}$ and reconstructed $Cd_{68}Se_{55}Zn_{524}S_{462}Cl_{150}$ core/shell models. (B) The DOS of each system. (C) Contour plots of the HOMO and LUMO of each system.

suggesting a type $I^{1/2}$ band alignment. It should be noted that the size of the core and shell are expected to influence the amount of quantum confinement and hence the alignment of the band edges of the two materials. Hence, for further study of these core/shell models, the effect of the core and shell size must be carefully considered. Nevertheless, these results show that, given proper termination of the QD surface, DFT can be used to study larger QDs and core/shell systems.

7.2.4 Discussion

The preceding sections clearly and systematically show that surface reconstructions can lead to DFT models that predict semiconductor behavior (i.e., bandgap > 0), with delocalized HOMO and LUMO levels. Three major questions now remain: 1) Why does

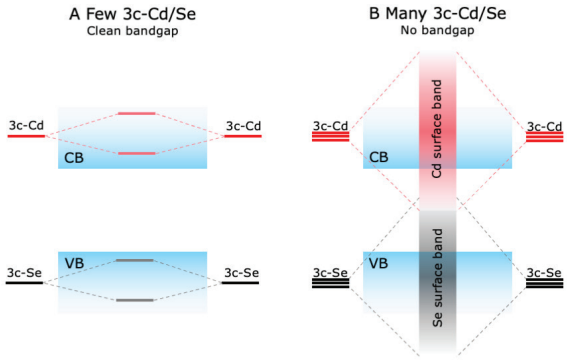

Figure 7.5. Formation of surface-localized bands in unreconstructed QDs. (A) As all atoms in CdSe are sp^3 hybridized, the three-coordinated Se atoms (3c-Se) at the ($\overline{111}$) surface will each have one dangling orbital. Dangling orbitals of neighboring Se atoms may couple to form surface-localized orbitals. If the facet is small, only few 3c-Se atoms are present per facet and the surface-localized orbitals remain in the VB. 3c-Cd atoms at the (111) facets may form surface-localized orbitals in the CB via an analogous process (shown in red). (B) If the QD becomes large enough, many 3c-Se atoms can couple to form surface-localized bands. If the coupling is large enough, part of the surface band may be pushed into the bandgap. 3c-Cd atoms can form a surface-localized band from the CB in the same way. If the Cd and Se surface bands overlap, the system becomes metallic.

surface reconstruction lead to delocalization and the formation of a bandgap?; 2) Why is surface localization not observed in models passivated with pseudo-hydrogen?; and 3) Are the surface reconstructions used for the models in this work also present under experimental conditions (i.e., does surface reconstruction lower the total energy)?

Regarding question 1, it may be expedient to first understand why the *absence* of surface reconstruction leads to a metallic system. Although we currently do not fully understand why this happens, we speculate that the surface-localized levels in the bandgap are the result of coupling between the dangling bonds at the (111) or ($\overline{111}$) facets. In the absence of any reconstruction, the ($\overline{111}$) facet is terminated by three-coordinated Se atoms. As all atoms are sp^3 hybridized, each surface Se atom has one dangling orbital, the energy of which normally lies inside the VB.[13] The dangling orbitals of neighboring Se atoms may couple with each other to form bonding and anti-bonding surface-localized orbitals (see Figure 7.5A). The bigger the QD (and hence its facets) becomes, the more Se atoms can couple, leading to the formation of a band of surface-localized orbitals. If the QD becomes large enough, the coupling between the dangling orbitals may be large enough to push part of the surface-localized band into the bandgap, as shown in Figure 7.5B. Cd atoms on the (111) facets may lead to surface-localized bands that are pushed down from the CB band through an entirely analogous process. If the Se- and Cd-based surface bands overlap, the system becomes metallic (see Figure 7.5B).

Surface reconstruction in QDs may then be rationalized by the Jahn-Teller theorem,[57] which

states that a non-linear system with electronic degeneracy will remove this degeneracy through a structural distortion that lowers both the symmetry and the total energy of the system. Before surface reconstruction, the QD behaves as a metallic system, with a high density of (nearly) degenerate states around the Fermi level. Surface reconstruction lifts this degeneracy by lowering the energy of the occupied orbitals and increasing the energy of the unoccupied ones, thus creating a bandgap. Although surface reconstruction may increase the energy of the QD surfaces by breaking bonds or increasing strain, this energy increase is compensated by the energy that is gained through the formation of the bandgap.

This line of reasoning may also explain why surface states are not found in models passivated with pseudo-hydrogen atoms (question 2). As all QD atoms in such systems are 4-fold coordinated, there is essentially no real surface. Any surface-localized orbital would be split out of the bandgap through the interaction with the pseudo-hydrogens. As a result, there is no metallic behavior, no surface-localized HOMO and LUMO and also no driving force for reconstruction.

Regarding question 3, it is difficult to ascertain what happens on the surface of real QDs under experimental conditions. As explained in the preceding section, multiple reconstructions have been proposed or observed, depending on the preparation conditions. Although we have focused on and obtained good results with the (2x2) reconstructions for both (111) and ($\overline{111}$) facets (Figures 7.3A/B), this does not mean other surface motifs cannot work as well. It may be possible that the real QD surface is a hybrid form between the reconstructions of Section 7.2.3 and the ligand passivations of Section 7.2.2. Another interesting question is whether delocalization of the band edges truly requires such high-symmetry reconstructed facets as studied here, or that a collection of disorganized surface defects can also be sufficient to open up the bandgap (without introducing new localized states due to, for example, two-fold coordinated chalcogenides).[13] Calculating the electronic structure of QDs with the same total number of atoms but differing surface geometries may prove insightful for this. Mapping the QD surface with atomic resolution using, for example, scanning tunneling microscopy, will likely also play a pivotal role in answering this question.

7.3 Conclusions

In conclusion, we have used DFT calculations to study the electronic properties of larger QDs (up to ~4.5 nm in diameter) with realistic surface passivation. It is found that increasing the size of the QD leads to the disappearance of the bandgap and the localization of the HOMO and LUMO on the surface. Additional ligand passivation cannot solve this problem completely. Although L-type amine ligands slightly delocalize the LUMO and Z-type $CdCl_2$ ligands lead to more delocalization of the HOMO, both fail to effectively open up the bandgap. In contrast, the introduction of surface reconstructions on the (111) and ($\overline{111}$) facets leads to the delocalization of both the HOMO and LUMO, and a significant increase of the bandgap. This result may be seen as a Jahn-Teller distortion, where the electronic degeneracy of the metallic system is lifted by lowering the symmetry of the system and the concomitant creation of a bandgap. These results show that the QD surface plays a pivotal role in the delocalization of the wavefunction, which depends not

only on the presence of (in)organic ligands but also on the surface geometry of the QD facets.

7.4 Methods

Geometry optimizations were carried out at the DFT level using a PBE exchange-correlation functional[58] and double-ζ basis set, as implemented in the CP2K quantum chemistry software package.[52] Relativistic effects were taken into account via effective core potentials. Structures were relaxed until the following criteria were met: max_force: 4.5×10^{-4} Ha/bohr; rms_force: 3.0×10^{-4} Ha/bohr; max_step: 3.0×10^{-3} bohr; rms_step: 1.5×10^{-3} bohr. For the core/shell QD without surface reconstructions, it was necessary to increase max_force to 2.5×10^{-3} Ha/bohr, which might be indicative of strain at the core/shell interface. Due to their large size (>2000 atoms), the Cd_{640} models with amine ligands were optimized with more relaxed criteria: max_force: 6.0×10^{-4} Ha/bohr; rms_force: 3.0×10^{-4} Ha/bohr; max_step: 2.0×10^{-2} bohr; rms_step: 2.0×10^{-3} bohr. The IPR and the COOP (the computational details of which have been discussed previously)[59] were calculated using the workflows implemented in the Nano-QMFlows package.[60] Further details are given in the main text and the Appendix.

References

1. Pascazio, R., Zito, J. & Infante, I. An Overview of Computational Studies on Colloidal Semiconductor Nanocrystals. Chim. Int. J. Chem. 75, 427–434 (2021).
2. Prezhdo, O. V. Photoinduced dynamics in semiconductor quantum Dots: Insights from time-domain ab initio studies. Acc. Chem. Res. 42, 2005–2016 (2009).
3. Kilina, S. V., Tamukong, P. K. & Kilin, D. S. Surface Chemistry of Semiconducting Quantum Dots: Theoretical Perspectives. Acc. Chem. Res. 49, 2127–2135 (2016).
4. Hong, Y., Wu, Y., Wu, S., Wang, X. & Zhang, J. Overview of Computational Simulations in Quantum Dots. Isr. J. Chem. 59, 661–672 (2019).
5. Hens, Z. & De Roo, J. Atomically Precise Nanocrystals. J. Am. Chem. Soc. 142, 15627–15637 (2020).
6. Eichkorn, K. & Ahlrichs, R. Cadmium selenide semiconductor nanocrystals: A theoretical study. Chem. Phys. Lett. 288, 235–242 (1998).
7. Puzder, A., Williamson, A. J., Gygi, F. & Galli, G. Self-healing of CdSe nanocrystals: First-principles calculations. Phys. Rev. Lett. 92, 1–4 (2004).
8. Deglmann, P., Ahlrichs, R. & Tsereteli, K. Theoretical studies of ligand-free cadmium selenide and related semiconductor clusters. J. Chem. Phys. 116, 1585–1597 (2002).
9. Voznyy, O. Mobile Surface Traps in CdSe Nanocrystals with Carboxylic Acid Ligands. J. Phys. Chem. C 115, 15927–15932 (2011).
10. Snee, P. T. DFT Calculations of InP Quantum Dots: Model Chemistries, Surface Passivation, and Open-Shell Singlet Ground States. J. Phys. Chem. C 125, 11765–11772 (2021).
11. Rusishvili, M., Wippermann, S., Talapin, D. V. & Galli, G. Stoichiometry of the Core Determines the Electronic Structure of Core–Shell III–V/II–VI Nanoparticles. Chem. Mater. 32, 9798–9804 (2020).
12. Yazdani, N., Bozyigit, D., Vuttivorakulchai, K., Luisier, M., Infante, I. & Wood,

V. Tuning Electron-Phonon Interactions in Nanocrystals through Surface Termination. Nano Lett. 18, 2233–2242 (2018).
13. Houtepen, A. J., Hens, Z., Owen, J. S. & Infante, I. On the Origin of Surface Traps in Colloidal II–VI Semiconductor Nanocrystals. Chem. Mater. 29, 752–761 (2017).
14. Voznyy, O., Thon, S. M., Ip, A. H. & Sargent, E. H. Dynamic Trap Formation and Elimination in Colloidal Quantum Dots. J. Phys. Chem. Lett. 4, 987–992 (2013).
15. du Fossé, I., Boehme, S. C., Infante, I. & Houtepen, A. J. Dynamic Formation of Metal-Based Traps in Photoexcited Colloidal Quantum Dots and Their Relevance for Photoluminescence. Chem. Mater. 33, 3349–3358 (2021).
16. Groeneveld, E., Delerue, C., Allan, G., Niquet, Y. M. & De Mello Donegá, C. Size dependence of the exciton transitions in colloidal CdTe quantum dots. J. Phys. Chem. C 116, 23160–23167 (2012).
17. Keuleyan, S. E., Guyot-Sionnest, P., Delerue, C. & Allan, G. Mercury Telluride Colloidal Quantum Dots: Electronic Structure, Size-Dependent Spectra, and Photocurrent Detection up to 12 μm. ACS Nano 8, 8676–8682 (2014).
18. Allan, G. & Delerue, C. Tight-binding calculations of the optical properties of HgTe nanocrystals. Phys. Rev. B - Condens. Matter Mater. Phys. 86, 1–6 (2012).
19. Moreels, I., Lambert, K., Smeets, D., De Muynck, D., Nollet, T., Martins, J. C., Vanhaecke, F., Vantomme, A., Delerue, C., Allan, G., et al. Size-dependent optical properties of colloidal PbS quantum dots. ACS Nano 3, 3023–3030 (2009).
20. Califano, M. & Gómez-Campos, F. M. Universal Trapping Mechanism in Semiconductor Nanocrystals. Nano Lett. 13, 2047–2052 (2013).
21. Gómez-Campos, F. M. & Califano, M. Hole surface trapping in CdSe nanocrystals: Dynamics, rate fluctuations, and implications for blinking. Nano Lett. 12, 4508–4517 (2012).
22. Wang, L. W. & Zunger, A. Pseudopotential calculations of nanoscale CdSe quantum dots. Phys. Rev. B - Condens. Matter Mater. Phys. 53, 9579–9582 (1996).
23. Fu, H. & Zunger, A. InP quantum dots: Electronic structure, surface effects, and the redshifted emission. Phys. Rev. B - Condens. Matter Mater. Phys. 56, 1496–1508 (1997).
24. Delerue, C. J. & Lannoo, M. Nanostructures: Theory and Modeling. vol. 59 (Springer, 2004).
25. Cosseddu, S. & Infante, I. Force field parametrization of colloidal CdSe nanocrystals using an adaptive rate monte carlo optimization algorithm. J. Chem. Theory Comput. 13, 297–308 (2017).
26. Pascazio, R., Zaccaria, F., van Beek, B. & Infante, I. Classical Force-Field Parameters for CsPbBr 3 Perovskite Nanocrystals. J. Phys. Chem. C 126, 9898–9908 (2022).
27. Zhang, H., Ma, X., Lin, Q., Zeng, Z., Wang, H., Li, L. S., Shen, H., Jia, Y. & Du, Z. High-Brightness Blue InP Quantum Dot-Based Electroluminescent Devices: The Role of Shell Thickness. J. Phys. Chem. Lett. 11, 960–967 (2020).
28. Voigt, D., Bredol, M. & Gonabadi, A. A general strategy for CuInS2 based quantum dots with adjustable surface chemistry. Opt. Mater. (Amst). 115, 110994 (2021).
29. Voznyy, O. & Sargent, E. H. Atomistic model of fluorescence intermittency of colloidal quantum dots. Phys. Rev. Lett. 112, 1–5 (2014).
30. Singh, S., Tomar, R., ten Brinck, S., De Roo, J., Geiregat, P., Martins, J. C., Infante,

I. & Hens, Z. Colloidal CdSe Nanoplatelets, A Model for Surface Chemistry/ Optoelectronic Property Relations in Semiconductor Nanocrystals. J. Am. Chem. Soc. 140, 13292–13300 (2018).
31. Brus, L. Electronic wave functions in semiconductor clusters: Experiment and theory. J. Phys. Chem. 90, 2555–2560 (1986).
32. Chukwuocha, E. O., Onyeaju, M. C. & Harry, T. S. T. Theoretical Studies on the Effect of Confinement on Quantum Dots Using the Brus Equation. World J. Condens. Matter Phys. 02, 96–100 (2012).
33. Nienhaus, L., Goings, J. J., Nguyen, D., Wieghold, S., Lyding, J. W., Li, X. & Gruebele, M. Imaging Excited Orbitals of Quantum Dots: Experiment and Electronic Structure Theory. J. Am. Chem. Soc. 137, 14743–14750 (2015).
34. Maltezopoulos, T., Bolz, A., Meyer, C., Heyn, C., Hansen, W., Morgenstern, M. & Wiesendanger, R. Wave-Function Mapping of InAs Quantum Dots by Scanning Tunneling Spectroscopy. Phys. Rev. Lett. 91, 196804 (2003).
35. Maruccio, G. & Wiesendanger, R. Scanning Tunneling Spectroscopy of Semiconductor Quantum Dots and Nanocrystals. in Quantum Materials, Lateral Semiconductor Nanostructures, Hybrid Systems and Nanocrystals (ed. Heitmann, D.) 183–216 (Springer, 2010). doi:https://doi.org/10.1007/978-3-642-10553-1.
36. Shirasaki, Y., Supran, G. J., Bawendi, M. G. & Bulović, V. Emergence of colloidal quantum-dot light-emitting technologies. Nat. Photonics 7, 13 (2013).
37. Donegá, C. de M. Synthesis and properties of colloidal heteronanocrystals. Chem. Soc. Rev. 40, 1512–1546 (2011).
38. Chadi, D. J. Vacancy-induced 2×2 reconstruction of the Ga(111) surface of GaAs. Phys. Rev. Lett. 52, 1911–1914 (1984).
39. Chadi, D. J. Atomic structure of the (2×2) reconstructed GaAs(1^{-} 1^{-} 1^{-}) surface: A multivacancy model. Phys. Rev. Lett. 57, 102–105 (1986).
40. Biegelsen, D. K., Bringans, R., Northrup, J. & Swartz, L.-E. Reconstructions of GaAs(1^{-} 1^{-} 1^{-}) surfaces observed by scanning tunneling microscopy. Phys. Rev. Lett. 65, 452–455 (1990).
41. Duke, C. B. Semiconductor Surface Reconstruction: The Structural Chemistry of Two-Dimensional Surface Compounds. Chem. Rev. 96, 1237–1260 (1996).
42. du Fossé, I., ten Brinck, S., Infante, I. & Houtepen, A. J. Role of Surface Reduction in the Formation of Traps in n-Doped II–VI Semiconductor Nanocrystals: How to Charge without Reducing the Surface. Chem. Mater. 31, 4575–4583 (2019).
43. du Fossé, I., Lal, S., Hossaini, A. N., Infante, I. & Houtepen, A. J. Effect of Ligands and Solvents on the Stability of Electron Charged CdSe Colloidal Quantum Dots. J. Phys. Chem. C 125, 23968–23975 (2021).
44. Anderson, N. C., Hendricks, M. P., Choi, J. J. & Owen, J. S. Ligand Exchange and the Stoichiometry of Metal Chalcogenide Nanocrystals: Spectroscopic Observation of Facile Metal-Carboxylate Displacement and Binding. J. Am. Chem. Soc. 135, 18536–18548 (2013).
45. Greaney, M. J., Couderc, E., Zhao, J., Nail, B. A., Mecklenburg, M., Thornbury, W., Osterloh, F. E., Bradforth, S. E. & Brutchey, R. L. Controlling the Trap State Landscape of Colloidal CdSe Nanocrystals with Cadmium Halide Ligands. Chem. Mater. 27, 744–756 (2015).

46. Voznyy, O., Zhitomirsky, D., Stadler, P., Ning, Z., Hoogland, S. & Sargent, E. H. A Charge-Orbital Balance Picture of Doping in Colloidal Quantum Dot Solids. ACS Nano 6, 8448–8455 (2012).
47. Drijvers, E., De Roo, J., Martins, J. C., Infante, I. & Hens, Z. Ligand Displacement Exposes Binding Site Heterogeneity on CdSe Nanocrystal Surfaces. Chem. Mater. 30, 1178–1186 (2018).
48. Kirkwood, N., Monchen, J. O. V., Crisp, R. W., Grimaldi, G., Bergstein, H. A. C., du Fossé, I., van der Stam, W., Infante, I. & Houtepen, A. J. Finding and Fixing Traps in II–VI and III–V Colloidal Quantum Dots: The Importance of Z-Type Ligand Passivation. J. Am. Chem. Soc. 140, 15712–15723 (2018).
49. Page, R. C., Espinobarro-Velazquez, D., Leontiadou, M. A., Smith, C., Lewis, E. A., Haigh, S. J., Li, C., Radtke, H., Pengpad, A., Bondino, F., et al. Near-Unity Quantum Yields from Chloride Treated CdTe Colloidal Quantum Dots. Small 11, 1548–1554 (2015).
50. Azpiroz, J. M., Ugalde, J. M. & Infante, I. Benchmark Assessment of Density Functional Methods on Group II-VI MX (M = Zn, Cd; X = S, Se, Te) Quantum Dots. J. Chem. Theory Comput. 10, 76–89 (2014).
51. te Velde, G., Bickelhaupt, F. M., Baerends, E. J., Fonseca Guerra, C., van Gisbergen, S. J. A., Snijders, J. G. & Ziegler, T. Chemistry with ADF. J. Comput. Chem. 22, 931–967 (2001).
52. Hutter, J., Iannuzzi, M., Schiffmann, F. & VandeVondele, J. cp2k: atomistic simulations of condensed matter systems. Wiley Interdiscip. Rev. Comput. Mol. Sci. 4, 15–25 (2014).
53. Boles, M. A., Ling, D., Hyeon, T. & Talapin, D. V. The surface science of nanocrystals. Nat. Mater. 15, 141–153 (2016).
54. Haberern, K. W. & Pashley, M. D. GaAs(111)A-(2×2) reconstruction studied by scanning tunneling microscopy. Phys. Rev. B 41, 3226–3229 (1990).
55. Chadi, D. J. Atomic structure of polar (111) surfaces of GaAs and ZnSe. J. Vac. Sci. Technol. A Vacuum, Surfaces, Film. 4, 944–946 (1986).
56. Manna, L., Wang, L. W., Cingolani, R. & Alivisatos, A. P. First-Principles Modeling of Unpassivated and Surfactant-Passivated Bulk Facets of Wurtzite CdSe: A Model System for Studying the Anisotropic Growth of CdSe Nanocrystals. J. Phys. Chem. B 109, 6183–6192 (2005).
57. Jahn, H. A. & Teller, E. Stability of polyatomic molecules in degenerate electronic states - I—Orbital degeneracy. Proc. R. Soc. London. Ser. A - Math. Phys. Sci. 161, 220–235 (1937).
58. Perdew, J. P., Burke, K. & Ernzerhof, M. Generalized Gradient Approximation Made Simple. Phys. Rev. Lett. 77, 3865–3868 (1996).
59. du Fossé, I., Mulder, J. T., Almeida, G., Spruit, A. G. M., Infante, I., Grozema, F. C. & Houtepen, A. J. Limits of Defect Tolerance in Perovskite Nanocrystals: Effect of Local Electrostatic Potential on Trap States. J. Am. Chem. Soc. 144, 11059–11063 (2022).
60. Zapata, F., Ridder, L., Hidding, J., Jacob, C. R., Infante, I. & Visscher, L. QMflows: A Tool Kit for Interoperable Parallel Workflows in Quantum Chemistry. J. Chem. Inf. Model. 59, 3191–3197 (2019).

Appendix

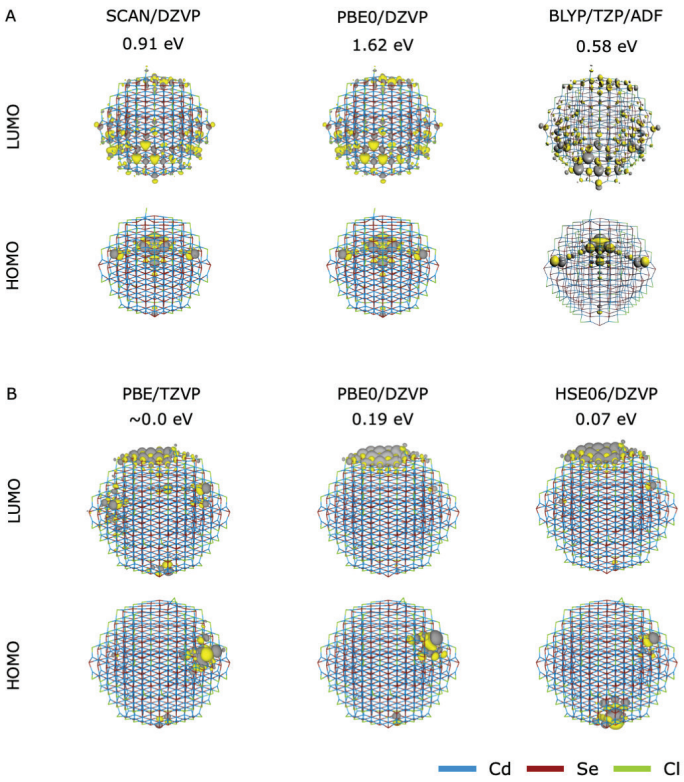

Figure A7.1. Delocalization and bandgap as computed with different basis sets, functionals and software packages. (A) Contour plots of the HOMO and LUMO of Cd_{176}, as shown in Figure 7.1. The size of the bandgap is given above each plot of the LUMO. (B) Contour plots of the HOMO and LUMO of Cd_{360}. To limit the computational cost, all calculations are single point calculations based on the optimized structures shown in Figure 7.1. All calculations were carried out using the CP2K software package, with the exception of the BLYP/TZP/ADF calculation, which was computed in ADF.[51]

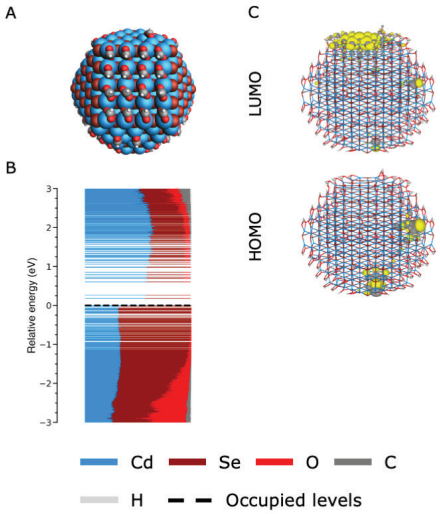

Figure A7.2. Details of Cd_{360} with formate ligands instead of chlorides. (A) Structure, (B) DOS and (C) contour plots of the HOMO and LUMO.

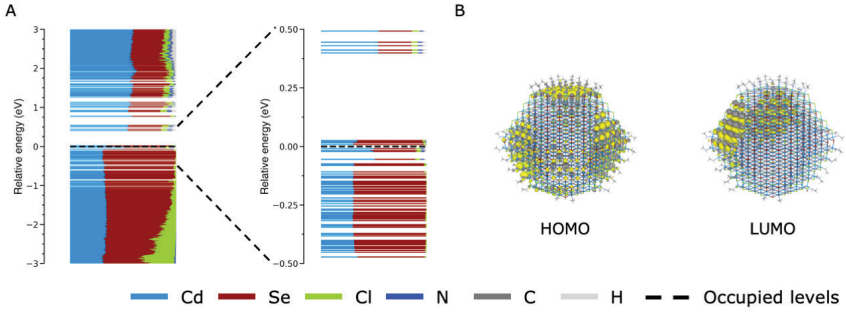

Figure A7.3. Details of Cd_{640} with amine passivation. (A) DOS with enlarged view around the Fermi level. Note the large Cd contribution to the VB edge. The ratio of Cd/Se contribution to the HOMO is 1.25, while it is only 0.42 for Cd_{68} and 0.40 for Cd_{640} with surface reconstructions. (B) Contour plots of the HOMO and LUMO. Note how the HOMO is mainly localized on Cd-terminated and thus amine-passivated (111) facets. These results suggest the HOMO is formed by a Cd 5s derived level and may explain the large PR value of the HOMO in Figure 7.2C.

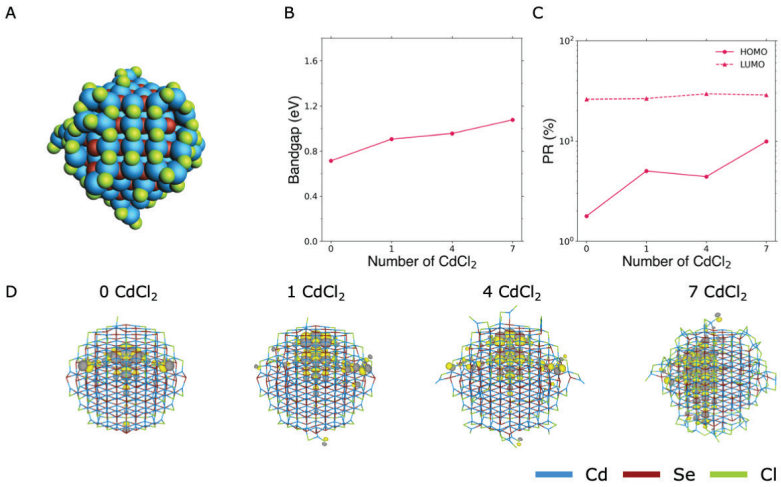

Figure A7.4. Effect of the number of Z-type ligands on the bandgap and delocalization. (A) Structure of Cd_{176} with 7 $CdCl_2$ ligands on each ($\overline{111}$) facet. (B) Bandgap and (C) PR of the HOMO and LUMO of Cd_{176} with 0, 1, 4 and 7 $CdCl_2$ ligands per facet. (D) The HOMO of each system.

7

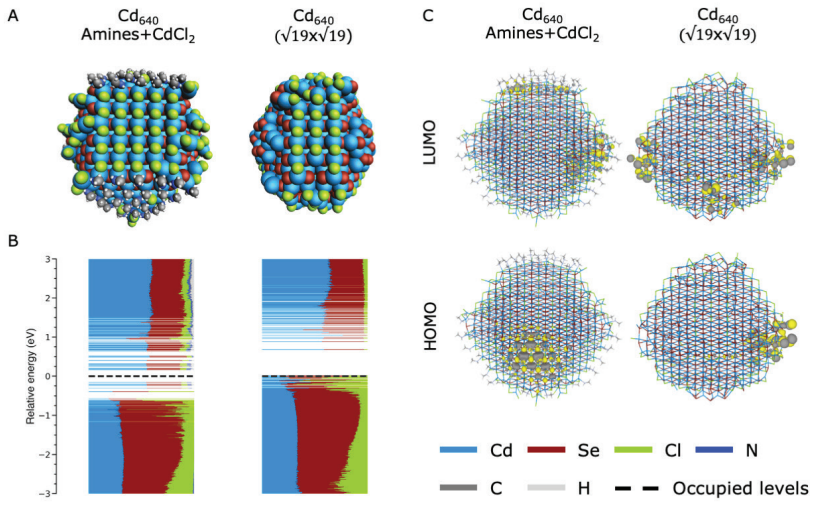

Figure A7.5. Details of Cd_{640} with both amine and $CdCl_2$ ligands, and Cd_{640} with the (√19x√19) surface reconstruction as shown in Figure 7.3D. (A) Structures of the two QDs. Note that the "normal" (2x2) vacancy reconstruction has been used for the (111) facets of the surface reconstructed model. (B) DOS and (C) contour plots of the HOMO and LUMO of each system.

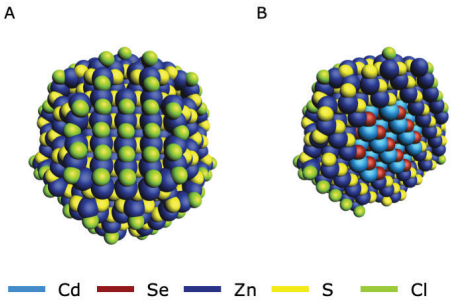

Figure A7.6. Structure of the core/shell QD model shown in Figure 7.4. (A) External view of the $Cd_{68}Se_{55}Zn_{524}S_{462}Cl_{150}$ model (as also shown in the main text). (B) Sliced view of the QD, showing the CdSe core.

Summary and Outlook

A quantum dot (QD) can be defined as a nanoparticle of a semiconductor material that is so small that quantum confinement takes place. This effect causes several of the properties of the QD to become dependent on the size of the particle, leading to a bandgap and hence a color that can be tuned by simply varying the QD size. Due to this size-tuneability, high quantum yield, and relatively cheap and easy solution-based processing, QDs are very interesting for application in devices. Unfortunately, certain atomic configurations, usually present at the QD surface, can lead to localized states that form an energy level inside the bandgap, so-called "trap states". Traps can capture charge carriers, which often limits the efficiency of QD-based devices. Therefore, this thesis is dedicated to investigating the atomistic nature of these trap states and finding strategies to passivate (i.e., remove) them.

The main concepts that are used in this thesis are explained in **Chapter 1**. First, an overview is given of how our understanding of traps has developed over the years. From simply positing that some trap state must be present somewhere on the QD surface, we have come to understand that only specific configurations of atoms lead to trap states, and that a variety of factors (e.g., ligands, charge balance, thermal motion) can influence whether a trap is formed or not. Next, the basics of density functional theory (DFT) calculations are explained, which are used extensively in Chapters 3-7 to study traps on an atomistic scale.

We begin our investigation of trap states with the spectroelectrochemical study presented in **Chapter 2**. CdTe QDs are passivated with different metal-chloride salts, after which their absorption and photoluminescence (PL) are studied as a function of the applied potential. Untreated films of CdTe QDs show a strong increase in PL when the Fermi-level is raised electrochemically, indicating that trap states are filled with electrons. Upon passivation with the Z-type ligand $CdCl_2$, the steady state PL intensity showed a 40-fold increase, and became independent of the applied potential. Passivation with $ZnCl_2$ made the PL less dependent on the applied potential, but only increased the steady state PL by a factor of four. Elemental analysis suggested that, while $CdCl_2$ binds as a Z-type ligand, $ZnCl_2$ only binds to the surface as an X-type Cl^- ligand. These results indicate that in-gap states in CdTe QDs are mainly due to undercoordinated Te-atoms (which are passivated via Z-type ligands), but that other, likely metal-based, traps, which are passivated via X-type ligands, are also present.

In **Chapter 3**, we use DFT calculations to elucidate the nature of the metal-based traps proposed in Chapter 2. As only chalcogenide-based traps were found in charge balanced QDs, this study focused on charge unbalanced systems. Charging QDs with excess electrons can lead to trap formation in two ways. Firstly, if QDs are perfectly passivated (by having all X-type ligands in the optimal position), charging will eventually lead to the reduction of surface Cd atoms, followed by their ejection from the lattice and the formation of a trap state. Secondly, if the QD is suboptimally passivated by moving one Cl^-

ligand from a (100) facet to a nearby (111) facet, the addition of only one electron will lead to the formation of a Cd-Cd dimer and an in-gap state. L-type amine ligands can sterically block Cd dimerization, which may explain why addition of amines has been observed to increase the PL QY of QDs.

Where the preceding chapter focused on metal-metal dimerization in charge unbalanced QDs, **Chapter 4** looks deeper into the possibility of dimerization in charge balanced but photoexcited QDs. We return to the suboptimally passivated QD from Chapter 3, but instead of charging it, we approach the excited state by forcing a triplet state, which puts one electron in the conduction band (CB) and leaves a hole in the valence band (VB). Ab initio molecular dynamics simulations show that Cd-Cd dimers are transient in nature, appearing and disappearing on the picosecond time scale when the QD is in the excited state. Formation of the dimer traps the CB electron in a trap state, from which nonradiative recombination is much faster than radiative recombination. These results show that photoexcitation can lead to the creation of transient trap states that would not have formed in the ground state.

In **Chapter 5**, we return to the reduction of surface Cd in perfectly passivated QDs (as defined in Chapter 3). Specifically, we investigate the effect of various X- and L-type ligands, and solvents on the energetics of surface reduction. As also observed in previous experiments, we find that X-type ligands can significantly shift the energy of the CB and VB levels. However, as the in-gap state related to reduced surface Cd largely moves in the same direction, shifting the band edges only has a minor effect on the stability of electron charged QDs. In contrast, binding L-type ligands directly to the Cd sites that are most prone to reduction significantly stabilizes the system against surface reduction. As the L-type ligands bind more weakly after reduction of the Cd, charge localization and concomitant reduction lead to a decrease in binding energy, making reduction no longer energetically favorable. Increasing the solvent polarity also stabilizes electron charged systems, showing that the complete ligand shell and the details of the environment all play a role in the energetics of surface reduction.

Chapter 6 turns to $CsPbBr_3$ nanocrystals (NCs). Due to the electronic structure of their CB and VB, lead halide perovskite NCs are said to be defect tolerant, which means that undercoordinated ions only form localized levels close to or inside the band edges. Yet, various studies show that undercoordinated surface Br^- ions can still form deep trap states. In this study, we argue that the traditional picture of defect tolerance is incomplete and should also include the effect of the local electrostatic potential. We show that surface Br^- ions experience a destabilizing electrostatic potential, which increases the energy of the localized states and pushes the trap levels into the bandgap. Addition of positive ions can electrostatically passivate the deep traps through ionic interactions, indicating that covalent ligand binding is not always necessary for trap passivation.

Lastly, in **Chapter 7**, we seek the limits of the QD models that were used throughout this thesis. In order to study realistically sized QDs and core/shell systems, the size of the model system has to be increased significantly. However, simply making the model system (as used in Chapters 3-5) larger leads to localization of the band edge levels on the

QD surface. In this study we show that, although addition of Z- or L-type ligands slightly improves the delocalization, surface reconstructions are needed to delocalize the band edges entirely. These surface reconstructions may be understood as a type of Jahn-Teller distortion, where reorganization of the QD facets converts a metallic system (i.e., bandgap ≈ 0) into a semiconducting one (bandgap > 0).

Although DFT is an extremely valuable tool for investigating the atomistic nature of traps in QDs, one has but to look at the limitations and challenges of DFT in Chapter 1 (section 1.3.2) to understand how much work still can and must be done. An obvious first step would be to continue the research presented in Chapter 7. In order to investigate traps in a meaningful way with our model system, we first have to understand the behavior of the model system without traps. Once we have overcome this hurdle, the way lies open to the study of, for example, realistically sized core/shell systems. However, trap formation is not just affected by the inorganic part of the QD, but also by all the other ligands and solvent molecules that surround it (chapter 5); by the electronic state of the QD (i.e., ground state or excited state); and by the random thermal movement of all those atoms (Chapter 4). Including all these effects would require a computational power that vastly exceeds current practical limits. Therefore, for future research it will always remain important to realize that we study, not real QDs, but models of real QDs; and that the value of the obtained results is limited by our understanding of the model. Thus, instead of only focusing on making the model more and more complicated (in an attempt to make it more realistic), much can be gleaned from trying to understand the strengths and weaknesses of more "simplistic" models, like the ones used in this thesis.

Samenvatting en Vooruitzichten

Een kwantumstip (KS) kan worden gedefinieerd als een nanodeeltje van een halfgeleidermateriaal, dat zo klein is dat "kwantum opsluiting" plaatsvindt. Door dit effect gaan de eigenschappen van de KS afhangen van de grootte van het deeltje, hetgeen leidt tot een bandkloof en daardoor een kleur die aangepast kunnen worden door de grootte van de KS te variëren. Door deze grootte-afhankelijke eigenschappen, hoge kwantum efficiëntie, en relatief goedkope en makkelijke verwerking op basis van vloeistoffen, zijn KS'en erg interessant voor toepassing in apparaten. Helaas kunnen sommige atomaire configuraties, die vaak op het oppervlak van de KS aanwezig zijn, leiden tot gelokaliseerde toestanden die een energieniveau vormen in de bandkloof, zogenaamde "valkuil toestanden". Valkuil toestanden kunnen ladingsdragers vangen, wat vaak de efficiëntie van apparaten op basis van KS'en vermindert. Deze thesis is daarom gewijd aan het onderzoeken van de atomaire aard van deze valkuil toestanden en het vinden van strategieën om ze te "passiveren" (te verwijderen).

De belangrijkste concepten die in deze thesis worden gebruik, worden uitgelegd in **Hoofdstuk 1**. Er wordt allereerst een overzicht gegeven over hoe onze kennis van valkuil toestanden zich over de jaren heeft ontwikkeld. Hoewel we initieel simpelweg aannamen dat ergens op het KS-oppervlak een zekere valkuil toestand zat, begrijpen we nu dat slechts specifieke configuraties van atomen tot valkuil toestanden leiden en dat een veelvoud aan factoren (zoals liganden, ladingsbalans en thermische beweging) de vorming van een valkuil toestand kan beïnvloeden. Daarna wordt de basis van dichtheidsfunctionaaltheorie (DFT) berekeningen uitgelegd, die in Hoofdstukken 3-7 veelvuldig worden gebruikt om valkuil toestanden op een atomaire schaal te onderzoeken.

We beginnen ons onderzoek naar valkuil toestanden met de spectro-elektrochemische studie in **Hoofdstuk 2**. CdTe KS'en worden gepassiveerd met verschillende metaalchloride zouten, waarna hun absorptie en fotoluminescentie (FL) wordt bestudeerd als functie van de aangebrachte potentiaal. Onbehandelde films van CdTe KS'en laten een sterke toename van de FL zien wanneer het Ferminiveau elektrochemisch wordt verhoogd, hetgeen aangeeft dat valkuil toestanden worden gevuld met elektronen. Na passivatie met het Z-type ligand $CdCl_2$, wordt de FL-intensiteit zowel 40 keer groter als onafhankelijk van de aangebrachte potentiaal. Passivatie met $ZnCl_2$ zorgt er ook voor dat de FL minder varieert als functie van de potentiaal, maar verhoogt de FL slechts met een factor vier. Elementaire analyse wijst erop dat $CdCl_2$ als een Z-type ligand aan het oppervlak bindt en $ZnCl_2$ als een X-type Cl^- ligand. Deze resultaten laten zien dat valkuil toestanden op CdTe KS'en vooral te wijten zijn aan onder-gecoördineerde Te-atomen (die gepassiveerd worden met Z-type liganden), maar dat er ook andere valkuil toestanden aanwezig zijn, waarschijnlijk gelokaliseerd op metaalatomen, die met X-type liganden kunnen worden gepassiveerd.

In **Hoofdstuk 3** gebruiken we DFT-berekeningen om meer te weten te komen over de op metaal gelokaliseerde valkuil toestanden, die in Hoofdstuk 2 werden voorgesteld. Aangezien voor lading-gebalanceerde KS'en alleen valkuil toestanden op chalcogenide atomen zijn gevonden, focust dit hoofdstuk op lading-ongebalanceerde systemen. Het opladen van een KS met extra elektronen kan op twee manieren leiden tot de formatie van een valkuil toestand. Ten eerste, als KS'en perfect gepassiveerd zijn (door alle X-type liganden op de optimale positie te hebben), leidt oplading uiteindelijk tot de reductie van Cd-atomen op het oppervlak, wat gevolgd wordt door de expulsie van die atomen uit het atoomrooster en de formatie van een valkuil toestand. Ten tweede, in het geval van een suboptimaal gepassiveerde KS waar één Cl^- ligand van een (100) naar een (111) facet is verplaatst, leidt de toevoeging van één elektron al tot de formatie van een Cd-Cd dimeer en een valkuil toestand. L-type amine liganden kunnen de dimerisatie van Cd-atomen voorkomen door sterische hindering, wat zou kunnen verklaren waarom in experimenten toevoeging van amines vaak tot een toename van de FL-efficiëntie leidt.

Waar het voorgaande hoofdstuk keek naar metaal-metaal dimerisatie in lading-ongebalanceerde KS'en, kijkt **Hoofdstuk 4** naar de mogelijkheid van dimerisatie in lading-gebalanceerde, maar foto-geëxciteerde KS'en. Hiervoor nemen we weer de suboptimaal gepassiveerde KS uit Hoofdstuk 3, maar in plaats van hem op te laden, benaderen we de geëxciteerde toestand door een triplet toestand te forceren, hetgeen één elektron in de geleidingsband (GB) en één gat in de valentieband (VB) plaatst. Middels ab initio moleculaire dynamica berekeningen laten we vervolgens zien dat Cd-Cd dimeren tijdelijk van aard zijn. In de geëxciteerde toestand verschijnen en verdwijnen ze op een tijdsschaal van enkele picoseconden. De formatie van de dimeer vangt het elektron uit de GB in een valkuil toestand, waarvandaan non-radiatieve recombinatie veel sneller is dan radiatieve recombinatie. Deze resultaten laten zien dat foto-excitatie kan leiden tot de formatie van tijdelijke valkuil toestanden, die niet zouden vormen in de grondtoestand.

In **Hoofdstuk 5** keren we terug naar de reductie van oppervlakte Cd in perfect gepassiveerde KS'en (zoals gedefinieerd in Hoofdstuk 3). We kijken specifiek naar het effect van verscheidene X- en L-type liganden, en oplosmiddelen op de energie die oppervlaktereductie oplevert of kost. Zoals ook eerder waargenomen, vinden we dat X-type liganden de energie van de GB en VB significant kunnen veranderen. Echter, omdat de valkuil toestand gerelateerd aan het gereduceerde oppervlakte Cd grotendeels in dezelfde richting schuift, heeft het verschuiven van de GB en VB slechts een klein effect op de stabiliteit van opgeladen KS'en. Daarentegen bieden L-type liganden, die direct aan de Cd-atomen binden die het makkelijkst reduceren, veel stabilisatie tegen oppervlaktereductie. Omdat de L-type liganden na Cd-reductie minder sterk binden aan de Cd-atomen, zorgt de lokalisatie van lading en de daaropvolgende reductie tot een vermindering van de bindingsenergie. Dit maakt oppervlakte reductie niet langer energetisch voordelig. De stabiliteit van opgeladen KS'en kan ook worden vergroot door de polariteit van het oplosmiddel te vergroten, wat laat zien dat het geheel van liganden en de details van de omgeving allemaal een rol spelen in de energetica van oppervlaktereductie.

Voor **Hoofdstuk 6** kijken we naar $CsPbBr_3$ nanokristallen (NK'en). Door de elektronische structuur van hun GB en VB worden lood halide perovskiet NK'en als “defect tolerant”

beschouwd, wat betekent dat onder-gecoördineerde ionen alleen gelokaliseerde niveaus in of dicht bij de GB- en VB-rand vormen. Desalniettemin tonen meerdere studies aan dat onder-gecoördineerde Br^- ionen nog steeds voor valkuil toestanden kunnen zorgen die diep in de bandkloof liggen. In dit onderzoek beargumenteren we dat het traditionele idee van defect tolerantie niet compleet is en ook het effect van de lokale elektrostatische potentiaal zou moeten meenemen. We laten zien dat Br^- ionen op het oppervlak een destabiliserende elektrostatische potentiaal ervaren, die de energie van de gelokaliseerde toestanden verhoogt en zodoende de valkuil toestanden de bandkloof induwt. Door de toevoeging van positieve ionen kunnen deze toestanden elektrostatisch worden gepassiveerd. Dit gaat via ionische interacties, hetgeen laat zien dat een covalente binding met een ligand niet altijd nodig is om valkuil toestanden te passiveren.

Tenslotte zoeken we in **Hoofdstuk 7** de grenzen op van het KS-model dat we in deze thesis gebruikt hebben. Om KS'en van een realistische grootte en met schillen te kunnen onderzoeken, dienen de afmetingen van het KS-model significant te worden vergroot. Echter, door simpelweg het model (zoals dat gebruikt is in Hoofdstukken 3-5) groter te maken, lokaliseren de GB en VB randen zich op het oppervlak van de KS. In dit onderzoek laten we zien dat, hoewel de toevoeging van Z- of L-type liganden de delokalisatie enigszins verbetert, oppervlaktereconstructies noodzakelijk zijn om de niveaus volledig te delokaliseren. Deze oppervlaktereconstructies kunnen mogelijk beschouwd worden als een soort Jahn-Teller distortie, waarbij de reorganisatie van het KS-oppervlak leidt tot de transitie van een metallisch (bandkloof ≈ 0) naar een halfgeleidend systeem (bandkloof > 0).

Ofschoon DFT zeer waardevol is om de atomaire aard van valkuil toestanden in KS'en te onderzoeken, volstaat een enkele blik op de limitaties en uitdagingen van DFT in Hoofdstuk 1 (sectie 1.3.2) om in te zien hoeveel werk nog moet worden verzet. Een duidelijke eerste stap ligt in het voortzetten van het onderzoek gepresenteerd in Hoofdstuk 7. Om valkuil toestanden goed te kunnen onderzoeken in ons modelsysteem, dienen we eerst de eigenschappen van het systeem zonder valkuil toestanden beter te begrijpen. Als deze horde eenmaal genomen is, kunnen bijvoorbeeld KS'en met verschillende schillen onderzocht worden. De formatie van valkuil toestanden wordt echter niet alleen door het anorganische gedeelte van de QD beïnvloedt, maar ook door alle liganden en oplosmiddelen daaromheen (Hoofdstuk 5); door de elektronische toestand van de KS (de grondtoestand of de geëxciteerde toestand); en door de willekeurige thermische beweging van al deze atomen (Hoofdstuk 4). Al deze effecten tegelijk toevoegen zou een computerkracht vereisen die de huidige praktische beperkingen ver ontstijgt. Voor vervolgstudies is het daarom zaak om te beseffen dat we geen berekeningen doen aan echte KS'en, maar aan modellen van echte KS'en; en dat de wetenschappelijke waarde van de verkregen resultaten gelimiteerd wordt door ons begrip van het KS-model. In plaats van alleen te focussen op het groter en ingewikkelder maken van het model (in een poging om het realistischer te maken), kan daarom nog veel inzicht verkregen worden door te bestuderen wat de sterke en zwakke kanten van meer "simplistische" modellen zijn, zoals het model dat in deze thesis gebruikt is.

Acknowledgements

Daunted by the arduous task of having to thank all those who have helped me in the course of the past four years (where accidentally forgetting to mention someone would be tantamount to anathema), I had initially intended to give here an enumeration of those that I specifically did *not* wish to thank. However, after some gentle expostulation from my surroundings, public opinion may rest assured that I have been dissuaded from undertaking such a revolutionary enterprise, and will now continue, in accordance with academic propriety, to express gratitude instead of reservations.

First and foremost, I would like to thank my two promoters. **Arjan**, nobody knows what would have happened if you had not offered me this PhD position (or if you had broached the subject whilst I was not stuck with my hands in the glovebox and had hence been at liberty to run away), but I do know that I am glad that you did. I will not resort to empty platitudes or assert that the past four years were solely composed of the proverbial rainbows and Kumbaya-singing jamborees. What I will say is that, through all the ups and downs, I have learned a lot, worked with wonderful colleagues, received support and guidance when I needed it, and have been enabled to make a humble contribution to society, and for that I am utterly grateful. For sooth, one can expect little more from one's working conditions (but easily receive a whole lot less).

Ferdinand, although we did not meet each other particularly often, every time we did meet, you managed to teach me something new about computational chemistry. Your pragmatic and practical advice has always been of great help, and I always enjoyed the DFT work discussions (which, quite oxymoronically, are not limited to DFT).

Ivan, you have been absolutely indispensable in the completion of this thesis, both through your previous studies, which provided many of the QD models and computational methods used in this thesis; and your personal guidance and support throughout these four years, introducing me to the wondrous world of DFT calculations by teaching me the tricks of the trade at the VU in Amsterdam and the IIT in Genova.

Of all my great colleagues at the OM group, it will come to no surprise that I mention **Jence** (Theodosius) first. We first met each other during our Master in Chemical Engineering, and, owing to our similar, perhaps slightly cynical dispositions, we still accept each other's existence with slightly less disinclination than is our wont with other (as not to say most) people, six years on. In fact, during these four years, you have been of great support to me, and I thoroughly enjoyed the times we could collaborate on a project. Moreover, you can prize yourself in knowing that, excluding myself, you are the only person on this planet to whom the following collection of words presents more than just an enigmatic collection of bizarre ululations: broccoli, plaskantje, Pinkela.

Maarten, I greatly enjoyed sharing an office with you, and, judging from the salient absence of complaints filed against me, I think I may be as presumptuous as to assume the feeling to be mutual. Our numerous discussions covered a wide range of topics, including DFT calculations on InP QDs, cupcakes, and your quest for supporting the local insect population on your (admittedly rather tempest-tossed) balcony. I wish you the best of luck, both in donning your balcony in the richest verdure and in finishing your PhD, and am confident you will succeed in both.

Jaco, working with you has been both great fun and highly informative. I have learned a lot from you about operating the TA set-up, and, although no TA-data have made it into this thesis, they did end up in Science Advances (see List of Publications), which would not have been possible without your, **Gianluca's**, and **Jos's** guidance.

Due to fact that many people left the group right after I started (between which occurrences a causal connection has never been proven), compounded by an unexpected move to a new office after one year, I have amassed quite the number of officemates. **Deepika**, take good care of the house plant cuttings I gave you. Do send me pictures every once in while of how they grow! **Aditya**, **Prashant**, **Guilherme** and **Hamit**, at one point or another we shared an office. I hope any incidental caterwauling on my part (which I would insist was actually a pitch-perfect representation of something like Beethoven's Große Fuge) has not disturbed you too much. Special thanks are in order for **María**, who not only dared to undertake the daunting task of taking a picture of me when one was requested for the "Golden Master Award" (vide infra), but moreover completed the task with such éclat, that her photograph now also adorns the chapter "About the Author". **Maryam**, thank you for introducing me to the wondrous world of Adobe InDesign, which has been instrumental in finalizing this thesis. I would also like to extend my gratitude to the entire **OM group**. You are all kind and caring people, which is no trivial matter and certainly not something that should be taken for granted.

Ward, as my supervisor during my master thesis project, you have played a pivotal role in the long process that eventually culminated in this thesis. Although many people would not find it particularly flattering, I know you will understand what I mean in saying that you were a thoroughly acceptable supervisor (the attentive reader might notice that person-specific lingo is a recurring theme here). If it had not been for your supervision, my master project might have ended a whole lot less acceptably than it did, and who knows what would have become of me then.

During my PhD, I have had the honor of supervising multiple bachelor and master students. **Aydin**, due to some global health inconveniences that shall not be named further, I do not think we ever met during the entire duration of your bachelor project, communicating solely via digital means. Undeterred by these conditions, you worked with great diligence, generating many useful results that eventually even led to the publication of a scientific paper, a most remarkable achievement. **Mirjam**, you had the luxury of having not one but two supervisors, working with both Jaco and me. I look back fondly on the Zoom meetings we had with the three of us, where we would spend hours on the modeling of "wiggles", occasionally beguiling the time by the creation of increasingly elaborate

memes. Due to circumstances, your results on phonon coupling did not make it into this thesis, but rest assured that the quality of your master thesis had nothing to do with that. **Anne**, somehow you managed to surpass Mirjam's already notable accomplishment of acquiring two supervisors, by rallying three. As also mentioned in the speech given at your graduation ceremony (regarding which I have to take the responsibility for any occasional grandiloquence), you signed up for an experimental master thesis project, but ended up doing computational work. Nevertheless, it led to the results that form the basis of Chapter 6 in this thesis. **Snigdha**, you continued where Aydin had left off, generating the data now presented in Chapter 5. I could talk about your scrupulous working attitude and quick mind, or how you went on to become a PhD candidate at the University of Oxford; but instead, I would like to mention that it is rare to encounter such a congenial spirit, and I am glad we still keep in touch. **Ruud**, with you I once again continued my lucky streak of hard-working, talented students. Although we had initially intended to publish your results as a separate paper, they eventually found their place under the wings of an experimental study, contributing to a much more insightful discussion.

No PhD project is complete without collaborations with other groups or universities. **Stephanie**, thank you for teaching me how to use CP2K and working with me on the project that now constitutes Chapter 3. **Simon**, your help and insights were crucial for the work presented in Chapter 4. **Bas** and **Felipe**, thank you for helping me out during my brief sojourn at the eScience Center (which resulted in the workflows for computing the COOP and IPR, as used in Chapters 6 and 7), and whenever I ran into a problem whilst using Nano-QMFlows.

Vidya, when we first met, we were both master students at OM, and now we are both PhD candidates (although your position has led you to the other side of the Atlantic). I truly miss the times when we would attend the performances of the Rotterdam Philharmonic Orchestra on a monthly basis. Casting angry glances at octogenarians whose conduct is in violation of the strict concert etiquette is much more fun when done with two sets of eyes. I wish you the best of luck with finishing your PhD and sincerely hope our gaze shall rest once again on the wizened and hoary heads of our fellow concert goers.

Quaint though it may seem, here I would also like to thank my **garden** (I actually claimed both my parents' and my sister's garden as my own, but let us not dwell on such minor details). Although quite aware that plants are generally not in the habit of reading and hence cannot appreciate this brief exaltation, I felt these acknowledgements would be incomplete without my mentioning the sublime serenity and joy that are enkindled by observing how plants thrive and insect life teems by dint of one's own gentle but incisive hand; and should these words inspire but a single soul to trade their flagstones for foliage, I would already consider this thesis to be a success.

Last, but definitely not least, my thanks go out to my **parents**, my **sister**, and our cats, **Gizmo** and **Muffin**, for believing in me when I doubted myself, for supporting me throughout these four years, and for providing me with the stability of a loving home (though the feline contribution had perhaps a slight tendency towards pandemonium). This thesis would not have been possible without you.

List of Publications

This thesis was based on the following publications:

• Ward van der Stam, Indy du Fossé, Gianluca Grimaldi, Julius O. V. Monchen, Nicholas Kirkwood, Arjan J. Houtepen. "Spectroelectrochemical Signatures of Surface Trap Passivation on CdTe Nanocrystals". Chemistry of Materials, 2018, 30 (21), 8052-8061. (Chapter 2)

• Indy du Fossé, Stephanie ten Brinck, Ivan Infante, Arjan J. Houtepen. "Role of Surface Reduction in the Formation of Traps in n-Doped II–VI Semiconductor Nanocrystals: How to Charge without Reducing the Surface". Chemistry of Materials, 2019, 31 (12), 4575-4583. (Chapter 3)

• Indy du Fossé, Simon C. Boehme, Ivan Infante, Arjan J. Houtepen. "Dynamic Formation of Metal-Based Traps in Photoexcited Colloidal Quantum Dots and Their Relevance for Photoluminescence". Chemistry of Materials, 2021, 33 (9), 3349-3358. (Chapter 4)

•Indy du Fossé, Snigdha Lal, Aydin Najl Hossaini, Ivan Infante, Arjan J. Houtepen. "Effect of Ligands and Solvents on the Stability of Electron Charged CdSe Colloidal Quantum Dots". Journal of Physical Chemistry C, 2021, 125 (43), 23968-23975. (Chapter 5)

• Indy du Fossé, Jence T. Mulder, Guilherme Almeida, Anne G. M. Spruit, Ivan Infante, Ferdinand C. Grozema, Arjan J. Houtepen. "Limits of Defect Tolerance in Perovskite Nanocrystals: Effect of Local Electrostatic Potential on Trap States". Journal of the American Chemical Society, 2022, 144 (25), 11059-11063. (Chapter 6)

Other publications:

• Jara Garcia Santaclara, Alma I. Olivos-Suarez, Indy du Fossé, Arjan J. Houtepen, Johannes Hunger, Freek Kapteijn, Jorge Gascon, Monique A. van der Veen. "Harvesting the photoexcited holes on a photocatalytic proton reduction metal–organic framework". Faraday Discussions, 2017, 201, 71-86.

• Nicholas Kirkwood, Julius O. V. Monchen, Ryan W. Crisp, Gianluca Grimaldi, Huub A. C. Bergstein, Indy du Fossé, Ward van der Stam, Ivan Infante, Arjan J. Houtepen. "Finding and Fixing Traps in II–VI and III–V Colloidal Quantum Dots: The Importance of Z-Type Ligand Passivation". Journal of the American Chemical Society, 2018, 140 (46), 15712-15723.

• Gianluca Grimaldi, Jaco J. Geuchies, Ward van der Stam, Indy du Fossé, Baldur Brynjarsson, Nicholas Kirkwood, Sachin Kinge, Laurens D. A. Siebbeles, Arjan J. Houtepen.

"Spectroscopic Evidence for the Contribution of Holes to the Bleach of Cd-Chalcogenide Quantum Dots". Nano Letters, 2019, 19 (5), 3002-3010.

• Gianluca Grimaldi, Mark J. van den Brom, Indy du Fossé, Ryan W. Crisp, Nicholas Kirkwood, Solrun Gudjonsdottir, Jaco J. Geuchies, Sachin Kinge, Laurens D. A. Siebbeles, Arjan J. Houtepen. "Engineering the Band Alignment in QD Heterojunction Films via Ligand Exchange". The Journal of Physical Chemistry C, 2019, 123 (49), 29599-29608.

• Jaco J. Geuchies, Baldur Brynjarsson, Gianluca Grimaldi, Indy du Fossé, Robbert Dijkhuizen, Marijn Koel, Solrun Gudjonsdottir, Ward van der Stam, Wiel H. Evers, Pieter Geiregat, Zeger Hens, Arjan J. Houtepen. "Quantitative electrochemical control over optical gain in colloidal quantum-dot and quantum-well solids". Physical Chemistry of Semiconductor Materials and Interfaces XIX, 2020, 11464, 43-61.

• Shuai Fu, Indy du Fossé, Xiaoyu Jia, Jingyin Xu, Xiaoqing Yu, Heng Zhang, Wenhao Zheng, Sven Krasel, Zongping Chen, Zhiming M. Wang, Klaas-Jan Tielrooij, Mischa Bonn, Arjan J. Houtepen, Hai I. Wang. "Long-lived charge separation following pump-wavelength–dependent ultrafast charge transfer in graphene/WS2 heterostructures". Science Advances, 2021, 7 (9), eabd9061.

• Jence T. Mulder, Indy du Fossé, Maryam Alimoradi Jazi, Liberato Manna, Arjan J. Houtepen. "Electrochemical p-Doping of CsPbBr3 Perovskite Nanocrystals". ACS Energy Letters, 2021, 6 (7), 2519-2525.

• Jaco J. Geuchies, Robbert Dijkhuizen, Marijn Koel, Gianluca Grimaldi, Indy du Fossé, Wiel H. Evers, Zeger Hens, Arjan J. Houtepen. "Zero-Threshold Optical Gain in Electrochemically Doped Nanoplatelets and the Physics Behind It". ACS Nano, 2022, 16 (11), 18777-18788.

• Reinout F. Ubbink, Guilherme Almeida, Hodayfa Iziyi, Indy du Fossé, Ruud Verkleij, Swapna Ganapathy, Ernst R. H. van Eck, Arjan J. Houtepen. "A Water-Free In Situ HF Treatment for Ultrabright InP Quantum Dots". Chemistry of Materials, 2022, 34 (22), 10093-10103.

• Jence T. Mulder, Michael Meijer, J. Jasper van Blaaderen, Indy du Fossé, Kellie Jenkinson, Sara Bals, Liberato Manna, Arjan J. Houtepen. "Understanding and Preventing Photoluminescence Quenching to Achieve Unity Photoluminescence Quantum Yield in Yb:YLF Nanocrystals". Submitted.

About the Author

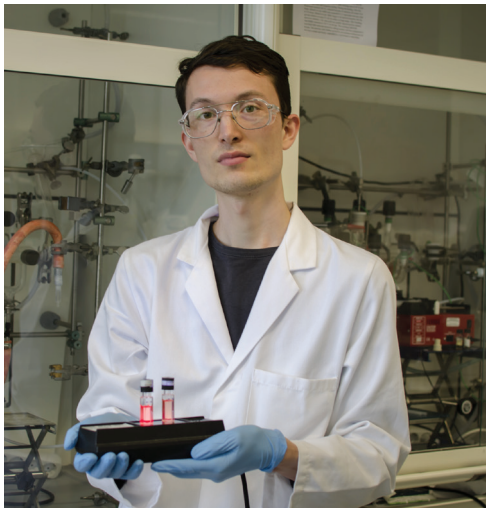

Indy du Fossé was born on the 25th of February 1995 in the town of Spijkenisse, a place few would be inclined to call attractive, but he is still happy to call his home. In 2013, he graduated from PENTA College CSG Scala Rietvelden, after which he continued his studies at Delft University of Technology. There he studied Molecular Science and Technology, resulting in the "Jong Talent Aanmoedigingsprijs" for the completion of his propedeuse in 2014, and his cum laude bachelor's degree in 2016. The results he obtained for his bachelor thesis, on the charge transfer between a photoexcited metal-organic framework and different molecular charge acceptors, were later used for a publication in Faraday Discussions (see List of Publications). Extending his sojourn at Delft University of Technology, he finished his master's degree in Chemical Engineering cum laude in 2018, receiving the KNCV Golden Master Award for his master thesis in 2019. In September 2018, he prolonged his stay at Delft once again (thus quite stepping over the limit of what could reasonably be deemed a "sojourn") when he commenced his PhD project "Combined Theoretical and Optical Studies of Quantum Dot Surfaces" in the Optoelectronic Materials section, under the supervision of Prof. dr. Arjan J. Houtepen.

Either to parry the pangs of ennui, or to satisfy his striving for accomplishment (alas, usually quite in vain), Indy has dabbled in a myriad of hobbies during the last quarter century, ranging from following a course on the history of architecture to joining a youth circus. He is an avid fan of classical music, a reasonably skilled pianist, and has recently joined the choir "Kleinkoor Ars Nova", where he rummages amongst the octogenarians on a weekly basis. In addition, he enjoys reading "classic" literature (the exact definition of which interests him little), visiting art museums, and gardening in his backyard.